Novel Isotope Techniques for Basin Exploration: In Situ Geochronology and Metal Isotope Analysis of Mid-Cambrian Authigenic Minerals from the Georgina Basin, Australia

Zhufu Shao

This thesis is submitted in fulfilment of the requirements for the degree of Doctor of Philosophy

School of Physics, Chemistry and Earth Sciences

Faculty of Sciences, Engineering and Technology

The University of Adelaide

May 2025

Table of Contents

Abstract

The Cambrian Period witnessed the rapid diversification of metazoan clades during the "Cambrian Explosion," reflecting significant shifts in oceanic biogeochemical, ecological dynamics, and redox conditions across the Ediacaran–Cambrian transition. This interval is also characterized by high-frequency global disturbances in the carbon cycle, with up to ten marine δ^{13}C excursions identified. Among these, the Drumian carbon isotope excursion (DICE), a major negative δ^{13}C shift near the Wuliuan–Drumian boundary (~504.5 Ma), is associated with global sea-level rise and extinction events. In contrast to the well-documented marine δ^{13}C excursions, the mid-Cambrian seawater chemistry recorded by non-traditional metal isotopes such as potassium (δ^{41}K) and magnesium (δ^{26}Mg) remains poorly constrained.

To address this gap, this thesis integrates novel *in situ* (LA-ICP-MS/MS) dating of marine authigenic minerals (glauconite, calcite, dolomite, and apatite) along with δ^{41}K and δ^{26}Mg analyses, complemented by conventional C–O–Sr isotope data from bulk carbonates and phosphatic fossils (e.g., small shelly fossils and linguliform brachiopods). The study focuses on mid-Cambrian shallow marine carbonate sequences from the Georgina Basin (~505 ± 3 Ma), aiming to constrain depositional ages, assess diagenetic alteration, and reconstruct seawater chemistry.

A triple *in situ* geochronological approach was employed, combining Rb–Sr dating of glauconite, U–Pb dating of carbonates, and both U–Pb and Lu–Hf dating of apatite. Glauconite Rb–Sr dating yielded systematically younger ages between 452 ± 13 Ma and 351 ± 8 Ma, corresponding to two episodes of the Alice Springs Orogeny (~450–300 Ma). In contrast, well-preserved micrite and fine-crystalline dolomite yielded U–Pb ages of 500 ± 17 Ma and 513 ± 19 Ma, consistent with depositional timing. Apatite U–Pb dating yielded scattered and partially reset ages due to diagenetic uranium (U) loss, while Lu–Hf dating yielded ages from 497 ± 69 Ma to 493 ± 74 Ma that overlap with the estimated depositional ages, despite large uncertainties caused by low Lu concentrations.

Solution-based MC-ICP-MS analyses of glauconite show variable δ^{41}K (NIST 3141a) values from -0.41‰ to -0.11‰ and δ^{26}Mg (DSM3) values from -0.52‰ to 0.61‰. These variations are attributed to two factors: progressive illitization, which increases both δ^{41}K and δ^{26}Mg values, and the impact of carbonate micro-inclusions, which tend to lower δ^{26}Mg. Mineralogical and chemical data confirm post-depositional changes, including secondary dolomite, calcite, and apatite inclusions. However, the least altered glauconite samples (with Rb–Sr ages near the depositional age) may preserve original seawater signatures. Assuming that K and Mg isotope fractionations between modern seawater and glauconite ($\Delta^{41}\mathrm{K}_{\text{sw-glauconite}}$ = ~+0.90‰; $\Delta^{26}\mathrm{Mg}_{\text{sw-glauconite}}$ = ~0.00‰) were similar during the mid-Cambrian, these glauconite-based estimates of δ^{41}K and δ^{26}Mg values for mid-Middle Cambrian seawater range from +0.45 to +0.65‰, and -0.20 to +0.10‰, respectively. Both paleo-seawater δ^{41}K and δ^{26}Mg values are systematically higher than those of modern seawater (δ^{41}K = +0.12‰ and δ^{26}Mg = -0.83‰).

Mid-Cambrian carbonate samples from the Georgina Basin exhibit δ^{26}Mg values ranging from -3.05‰ to -1.00‰, reflecting a clear mixing trend between calcite and dolomite. Dolostones with Mg/Ca molar ratios ~1 show higher δ^{26}Mg values (-1.92‰ to -1.00‰) and are relatively resistant to diagenetic alteration. These dolostones likely preserve the primary mid-Cambrian seawater signature and/or that of dolomitizing fluids. Using an estimated Mg isotope fractionation factor between seawater and dolomite ($\Delta^{26}\mathrm{Mg}_{\text{sw–dolomite}}$ = ~1.73–2.00‰), the δ^{26}Mg value of mid-Cambrian seawater is inferred to be approximately -0.19 to +0.08‰. This estimate aligns with previous studies and agrees well with δ^{26}Mg values reconstructed from coeval glauconite (-0.20 to +0.10‰).

In summary, this thesis demonstrates the potential and limitations of applying novel *in situ* geochronology techniques, including Rb–Sr, Lu–Hf, U–Pb, to ancient marine archives such as authigenic carbonates, clay minerals and apatite to constrain their depositional and formation ages. The integrated use of non-traditional metal isotope proxies (δ^{41}K and δ^{26}Mg) and traditional tracers (δ^{13}C, δ^{18}O, and ^{87}Sr/^{86}Sr) provides valuable tools for reconstructing mid-Cambrian seawater chemistry and tracing the influence of non-marine diagenetic or dolomitizing fluid. These approaches provide new insights into the preservation of isotopic signatures in marine sediments and enable the differentiation of primary marine signals from diagenetic overprints.

Declaration

I certify that this work contains no material which has been accepted for the award of any other degree or diploma in my name in any university or other tertiary institution and, to the best of my knowledge and belief, contains no material previously published or written by another person, except where due reference has been made in the text. In addition, I certify that no part of this work will, in the future, be used in a submission in my name for any other degree or diploma in any university or other tertiary institution without the prior approval of the University of Adelaide and where applicable, any partner institution responsible for the joint award of this degree.

The author acknowledges that copyright of published works contained within this thesis resides with the copyright holder(s) of those works.

I give permission for the digital version of my thesis to be made available on the web, via the University's digital research repository, the Library Search and also through web search engines, unless permission has been granted by the University to restrict access for a period of time.

I acknowledge the support I have received for my research through the provision of an Australian Government Research Training Program Scholarship.

Zhufu Shao

26th May 2025

Acknowledgements

Firstly, I would like to sincerely thank my supervisors, Juraj Farkaš, Alan Collins, and Stijn Glorie, for their invaluable guidance and continuous support throughout my PhD journey. Their expertise and insightful advice have greatly influenced my research and academic development. I am particularly grateful for their constructive feedback and support in project design, data collection, interpretation, and manuscript preparation.

I sincerely thank all the MIG and TES group members, including Darwin, Stefan, Morgan, Cecilia, Yaser, Elnaz, Jarred, Alex, Angus, Melissa, Alejandra, Zara, Ananyaa, Dana, Georgina, Shengxian, Dongtao, and Ruiqi, for their warm support. Whether through help with data processing, engaging discussions, or group activities, your kindness made me feel at home. You have greatly enriched my experience, both professionally and personally, and your contributions have positively impacted my research.

I am also grateful to all the collaborators who supported the experiments and data collection. Special thanks to Xinyuan, Yisheng, and Juzer from the University of Minnesota for assistance with K and Mg isotope analysis; Rob for C, O, and Sr isotope analysis; Sarah for LA-ICP-MS/MS work; Ben for EPMA analysis; Nobuyuki and Sean for SEM-EDS work; and Glenn and Jack from Macquarie University for fossil separation.

I would like to acknowledge the financial support provided by the University of Adelaide, the Australian Research Council (ARC), and MinEx CRC, all of which made this research possible.

Finally, I am deeply grateful to my family. My heartfelt thanks go to my wife, Lynn, who has selflessly supported our family while working and caring for our children, allowing me to relocate to Adelaide and fully dedicate myself to my PhD. During this time, our son was born, and I truly appreciate the continued support from my parents and parents-in-law, who helped care for our two children. My lovely daughter and son have also given me endless support. Their love and dedication have given me the strength and courage to keep moving forward.

I also dedicate this thesis to my late father, with love and remembrance.

PhD Research Outputs

Journal Articles

1. Chapter 2 has been published in the journal *Chemical Geology*.
2. Chapter 3 is to be submitted to the journal *Earth and Planetary Science Letters*.
3. Chapter 4 is to be submitted to the journal *Geochimica et Cosmochimica Acta*.

Zhufu Shao, Juraj Farkaš, Stijn Glorie, Alan S. Collins, Sarah E. Gilbert, Darwinaji Subarkah. 2025. Dating of Marine Authigenic Minerals via *in situ* Rb–Sr, U–Pb, and Lu–Hf: Insights into Deposition, Diagenesis, and Tectonics in Sedimentary Basins. (published in *Chemical Geology*).

Zhufu Shao, Juraj Farkaš, Xin-Yuan Zheng, Alan S. Collins, Stefan C. Löhr, Andre Baldermann. 2025. Coupling Potassium and Magnesium Isotope Proxies (δ^{41}K and δ^{26}Mg) in Cambrian Glauconites to Constrain Paleo-Seawater Composition and Diagenetic Alteration. (To be submitted to *Earth and Planetary Science Letters*).

Zhufu Shao, Juraj Farkaš, Xin-Yuan Zheng, Glenn A. Brock, Alan S. Collins. 2025. Magnesium isotope constraints on the mid-Cambrian seawater, marine Mg cycling and dolomitization during the Drumian Carbon Isotope Excursion (DICE) event. (To be submitted to *Geochimica et Cosmochimica Acta*).

Conference Abstracts

1. **Zhufu Shao**, Juraj Farkaš, Xin-Yuan Zheng, Alan S. Collins, Stefan Löhr. Potassium Isotope Variations (δ^{41}K) in Cambrian Glauconites from Australia and China: Insights into Paleo-Seawater and Diagenetic Alteration. Goldschmidt 2025 Conference. *Goldschmidt*, 2025.
2. **Zhufu Shao**, Juraj Farkaš, Alan S. Collins, Stijn Glorie, Darwinaji Subarkah, Sarah E. Gilbert, Stefan Löhr, Charles Verdel, Diana Zivak, Carl Spandler. *In situ* triple-dating (Rb–Sr, Lu–Hf, U–Pb) of carbonate-hosted glauconite and apatite from the Middle Cambrian Georgina Basin, Australia. Goldschmidt 2023 Conference. *Goldschmidt*, 2023.
3. Darwinaji Subarkah, Angus Nixon, Alan S. Collins, Sarah E. Gilbert, Morgan L. Blades, Georgina M. Virgo, Alexander Simpson, **Zhufu Shao**, Juraj Farkaš. New ways to date old rocks: novel applications of *in situ* geochronology to constrain the sedimentary archive. Goldschmidt 2023 Conference. *Goldschmidt*, 2023.
4. **Zhufu Shao**, Juraj Farkaš, Alan S. Collins, Sarah E. Gilbert, Darwinaji Subarkah. Diagenetic Constraints on Glauconite Rb–Sr Ages: *in situ* LA-ICP-MS/MS, Geochronology, Micropetrography, and Elements—a Case Study from the Mid-Cambrian Georgina Basin, Australia. IAGS 2024 Conference, IAGS. 2024.

Chapter 1: Introduction

1.1 Thesis Aims and Rationale

Sedimentary basin and rocks host abundant mineral and energy resources, including hydrocarbons and various types of ore deposits, and also preserve valuable records of the long-term environmental, climatic, and biological evolution. Constraining the timing of marine sediment deposition as well as hydrocarbon accumulation, metal mineralization, and sedimentary rock diagenesis is crucial for both resource exploration and fundamental geological research (Wu et al., 2023). However, a direct dating of sediment deposition and the timing of diagenesis and subsequent tectonic events remain significant challenges for geochronologists, particularly in fossil-poor Precambrian strata (Shao et al., 2025). In recent years, newly developed LA-ICP-MS/MS geochronology techniques, such as *in situ* Rb–Sr, U–Pb and Lu-Hf dating, have been applied to marine sedimentary rocks and authigenic minerals (Clauer et al., 2019; Löhr et al., 2024; Redaa et al., 2021; Redaa et al., 2023; Subarkah et al., 2022; Glorie et al., 2022; Glorie et al., 2023; Lan et al., 2025).

Related to the above, marine authigenic / diagenetic processes in the ocean such as reverse weathering acts as a critical sink for the continental- and/or seafloor-derived elemental fluxes, including alkali and alkaline earth metals (e.g., K^+, Mg^{2+}, Ca^{2+}, and Li^+) which tend to be incorporated into the formation of marine authigenic clays and carbonates (Farkaš et al., 2025; Li et al., 2022; Zheng et al., 2022a). Together with continental silicate weathering and carbonate reactions, marine reverse weathering plays a key role in regulating global carbon cycling and thus the climate stability on Earth (Baldermann et al., 2025; Isson and Rauzi, 2024; Isson and Planavsky, 2018; Li et al., 2022; Mu et al., 2024; Xia et al., 2024). Stable K and Mg isotopes, expressed as $\delta^{41}K$ and $\delta^{26}Mg$ (in per mil, ‰), exhibit significant isotope fractionation during low-temperature biogeochemical processes, offering valuable insights into the pathways of silicate/carbonate and reverse weathering processes, and the evolution of seawater chemistry through geological time (Li et al., 2022; Ramos et al., 2018; Teng et al., 2010; Xia et al., 2024; Zheng et al., 2022a).

Thus far, most research on K and Mg isotopes has focused either on high-temperature igneous rocks and low-temperature carbonate or continental weathering systems. In contrast, no robust reconstruction of paleo-seawater δ^{41}K has yet been established. Studies on marine authigenic clays or siliciclastic sedimentary archives remain in their infancy, with only a few published studies and limited δ^{41}K and δ^{26}Mg datasets available to date. As a relatively ubiquitous marine authigenic silicate phase, glauconite is a potential promising archive for reconstructing paleo-seawater K and Mg isotope composition through time (Löhr et al., 2023; Löhr et al., 2025, under review; Shaikh et al., 2024). However, the effects of diagenesis/burial processes on glauconite-based δ^{41}K and δ^{26}Mg proxies, and their possible resetting, remain poorly constrained, especially for ancient glauconite pellets with prolonged diagenetic and deep burial histories. This thesis thus aims to address those knowledge gaps by investigating stable K and Mg isotope variations, coupled with in situ Rb-Sr dating, applied to the Cambrian glauconites. The Cambrian was a key period in Earth's history, marked by the assembly of Gondwana, global warming, and most importantly, the Cambrian explosion of complex animal life, marking a major biological and geochemical shift on our planet during this time (Peters and Gaines, 2012; Scotese et al., 2021; Sun et al., 2023; Wang et al., 2024; Zhang et al., 2020). Several global marine carbon isotope (δ^{13}C) excursions have been identified throughout the Cambrian, indicating connections between marine C cycle, frequent environmental changes and complex cycles of extinction and radiation (Gill et al., 2011; Wang et al., 2024; Zhang et al., 2020; Zhu et al., 2006). Among these, the Drumian carbon isotope excursion (DICE), a significant negative δ^{13}C shift near the Wuliuan–Drumian boundary at ca. 504.5 Ma (Babcock et al., 2004; Babcock et al., 2007; Howley and Jiang, 2010; Yang et al., 2021; Zhu et al., 2006), has also been recorded in the Georgina Basin, Australia (Pagès and Schmid, 2016; Pagès et al., 2016).

The Georgina Basin in Australia, which is the primary research target for this thesis, comprises the Neoproterozoic to Paleozoic strata deposited in a polyphase intracratonic basin that forms part of the Centralian Superbasin (Kruse et al., 2013; Walter et al., 1995). The Cambrian deposition in the Georgina Basin is characterized by rift-related basin setting in the southern depocenter, and shallow marine carbonate platform deposition in the north (Kruse et al., 2013; Pagès and Schmid, 2016). This basin hosts significant economic potential for both hydrocarbons and minerals, including phosphorite, zinc and lead (Carr et al., 2016; Dunster et al., 2007; Kruse et al., 2013; Tenthorey and Ayling, 2021; Valetich et al., 2022). However, the links between sedimentary records, ocean chemistry and global elemental cycles, recorded in the Georgina Basin, remain poorly understood, and its global correlation is also mostly unresolved. To address this knowledge gap, establishing an absolute chronostratigraphic framework for the Georgina basin and its marine archives and proxy records is essential and also relevant for the correlations within the Centralian Superbasin and global comparisons. Additionally, new metal isotope proxies, such as δ^{41}K and δ^{26}Mg tracers, have also proven valuable in reconstructing diagenetic histories of marine archives, and potentially the paleo-seawater composition, with implications for past changes in continental weathering, dolomitization, global carbon cycle, and climate change (Li et al., 2022; Ramos et al., 2018; Teng et al., 2010; Xia et al., 2024). However, the successful application of these novel isotope proxies largely depends on a better understanding of the post-depositional impacts on these isotopic systems, particularly linked to diagenesis, burial, later stage dolomitization, fluid-rock interactions, hydrothermal activity and tectonics (Bialik et al., 2018; Hu et al., 2017; Hu et al., 2019; Li et al., 2022; Parendo et al., 2022; Qiu et al., 2024; Xia et al., 2024).

Hence, this thesis aims to enhance our understanding of the above processes on marine isotope proxies and *in situ* dating applied to the Cambrian archives such as authigenic clays (glauconite), carbonates (calcite, dolomite) and phosphates deposited in the Georgina Basin. Specifically, this thesis focuses on the mid-Cambrian (Miaolingian) shallow marine carbonate sequences (hosting glauconite pellets and apatite grains) which have an estimated depositional age of ca. 505 ± 3 Ma (Laurie, 2022; Pagès and Schmid, 2016; Pagès et al., 2016; Smith et al., 2013).

The first objective was to apply and test *in situ* LA-ICP-MS geochronology methods to directly date marine authigenic mineral phases (silicates/clays, carbonates, phosphates) using a triple-dating approach. This approach combines Rb–Sr dating of glauconite, U–Pb dating of carbonate minerals, and both U–Pb and Lu–Hf dating of apatite.

The second objective was to evaluate the effects of diagenetic and post-depositional overprinting of the above geochronometers or radiometric ages in authigenic minerals, with a particular focus on the diagenetic resetting of Rb–Sr ages in glauconite associated with local/regional tectonic or orogenic events impacting the Georgina Basin.

The third objective was to reconstruct the K and Mg isotopic composition of the mid-Cambrian seawater based on $\delta^{41}K$ and $\delta^{26}Mg$ analysis (via solution MC-ICP-MS) of marine authigenic clays (glauconite) and carbonates; and to assess the impact of diagenetic processes on these metal isotope proxies.

The fourth objective was to investigate the sedimentary and paleo-depositional environment, marine Mg cycling, and dolomitization processes through an integrated chemostratigraphic approach. This involves the use of $\delta^{26}Mg$, $\delta^{13}C$, $\delta^{18}O$, and $^{87}Sr/^{86}Sr$ isotope proxies recorded in mid-Cambrian carbonates (dolostones, limestones) from the Georgina Basin, alongside an evaluation of diagenetic overprinting on these isotope proxies. An additional or related aim of this objective was to facilitate global stratigraphic correlation, particularly between Australia (Georgina Basin) and other continents/paleo-locations (China) during the Miaolingian, using C isotope records associated with the DICE event.

Overall, this thesis integrates innovative geochronological methods, including *in situ* Rb–Sr, U–Pb and Lu–Hf dating, with stable metal isotope proxies in marine authigenic clays ($\delta^{41}K$ and $\delta^{26}Mg$) and carbonates ($\delta^{26}Mg$), together with traditional isotopic systems ($\delta^{13}C$, $\delta^{18}O$, and $^{87}Sr/^{86}Sr$), to date marine sedimentary rocks, reconstruct paleo-seawater geochemistry and evaluate diagenetic processes, based on the case studies from the Georgina Basin in Australia.

1.2 Geological Background

The Centralian Superbasin in Australia is a large intracratonic basin that comprises strata from the Neoproterozoic to the early Paleozoic and covers extensive regions of northern, central, and southern Australia (Fig. 1). This large depositional system is subdivided into the Centralian A Superbasin, which comprises Neoproterozoic sequences, and the Centralian B Superbasin, which contains Cambrian to Devonian strata. The two systems are separated by a major unconformity associated with the Petermann Orogeny (Fig. 1; Munson et al., 2013).

The Georgina Basin is located in the northeastern part of the Centralian Superbasin (Fig. 1), extending from the Northern Territory into Queensland and covering an area of approximately 3.3 × 10^5 km^2 (Dunster et al., 2007; Khider, 2021; Kruse et al., 2013; Walter et al., 1995). This basin comprises two distinct domains: (1) the southern basinal depocenter, located south of 21°S, which hosts Cryogenian to Devonian successions; and (2) the central and northern platform, located north of 21°S, which predominantly consists of Neoproterozoic and mid-Cambrian carbonate platform sequences (Bradshaw et al., 2021; Khider, 2021; Kruse et al., 2013; Munson, 2014; Tenthorey and Ayling, 2021).

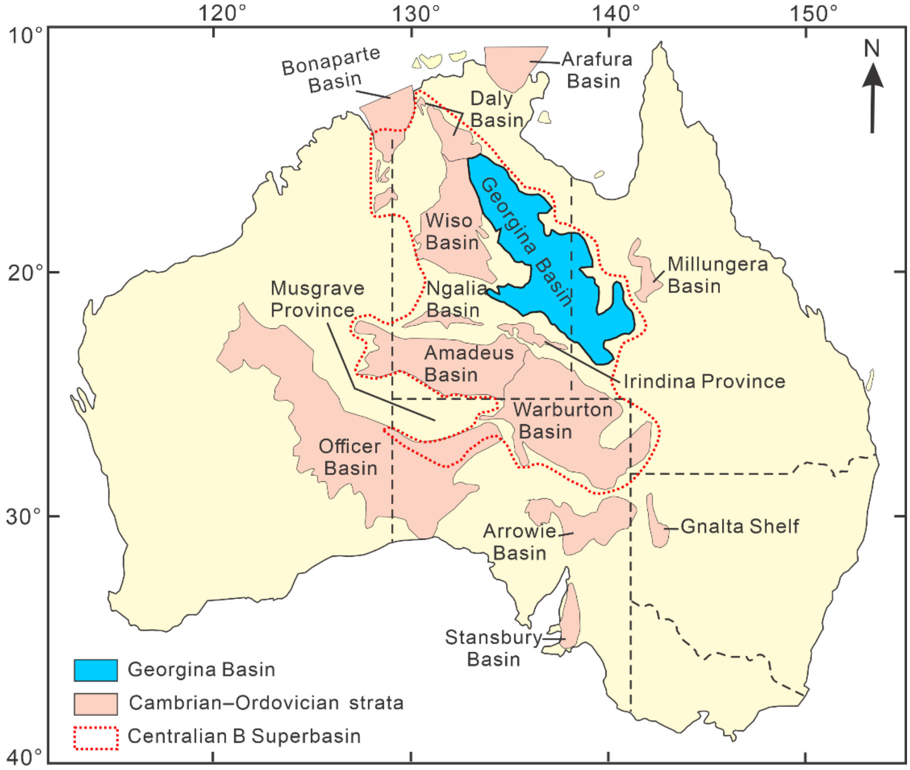

Figure 1: Distribution of the Centralian B Superbasin and location of the Georgina Basin (modified from Munson et al., 2013)

The Georgina Basin is divided into eight sub-basins or structural components/belts. To the north, the Undilla Sub-basin and the Central Sub-basin are separated by the Alexandria-Wonarah Block. To the south, the Dulcie Syncline and Toko Syncline connect the Elkedra Shelf in the west to the Burke River Structure Belt in the east (Fig. 2a; Khider et al., 2021; Pagès et al., 2016; Smith et al., 2013).

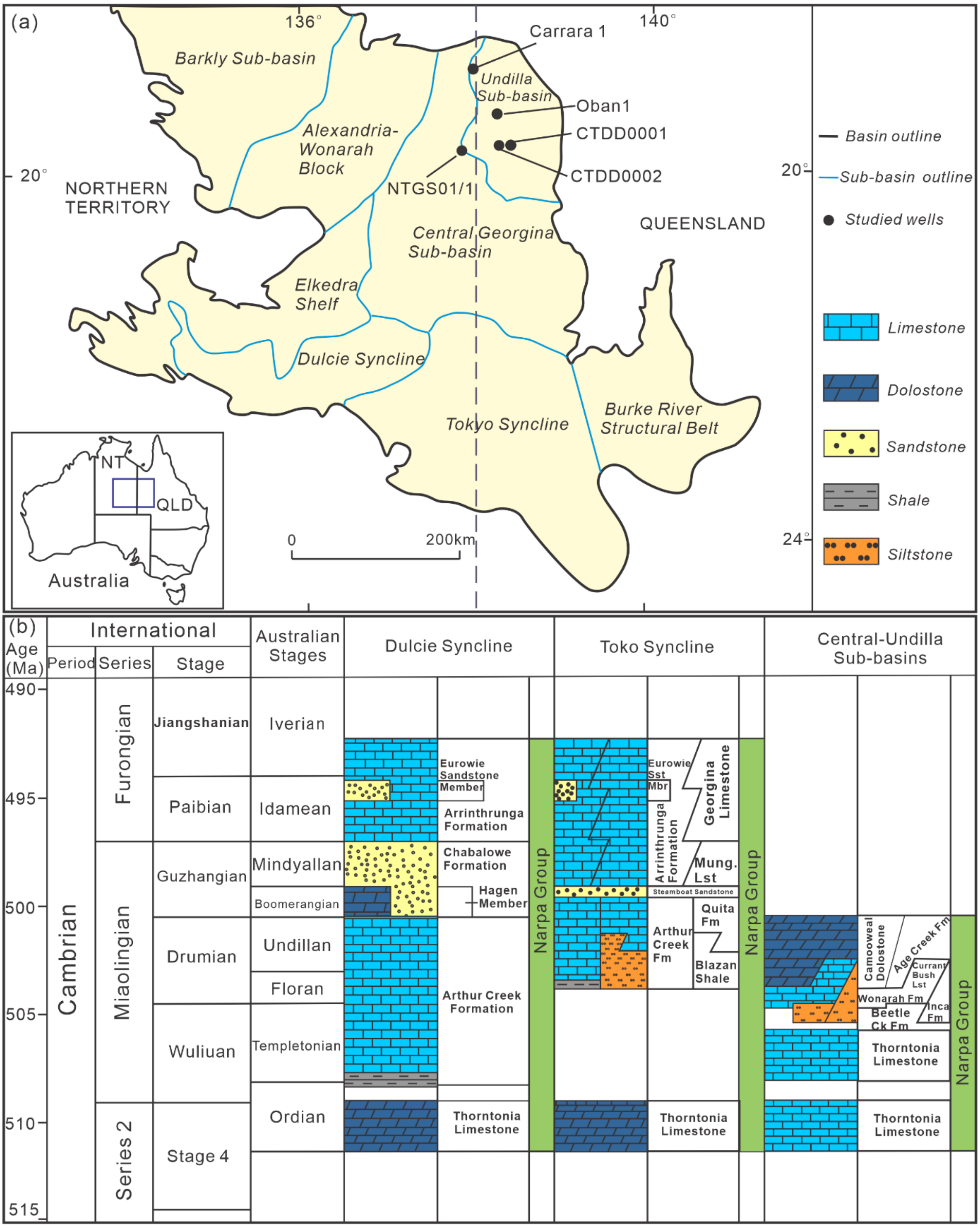

Figure 2. (**a**) Location of the Georgina Basin in Australia (adapted from Kruse et al., 2013; Walter et al., 1995); (**b**) Stratigraphy of the Middle Cambrian Narpa Group (adapted from Laurie, 2022; Pagès and Schmid, 2016; Smith et al., 2013).

The stratigraphy of the Georgina Basin comprises: 1) Neoproterozoic (ca. 850–570 Ma) rift-related fluvioglacial to marine siliciclastic rocks with a minor carbonate component; 2) Cambrian to Ordovician (ca. 530–450 Ma) marine carbonate-dominated sequences interbedded with siltstone, shale, and volcanic rocks; and 3) Devonian foreland siliciclastic rocks, including aeolian and fluvial-delta to shallow marine deposits, scattered throughout the basin (Dunster et al., 2007; Khider et al., 2021; Walter et al., 1995). The sedimentary sequences are unevenly distributed, forming a wedge that ranges in thickness from 1500 meters in the southern depocenter to 300 meters in the north, and the sediments of the Georgina Basin are overlain by Mesozoic strata of the Eromanga Basin (Carr et al., 2016).

The geological, depositional and tectonic evolution of the Georgina Basin began with sag-related siliciclastic deposition of the Tonian Plenty Group on the Mesoproterozoic basement (Khider et al., 2021). This development was interrupted by several orogenic events, the most significant of which were the Petermann and Alice Springs Orogenies (Haines et al., 2001; Hand et al., 1999; Khider et al., 2021; Kruse et al., 2013; Nixon et al., 2022; Piazolo et al., 2020; Varga et al., 2022). The Petermann Orogeny (570–530 Ma), a north–south compressional event, caused regional uplift and a major sedimentary hiatus in the Georgina Basin, marking the termination of Centralian Superbasin A (Kruse et al., 2013). The Alice Springs Orogeny (450–300 Ma) represented another phase of north–south compressional deformation, which led to widespread thrusting, uplift, and exhumation, and ultimately terminated Centralian Superbasin B (Haines et al., 2001; Nixon et al., 2022; Piazolo et al., 2020; Varga et al., 2022). Following the eruption of the Kalkarindji Large Igneous Province (LIP) around 511 Ma in the late Early Cambrian (Glass and Phillips, 2006; Khider et al., 2021; Nixon et al., 2022), rift-related sedimentation resumed in the Georgina Basin. This led to the deposition of platform to marine facies of the mid-Cambrian Narpa Group (Fig. 2b; Kruse et al., 2013; Pagès and Schmid, 2016), which is the main focus of this thesis. The Narpa Group consists of two depositional sequences (Southgate and Shergold, 1991). Sequence 1 (Ordian) includes the Thorntonia Limestone in the southern basin, which is equivalent to the lower Thorntonia Limestone and Waterhole Formation in the Undilla Subbasin, as well as the Gum Ridge Formation in the Barkly Subbasin. Sequence 2 (latest Ordian–Mindyallan) represents a transgressive phase characterized by deeper marine carbonaceous black shales and the carbonates of the Arthur Creek Formation in southern depocenters, with increasing siliciclastic input. This sequence is correlated with the upper Thorntonia Limestone, Wonarah Formation, Inca Formation, Ranken Formation, Currant Bush Limestone, and Camooweal Formation in the Undilla Subbasin, and the Anthony Lagoon Formation in the Barkly Subbasin (Kruse et al., 2013).

A diverse assemblage of small shelly fossils (SSF) has been identified within the Cambrian sequences of the Georgina Basin, including trilobites, brachiopods, molluscs, echinoderms, archaeocopids, sponge spicules, hyoliths, and algae (Kruse et al., 2013; Pagès et al., 2016). Biostratigraphic studies indicate that the Narpa Group spans from the late Stage 4 to the Furongian in the southern Georgina Basin, and from the late Stage 4 to the Drumian in the Undilla Subbasin. The upper sequence (Sequence 2) extends from the middle Wuliuan to the middle Drumian of the Miaolingian Series (Laurie, 2022; Percival and Kruse, 2014; Smith et al., 2015).

1.3 Samples, Methods and Techniques

1.3.1 Samples

In this thesis, a total of 246 samples from the Georgina Basin were analyzed, including 15 samples for geochronology (Rb–Sr, Lu–Hf, U–Pb), 12 separated glauconite samples for metal isotope analysis (δ^{41}K and δ^{26}Mg), 212 bulk carbonate samples for C and O isotope analysis, 18 phosphatic microfossil samples for Sr isotopes (^{87}Sr/^{86}Sr), and 51 carbonate samples for Mg isotope (δ^{26}Mg) analysis.

Specifically, Chapter 2 presents triple-dating geochronological results from 15 samples (carbonates, phosphates) analyzed via LA-ICP-MS/MS. Chapter 3 presents and discusses metal isotope data from 12 separated glauconite samples analyzed for K and Mg isotopes, including 10 from the Georgina Basin (Australia) and 2 from the North China Craton (China). Finally, Chapter 4 focuses on the multi-isotope proxies or chemostratigraphy results from the Georgina Basin, based on a total of 230 samples, comprising 212 carbonate samples for C and O isotope analysis, 18 phosphatic microfossil samples for Sr isotope analysis, and 51 carbonate samples for Mg isotope analysis.

1.3.2 Methods and Techniques

(1) Petrographical and Mineralogical Study

A total of 108 thin sections were prepared and examined under a Leica DM 2700 P polarizing microscope for petrographic and mineralogical analysis. Scanning electron microscopy (SEM), backscattered electron (BSE) imaging, and mineral liberation analysis (MLA) were conducted on polished mounts using a Hitachi SU3800 SEM equipped with an energy-dispersive X-ray spectrometer (EDS) at University of Adelaide. Mineral mapping and data processing were performed using the Advanced Mineral Identification and Characterization System (AMICS) software (Bruker Nano GmbH). In addition, four glauconite-rich samples were analyzed using a high-resolution 'Nanomin' approach via a high-resolution FEI Teneo LoVac field emission SEM equipped with dual Bruker XFlash Series 6 EDS detectors at Macquarie University.

(2) Electron Probe Microanalysis (EPMA)

The elemental composition of selected samples or authigenic phases (primarily glauconite pellets) was determined using a Cameca SX-Five electron probe microanalyzer (EPMA) at Adelaide Microscopy. Major elements (Ca, Mg, Al, Si, P, K, Fe) and minor elements (Na, Ti) were measured, with oxygen (O) content calculated by stoichiometry. Glauconite reference material GL-O was also analyzed for comparison (Löhr et al., 2024). In addition, detailed elemental mapping was performed on three glauconite grains to identify mineral inclusions and assess potential diagenetic alterations.

(3) *In Situ* Dating and LA-ICP-MS/MS Analysis

The Rb–Sr and Lu–Hf negative beta decay systems, along with U–Pb decay chain system, represent valuable dating tools for various geochronology applications. Rubidium (Rb) has two naturally occurring isotopes, ^{85}Rb and ^{87}Rb. The latter undergoes a negative beta decay to form radiogenic ^{87}Sr with a half-life of approximately 49 billion years (Redaa et al., 2021). In Rb–Sr dating, the measured ^{87}Rb/^{86}Sr and ^{87}Sr/^{86}Sr ratios are plotted on an isochron diagram, where the slope of the line (i.e., isochron) corresponds to the sample's age (Hogmalm et al., 2017; Nebel, 2014; Redaa et al., 2021; Zack and Hogmalm, 2016). Similarly, in the Lu–Hf beta decay system, ^{176}Lu decays to ^{176}Hf with a half-life of ~37.12 Ga and the ^{176}Lu/^{177}Hf and ^{176}Hf/^{177}Hf ratios are measured to construct an isochron for age determination (Simpson et al., 2021a).

Traditional analytical approaches for mineral or bulk-rock geochronology involve mineral separation, acid digestion, column chemistry followed by a solution-based thermal ionization (TIMS) or inductively coupled plasma mass spectrometry (MC-ICP-MS). These traditional geochronological methods are time-consuming and require a specialized clean lab, isotope spikes, and multi-collector mass spectrometers. Additionally, bulk mineral digestion loses the petrographic context of the mineral and can contaminate samples due to presence of mineral micro-inclusions or procedural blanks, further complicating interpretations of the solution-based geochronology data (Wu et al., 2022).

An inductively-coupled plasma mass spectrometry that uses a collision/reaction cell technology (ICP-MS/MS) is capable of resolving isobaric interferences that previously hindered precise isotope ratio measurement using conventional ICP-MS techniques. When coupled with laser ablation (LA) micro-sampling, this new technology allows for rapid *in situ* determinations of isotope and elemental ratios in solid materials (Balcaen et al., 2015; Cheng et al., 2008; Hogmalm et al., 2017; Redaa et al., 2021; Simpson et al., 2021a; Zack et al., 2016). These novel and *in situ* dating techniques thus enable rapid online separation of the parent isotope (e.g., ^{87}Rb or ^{176}Lu) from the isobaric daughter (e.g., ^{87}Sr or ^{176}Hf) by introducing a reaction gas (such as N_2O, SF_6, CH_3F, NH_3, or O_2) between two quadrupoles in the ICP-MS/MS instrument (Glorie et al., 2024a; Glorie et al., 2024b; Hogmalm et al., 2017; Redaa et al., 2021; Zack and Hogmalm, 2016). *In situ* LA-ICP-MS/MS U–Pb geochronology has also been successfully developed for carbonate minerals with low U contents (Elisha et al., 2021; Roberts et al., 2017; Subarkah et al., 2024; Wu et al., 2022).

In this thesis, the LA-ICP-MS/MS analyses and *in situ* dating were conducted at Adelaide Microscopy using an Agilent 8900X ICP-MS/MS, coupled with a RESOlution-LR ArF 193 nm excimer laser ablation system. A reaction/collision cell between two quadrupoles (Q1 and

Q2) enabled the online chemical separation of the parental isotope from the daughter isotope by introducing a reaction gas, which resolves isobaric interference through a mass shift. Major and trace element concentrations were collected simultaneously during analysis. Data processing was performed using the LADR software (Norris and Danyushevsky, 2018), and ages were calculated and plotted with IsoplotR (Vermeesch, 2018).

In situ Rb–Sr dating of glauconite pellets was performed following the methods described by Glorie et al. (2024a) and Löhr et al. (2024). U–Pb dating of carbonate minerals followed the protocols outlined by Gilbert and Glorie (2020) and Simpson et al. (2021b). U–Pb dating of apatite followed the procedures detailed in Glorie et al. (2019) and Gillespie et al. (2018), while Lu–Hf dating of apatite was performed according to the method described by Simpson et al. (2021a). Full methodological details are provided in Chapter 2.

(4) Carbonate C and O Isotope Analysis via IRMS

Carbonate samples were micro-drilled into powder and weighed into exetainer vials. Each vial was purged using He gas and then reacted with 105% phosphoric acid (H_3PO_4) at 70 °C for approximately two hours. The evolved CO_2 was analyzed for carbon and oxygen isotopes using a Nu Instruments Horizon Isotope Ratio Mass Spectrometer (IRMS) in continuous flow mode with in-line GasPrep carbonate preparation system at the University of Adelaide. Isotopic measurements were calibrated against the Vienna Pee Dee Belemnite (VPDB) standard. Internal standards ANU-P3 and UAC were used to monitor accuracy, while reference materials CO-8 and NBS 19 were employed to assess the overall quality of the data. Full methodological details are provided in Chapter 5.

(5) Phosphatic Microfossils Sr Isotope Analysis via TIMS/ATONA

Phosphatic microfossil separation was carried out at Macquarie University using 10% acetic acid to dissolve carbonate minerals, following the procedures described by Liu et al. (2022). The fossil fragments were then cleaned with ethanol and rinsed with 0.5% acetic acid before being digested in 6 N HCl. Sr was purified using conventional Sr-Spec resin chromatography in HNO_3. The $^{87}Sr/^{86}Sr$ ratios were measured at the University of Adelaide using an Isotopx Phoenix Thermal Ionization Mass Spectrometer (TIMS) equipped with an ATONA signal amplification system. Reference material SRM987 and JCP-1 were used for calibration and quality control. Full methodological details are provided in Chapter 2.

(6) Glauconite K and Mg Isotope Analysis via MC-ICP-MS

Stable K and Mg isotope analyses of separated glauconite pellets were conducted at the University of Minnesota. Given that one of the aims of this study is to evaluate the impact of diagenesis on glauconite K and Mg isotopes, we chose not to grind or leach the separated glauconite grains into powder or leach out the remaining carbonate with 1 N HCl before total digestion in HF and HNO_3 mixture (primary to avoid possible procedural effects on exchangeable cations during a sample treatment). Thus, the glauconite separates were completely dissolved using a concentrated HF and HNO_3 mixture, and an aliquot of the solution was used for elemental analysis via ICP MS/MS (an iCAP TQ triple quadrupole), while another aliquot was reserved for K and Mg purification via eluent chromatography prior to isotope analysis. Briefly, K fraction was purified from glauconite matrix following the method described by Zheng et al. (2022b), which involves two-stage cation exchange chromatography columns with 0.4 N HCl working acid. Subsequently, Mg fraction was then collected and further purified using a three-stage column procedure, as outlined by Li et al. (2012).

High-precision K and Mg isotope measurements were performed using a Nu Sapphire multi-collector inductively coupled plasma mass spectrometer (MC-ICP-MS/MS). A standard-sample-standard bracketing method was used to correct for instrumental mass bias, using NIST 3141a and DSM3, as bracketing standards for K and Mg, respectively. For K isotope analysis ($\delta^{41}K$), additional reference materials such as UMN-K, seawater, AGV-2a, and BHVO-2 were used to assess the accuracy and reproducibility. For Mg isotope analysis ($\delta^{26}Mg$), the reference materials included seawater, Cambridge-1, AGV-2a, and BHVO-2. Full methodological details for metal isotope analysis used in this study are provided in Chapter 4.

(7) Carbonate Mg Isotope Analysis via MC-ICP-MS

Carbonate Mg stable isotope analysis was performed at the University of Minnesota. Sample digestion followed the protocols of Chen et al. (2020) and Ning et al. (2020), while Mg purification was performed using a three-step process outlined by Li et al. (2012). Mg isotopes were measured with a Nu Sapphire MC-ICP-MS/MS. A standard-sample-standard bracketing method was used to correct for instrumental mass bias, with DSM 3 as the bracketing standard. Seawater, Cambridge-1, AGV-2a, BHVO-2, and JDo-1 were used as external standards for quality control. Full methodological details are provided in Chapter 5.

1.4 Thesis Outline

This thesis is divided into 5 chapters, starting with an Introductory chapter that outlines the aims and rationale of the research, the geological background, as well as the samples and methods employed. Chapters 2 focuses primarily on *in situ* LA-ICP-MS/MS geochronology. Chapter 3 investigates glauconite K and Mg isotope variations to constrain seawater geochemistry and diagenetic alteration. Chapter 4 presents an integrated chemostratigraphic study based on a multi-proxy approach including δ^{26}Mg, δ^{13}C, δ^{18}O, and ^{87}Sr/^{86}Sr isotope tracers. Finally, Chapter 5 provides a review of the main findings and conclusions from the preceding chapters and also outlines priorities for future research. The main aims or key results from these case studies or individual chapters are also provided below.

1.4.1 Chapter 2

This study applied novel *in situ* LA-ICP-MS/MS geochronology to date various authigenic minerals (carbonates, phosphates, and clays) from the mid-Cambrian (Miaolingian) shallow marine carbonate sequence, with an expected depositional age of ca. 505 ± 3 Ma.

In situ Rb–Sr dating of glauconite yielded systematically younger ages, ranging from 452 ± 13 Ma to 351 ± 8 Ma, coeval with two episodes of the Alice Springs Orogeny affecting the Georgina Basin. In contrast, a well-preserved micrite and a fine crystalline dolomite yielded U–Pb ages of 500 ± 17 Ma and 513 ± 19 Ma, respectively, consistent with the mid-Cambrian depositional age. Another coarse crystalline dolomite yielded an age of 478 ± 23 Ma, with a significantly lower initial Pb value. *In situ* Lu–Hf dating of apatite from three bioclastic dolostone samples yielded ages of 497 ± 69 Ma, 495 ± 79 Ma, and 493 ± 74 Ma, which also overlap with the depositional window, although with large uncertainties. A bioclastic phosphorite sample yielded a Lu–Hf age of 425 ± 49 Ma, coeval with the Rodingan event. The results also suggest that the Lu–Hf system is more reliable for dating authigenic apatite than the U–Pb system.

1.4.2 Chapter 3

This chapter presents δ^{41}K and δ^{26}Mg isotopic data from the mid-Cambrian glauconite samples collected from the Georgina Basin in Australia and the North China Craton, to assess diagenetic effects on K and Mg isotopes in glauconite and to reconstruct Cambrian seawater signatures. Petrographic and elemental analysis reveals elevated porosity, illitization, and secondary mineral inclusions, indicating post-depositional alteration. Isotopic data show significant variability, with δ^{41}K ranging from -0.41 ‰ to -0.11 ‰ and δ^{26}Mg from -0.52 ‰ to 0.61 ‰. Progressive illitization of glauconite leads to increases in both δ^{41}K and δ^{26}Mg values, while carbonate micro-inclusions (e.g., dolomite, calcite) tend to lower δ^{26}Mg. Minimally altered glauconite may retain mid-Cambrian seawater isotopic signatures. Assuming the isotopic fractionation between present-day seawater and glauconite ($\Delta^{41}K_{\text{sw-glauconite}}$ = ~+0.90‰, $\Delta^{26}Mg_{\text{sw-glauconite}}$ = ~0.00‰) also applies to the mid-Cambrian (Löhr et al., 2023; Löhr et al., 2025, under review; Shaikh et al., 2024), the inferred δ^{41}K and δ^{26}Mg values for mid-Middle Cambrian seawater are estimated to range from +0.45 to +0.65‰, and -0.20 to +0.10‰, respectively. The higher δ^{41}K in mid-Cambrian seawater suggests increased reverse weathering, likely associated with higher atmospheric CO_2 and rising temperatures during this period.

1.4.3 Chapter 4

This study employs a multi-proxy δ^{26}Mg, δ^{13}C, δ^{18}O, and ^{87}Sr/^{86}Sr chemostratigraphy of marine carbonates (and phosphatic microfossils for Sr isotopes) to reconstruct mid-Cambrian seawater chemistry, dolomitization processes, and assess diagenetic impacts on these isotope proxies in marine archives of the Narpa Group from the Georgina Basin, Australia.

The sedimentary records of the Narpa Group from three wells reveal a transgressive–regressive cycle, subdivided into lowstand, transgressive, and regressive stages, with suboxic to anoxic redox conditions prevailing in the basin during the transgressive phase. The negative DICE $\delta^{13}C$ shift of up to -3.89‰ is observed and commonly interpreted as reflecting marine redox changes and associated upwelling of ^{12}C-rich anoxic waters during rapid global transgression. Carbonate $^{87}Sr/^{86}Sr$ values in low-Mg limestones match those expected for the mid-Cambrian seawater, indicating minimal alteration, while higher or more radiogenic (non-marine) $^{87}Sr/^{86}Sr$ ratios correlate with higher Mn/Sr, Mg/Ca ratios, and Al, Rb concentrations, suggesting combined influences from detrital input of silicate minerals, and dolomitization processes. Phosphatic microfossils exhibit variable $^{87}Sr/^{86}Sr$ values, with smaller fossils showing more radiogenic and non-marine values, indicating higher diagenetic alteration compared to larger microfossils. Carbonate (dolostone) $\delta^{26}Mg$ values range from -3.05‰ to -1.00‰ and seem to be less affected by alteration (compared to limestones), thus potentially preserving primary paleo-seawater Mg signature and partial dolomitization effects. Based on an estimated $\delta^{26}Mg$ fractionation factor between modern seawater and recent dolomite ($\Delta^{26}Mg_{sw\text{–}dolomite}$ = ~1.73 to 2.00‰), the mid-Cambrian seawater $\delta^{26}Mg$ (DSM3) value is estimated to be approximately -0.19 to +0.08‰. This estimate is consistent with previous studies on the Cambrian marine archives, but is systematically heavier than the modern seawater $\delta^{26}Mg$ (DSM3) value of -0.83‰ (Ling et al., 2011). Finally, dolomite-based $\delta^{26}Mg$ chemostratigraphy of mid-Cambrian carbonates from the Georgina Basin points to an impact of fluid-rock interactions or Mg-rich brine flows during dolomitization. Penecontemporaneous dolomitization might be linked to progressively increasing $\delta^{26}Mg$ values up the stratigraphic column, while seepage-reflux dolomitization is hypothesized to display a downward increase in $\delta^{26}Mg$ values or trend.

1.4.4 Chapter 5

This chapter summarizes the key findings from Chapters 2 to 5 and discusses both the potential and limitations of applying novel isotopic techniques for basin exploration. The implications of these techniques for chronostratigraphy, burial and post-depositional history, and the identification of diagenetic and dolomitizing fluid sources are highlighted. This summary also highlights the use of *in situ* geochronology (i.e., triple-dating) of sedimentary rocks and marine archives, combined with novel metal isotope proxies, to reconstruct paleo-seawater composition and to evaluate diagenetic resetting of radiogenic and stable isotope systems. Finally, this chapter outlines future research directions to further advance and validate the key findings of this thesis.

1.5 References

Babcock, L.E., Rees, M.N., Robison, R.A., Langenburg, E.S. and Peng, S., 2004. Potential Global Standard Stratotype-section and Point (GSSP) for a Cambrian stage boundary defined by the first appearance of the trilobite Ptychagnostus atavus, Drum Mountains, Utah, USA. Geobios, 37(2): 149-158.

Babcock, L.E., Robison, R.A., Rees, M.N., Peng, S. and Saltzman, M.R., 2007. The global boundary stratotype section and point (GSSP) of the Drumian Stage (Cambrian) in the Drum Mountains, Utah, USA. Episodes Journal of International Geoscience, 30(2): 85-95.

Balcaen, L., Bolea-Fernandez, E., Resano,M., Vanhaecke, F., 2015. Inductively coupled plasma -tandem mass spectrometry (ICP-MS/MS): a powerful and universal tool for the interference-free determination of (ultra) trace elements - a tutorial review. Anal. Chim. Acta 894, 7–19.

Baldermann, A., Banerjee, S., Löhr, S.C., Rudmin, M., Warr, L.N., Chakraborty, A., 2025. Exploring reverse silicate weathering across geological time: a review. Clay Minerals, 1-93.

Bialik, O.M., Wang, X., Zhao, S., Waldmann, N.D., Frank, R. and Li, W., 2018. Mg isotope response to dolomitization in hinterland-attached carbonate platforms: outlook of δ26Mg as a tracer of basin restriction and seawater Mg/Ca ratio. Geochimica et Cosmochimica Acta, 235: 189-207.

Bradshaw, B.E., Khider K., MacFarlane S., Carr L. and P., H., 2021. Tectonostratigraphic Evolution of the Centralian Superbasin (Australia) Revealed Through Three-Dimensional Well Correlations, Geoscience Australia.

Carr, L., Korsch, R.J., Reese, B., Palu, T., 2016. Onshore Basin Inventory: the McArthur, South Nicholson, Georgina, Wiso, Amadeus, Warburton, Cooper and Galilee basins, central Australia. Geoscience Australia.

Chen, X.-Y., Teng, F.-Z., Huang, K.-J. and Algeo, T.J., 2020. Intensified chemical weathering during Early Triassic revealed by magnesium isotopes. Geochimica et Cosmochimica Acta, 287: 263-276.

Cheng, P., Koyanagi, G.K., Bohme, D.K., 2008. On the chemical resolution of the 87Rb+ (s0)/87Sr+ (s1) isobaric interference: a kinetic search for an optimum reagent. Anal. Chim. Acta 627, 148–153.

Clauer, N., Zwingmann, H., Todd, A., Aubert, A., 2019. Potassium-argon timing of episodic mica and illite crystallization in highly indurated Hassi Messaoud (Algeria) hydrocarbon-bearing sandstones. AAPG Bulletin, 103(1): 215-240.

Dunster, J., Kruse, P., Duffett, M., Ambrose, G., 2007. Geology and resource potential of the southern Georgina Basin. Digital information package DIP007. Darwin: Northern Territory Geological Survey.

Elisha, B., Nuriel, P., Kylander-Clark, A., Weinberger, R., 2021. Towards in situ U–Pb dating of dolomite. Geochronology, 3(1): 337-349.

Farkaš, J., Wallmann, K., Mosley, L., Staudigel, P., Zheng, X.-Y., Leyden, E., Shao, Y., Fryda, J., Holmden, C., Eisenhauer, A., 2025. Alkalinity and elemental cycles in present and past ocean: Insight from geochemical modeling and alkali and alkaline earth metal isotopes. Treatise on Geochemistry (Third Edition), pp. 33-87.

Gilbert, S.E., Glorie, S., 2020. Removal of Hg interferences for common Pb correction when dating apatite and titanite by LA-ICP-MS/MS. Journal of Analytical Atomic Spectrometry, 35(7): 1472-1481.

Gill, B.C., Lyons, T.W., Young, S.A., Kump, L.R., Knoll, A.H. and Saltzman, M.R., 2011. Geochemical evidence for widespread euxinia in the Later Cambrian ocean. Nature, 469(7328): 80-83.

Gillespie, J., Glorie, S., Khudoley, A., Collins, A. S., 2018. Detrital apatite U-Pb and trace element analysis as a provenance tool: Insights from the Yenisey Ridge (Siberia). Lithos 314: 140-155.

Glass, L.M. and Phillips, D., 2006. The Kalkarindji continental flood basalt province: A new Cambrian large igneous province in Australia with possible links to faunal extinctions. Geology, 34(6): 461-464.

Glorie, S., Burke, T., Hand, M., Simpson, A., Gilbert, S., Wade, B., 2022. In situ Lu–Hf phosphate geochronology: Progress towards a new tool for space exploration. Geoscience Frontiers, 13(3): 101375.

Glorie, S., Mulder, J., Hand, M., Fabris, A., Simpson, A., Gilbert, S., 2023. Laser ablation (in situ) Lu-Hf dating of magmatic fluorite and hydrothermal fluorite-bearing veins. Geoscience Frontiers, 14(6): 101629.

Glorie, S., Gilbert, S.E., Hand, M., Lloyd, J.C., 2024a. Calibration methods for laser ablation Rb–Sr geochronology: comparisons and recommendation based on NIST glass and natural reference materials. Geochronology, 6(1): 21-36.

Glorie, S., Hand, M., Mulder, J., Simpson, A., Emo, R. B., Kamber, B., Fernie, N., Nixon, A., Gilbert, S., 2024b. Robust laser ablation Lu–Hf dating of apatite: an empirical evaluation. Geological Society, London, Special Publications, 537(1): 165-184.

Glorie, S., Jepson, G., Konopelko, D., Mirkamalov, R., Meeuws, F., Gilbert, S., Gillespie, J., Collins, A., Xiao, W., Dewaele, S., 2019. Thermochronological and geochemical footprints of post-orogenic fluid alteration recorded in apatite: Implications for mineralisation in the Uzbek Tian Shan. Gondwana Research 71, 1-15.

Haines, P.W., Hand, M. and Sandiford, M., 2001. Palaeozoic synorogenic sedimentation in central and northern Australia: a review of distribution and timing with implications for the evolution of intracontinental orogens. Australian Journal of Earth Sciences, 48(6): 911-928.

Hand, M., Mawby, J., Kinny, P. and Foden, J., 1999. U–Pb ages from the Harts Range, central Australia: evidence for early Ordovician extension and constraints on Carboniferous metamorphism. Journal of the Geological Society, 156(4): 715-730.

Hogmalm, K.J., Zack, T., Karlsson, A.K.-O., Sjöqvist, A.S., Garbe-Schönberg, D., 2017. In situ Rb–Sr and K–Ca dating by LA-ICP-MS/MS: an evaluation of N 2 O and SF 6 as reaction gases. Journal of Analytical Atomic Spectrometry, 32(2): 305-313.

Howley, R.A. and Jiang, G., 2010. The Cambrian Drumian carbon isotope excursion (DICE) in the Great Basin, western United States. Palaeogeography, Palaeoclimatology, Palaeoecology, 296(1-2): 138-150.

Hu, Z., Hu, W., Liu, C., Sun, F., Liu, Y. and Li, W., 2019. Conservative behavior of Mg isotopes in massive dolostones: From diagenesis to hydrothermal reworking. Sedimentary Geology, 381: 65-75.

Hu, Z., Hu, W., Wang, X., Lu, Y., Wang, L., Liao, Z. and Li, W., 2017. Resetting of Mg isotopes between calcite and dolomite during burial metamorphism: Outlook of Mg isotopes as geothermometer and seawater proxy. Geochimica et Cosmochimica Acta, 208: 24-40.

Isson, T., Rauzi, S., 2024. Oxygen isotope ensemble reveals Earth’s seawater, temperature, and carbon cycle history. Science 383, 666-670.

Isson, T.T., Planavsky, N.J., 2018. Reverse weathering as a long-term stabilizer of marine pH and planetary climate. Nature 560, 471-475.

Khider, K., MacFarlane, S., Bradshaw, B.E., Carr, L. and Henson, P., 2021. The Centralian Superbasin (Canning, Amadeus, Georgina and Officer basins) Stratigraphic Review and Well Correlations.

Kruse, P., Dunster, J., Munson, T., 2013. Chapter 28: Georgina Basin, in Geology and Mineral Resources of the Northern Territory, Darwin: Northern Territory Geol. Surv. 28.1-28.56.

Lan, Z., Glorie, S., Löhr, S.C., Wang, R., Shen, B., 2025. Apatite Lu− Hf dating of late Archean banded iron formations. Geology, 53 (4): 338–342.

Laurie, J.R., 2022. Report on the biostratigraphy of the Georgina Basin succession in NDI Carrara 1. 1-7.

Li, W., Chakraborty, S., Beard, B.L., Romanek, C.S., Johnson, C.M., 2012. Magnesium isotope fractionation during precipitation of inorganic calcite under laboratory conditions. Earth and Planetary Science Letters 333, 304-316.

Li, W., Liu, X.-M., Wang, K., McManus, J., Haley, B.A., Takahashi, Y., Shakouri, M., Hu, Y., 2022. Potassium isotope signatures in modern marine sediments: Insights into early diagenesis. Earth and Planetary Science Letters 599, 117849.

Ling, M.X., Sedaghatpour, F., Teng, F.Z., Hays, P.D., Strauss, J., Sun, W., 2011. Homogeneous magnesium isotopic composition of seawater: an excellent geostandard for Mg isotope analysis. Rapid Communications in Mass Spectrometry 25, 2828-2836.

Liu, K., Jiang, M., Huang, T., Zhang, L., Wang, Y. and Chen, D., 2022. A reassessment on the timing and potential drivers of the major seawater ^{87}Sr/^{86}Sr drop in the Ordovician Period: New evidence from conodonts in China. Chemical Geology: 120906.

Löhr, C.S., Zheng, X.-Y., Farkaš, J., Abbott, N.A., Baldermann, A., Weissgerber, J., 2025. Marine clay authigenesis controls seawater potassium isotope composition. Under review.

Löhr, S., Zheng, X., Lv, Y., Weissgerber, J., Baldermann, A., Farkas, J., Abbott, A.N., 2023. Mineralogical, chemical and isotopic evolution of recent glauconite in two contrasting marine settings, Goldschmidt 2023 Conference. Goldschmidt.

Löhr, S. C., Khazaie, E., Farkas, J., Baldermann, A., Gilbert, S., Maas, R., Subarkah, D., Collins, A. S., 2024. Origin and Significance of Age Variability in the Glauconite Reference Material GL-O: Implications for In Situ Rb-Sr Geochronology. Geostandards and Geoanalytical Research, 49(1): 197-216.

Mu, J., Chen, T., Yu, Q., An, S., Chen, J., Shi, X., Li, W., 2024. Potassium isotopic signatures of modern offshore detrital sediments from different climatic regimes and the implications. Science China Earth Sciences 67, 405-419.

Munson, T., 2014. Petroleum geology and potential of the onshore Northern Territory, 2014. Northern Territory Geological Survey.

Munson TJ, Kruse PD and Ahmad M, 2013. Chapter 22: Centralian Superbasin: in Ahmad M and Munson TJ (compilers). Geology and mineral resources of the Northern Territory. Northern Territory Geological Survey, Special Publication 5.

Nebel, O., 2014. Rb-Sr dating, Encyclopedia of scientific dating methods. Springer, pp. 686-698.

Ning, M., Lang, X., Huang, K., Li, C., Huang, T., Yuan, H., Xing, C., Yang, R. and Shen, B., 2020. Towards understanding the origin of massive dolostones. Earth and Planetary Science Letters, 545: 116403.

Nixon, A., Glorie, S., Fernie, N., Hand, M., De Vries Van Leeuwen, A., Collins, A., Hasterok, D. and Fraser, G., 2022. Intracontinental fault reactivation in high heat production areas of central Australia: insights from apatite fission track thermochronology. Geochemistry, Geophysics, Geosystems, 23(12): e2022GC010559.

Norris, A., Danyushevsky, L., 2018. Towards estimating the complete uncertainty budget of quantified results measured by LA-ICP-MS. Goldschmidt: Boston, MA, USA.

Pagès, A. and Schmid, S., 2016. Euxinia linked to the Cambrian Drumian carbon isotope excursion (DICE) in Australia: Geochemical and chemostratigraphic evidence. Palaeogeography, Palaeoclimatology, Palaeoecology, 461: 65-76.

Pagès, A., Schmid, S., Edwards, D., Barnes, S., He, N. and Grice, K., 2016. A molecular and isotopic study of palaeoenvironmental conditions through the middle Cambrian in the Georgina Basin, central Australia. Earth and Planetary Science Letters, 447: 21-32.

Parendo, C.A., Jacobsen, S.B., Plank, T., 2022. Potassium-isotope variations of marine sediments adjacent to the Izu-Bonin Trench and Nankai Trough. Geochimica et Cosmochimica Acta 337, 166-181.

Percival, I.G., Kruse, P.D., 2014. Middle Cambrian brachiopods from the southern Georgina Basin of central Australia. Memoirs of the Association of Australasian Palaeontologists(45): 349-402.

Peters, S.E. and Gaines, R.R., 2012. Formation of the ‘Great Unconformity’as a trigger for the Cambrian explosion. Nature, 484(7394): 363-366.

Piazolo, S., Daczko, N.R., Silva, D. and Raimondo, T., 2020. Melt-present shear zones enable intracontinental orogenesis. Geology, 48(7): 643-648.

Qiu, K.-F., Romer, R.L., Long, Z.-Y., Yu, H.-C., Turner, S., Wan, R.-Q., Li, X.-Q., Gao, Z.-Y., Deng, J., 2024. Potassium isotopes as a tracer of hydrothermal alteration in ore systems. Geochimica et Cosmochimica Acta 368, 185-196.

Ramos, D.P.S., Morgan, L.E., Lloyd, N.S., Higgins, J.A., 2018. Reverse weathering in marine sediments and the geochemical cycle of potassium in seawater: Insights from the K isotopic composition (41K/39K) of deep-sea pore-fluids. Geochimica et Cosmochimica Acta 236, 99-120.

Redaa, A., Farkaš, J., Gilbert, S., Collins, A. S., Wade, B., Löhr, S., Zack, T., Garbe-Schönberg, D., 2021. Assessment of elemental fractionation and matrix effects during in situ Rb–Sr dating of phlogopite by LA-ICP-MS/MS: implications for the accuracy and precision of mineral ages. Journal of Analytical Atomic Spectrometry, 36(2): 322-344.

Redaa, A., Farkaš, J., Gilbert, S., Collins, A. S., Löhr, S., Vasegh, D., Forster, M., Blades. M., Zack., T., Giuliani, A., Maas, R., Baldermann, A., Dietzel, M., Garbe‐Schönberg, D., 2023. Testing Nano-Powder and Fused-Glass Mineral Reference Materials for In Situ Rb-Sr Dating of Glauconite, Phlogopite, Biotite and Feldspar via LA-ICP-MS/MS. Geostandards and Geoanalytical Research, 47(1): 23-48.

Roberts, N. M., Rasbury, E. T., Parrish, R. R., Smith, C. J., Horstwood, M. S., Condon, D. J., 2017. A calcite reference material for LA-ICP-MS U-Pb geochronology. Geochemistry, Geophysics, Geosystems, 18(7): 2807-2814.

Scotese, C.R., Song, H., Mills, B.J., van der Meer, D.G., 2021. Phanerozoic paleotemperatures: The earth’s changing climate during the last 540 million years. Earth-Science Reviews 215, 103503.

Shaikh, J.I., Löhr, S., Baldermann, A., Farkaš, J., Abbott, A.N., Zheng, X.-Y., 2024. Marine glauconites: A potential new archive of paleo seawater magnesium isotopes, Goldschmidt Conference 2024. Goldschmidt.

Shao, Z., Farkaš, J., Glorie, S., Collins, S.A., Gilbert, E.S., Subarkah, D., 2025. Dating of marine authigenic minerals via in situ Rb–Sr, U–Pb, and Lu–Hf: A case study from the Georgina Basin, Australia. Chemical Geology: 123042.

Simpson, A., Glorie, S., Morley, C. K., Roberts, N. M., Gillespie, J., Lee, J. K., 2021b. In-situ calcite U-Pb geochronology of hydrothermal veins in Thailand: New constraints on Indosinian and Cenozoic deformation. Journal of Asian Earth Sciences, 206: 104649.

Simpson, A., Gilbert, S., Tamblyn, R., Hand, M., Spandler, C., Gillespie, J., Nixon, A., Glorie, S., 2021a. In-situ LuHf geochronology of garnet, apatite and xenotime by LA-ICP-MS/MS/MS. Chemical Geology 577, 120299.

Smith, P.M., Brock, G.A., Paterson, J.R., 2015. Fauna and biostratigraphy of the Cambrian (Series 2, Stage 4; Ordian) Tempe Formation (Pertaoorrta Group), Amadeus Basin, Northern Territory. Alcheringa: An Australasian Journal of Palaeontology, 39(1): 40-70.

Southgate, P. and Shergold, J., 1991. Application of sequence stratigraphic concepts to Middle Cambrian phosphogenesis, Georgina Basin, Australia. BMR Journal of Australian Geology and Geophysics, 12(2): 119-144.

Subarkah, D., Blades, M. L., Collins, A. S., Farkaš, J., Gilbert, S., Löhr, S. C., Redaa, A., Cassidy, E., Zack, T., 2022. Unraveling the histories of Proterozoic shales through in situ Rb-Sr dating and trace element laser ablation analysis. Geology, 50(1): 66-70.

Subarkah, D., Nixon, A. L., Gilbert, S. E., Collins, A. S., Blades, M. L., Simpson, A., Lloyd, J., Virgo, G. M., Farkaš, J., 2024. Double dating sedimentary sequences using new applications of in-situ laser ablation analysis. Lithos, 480: 107649.

Sun, Y., Ouyang, Q., Lang, X., Pang, K., Wu, C., Chen, Z., Zhou, C., 2023. Global sea-level fall triggered Ediacaran–Cambrian unconformity in North China craton. Earth and Planetary Science Letters 622, 118411.

Teng, F.-Z., Li, W.-Y., Rudnick, R.L., Gardner, L.R., 2010. Contrasting lithium and magnesium isotope fractionation during continental weathering. Earth and Planetary Science Letters 300, 63-71.

Tenthorey, E., and B. Ayling. 2021. Geomechanical evaluation of a middle Cambrian unconventional oil and gas play in the southern Georgina Basin, northern Australia. Australian Journal of Earth Sciences 68.5: 697-716.

Valetich, M., Zivak D., Spandler C., Degeling H., Grigorescu M. 2022. REE enrichment of phosphorites: An example of the Cambrian Georgina Basin of Australia." Chemical Geology 588: 120654.

Varga, J., Raimondo, T., Morrissey, L., Kelsey, D.E. and Hand, M., 2022. Pressure-temperature-time constraints on gneiss dome formation in an intracontinental orogen. Journal of Metamorphic Geology, 40(3): 457-488.

Vermeesch, P., 2018. IsoplotR: A free and open toolbox for geochronology. Geoscience Frontiers, 9(5): 1479-1493.

Walter, M., Veevers, J., Calver, C., Grey, K., 1995. Neoproterozoic stratigraphy of the Centralian superbasin, Australia. Precambrian Research, 73(1-4): 173-195.

Wang, H., Zhang, H., Zhang, Y., Cheng, B., Deng, Q., Wang, D., Zhao, G. and Liao, Z., 2024. Sedimentary facies controlled biogeochemical process of biotic extinction and turnover across the Cambrian SPICE event. Communications Earth & Environment, 5(1): 683.

Wu, Y., Bai, X.-J., Shi, H.-S., He, L.-Y., Qiu, H.-N., 2023b. Dating of authigenic minerals in sedimentary rocks: A review. Earth-Science Reviews, 241: 104443.

Wu, S., Yang, Y., Roberts, N. M., Yang, M., Wang, H., Lan, Z., Xie, B., Li, T., Xu, L., Huang, C., Xie, L., Yang, J., Wu, F., 2022. In situ calcite U− Pb geochronology by high-sensitivity single-collector LA-SF-ICP-MS. Science China Earth Sciences, 65(6): 1146-1160.

Xia, Z., Li, S., Hu, Z., Bialik, O., Chen, T., Weldeghebriel, M.F., Fan, Q., Fan, J., Wang, X., An, S., 2024. The evolution of Earth’s surficial Mg cycle over the past 2 billion years. Science Advances 10, eadj5474.

Yang, X., Li, Z., Gao, B. and Zhou, Y., 2021. The Cambrian Drumian carbon isotope excursion (DICE) in the Keping area of the northwestern Tarim Basin, NW China. Palaeogeography, Palaeoclimatology, Palaeoecology, 571: 110385.

Zack, T., Hogmalm, K.J., 2016. Laser ablation Rb/Sr dating by online chemical separation of Rb and Sr in an oxygen-filled reaction cell. Chemical Geology, 437: 120-133.

Zhang, Y., Yang, T., Hohl, S.V., Zhu, B., He, T., Pan, W., Chen, Y., Yao, X. and Jiang, S., 2020. Seawater carbon and strontium isotope variations through the late Ediacaran to late Cambrian in the Tarim Basin. Precambrian Research, 345: 105769.

Zheng, X.-Y., Beard, B.L., Neuman, M., Fahnestock, M.F., Bryce, J.G., Johnson, C.M., 2022a. Stable potassium (K) isotope characteristics at mid-ocean ridge hydrothermal vents and its implications for the global K cycle. Earth and Planetary Science Letters 593, 117653.

Zheng, X.-Y., Chen, X.-Y., Ding, W., Zhang, Y., Charin, S., Gérard, Y., 2022b. High precision analysis of stable potassium (K) isotopes by the collision cell MC-ICP-MS "Sapphire" and a correction method for concentration mismatch. Journal of Analytical Atomic Spectrometry 37, 1273-1287.

Zhu, M.-Y., Babcock, L.E. and Peng, S.-C., 2006. Advances in Cambrian stratigraphy and paleontology: integrating correlation techniques, paleobiology, taphonomy and paleoenvironmental reconstruction. Palaeoworld, 15(3-4): 217-222.

Chapter 2: Dating of marine authigenic minerals via *in situ* Rb–Sr, U–Pb, and Lu–Hf: A case study from the Georgina Basin, Australia

This manuscript has been published in *Chemical Geology* (see also a full reference below)

Zhufu Shao, Juraj Farkaš, Stijn Glorie, Alan S. Collins, Sarah E. Gilbert, Darwinaji Subarkah (2025) Dating of marine authigenic minerals via *in situ* Rb–Sr, U–Pb, and Lu–Hf: A case study from the Georgina Basin, Australia. *Chemical Geology*, Volume 695, p. 123041. https://doi.org/10.1016/j.chemgeo.2025.123042.

Statement of Authorship

Title of Paper	Dating of marine authigenic minerals via in situ Rb–Sr, U–Pb, and Lu–Hf: A case study from the Georgina Basin, Australia
Publication Status	☒ Published ☐ Accepted for Publication ☐ Submitted for Publication ☐ Unpublished and Unsubmitted work written in manuscript style
Publication Details	This manuscript has been published in *Chemical Geology*.

Principal Author

Name of Principal Author (Candidate)	Zhufu Shao		
Contribution to the Paper	Work planning, sample preparation, laboratory analyses, data acquisition, processing, interpretation, and manuscript writing		
Overall percentage (%)	80%		
Certification:	This paper reports on original research I conducted during the period of my Higher Degree by Research candidature and is not subject to any obligations or contractual agreements with a third party that would constrain its inclusion in this thesis. I am the primary author of this paper.		
Signature		Date	06-May-25

Co-Author Contributions

By signing the Statement of Authorship, each author certifies that:

i. the candidate's stated contribution to the publication is accurate (as detailed above);

ii. permission is granted for the candidate in include the publication in the thesis; and

iii. the sum of all co-author contributions is equal to 100% less the candidate's stated contribution.

Name of Co-Author	Juraj Farkaš
Contribution to the Paper	Supervised work, helped with data interpretation and manuscript revision

Signature		Date	May 10, 2025

Name of Co-Author	Stijn Glorie		
Contribution to the Paper	Supervised work, helped with data interpretation and manuscript revision.		
Signature		Date	07-May-25

Name of Co-Author	Alan S. Collins		
Contribution to the Paper	Supervised work, helped with data interpretation and manuscript revision.		
Signature		Date	21-05-25

Name of Co-Author	Sarah E. Gilbert		
Contribution to the Paper	Assisted with *in situ* Rb–Sr dating, data process and interpretation and manuscript revision.		
Signature		Date	06-May-25

Name of Co-Author	Darwinaji Subarkah		
Contribution to the Paper	Helped with data interpretation and manuscript revision.		
Signature		Date	10-May-25

Abstract

The *in situ* laser ablation–inductively coupled plasma tandem mass spectrometry (LA-ICP-MS/MS) technique enables rapid, high-resolution isotopic analysis with minimal contamination, ideal for dating authigenic minerals. This study employs LA-ICP-MS/MS triple dating (Rb–Sr, U–Pb, Lu–Hf) on key authigenic minerals from the mid-Cambrian (~505 ± 3 Ma) marine sequence of Australia's Georgina Basin. Glauconite, micrite, dolomite, and apatite were analyzed to constrain depositional ages and diagenetic overprints. Glauconite exhibits high porosity, extensive illitization, and secondary minerals, reflecting post-depositional alteration. *In situ* Rb–Sr dating of glauconite yielded systematically younger ages (452 ± 13 Ma to 351 ± 8 Ma) coeval with two episodes of the Alice Springs Orogeny. Well-preserved micrite and fine dolomite yielded U–Pb ages of 500 ± 17 Ma and 513 ± 19 Ma, consistent with the depositional age, whereas a coarser dolomite yielded a younger age of 478 ± 23 Ma with lower initial Pb. *In situ* Lu–Hf dating of apatite from three dolostone samples yielded ages of 497 ± 69 Ma, 495 ± 79 Ma, and 493 ± 74 Ma, overlapping with the depositional window despite notable uncertainties. A phosphorite sample yielded a Lu–Hf age of 425 ± 49 Ma, coeval with the Rodingan event. *In situ* U–Pb apatite ages yielded dispersed and unrealistic ages demonstrating that the Lu–Hf system provides more robust ages than U–Pb for authigenic apatite, whereas Rb–Sr ages reflect diagenetic resetting during orogeny. The integration of three radiometric systems provides a refined framework for reconstructing the basin's depositional and diagenetic history.

Keywords: *In situ* dating, Rb–Sr, U–Pb, Lu–Hf, Authigenesis, Diagenesis, Georgina Basin

2.1 Introduction

Dating the age of sediment deposition and constraining the timing of diagenesis and later tectonic events presents a significant challenge for geochronologists. For detrital sediments, a maximum depositional age can be derived by dating detrital minerals, commonly zircon, but also mica, rutile, garnet, apatite, *etc*. For sediments deposited near volcanic regions, precise ages can be obtained by U–Pb dating zircons in tuff layers using thermal ionization mass spectrometry (TIMS). However, many sediments are deposited without tuff beds, and many are not composed of detrital minerals. Additionally, many detrital sediments are sourced from areas that are much older than the sediments themselves.

In contrast to detrital studies, authigenic mineral geochronology focuses on dating minerals that crystallize during deposition or form after deposition within the sediments. These minerals not only help determine the age of deposition but also serve as geochemical archives for palaeoenvironment, palaeoclimate, tectonic activity, burial diagenesis, hydrocarbon accumulation, and metal mineralization processes (Aubineau et al., 2024; Clauer, 2020; Clauer et al., 2019; Lan et al., 2022; Pan et al., 2020; Subarkah et al., 2024; Wu et al., 2023b).

Traditional mineral or bulk-rock geochronology uses column chemistry followed by TIMS or inductively coupled plasma mass spectrometry (MC-ICP-MS). These processes are time-consuming and require a specialized clean lab. Additionally, bulk mineral digestion loses the petrographic context of the mineral and can contaminate samples due to radiogenic inclusions or complicate interpretations due to water-rock interactions after mineral formation. To address this issue, in situ dating techniques have been developed (Hogmalm et al., 2017; Löhr et al., 2024; Scheiblhofer et al., 2022; Solé, 2021). Among these, laser ablation inductively coupled plasma quadrupole tandem mass spectrometry (LA-ICP-MS/MS) enables *in situ* dating of isobaric radioactive systems such as Rb–Sr and Lu–Hf (Glorie et al., 2024a; Glorie et al., 2024b; Hogmalm et al., 2017; Redaa et al., 2021; Zack and Hogmalm, 2016). This technique has been successfully applied to Rb–Sr dating of authigenic clay minerals in shale (Subarkah et al., 2022a; Subarkah et al., 2022b), glauconite (Löhr et al., 2024; Loyola et al., 2025), and authigenic apatite (Glorie et al., 2020; Glorie et al., 2022; Glorie et al., 2023; Lan et al., 2025; Wu et al., 2023a). Additionally, in situ LA-ICP-MS/MS U–Pb geochronology has been developed for carbonate minerals with low U contents (Elisha et al., 2021; Roberts and Walker, 2016; Roberts et al., 2017; Subarkah et al., 2024; Wu et al., 2022) and has been widely applied to determine depositional ages (Li et al., 2023; Xiong et al., 2023), investigate diagenesis (Li et al., 2014; Li et al., 2023), analyse speleothems (Woodhead and Petrus, 2019), examine tectonic faults (Roberts and Walker, 2016; Simpson et al., 2021a), and assess hydrocarbon accumulation (Pan et al., 2020).

This study presents three in situ LA-ICP-MS/MS dating methods applied to mid-Cambrian shallow-water carbonate sequences from the Georgina Basin, Australia. These methods include in situ Rb–Sr dating of glauconite, in situ U–Pb dating of carbonate and apatite, and in situ Lu–Hf dating of apatite. We evaluate the ability of these techniques to date carbonate deposition versus recording diagenetic and other postdepositional isotopic resetting events. The significance of these postdepositional events is discussed in relation to the tectonic evolution of eastern Australia.

2.2 Geological Background

The Neoproterozoic to mid-Paleozoic polyphase intracratonic Georgina Basin represents the largest depositional system of the Centralian Superbasin. It is situated in the central Northern Territory and Queensland, covering approximately 3.3×10^5 km^2 (Fig. 1a; Dunster et al., 2007; Kruse et al., 2013; Walter et al., 1995). The Georgina Basin is divided into eight structural belts. To the north, the Undilla Subbasin and the Central Subbasin are separated by the Alexandria-Wonarah Block. To the south, the Dulcie Syncline and Toko Syncline connect the Elkedra Shelf in the west to the Burke River Structure Belt in the east (Fig. 1a; Khider et al., 2021; Pagès et al., 2016; Smith et al., 2013).

The stratigraphy of the Georgina Basin (Fig. 1) comprises: 1) Neoproterozoic (ca. 850–570 Ma) rift-related fluvioglacial to marine siliciclastic rocks with a minor carbonate component; 2) Cambrian to Ordovician (ca. 530–450 Ma) shallow marine carbonate-dominated sequences interbedded with siltstone, shale, and volcanic rocks; and 3) Devonian foreland siliciclastic rocks, including aeolian and fluvial-delta to shallow marine deposits, scattered throughout the basin (Dunster et al., 2007; Walter et al., 1995; Khider et al., 2021). The sedimentary sequences are unevenly distributed, forming a wedge that ranges in thickness from 1500 m in the southern depocenter to 300 m in the north. The sediments of the Georgina Basin are overlain by Mesozoic strata of the Eromanga Basin (Carr et al., 2016).

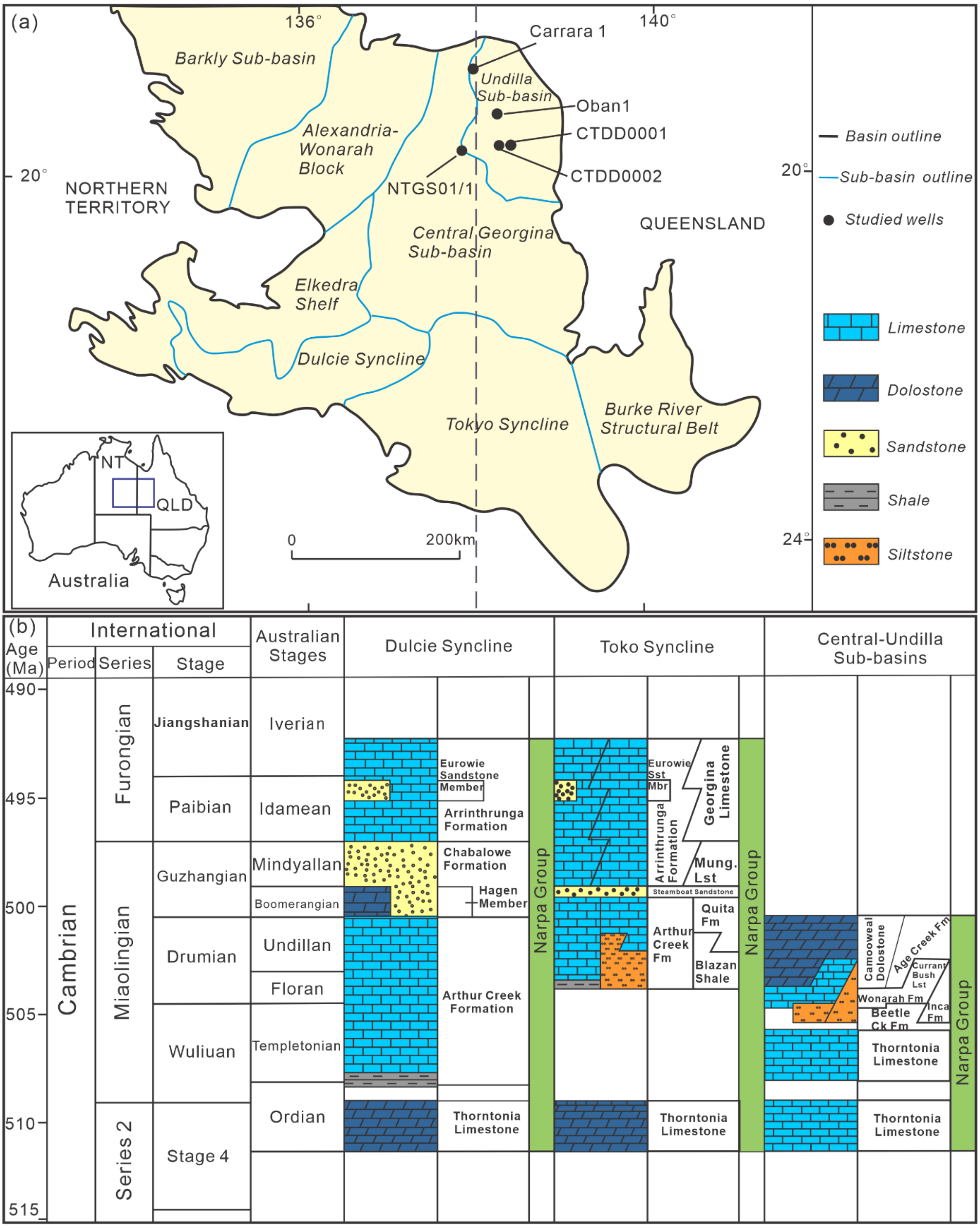

Figure 1. (**a**) Location of the Georgina Basin in Australia, with solid black circles indicating the studied wells (adapted from Kruse et al., 2013; Walter et al., 1995); (**b**) Stratigraphy of the Middle Cambrian Narpa Group (adapted from Laurie, 2022; Pagès and Schmid, 2016; Smith et al., 2013).

The evolution and marine deposition of the Georgina Basin were interrupted by several orogenies, with the most significant being the Petermann Orogeny (Huckitta Movement) and the Alice Springs Orogeny (Haines et al., 2001; Hand et al., 1999; Khider et al., 2021; Kruse et al., 2013; Nixon et al., 2022; Piazolo et al., 2020; Varga et al., 2022). The Petermann Orogeny (570–530 Ma) was a north-south compressional event that caused regional uplift and a sedimentary hiatus in the Georgina Basin, marking the end of Centralian Superbasin A (Kruse et al., 2013). The Alice Springs Orogeny (450–300 Ma) involved another north-south compressional deformation, leading to significant thrust-uplift and exhumation, which resulted in the termination of Centralian Superbasin B (Haines et al., 2001; Nixon et al., 2022; Piazolo et al., 2020; Varga et al., 2022).

Following the global transgression that occurred after the eruption of the Kalkarindji Large Igneous Province (LIP) around 511 Ma (Glass and Phillips, 2006; Khider et al., 2021; Nixon et al., 2022), the middle Cambrian Narpa Group carbonate ramp system was extensively deposited in the Georgina Basin. The Narpa Group consists of two sequences separated by an unconformity (Fig. 1b; Southgate and Shergold, 1991). Sequence 1 (Ordian) includes the Thorntonia Limestone in the southern basin, which is equivalent to the lower Thorntonia Limestone and Waterhole Formation in the Undilla Sub-basin, as well as the Gum Ridge Formation in the Barkly Sub-basin (Fig. 1b). The Thorntonia Limestone is composed of limestone, dolomitic limestone, dolostone, pyritic-carbonaceous dolostone, mudstone, and marl. It also locally includes basal sandstone and conglomerate, with phosphorite and chert nodules distributed throughout the strata (Dunster et al., 2007; Percival and Kruse, 2014). Sequence 2 (latest Ordian-Mindyallan) comprises deeper marine carbonaceous black shale and carbonate of the Arthur Creek Formation in the southern depocenters. This sequence is correlated with the upper Thorntonia Limestone, Wonarah Formation, Inca Formation, Ranken Formation, Currant Bush Limestone, and Camooweal Formation in the Undilla Sub-basin, as well as the Anthony Lagoon Formation in the Barkly Sub-basin. The Wonarah Formation consists of dolostone, calci/dolo-mudstone, and siltstone (Kruse et al., 2013). The Inca Formation is composed of laminated siliceous shale and siltstone, interbedded with limestone.

The Currant Bush Limestone primarily consists of limestone and dolomitic limestone, interbedded with marl, ooids, siltstone, and chert layers (Kruse et al., 2013). The Georgina Basin hosts world-class mid-Cambrian phosphate deposits along its basin edge and holds significant potential for both conventional and unconventional energy resources within the Cambrian Narpa Group, particularly in the Thorntonia Limestone and Arthur Creek “hot” shale (Kruse et al., 2013). Diverse small shelly fossils, including trilobites, brachiopods, molluscs, echinoderms, archaeocopides, sponge spicules, hyoliths, and algae, have been discovered within the Cambrian sequences of the Georgina Basin. Biostratigraphic studies have confirmed that the Narpa Group in the southern Georgina Basin ranges from the late Stage 4 to the Furongian, while in the Undilla Sub-basin, it spans from the late Stage 4 to the Drumian. The upper sequence (Sequence 2) in this study extends from the middle Wulian to the middle Drumian of the Miaolingian Series, with an estimated age of 505 ± 3 Ma (Laurie, 2022; Percival and Kruse, 2014; Smith et al., 2015).

2.3 Samples and Analytical Methods

2.3.1 Core Samples

In this study, we selected the Narpa Group from the Central-Undilla Sub-basins for geochronological analysis. A total of 15 samples were collected from five drill holes: NDI Carrara1, Oban1, CTDD0001, and CTDD0002 from the Undilla Subbasin, and NTGS01/1 from the Central Sub-basin of the Georgina Basin (Fig. 1a). The samples include one micrite from the Currant Bush Limestone, four dolostones from the Inca Formation, three dolostones and one bioclastic phosphorite from the Thorntonia Limestone, and six dolostones from the Wonarah Formation (Fig. 2).

2.3.2 Mineralogical Screening via SEM/EDS

The petrographic and mineralogical study was conducted on thin sections using a Leica DM 2700 P microscope. Scanning electron microscopy (SEM), backscatter electron (BSE) imaging, and mineral liberation analysis (MLA) were performed on polished mount samples with a

Hitachi SU3800 equipped with an energy-dispersive X-ray spectrometer (EDS) at Adelaide Microscopy, the University of Adelaide. Data processing and mineral mapping were done using Bruker Nano GmbH's Advanced Mineral Identification and Characterization System (AMICS) software.

Additionally, four glauconite-rich samples were analyzed using a high-resolution FEI Teneo LoVac field emission SEM with dual Bruker XFlash Series 6 EDS detectors at Macquarie University. EDS data processing and imaging were carried out with FEI Nanonin software.

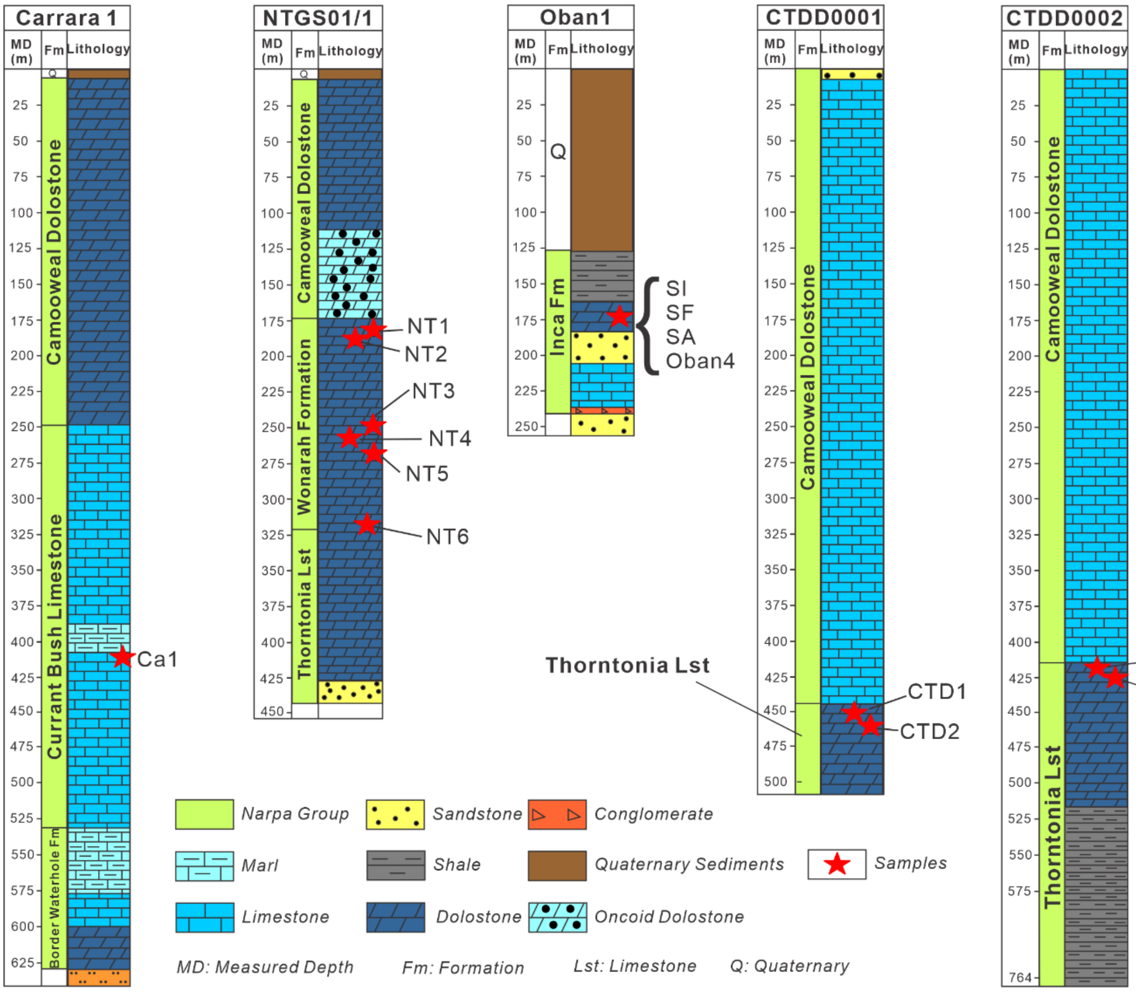

Figure 2. Stratigraphy and sample intervals (red stars) of the mid-Cambrian marine carbonates from the studied wells intersecting the Georgina Basin (modified after Kruse et al., 2013; Kruse, 2008; Laurie, 2022). (For interpretation of the references to colour in this figure legend, the reader is referred to the web version of this article.)

2.3.3 Glauconite Electron Probe Microanalysis (EPMA)

The elemental composition of glauconite pellets was quantified using a Cameca SX-Five electron probe microanalyzer (EPMA) at Adelaide Microscopy. Data acquisition and processing were carried out with PeakSite v6.2 microscopy software and Probe for EPMA software. Major elements including Ca, Mg, Al, Si, P, K, Fe, and minor elements Na and Ti, were measured, with oxygen (O) content determined by stoichiometry. A beam size of 5 µm was used at conditions of 15 kV/20 nA, with backscatter electron (BSE) images aiding the analysis. For comparison, the glauconite standard GL-O was also analyzed (see Löhr et al., 2024). In addition, detailed elemental mapping of three glauconite grains was performed to investigate mineral inclusions and potential diagenetic alterations.

2.3.4 LA-ICP-MS/MS Analysis

LA-ICP-MS/MS analyses and *in situ* dating were conducted at Adelaide Microscopy using an Agilent 8900x ICP-MS/MS, coupled with a RESOlution-LR ArF 193 nm excimer laser ablation system. A reaction/collision cell between two quadrupoles (Q1 and Q2) enabled the online chemical separation of the parental isotope from the daughter isotope by introducing a reaction gas, resolving isobaric interference through a “mass shift”. The ablated aerosol, generated in a He atmosphere mixed with Ar carrier gas, was transported to the ICP-MS via a “Squid” device (Laurin Technic Inc.) to smooth the signal. To enhance signal sensitivity, N_2 was added before the plasma (Hu et al., 2008). Major and trace element concentrations were collected simultaneously during analysis, with all laser settings and parameters listed in Supplementary File 1. Data processing was performed using the LADR software (Norris and Danyushevsky, 2018), and ages were calculated and plotted with IsoplotR (Vermeesch, 2018). Rb–Sr and Lu–Hf isochron dates are presented as inverse isochrons, and the U–Pb data are shown in Tera- Wasserburg concordia plots.

(1) Glauconite *in situ* Rb–Sr dating

In this study, 16 glauconite samples were analyzed over four analytical sessions. The reaction gas used in the ICP-MS/MS system was N_2O, which reacts with $^{87}Sr^+$ ions to form $^{87}Sr^{16}O^+$, while $^{87}Rb^+$ remains unreactive, enabling interference-free measurement of ^{87}Sr by separating it from ^{87}Rb through a mass shift of 16 amu. Although ^{87}Sr reacts effectively with N_2O, a small amount of unreacted ^{87}Sr affects the measurement of ^{87}Rb. To mitigate this issue, ^{87}Rb was calculated from the measured ^{85}Rb, assuming the natural isotope abundances. Analytical parameters are summarized in Supplementary Table S1. A circular laser beam (67 µm diameter), with a fluence of 3.5 J/cm^2 and a repetition rate of 5 Hz was used for the ablation. NIST 610 glass was used as a primary reference material to normalize the isotope ratios, correct for instrumental drift and down-hole fractionation, MDC phlogopite (the source for Mica-Mg, 519.4 ± 6.5 Ma, Hogmalm et al., 2017) was used as matrix correction reference material for matrix-introduced fractionation correction of $^{87}Rb/^{86}Sr$ (Glorie et al., 2024a; Löhr et al., 2024). Glauconite reference material GL-O was used as secondary standards for accuracy verification (Löhr et al., 2024; Redaa et al., 2023). The acquired Rb–Sr age for GL-O during this study ranged from 92.7 ± 3.1 Ma to 95.8 ± 7.9 Ma (Table 1; Supplementary Fig. S1; Table S2), consistent with its reported Rb–Sr age of 91.7 ± 7.1 Ma (Redaa et al., 2023), or K-Ar age of 95 ± 1Ma (Löhr et al., 2024; Odin, 1982). Elemental concentrations were calculated by normalizing to 95% cation oxides totals (5% allocated for water/OH), with measured ^{27}Al used for internal standard normalization.

Table 1. Corrected in situ Rb–Sr, U–Pb and Lu–Hf ages or dating results for the reference materials used in this study.

		GL-O			
Rb—Sr	Session No.	Age (Ma)	2s (Ma)	MSWD (n)	
	S1	92.7	3.1	1.2 (20)	
	S2	95.8	7.9	0.82 (20)	
	S3	94.6	3.2	0.60 (20)	
	S4	93.0	4.9	1.05 (20)	
	Expected age	95^a	1		
		Apatite 401			
U—Pb	Session No.	Age (Ma)	2s (Ma)	MSWD (n)	
	S1	523.8	7.8	0.26 (18)	
	S2	527.6	7.1	0.37 (22)	
	Expected age	525^b	8		
		Bamble1			HR

Lu–Hf	Session No.	Age (Ma)	2s (Ma)	MSWD (n)	Age (Ma)	2s (Ma)	MSWD (n)
	S1	1102.4	6.7	1.1 (26)	346.9	5.2	1.7 (19)
	S2	1099	9.1	2.3 (27)	345	3	0.68 (27)
	S3				349	4	0.98 (21)
	Expected age	1102[c]	5	0.8 (70)	343[d]	2	0.7 (96)

[a] Mean K–Ar age of bulk GL-O sample from Odin (1982); Löhr et al. (2024).

[b] ID-TIMS U–Pb age reported by Thompson et al. (2016).

[c] MC-ICP-MS Lu–Hf age from Simpson et al. (2024).

[d] Long-term weighted mean apatite Lu–Hf ages from Glorie et al. (2024b).

(2) Carbonate and apatite *in situ* U–Pb dating

In situ U–Pb dating of dolomite followed the protocols outlined by Gilbert and Glorie (2020), and Simpson et al. (2021a). The reaction gas used was NH_3, which reacts with Hg^+ ions to eliminate the isobaric interference of ^{204}Hg from ^{204}Pb, a circular laser beam with a diameter of 100 µm, a fluence of 8 J/cm^2, and a repetition rate of 5 Hz was employed for dolomite ablation (Supplementary Table S1). NIST 610 served as the primary standard for element concentrations and drift correction, while WC1 was used as the secondary standard for matrix fractionation correction of $^{238}U/^{206}Pb$. Elemental concentrations were calculated by normalizing to 100% cation-CO_3 totals, with measured ^{43}Ca used for internal standard normalization. The geochronology data are presented as 3D isochrons plotted on Tera-Wasserburg concordia plots, using $^{238}U/^{206}Pb$, $^{207}Pb/^{206}Pb$, and $^{204}Pb/^{206}Pb$ ratios, along with their 2s uncertainties or error correlations. WC1 yielded an age of 246.8 ± 4.2 Ma (Supplementary Fig. S3; Table S3), consistent with the reference age of 254.4 ± 6.4 Ma (Roberts et al., 2017).

The apatite U–Pb dating was conducted in two sessions. Session 1 was performed alongside carbonate U–Pb dating, using the same analytical settings but with a 30 µm laser spot. Session 2 followed the methods of Glorie et al. (2019) and Gillespie et al. (2018), analysing two samples (CTD1 and CTD3) using a 30 µm laser spot size and a repetition rate of 5 Hz (Supplementary File 1). In both sessions, NIST 610 and MAD apatite (U–Pb age of 473.5 ±

0.7 Ma, Chew et al., 2014; Thomson et al., 2012) were used as primary reference material to calibrate Pb/Pb and U/Pb, respectively. Apatite 401 (U–Pb age of 525 ± 8 Ma, Thompson et al., 2016) served as a secondary reference material to assess accuracy. The obtained U–Pb ages of apatite 401 in the two sessions were 524 ± 3.6 and 527.6 ±7.1 Ma (Table 1; Supplementary Files 4 & 6), in agreement with its reported age. Trace element data were collected simultaneously using ^{43}Ca as the internal standard element. Subsequently, only minerals with high Lu concentrations (>1 ppm) were selected for *in situ* Lu–Hf dating.

(3) Apatite in situ Lu–Hf dating

In situ Lu–Hf dating followed the method described by Simpson et al. (2021b). Samples were analyzed in three sessions using a laser beam diameter of 120 µm (for samples CTD1, CTD3 and CTD4) to 173 µm (for sample CTD2), a fluence of 3.5 J/cm^2, and a repetition rate of 10 Hz (Supplementary File 1). A reaction gas mixture of 10% NH_3 and 90% He was used to separate ^{176}Hf from ^{176}Lu and ^{176}Yb. Reaction products of ^{176}Hf and ^{178}Hf were measured at 258 and 260 amu, respectively, free from isobaric interferences. The ^{176}Lu concentration was calculated from measured ^{175}Lu, and ^{177}Hf was determined from measured ^{178}Hf, assuming their natural abundances as detailed in Simpson et al. (2021b). NIST 610 served as the primary reference material for normalization and drift corrections, and measured ^{43}Ca was used as the internal standard element. In sessions 1 and 2, apatite OD306 (1597 ± 7 Ma, Thompson et al., 2016) was used for matrix-dependent fractionation correction. The secondary reference material, HR1 apatite (343 ± 2 Ma, Glorie et al., 2024b) and Bamble1 apatite (1102 ± 5 Ma, Simpson et al., 2024) were used to verify accuracy. In the third session, Bamble 1 served as the secondary reference material for matrix-dependent fractionation correction, while HR1 was used as the secondary reference material for accuracy checking. Lu–Hf ages were anchored to an initial ^{177}Hf/^{176}Hf ratio of 3.55 ± 0.05, constraining the allowable variability during the regression to the full range of terrestrial ^{177}Hf/^{176}Hf ratios (Glorie et al., 2024b; Kharkongor et al., 2023; Simpson et al., 2024). The matrix fractionation-corrected Lu–Hf ages for secondary reference apatites Bamble 1 and HR-1 are 1095.6 ± 8.5 Ma and 343.8 ± 3.6 Ma, respectively.

During session 3, HR1 produced an age of 347 ± 4Ma (Table 1). All corrected Lu–Hf ages are consistent within uncertainties with previously reported dates (Glorie et al., 2024b; Simpson et al., 2024). All data and isochrons of the standards are provided in Supplementary Files 7 & 8.

2.4 Results

2.4.1 Mineralogy and Chemical Composition

The samples in this study are predominantly dolostone, except for one bioclastic phosphorite sample (CTD2; Fig. 3a, Fig. 4) and one micrite sample (Fig. 3b). Dolostone is categorized into three types: silty dolomicrite, sparry dolograinstone, and crystallized dolomite (Figs. 3c–f). Micrite is commonly present in the Currant Bush Formation in the Carrara1 drill core (Fig. 3b). It is interbedded with argillaceous micrite, calcareous marl and siltstone, with dolomite and quartz occurring as part of the micritic matrix. Sparry dolograinstone mainly developed in the Inca Formation of Oban1 and the lower Woarah Formation in NTGS01/1. It features grains of micritic dolomitic intraclasts and bioclasts with partial dolomitization along the grain rims. The matrix consists predominantly of recrystallized dolomite, ranging from 50 to 300 µm in size (Fig. 3c). Crystallized dolostone is mainly found in the Thortonia Limestone in CTDD0001 and CTDD0002 and the upper Wonarah Formation in NTGS01/1 (Figs. 3d–f). It is categorized into three groups based on crystal size: fine crystalline dolomite (<50 µm), medium crystalline dolomite (50–200 µm), and coarse crystalline dolomite (>200 µm). Coarse crystalline dolomite often exhibits foggy cores and bright rims with dolomite overgrowth zones at the edges (Fig. 3e).

Phosphatic bioclasts and glauconite pellets are abundant in the dolostone (Figs. 3 & 4). Common forms include pelletal, ellipsoidal, and elongate fossil apatite, ranging from 30 µm to 2 mm. Pelletal and elongated glauconite are also present, with some appearing as cementlike glauconite, ranging from 50 µm to 500 µm (Fig. 3e).

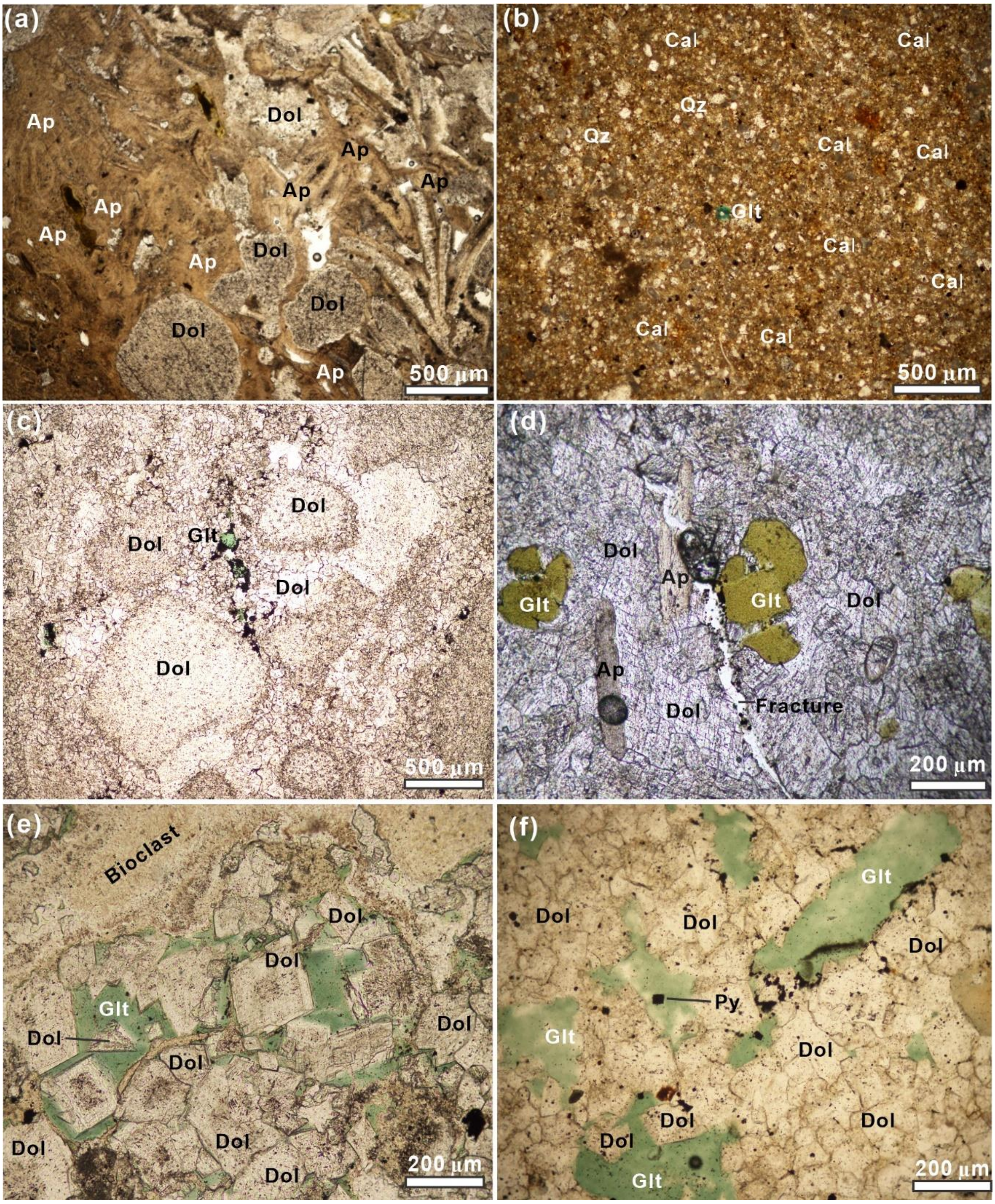

Figure 3. Lithology and mineralogy of carbonate-hosted glauconite and bioapatite from the middle Cambrian strata of the Georgina Basin. (**a**) Bioclastic phosphorite with micritic dolomite intraclasts embedded within fossil networks (CTD2, Thorntonia Limestone); (**b**) Argillaceous micrite containing dolomite, quartz and glauconite (Ca1, Currant Bush Limestone); (**c**) Sparry dolomitic grainstone, transitioning from matrix-supported to grain-supported, with partially dissolved and dolomitised glauconite (SI, Inca Formation); (**d**)

Medium to coarse crystalline dolomite with apatite and glauconite; glauconite partially replaced by dolomite, with microfractures present (CTD3, Thorntonia Limestone); (**e**) Coarse crystalline dolomite exhibiting foggy cores and bright rims, with glauconite partially replaced by dolomite (NT2, Thorntonia Limestone); (**f**) Medium to coarse crystalline dolomite containing partially dissolved and dolomitised glauconite, accompanied by pyrite inclusions (NT4, Wonarah Formation). Ap = apatite; Cal = calcite; Dol = dolomite; Glt = glauconite; Py = pyrite; Qz = quartz.

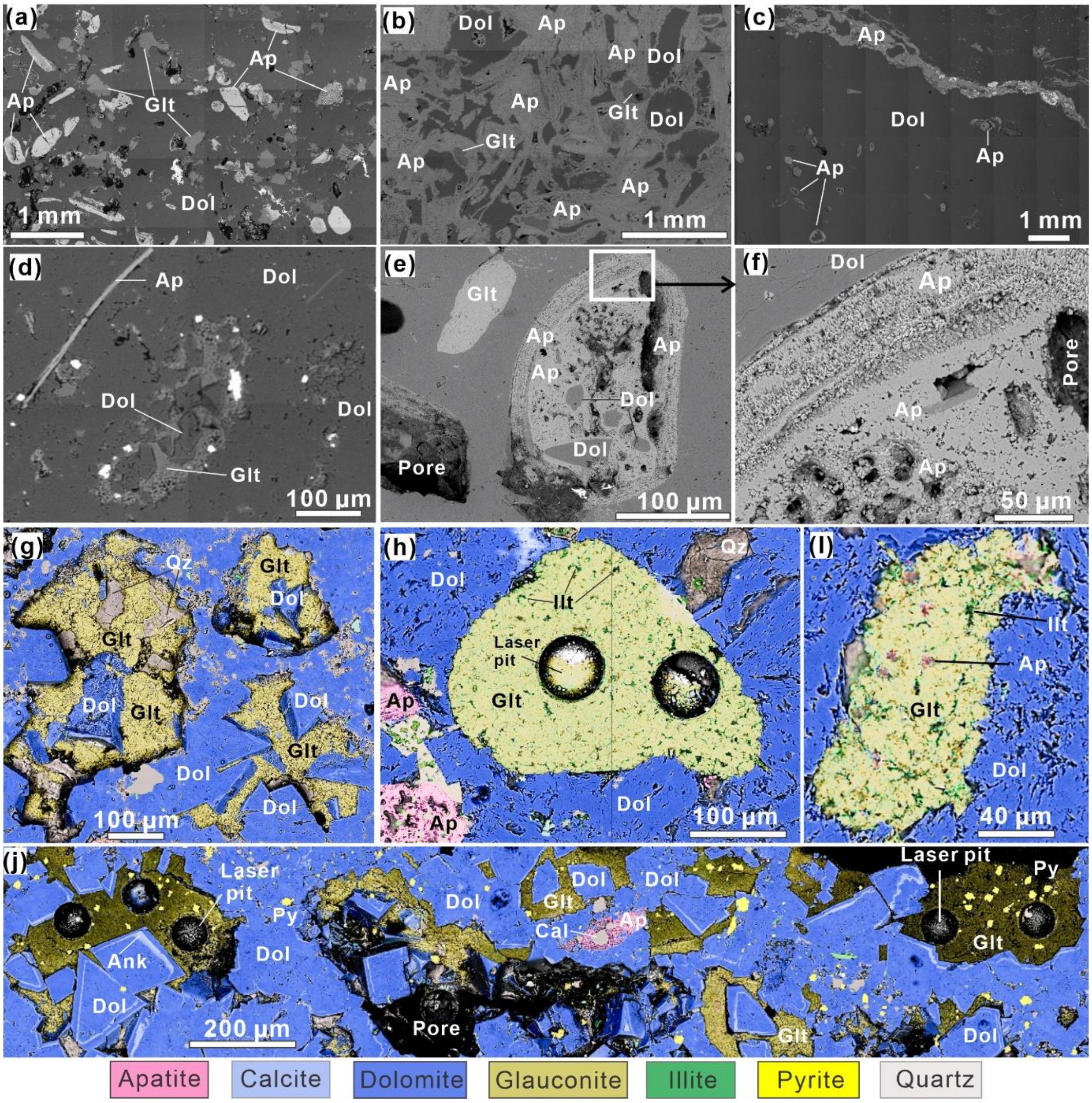

Figure 4. BSE images and nanomin minerals mapping of carbonate-hosted glauconite and apatite from the middle Cambrian Georgina Basin. (**a**) Porous dolostone with abundant apatite

and glauconite (CTD3, Thorntonia Limestone); (**b**) Bioclastic phosphorite with dolomite intraclasts and glauconite pellets (CTD2, Thorntonia Limestone); (**c**) Stylolite in dolostone infilled with crystalline apatite and dolomite (SA, Inca Formation); (**d**) Glauconite was dissolved and replaced by dolomite (Oban4, Inca Formation); (**e**) Porous dolostone containing glauconite and small shelly apatite, with apatite partially dissolved and replaced by dolomite (CTD3, Thorntonia Limestone); (**f**) High-resolution magnification of the area outlined in (**e**), showing oriented recrystallized apatite overgrowth layers in the fossil shell, highly porous; (**g**) Dissolved glauconite replaced by dolomite and calcite, highly porous (NT1, Wonarah Formation); (**h**) Illitised glauconite with illite present in the dissolved pores; craters are laser spots (CTD1, Thorntonia Limestone); (**i**) Illitised glauconite with apatite and calcite inclusions (SA, Inca Formation); (**j**) Glauconite dissolved and replaced by dolomite, ankerite, and pyrite, with apatite replaced by calcite; craters are laser spots (NT2, Wonarah Formation). Glt = glauconite; Dol = dolomite; Ap = apatite; Py = pyrite, Ilt = illite, Cal = calcite, Ank = ankerite.

The study area or investigated samples underwent extensive diagenesis, with dissolution and replacement being the most prevalent processes (Figs. 3c–f, 4). Medium to coarse crystalline dolomite underwent significant dolomitization (Figs. 3d–f, 4g, 4j), while dissolution residual structures are evident in the sparry dolograinstone (Fig. 3c). The rocks exhibit numerous microfractures and pores, some filled with organic matter, suggesting fluid-rock interaction (Figs. 3c–d, 4). Stylolites are commonly infilled with secondary apatite and dolomite, indicating pressure dissolution and subsequent re-crystallization or mineralization (Fig. 4c). Glauconite grains frequently show partial replacement by dolomite, calcite, and pyrite, or are infilled with apatite and illite within dissolved micropores, highlighting complex diagenetic pathways (Figs. 3d–f, 4a, 4d, 4g–j). Apatite also undergoes replacement by dolomite and calcite, with some fossil shells displaying recrystallized apatite (Figs.4e, 4f, 4j), illustrating the extensive alteration and recrystallization.

The chemical (major oxides) composition of glauconite reflects its maturity, heterogeneity and potential diagenetic alteration. Based on K_2O content, glauconite maturity is categorized as nascent (2–4%), slightly evolved (4–6%), evolved (6–8%), and highly evolved (>8%) (Odin and Matter, 1981). In the Georgina Basin, the EPMA analysis shows glauconite K_2O content ranges from 4.6% to 8.6%, with an average of 7.5%, indicating evolved glauconite grains or origins (Fig. 5a). Fe_2O_3 content varies from 0.67% to 17.4%, with an average of 10.2%. Data points with both low K_2O and Fe_2O_3 concentrations suggest possible glauconite dissolution. The Al_2O_3 content of glauconite ranges from 6.6% to 18.6% with a mean of 12.8%. A negative correlation exists between Fe_2O_3 and Al_2O_3, which is a common feature for glauconite grains (Löhr et al., 2024, and references therein). Anomalous points, characterised by low Fe_2O_3 and Al_2O_3 values but high CaO, P_2O_5 and MgO contents, likely indicate the presence of apatite, dolomite, and calcite micro-inclusions within the glauconite grains (Figs. 5b–d). All EPMA data are provided in the Supplementary File 9.

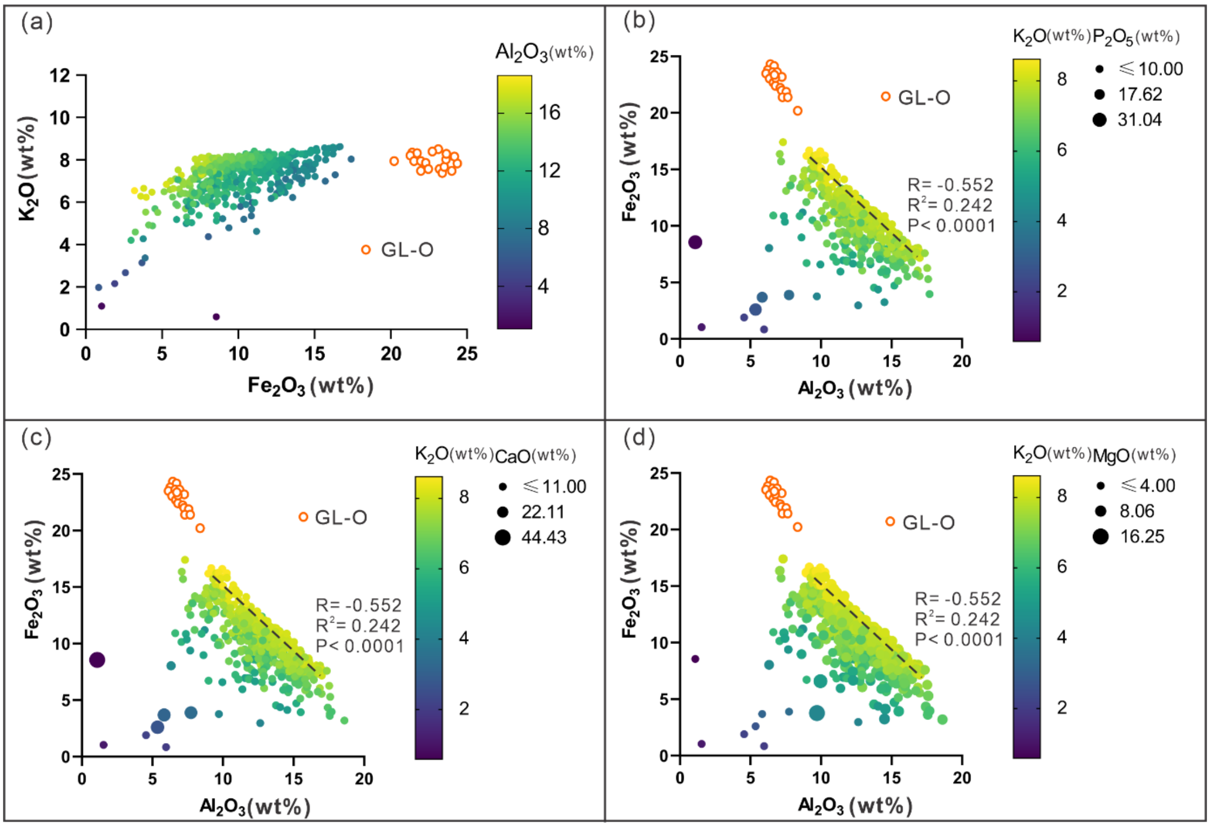

Figure 5. Cross plots of selected elements or major element oxides (in wt%) from studied glauconite grains and EPMA analysis. (**a**) Cross plot of glauconite K_2O vs. Fe_2O_3 with Al_2O_3 colour-coded; (**b**) Cross plot of glauconite Fe_2O_3 vs. Al_2O_3 with P_2O_5 colour-coded; (**c**) Cross

plot of glauconite Fe_2O_3 vs. Al_2O_3 with K_2O and CaO colour-coded; (**d**) Cross plot of glauconite Fe_2O_3 vs. Al_2O_3 with K_2O and MgO colour-coded.

As illustrated in Fig. 6, complex micro-scale heterogeneities within a single glauconite grain are highlighted by grain-scale EPMA mapping. A microfracture in Zone A (Fig. 6) has led to dissolution and illitization, characterised by increased Al and decreased Fe, with a slight reduction in K. Zones B, C, and D (Figs. 6a–c) show a negative correlation between Al and Fe, where higher Fe levels are associated with lower Al, while K concentrations remain stable. These variations may result from diagenetic alterations or differences in glauconite maturity. Apatite and dolomite inclusions within the glauconite grains (Figs. 6d–e) likely reflect diagenetic processes. Additionally, the presence of a Ti-rich mineral or micro-inclusion, likely related to a detrital phase, is noted (Fig. 6f).

2.4.2 *In situ* Glauconite Rb–Sr Ages

As presented in Table 2 and Fig. 7, *in situ* Rb–Sr ages for the Georgina Basin glauconites range from 452 ± 13 Ma to 351 ± 8 Ma (with initial $^{87}Sr/^{86}Sr$ ratios of 0.7087 ± 0.0035 and 0.7144 ± 0.0072, respectively). Additional isochrons and Rb–Sr ages are provided in Supplementary File 2. The Rb–Sr dating results show a departure from the expected mid-Cambrian depositional age of 505 ± 3 Ma (Kruse et al., 2013; Laurie, 2022; Percival and Kruse, 2014; Smith et al., 2015), which in turn confirms that the Rb–Sr isotope system in the studies glauconite was reset after the deposition. However, these Rb–Sr ages align well with the timing of the Alice Springs Orogeny, which occurred between ~450 and ~300 Ma (Haines et al., 2001; Nixon et al., 2022; Piazolo et al., 2020; Varga et al., 2021). This observation and agreement suggest a possible link and correlation between the local/regional tectonic activity and the resetting of glauconite Rb–Sr ages in the Georgina Basin.

In detail, glauconite pellets from samples NT1 and NT2, extracted from NTGS01/1 at depths of 183.5 m and 183.7 m, respectively, yielded distinct ages of 417 ± 6 Ma and 377 ± 7 Ma. This difference is notable given their close proximity of just 20 cm. Similarly, glauconite samples NT3 and NT4, taken from depths of 251.6 m and 251.85 m, respectively, produced ages of 396 ± 8 Ma and 351 ± 8 Ma respectively (Fig. 8). The initial $^{87}Sr/^{86}Sr$ ratios in glauconite also vary among samples, ranging from 0.7087 ± 0.0035 to 0.7229 ± 0.0070 (Table 2).

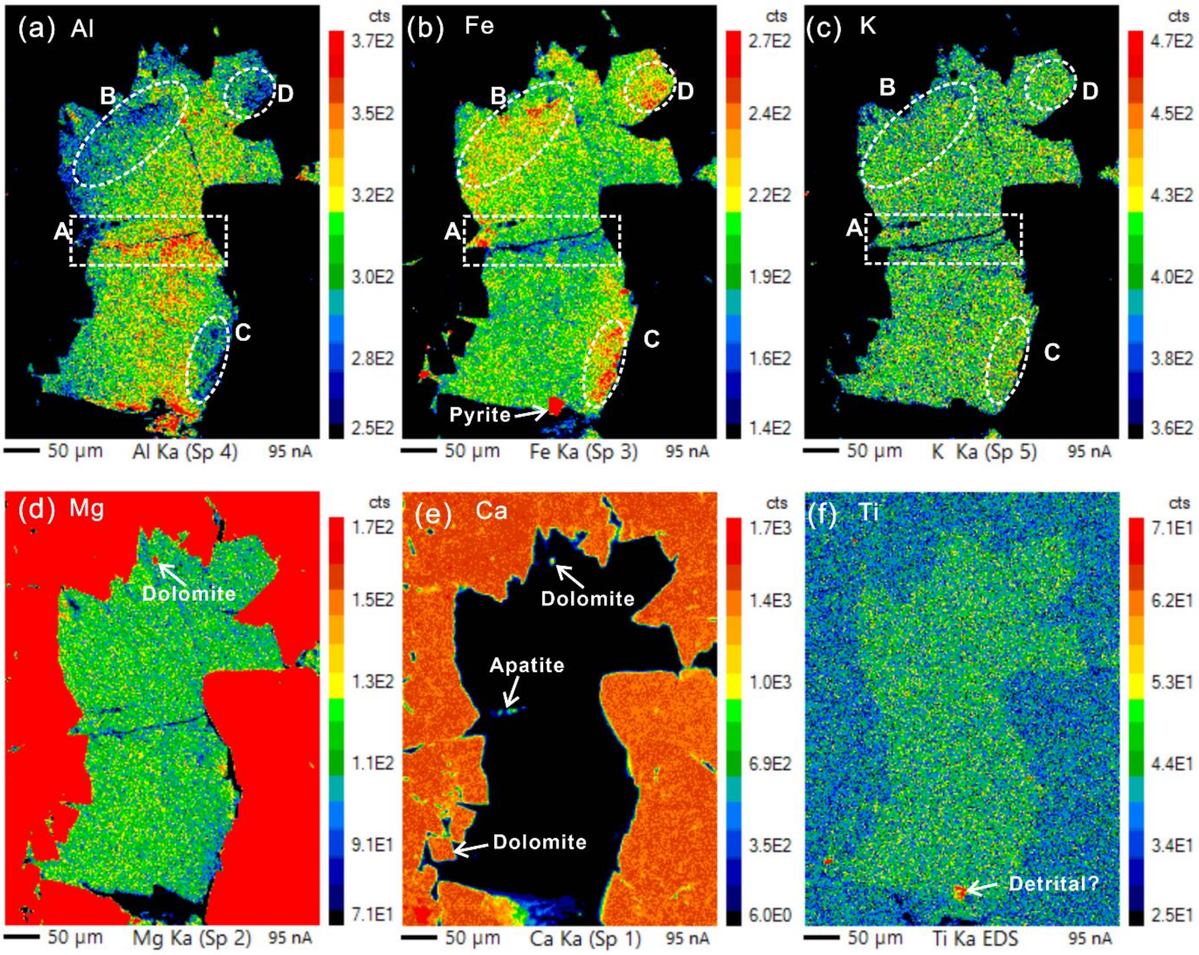

Figure 6. Grain-scale EPMA mapping of a single glauconite grain (CTD3, Thorntonia Limestone).

Table 2. Summary of *in situ* LA-ICP-MS/MS dating results, and sample lithologies, for the studied samples

Sample name	Well name	Depth (m)	Formation	Lithology	Glauconite Rb-Sr age (Ma)	Initial $^{87}Sr/^{86}Sr$	Carbonate U-Pb age (Ma)	Initial $^{207}Pb/^{206}Pb$	Apatite Lu-Hf age (Ma)
Ca1	Carrara1	412.9	Currant Bush Lst	Micrite			500.4 ± 16.6	0.829 ± 0.042	
CTD1	CTDD0001	447.1	Thorntonia Fm	Dolomite	402.7 ± 11.1	0.7159 ± 0.0078			497 ± 69
CTD2	CTDD0001	447.17	Thorntonia Fm	Phosphorite	388.7 ± 6.6	0.7128 ± 0.0041	513.5 ± 18.9	0.784 ± 0.028	422 ± 49
CTD3	CTDD0002	411.8	Thorntonia Fm	Dolomite	430.0 ± 12.7	0.7229 ± 0.0070	478 ± 23.2	0.650 ± 0.064	478 ± 78
CTD4	CTDD0002	412	Thorntonia Fm	Dolomite	414.0 ± 25.7	0.7214 ± 0.0074			493 ± 74
SA	Oban1	168.8	Inca Fm	Dolomite	452.0 ± 13.0	0.7087 ± 0.0035			
Oban4	Oban1	174.17	Inca Fm	Dolomite	439.6 ± 6.7	0.7128 ± 0.0026			
SF	Oban1	168.66	Inca Fm	Dolomite	429.2 ± 11.4	0.7136 ± 0.0038			
SI	Oban1	168.54	Inca Fm	Dolomite	429.2 ± 9.3	0.7135 ± 0.0036			
NT1	NTGS01/1	183.5	Wonarah Fm	Dolomite	417.4 ± 5.5	0.7144 ± 0.0060			
NT2	NTGS01/1	183.7	Wonarah Fm	Dolomite	377.4 ± 7.3	0.7152 ± 0.0054			
NT3	NTGS01/1	251.6	Wonarah Fm	Dolomite	396.2 ± 7.8	0.7182 ± 0.0062			
NT4	NTGS01/1	251.85	Wonarah Fm	Dolomite	350.5 ± 8.3	0.7144 ± 0.0072			
NT5	NTGS01/1	269.7	Wonarah Fm	Dolomite	421.9 ± 7.9	0.7103 ± 0.0042			
NT6	NTGS01/1	320	Wonarah Fm	Dolomite	427.9 ± 9.2	0.7094 ± 0.0042			

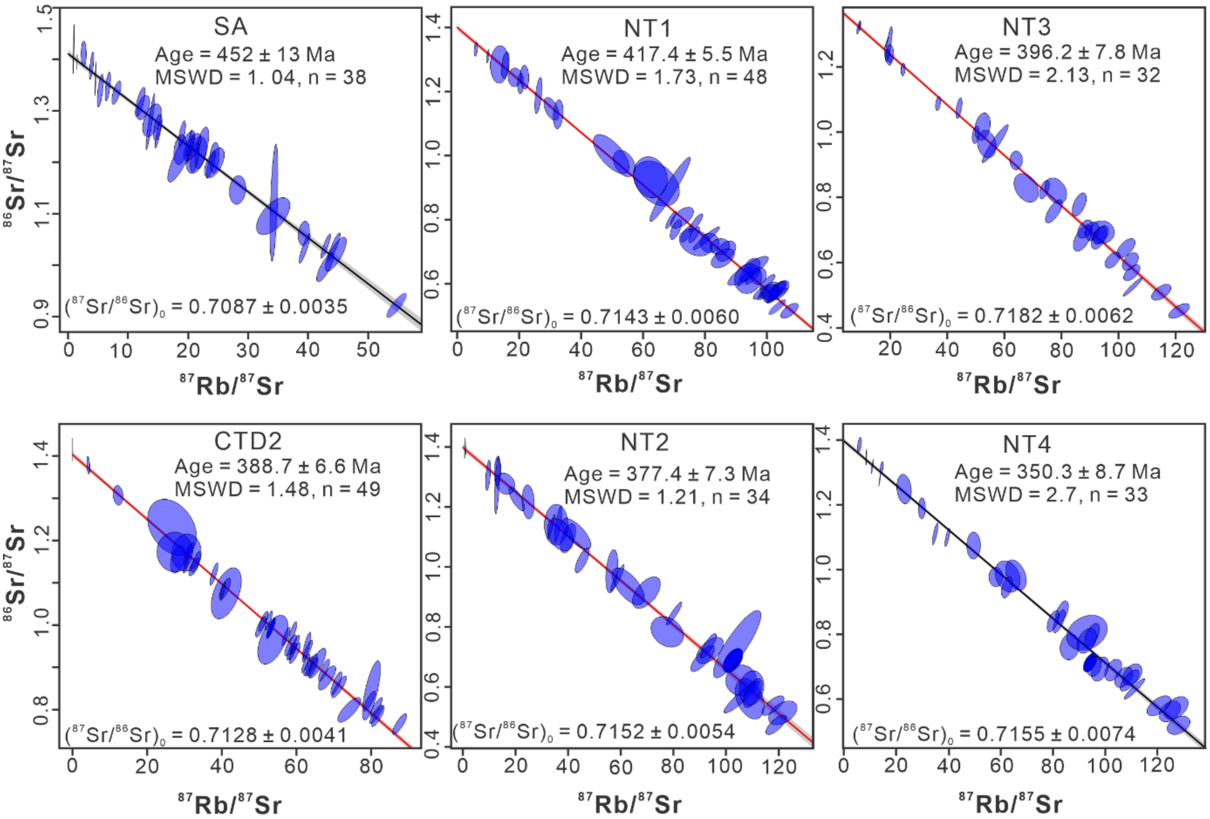

Figure 7. Selected glauconite Rb–Sr isochrons and ages from mid-Cambrian strata of the

Georgina Basin. Note that additional Rb–Sr isochron plots for remaining samples are presented in the Supplementary Material (Fig. S2).

2.4.3 *In situ* Carbonate U–Pb Ages

In situ carbonate U–Pb dating was conducted on samples Ca1 from drill hole Carral 1, CTD2 from drill hole CTDD0001, and CTD3 from drill hole CTDD0002. Measured U concentrations range from 3.0 to 8.1 ppm in Ca1, 0.1 to 22.2 ppm in CTD2, and 0.1 to 5.9 ppm in CTD3. The U–Pb ages are presented in Tera-Wasserburg concordia plots (Fig. 8).

Carbonate U–Pb dating revealed variations in ages and initial Pb ratios among the samples, and the micrite sample Ca1 yielded a lower intercept age of 500 ± 17 Ma, with an initial ^{207}Pb/^{206}Pb ratio of 0.829 ± 0.042 (MSWD = 4.9) (Fig. 8). The fine crystalline dolomite sample CTD2 produced an older apparent age of 513 ± 19 Ma, with an initial ^{207}Pb/^{206}Pb ratio of 0.781 ± 0.028 (MSWD = 4.6). In contrast, the medium to coarse crystalline dolomite sample CTD3 yielded a younger age of 478 ± 23 Ma, with a lower initial ^{207}Pb/^{206}Pb ratio of 0.650 ± 0.064. Sample CTD3 data exhibit significant dispersion, with an MSWD of 10. The initial Pb compositions of samples CTD2 and CTD3 deviate notably from the expected Cambrian seawater Pb isotope ratios based on Stacey and Kramers (1975). When anchored to an initial ^{207}Pb/^{206}Pb ratio of 0.85 ± 0.05, the two samples yielded ages of 514 ± 24 Ma and 474.5 ± 29.9 Ma, respectively.

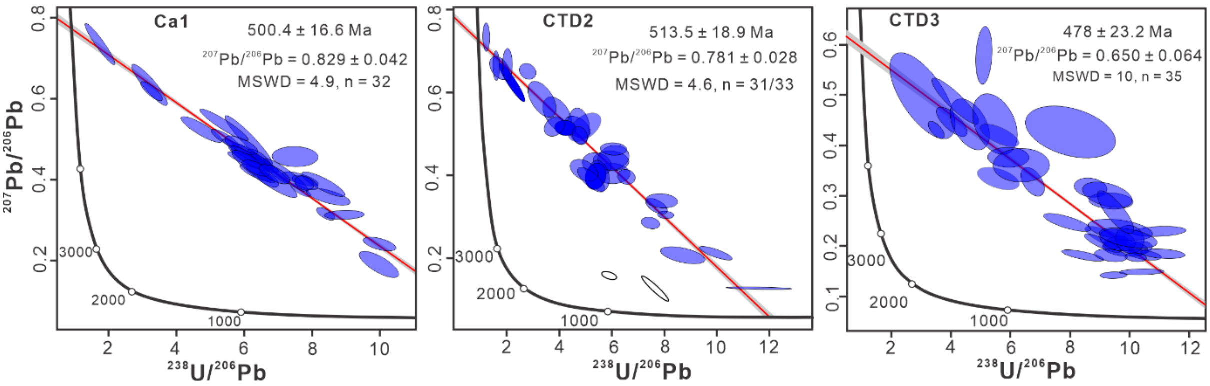

Figure 8. Tera-Wasserburg isochron plots of dolomite U–Pb ages from the Georgina Basin. The empty ellipses represent laser spots in sample CTD2 with apatite-dominated inclusions.

2.4.4 *In situ* apatite U–Pb and Lu–Hf Ages

In situ apatite U–Pb and Lu–Hf dating was conducted on samples CTD1 and CTD2 from drill hole CTDD0001, and CTD3 and CTD4 from drill hole CTDD0002. U concentrations range from 29.7 to 108.8 ppm in CTD1, 26.5 to 72.1 ppm in CTD2, 21.9 to 139.4 ppm in CTD3, and 30.3 to 95.4 ppm in CTD4.

The apatite U–Pb dating data are highly dispersed, regressing toward unrealistically younger ages with large uncertainties and initial $^{207}Pb/^{206}Pb$ ratios significantly lower than 0.85 (Figs. 9a–9d). All data points fall below the assumed isochron line, which has an expected age of 505 Ma (lower intercept) and an initial $^{207}Pb/^{206}Pb$ ratio of 0.85 (Fig. 9e). Additionally, the data exhibit varying degrees of U loss (Fig. 9f).

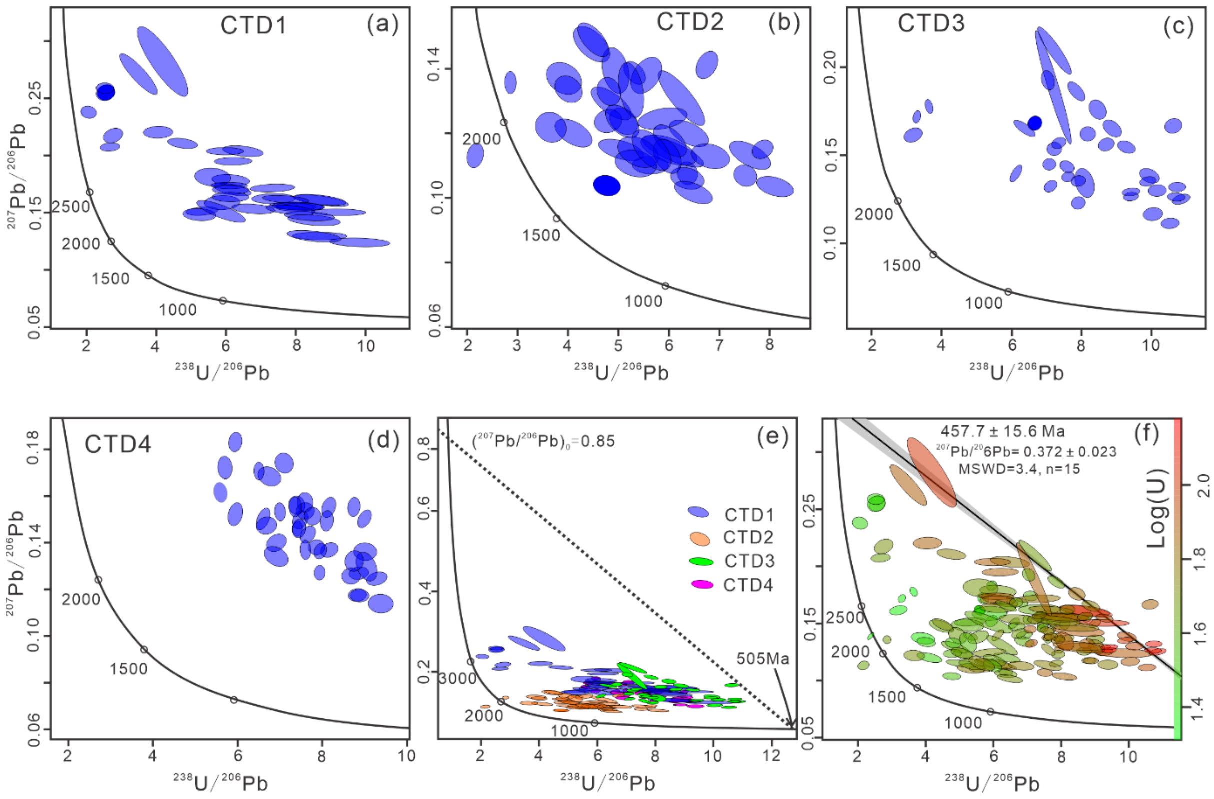

Figure 9. Tera-Wasserburg isochron plots of apatite U–Pb dating. (a)–(d) Isochron plots for each sample; (**e**) Isochron plot of four samples combined, with the dashed line representing the assumed isochron, having a Y-intercept (initial Pb ratio) of 0.85 and a lower intercept of 505

Ma; (**f**) Isochron plot of four samples combined, with U concentration (LogU) represented by color coding.

The Lu concentrations vary among the samples, but are generally low: CTD1 yielded Lu content ranging from 0.13 to 2.13 ppm, CTD2 from 0.50 to 0.97 ppm, CTD3 from 0.61 to 3.67 ppm, and CTD4 from 0.13 to 1.72 ppm. The obtained inverse isochrons and *in situ* Lu–Hf ages are as follows: CTD1 = 497 ± 69 Ma, CTD3 = 495 ± 79 Ma, and CTD4 = 493 ± 74 Ma. In contrast, sample CTD2, obtained from a phosphorite, produced an age of 425 ± 49 Ma (Fig. 10).

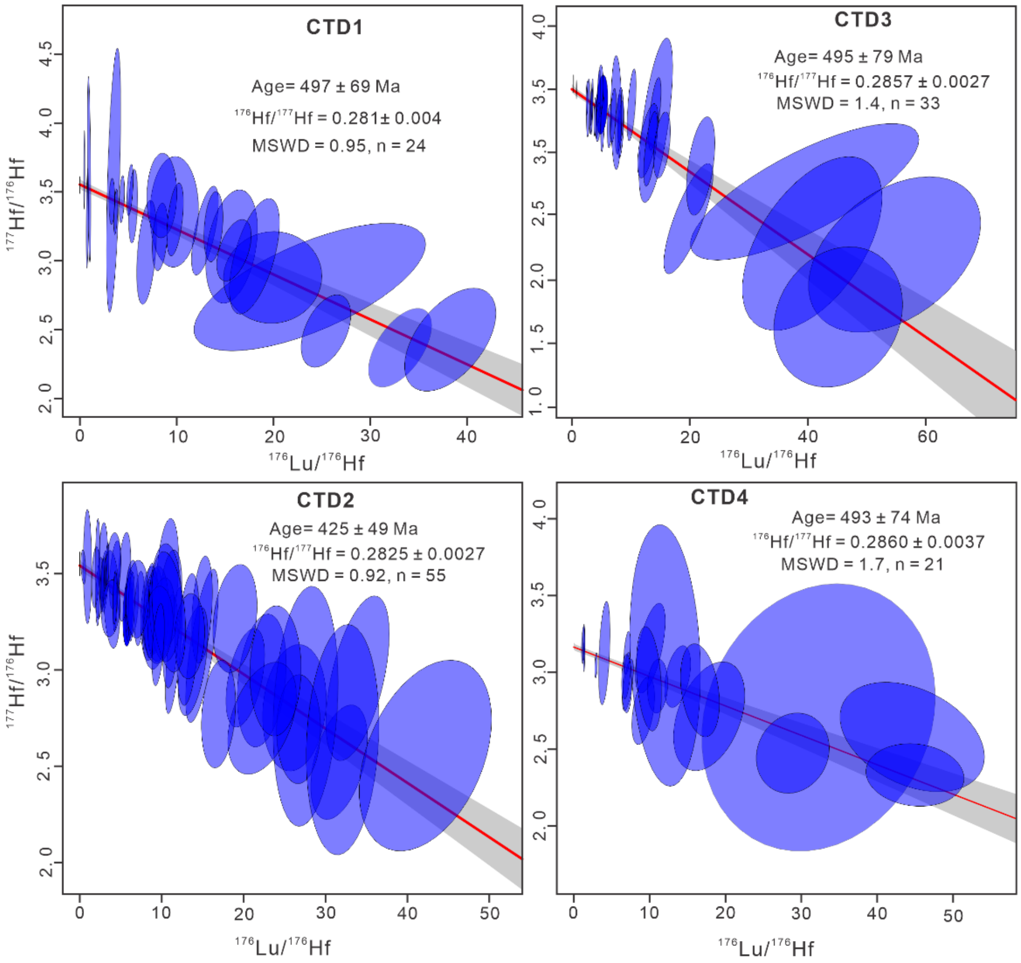

Figure 10. Inverse isochron ages for apatite acquired via *in situ* Lu–Hf dating.

2.5 Discussion

2.5.1 Constraining Depositional Age and Diagenesis via Authigenic Mineral Geochronometers

Biostratigraphic studies confirm that all samples in this study are from the middle Wuliuan to middle Drumian Stages of the Miaolingian Epoch, with an estimated depositional age of 505 ± 3 Ma (Kruse et al., 2013; Laurie, 2022; Percival and Kruse, 2014; Smith et al., 2015). Micrite sample Ca1 yielded a U–Pb age of 500 ± 17 Ma with an initial $^{207}Pb/^{206}Pb$ ratio of 0.829 ± 0.042, which aligns well with the expected depositional age (Figs. 8 & 11), indicating that the U–Pb system closed during or shortly after carbonate formation. In contrast, sample CTD2 also produced an age that overlaps with the depositional age but exhibits a lower initial Pb ratio of 0.781 ± 0.028. Diagenetic resetting of the U–Pb system in carbonate often results in younger ages and lower initial $^{207}Pb/^{206}Pb$ ratios than expected, due to either fluid-induced opening of the U–Pb system or Pb homogenization in a closed system (Ben-Israel et al., 2024; Neagu et al., 2025; Roberts et al., 2020). The deviation in sample CTD2 is likely due to U mobility (U loss), which partially disturbed the U–Pb system (Roberts et al., 2020), resulting in an older apparent age and a reduced initial Pb ratio. A similar process affected sample CTD3, where U mobilization caused an anticlockwise rotation of the isochron line. This disturbance resulted in a younger apparent age with a significantly lower initial Pb ratio of 0.650 ± 0.064. The pronounced influence of U mobility is further reflected in the high data scatter, as indicated by an elevated MSWD of 10 (Fig. 8).

The above interpretations of carbonate U–Pb dating results are supported by petrographical and mineralogical observations. Sample Ca1, primarily composed of argillaceous micrite, consists of fine-crystalline calcite that has remained largely unaltered (Fig. 3b). Sample CTD2, a bioclastic phosphorite, contains fine-crystalline dolomite intraclasts embedded within phosphatic fossil networks. While the dolomite grains or clasts are generally well-preserved, their rims exhibit minor recrystallization due to later diagenesis (Fig. 3a). Sample CTD3 is composed of euhedral to subhedral medium- to coarse-crystalline dolomite (Fig. 3d), indicative of a later stage dolomite recrystallization pointing to a partially open U–Pb system and U mobilization, compared to the best preserved samples.

The apatite U–Pb data yielded highly dispersed and unrealistic ages (Fig. 9), indicating isotopic disturbance. This suggests an open U–Pb system with varying degrees of U loss from the samples (Fig. 9f). This is similar to the previously mentioned U–Pb resetting in dolomites, but with a more pronounced alteration trend. The mobility of U also caused changes in Pb distribution within apatite, altering the Pb reservoir in the fluid-rock system, likely due to diagenetic dissolution and recrystallization (Figs. 4d & e).

The Lu–Hf dates of apatite from three bioclastic dolostone samples (CTD1, CTD3, and CTD4) are 497 ± 69 Ma, 495 ± 79 Ma, and 493 ± 93 Ma, respectively (Figs 10 & 11). Although these ages overlap with the depositional age, within their uncertainties, the uncertainties are large (ca. 15%), which hinders detailed interpretations. These uncertainties are primarily driven by low Lu concentrations, which reduce the precision of acquired in situ Lu–Hf ages. The average Lu concentration across three analyzed samples is ca. 2 ppm, limiting the accuracy of the Lu–Hf age calculations for apatite.

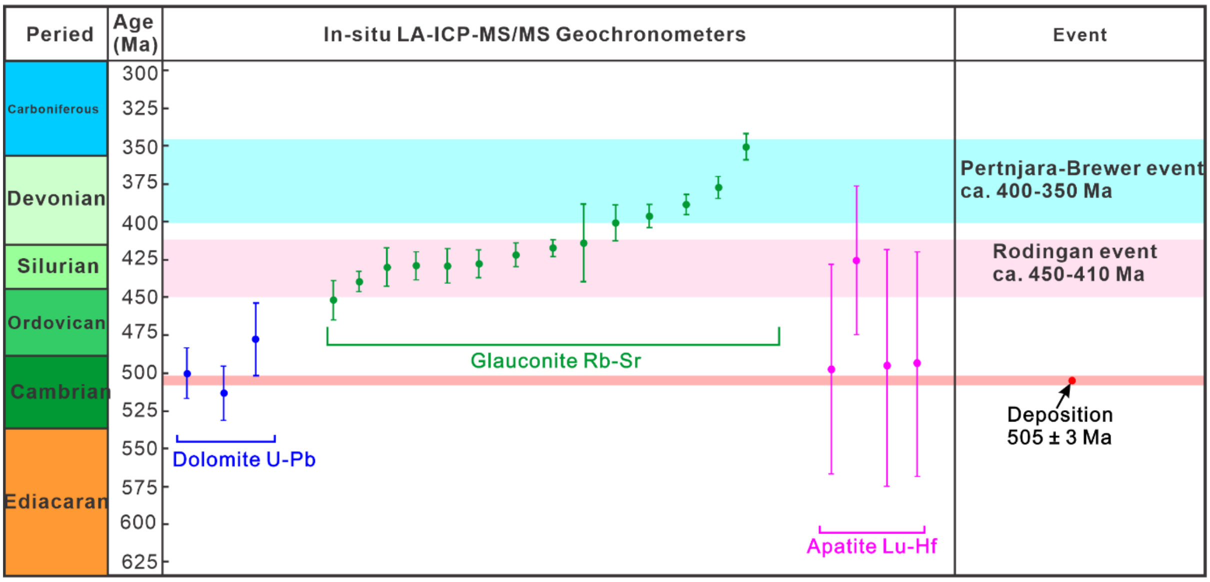

Figure 11. Summary of *in situ* LA-ICP-MS/MS dating results (Rb–Sr, U–Pb and Lu–Hf) for mid-Cambrian dolomite, glauconite and apatite from the Georgina Basin, plotted alongside the expected depositional age (~505 Ma), and major tectonic and orogenic events (refer to the references in the main text).

2.5.2 Altered apatite Lu–Hf Ages

Bioclastic phosphorite sample CTD2 yielded a Lu–Hf age of 425 ± 49 Ma (Figs. 10 & 11), which is younger than the expected depositional age and appears to correspond to the Rodingan orogenic event. This age may indicate late-stage phosphogenesis linked to fluid movement or recrystallisation during this event, as well as late-stage diagenesis/phosphogenesis (Fig. 4b), further supported by presence of stylolites filled with recrystallized apatite (Fig. 4c). Organic matter and bitumen are also commonly found in stylolites. High organic carbon content has been linked to a potential source of phosphorus for apatite formation in the Georgina Basin (Creveling et al., 2014). Intensive pressure dissolution within dolostone might have facilitated the decay of organic matter, releasing phosphorus that promoted secondary apatite precipitation. During the Alice Springs Orogeny, the southern margin of the Georgina Basin experienced intense thermal alteration (Munson, 2014), while peak basin-wide geothermal activity led to an elevated geothermal gradient (Dunster et al., 2007). The Alice Springs Orogeny likely accelerated diagenesis by increasing temperature and pressure, which in turn enhanced late-stage phosphogenesis. The younger Lu–Hf age of the phosphorite (425 ± 49 Ma) might be thus linked to later-stage alteration and hydrocarbon generation and accumulation, associated with widespread organic matter maturation and degradation.

2.5.3 Altered Glauconite Rb–Sr Ages

Glauconitization typically begins with the formation of Fe-smectite precursors, which result from the disaggregation of substrates such as detrital grains, carbonate debris, fecal pellets, and internal molds (Odin and Matter, 1981; Starzec et al., 2023). As glauconite matures, both Fe and K are progressively incorporated, leading to mineralogical changes and the development of highly evolved glauconite with a K_2O content exceeding 8%. The glauconitization process can take up to 1 million years (Baldermann et al., 2017; Rubio and López-Pérez, 2024). Evolved glauconite typically contains more than 15% Fe_2O_3 (Rubio and López-Pérez, 2024). This high iron content often correlates negatively with Al_2O_3, due to the substitution of Fe^{3+} for Al^{3+} at the octahedral sites within the mineral structure (López-Quirós et al., 2019).

Some studies have reported that glauconite Rb–Sr and/or K–Ar ages are generally 10–20% younger than their depositional ages (Morton and Long, 1984; Rafiei et al., 2023; Rubio and López-Pérez, 2024; Selby, 2009; Środoń et al., 2023). This age discrepancy or 'rejuvenation' may be attributed to several factors, including diagenetic illitization (Ireland et al., 1983; Scheiblhofer et al., 2022), alteration by meteoric water (Morton and Long, 1984), and/or the loss of Ar and Sr in expanded layers (Ireland et al., 1983; Selby, 2009).

Similar to the studies mentioned above, the acquired Rb–Sr glauconite ages from the Georgina Basin exhibit systematically younger or 'rejuvenated' ages compared to the expected depositional age, indicating significant post-depositional resetting (Fig. 11). The Rb–Sr ages can be categorized into two groups: Age group 1 spans from 452 ± 13 Ma to 414 ± 26 Ma, while Age Group 2 ranges from 403 ± 11 Ma to 351 ± 8 Ma (Figs. 7 & 11). These age groups align well with two episodes of the Alice Springs Orogeny—the Rodingan event and the Pertnjara-Brewer event, which impacted the Georgina Basin (Haines et al., 2001; Nixon et al., 2022; Piazolo et al., 2020; Varga et al., 2021).

The Alice Springs Orogeny, an intracontinental compressional tectonic event that occurred from the Late Ordovician to the Carboniferous periods (ca. 450–300 Ma), was characterised by a significant uplift, exhumation, reverse thrust faulting and folding across central Australia, including the Georgina Basin (Kruse et al., 2013). This orogeny is subdivided into three episodes: the Rodingan event (ca. 450–440 Ma), the Pertnjara-Brewer event (390–360 Ma) and the Mount Eclipse event (340–320 Ma) (Haines et al., 2001; Varga et al., 2021). Various types of sediment-hosted mineralization, including Pb-Zn and Cu, have been reported to be associated with the Alice Springs Orogeny in the Georgina Basin (Kruse et al., 2013).

Also, the generally highly evolved glauconite from the Georgina Basin, characterised by its high K_2O content, exhibits a negative correlation between Fe_2O_3 and Al_2O_3 contents (Fig. 5). Notably, the Fe_2O_3 concentration in the studied glauconites is systematically lower compared to the 'pristine' and much younger (ca. 95 Ma) glauconite standard GL-O. The observed loss of Fe_2O_3 in glauconites from the Georgina Basin is accompanied by a corresponding increase in Al_2O_3 content (Fig. 5). Similarly, highly evolved yet partly altered glauconites with such elevated Al (and low Fe) content are commonly observed in Precambrian strata. Previous studies have attributed these chemical changes to post-depositional diagenetic effects and recrystalization of glauconites (Środoń et al., 2023) and/or the pseudomorphic replacement of abiotic detrital minerals (Banerjee et al., 2016; Starzec et al., 2023).

In this study, glauconite samples were obtained from mid-Cambrian fossiliferous carbonate lithologies, and it is proposed that the observed high Al and low Fe contents are due to the aforementioned post-depositional recrystallization (Środoń et al., 2023), and likely later-stage diagenetic illitization (Fig. 4). A similar trend, where an increased Al content in glauconites was attributed to later-stage diagenetic alteration, was observed in Cretaceous strata (Banerjee et al., 2016). Illitization is prevalent in the studied mid-Cambrian glauconites from the Georgina Basin, as confirmed by both SEM-EDS (BSE-MLA) (Figs. 4h, 4i) and EPMA mapping (Fig. 6). Additionally, our data indicate that this secondary alteration process occurred more readily in microfractures and porous areas within glauconite pellets, where diagenetic fluids can more easily percolate, thus facilitating illitization.

Dolomite, calcite, and apatite inclusions were frequently observed within the mid-Cambrian glauconite grains (Figs. 3d–f; Figs. 4d, 4g–j). While some of these inclusions may share a cogenetic origin (Rafiei et al., 2023), they also indicate that dolomitization, calcification, and phosphatization of the glauconite pellets occurred during later-stage diagenesis. These diagenetic alteration phenomena are further supported by the presence of unusually high Mg, Ca, and P concentrations in selected glauconite grains, as revealed by EPMA screening (Fig. 5).

Additionally, dissolution effects were observed in both the glauconite grains and the carbonate matrix, particularly in porous and fractured areas (Figs. 3–4). These dissolution reactions likely altered the elemental composition of glauconite, promoting cation exchange and element loss, thereby contributing to the younger or ‘rejuvenated’ Rb–Sr glauconite ages observed from the mid-Cambrian strata of the Georgina Basin.

Overall, we conclude that the above diagenetic processes significantly contributed to the mobilization of Rb and Sr, causing resetting and secondary (post-depositional) re-equilibration of the Rb–Sr isotope system, resulting in the younger Rb–Sr isochron ages. Finally, the observed age variations, despite the close proximity of certain sample pairs within the studied cores (NT1 & NT2 and NT3 & NT4), likely reflect the impact of complex and localised diagenetic processes that affected each sample differently.

2.5.4 Lu–Hf Dating of Authigenic Apatite is More Robust than U–Pb

Our results also revealed that authigenic apatite U–Pb dating appears less reliable compared to Lu–Hf dating, despite the latter yielding larger (~15%) age uncertainities. We propose that the systematically younger and reset U–Pb apatite ages are due to low U concentrations and high common Pb content (Lan et al., 2025), or varying degrees of U and Pb loss and mobilization during the post-depositional and late diagenetic processes (Simpson et al., 2024). In contrast, apatite Lu–Hf dating appears to be more robust, likely due to its higher closure temperature (ca. 660 to 730 °C, Glorie et al., 2024b), which makes the Lu–Hf system less susceptible to post-depositional alteration and isotope resetting, even under deep burial diagenetic conditions (ca. 120 to 250 °C) in sedimentary basins. However, as mentioned, the precision of our current in situ Lu–Hf dating is limited by the generally lower Lu concentrations in apatites. Therefore, selecting samples with higher Lu concentrations, coupled with potential future developments and the application of a laser-based collision cell MC-ICP-MS, could further improve the precision of *in situ* Lu–Hf dating. Additionally, the long half-life of ^{176}Lu (~37.12 Ga) poses another challenge for dating younger samples. Systematic and detailed petrographic and microscopic screening of samples, along with high-resolution SEM/EDS imaging and elemental mapping, have proven crucial for effectively targeting suitable authigenic mineral phases for *in situ* dating, enabling successful data acquisition and geochronological interpretations.

2.6 Conclusions

This study successfully applied novel in situ LA-ICP-MS/MS geochronology to date various authigenic minerals (carbonates, phosphates, and clays) from marine sedimentary sequences, focusing on glauconite-bearing dolomitic and phosphate-rich lithologies within the mid-

Cambrian strata of the Georgina Basin in Australia.

This study revealed that glauconite Rb–Sr ages are all consistently younger (ranging from 452 ± 13 Ma to 351 ± 8 Ma) compared to the expected depositional age (505 ± 3 Ma). The *in situ* Rb–Sr ages can be broadly divided into two groups, corresponding to two episodes of the Alice Springs Orogeny. The first group aligns with the timing of the Rodingan event (450–440 Ma), while the second group aligns with the timing of the Pertnjara-Brewer event (390–360 Ma). We conclude that the glauconite Rb–Sr system is susceptible to post-depositional resetting due to later diagenetic and burial processes, likely linked to orogenic and tectonic events. These processes controlled alteration phenomena such as glauconite recrystallization, dissolution and illitization, which could explain the observed younger or 'rejuvenated' Rb–Sr ages.

In contrast, a well-preserved micrite sample yielded an *in situ* U–Pb age of 500 ± 17 Ma, which is consistent with the expected mid-Cambrian (~505 Ma) depositional age. Another sample of fine-grained dolomite produced an *in situ* U–Pb age of 513 ± 19 Ma, which also overlaps the depositional age within uncertainties. However, a medium- to coarse-crystalline dolomite produced a reset U–Pb age of 478 ± 23 Ma, with a much lower apparent initial Pb value. We argue that in this coarser, more altered dolomite, the U–Pb system became partially open due to secondary processes, such as U loss, which disturbed the U–Pb isochron and ages, resulting in low ^{207}Pb/^{206}Pb ratios and apparent reset ages.

The apatite samples from both dolostone and phosphorite also yielded reset U–Pb ages, which were affected by large uncertainties and much lower initial Pb ratios, indicating more extensive disturbance of the U–Pb system due to post-depositional alteration and the previously mentioned U loss phenomenon.

Finally, three apatite samples from dolostone yielded *in situ* Lu–Hf ages of 497 ± 69 Ma, 495 ± 79 Ma, and 493 ± 74 Ma, overlapping with the mid-Cambrian depositional age. However, the large age uncertainties (~15%) due to low Lu concentrations hinder a more robust interpretation of these ages. Additionally, apatite from the phosphorite sample yielded an *in situ* Lu–Hf age of 425 ± 49 Ma, corresponding to the Rodingan event, which may indicate that later-stage phosphogenesis in the Georgina Basin might be linked to the above post-depositional event.

Overall, this study demonstrates both the potential and limitations of using multiple *in situ* LA-ICP-MS/MS dating techniques (i.e., a triple dating approach based on Rb–Sr, U–Pb and Lu–Hf) for marine authigenic minerals. The laser-based *in situ* triple dating allows for the rapid and direct determination of depositional and/or diagenetic ages of authigenic minerals (carbonates, phosphates, clays) with high spatial resolution and minimal sample preparation. This approach enhances our understanding of basin evolution and associated post-depositional events, as illustrated by the study of the Georgina Basin in Australia.

2.7 Acknowledgments

This study was supported by an ARC Discovery Project (DP210100462) titled 'Glauconite: Archive Recording Timing and Triggers of Cambrian Radiation', an ARC Linkage Project (LP210200822) titled 'Novel Isotope Techniques to Explore the Centralian Superbasin, Australia', and an Australian Research Council Future Fellowship (FT210100906) and Laureate Fellowship (FL240100114). In addition, financial support from MinEx CRC via PhD research bursary to ZS is also acknowledged. Our thanks go to Professor Carl Spandler for providing some of the samples. We are grateful for the laboratory and technical assistance provided by Dr. Benjamin Wade with EPMA analysis, Dr. Nobuyuki Kawashima with SEM-EDS analysis, Dr. Sean Murray with high-resolution SEM-EDS analysis, and Dr. Stefan Löhr with processing high-resolution SEM-EDS data. Additionally, we thank Melissa Kharkongor and Alejandra Mejia for their help with Lu–Hf data processing. The authors also acknowledge the instruments and expertise of Microscopy Australia (ROR: 042mm0k03) at Adelaide Microscopy, University of Adelaide, enabled by NCRIS, university, and state government support. This study represents a contribution to the MinEx CRC (Contribution #286/81130467).

2.8 References

Aubineau, J., Séranne, M., Chi-Fru, E., Poujol, M., El Bamiki, R., Antonio, P. V. J., Muñoz, M., Elghali, A., Raji, O., Jouranar, E., Bodinier, J. L., Parat, F., 2024. Deciphering the U-Pb dates of sedimentary phosphates: a complex example from the Upper Cretaceous-Lower Paleogene series in northwestern Morocco. Chemical Geology, 661: 122178. https://doi.org/10.1016/j.chemgeo.2024.122178.

Baldermann, A., Dietzel, M., Mavromatis, V., Mittermayr, F., Warr, L. N., Wemmer, K., 2017. The role of Fe on the formation and diagenesis of interstratified glauconite-smectite and illite-smectite: A case study of Upper Cretaceous shallow-water carbonates. Chemical Geology, 453: 21-34. https://doi.org/10.1016/j.chemgeo.2017.02.008.

Banerjee, S., Bansal, U., Pande, K., Meena, S., 2016. Compositional variability of glauconites within the Upper Cretaceous Karai Shale Formation, Cauvery Basin, India: implications for evaluation of stratigraphic condensation. Sedimentary Geology, 331: 12-29. https://doi.org/10.1016/j.sedgeo.2015.10.012.

Ben-Israel, M., Holder, R. M., Nelson, L. L., Smith, E. F., Kylander-Clark, A. R., Ryb, U., 2024. Late Paleozoic oxygenation of marine environments supported by dolomite U-Pb dating. Nature Communications, 15(1): 2892. https://doi.org/10.1038/s41467-024-46660-7.

Blaise, T., Clauer, N., Cathelineau, M., Boiron, M. C., Techer, I., Boulvais, P., 2016. Reconstructing fluid-flow events in Lower-Triassic sandstones of the eastern Paris Basin by elemental tracing and isotopic dating of nanometric illite crystals. Geochimica et Cosmochimica Acta, 176: 157-184. https://doi.org/10.1016/j.gca.2015.12.018.

Carr, L., Korsch, R.J., Reese, B., Palu, T., 2016. Onshore Basin Inventory: the McArthur, South Nicholson, Georgina, Wiso, Amadeus, Warburton, Cooper and Galilee basins, central Australia. Geoscience Australia.

Chew, D., Petrus, J., Kamber, B., 2014. U–Pb LA–ICPMS dating using accessory mineral standards with variable common Pb. Chemical Geology, 363: 185-199. https://doi.org/10.1016/j.chemgeo.2013.11.006.

Clauer, N., 2020. The post-Variscan tectonic-thermal activity in the southeastern metalliferous province of the French Massif Central revisited with K-Ar ages of illite. Ore Geology Reviews, 117: 103300. https://doi.org/10.1016/j.oregeorev.2019.103300.

Clauer, N., Zwingmann, H., Todd, A., Aubert, A., 2019. Potassium-argon timing of episodic mica and illite crystallization in highly indurated Hassi Messaoud (Algeria) hydrocarbon-bearing sandstones. AAPG Bulletin, 103(1): 215-240. https://doi.org/10.1306/06071816525.

Creveling, J. R., Johnston, D. T., Poulton, S. W., Kotrc, B., März, C., Schrag, D. P., Knoll, A. H., 2014. Phosphorus sources for phosphatic Cambrian carbonates. GSA Bulletin, 126(1-2): 145-163. https://doi.org/10.1130/B30819.1.

Dunster, J., Kruse, P., Duffett, M., Ambrose, G., 2007. Geology and resource potential of the southern Georgina Basin. Digital information package DIP007. Darwin: Northern Territory Geological Survey.

Elisha, B., Nuriel, P., Kylander-Clark, A., Weinberger, R., 2021. Towards in situ U–Pb dating of dolomite. Geochronology, 3(1): 337-349. https://doi.org/10.5194/gchron-3-337-2021.

Gilbert, S.E., Glorie, S., 2020. Removal of Hg interferences for common Pb correction when dating apatite and titanite by LA-ICP-MS/MS. Journal of Analytical Atomic Spectrometry, 35(7): 1472-1481. https://doi.org/10.1039/d0ja00224k.

Gillespie, J., Glorie, S., Khudoley, A., Collins, A. S., 2018. Detrital apatite U-Pb and trace element analysis as a provenance tool: Insights from the Yenisey Ridge (Siberia). Lithos 314: 140-155. https://doi.org/10.1016/j.lithos.2018.05.026.

Glass, L.M., Phillips, D., 2006. The Kalkarindji continental flood basalt province: A new Cambrian large igneous province in Australia with possible links to faunal extinctions. Geology, 34(6): 461-464. https://doi.org/10.1130/G22122.1.

Glorie, S., Jepson, G., Konopelko, D., Mirkamalov, R., Meeuws, F., Gilbert, S., Gillespie, J., Collins, A., Xiao, W., Dewaele, S., 2019. Thermochronological and geochemical footprints of post-orogenic fluid alteration recorded in apatite: Implications for mineralisation in the Uzbek Tian Shan. Gondwana Research 71, 1-15. https://doi.org/10.1016/j.gr.2019.01.011.

Glorie, S., March, S., Nixon, A., Meeuws, F., O'Sullivan, G. J., Chew, D. M., Kirkland, C. L., Konopelko, D., De Grave, J., 2020. Apatite U–Pb dating and geochemistry of the Kyrgyz

South Tian Shan (Central Asia): Establishing an apatite fingerprint for provenance studies. Geosci. Front. 11 (6), 2003–2015. https://doi.org/10.1016/j.gsf.2020.06.003.

Glorie, S., Burke, T., Hand, M., Simpson, A., Gilbert, S., Wade, B., 2022. In situ Lu–Hf phosphate geochronology: Progress towards a new tool for space exploration. Geoscience Frontiers, 13(3): 101375. https://doi.org/10.1016/j.gsf.2022.101375.

Glorie, S., Mulder, J., Hand, M., Fabris, A., Simpson, A., Gilbert, S., 2023. Laser ablation (in situ) Lu-Hf dating of magmatic fluorite and hydrothermal fluorite-bearing veins. Geoscience Frontiers, 14(6): 101629. https://doi.org/10.1016/j.gsf.2023.101629.

Glorie, S., Gilbert, S.E., Hand, M., Lloyd, J.C., 2024a. Calibration methods for laser ablation Rb–Sr geochronology: comparisons and recommendation based on NIST glass and natural reference materials. Geochronology, 6(1): 21-36. https://doi.org/10.5194/gchron-6-21-2024.

Glorie, S., Hand, M., Mulder, J., Simpson, A., Emo, R. B., Kamber, B., Fernie, N., Nixon, A., Gilbert, S., 2024b. Robust laser ablation Lu–Hf dating of apatite: an empirical evaluation. Geological Society, London, Special Publications, 537(1): 165-184. https://doi.org/10.1144/SP537-2022-205.

Gopalan, K., 2008. Conjunctive K–Ca and Rb–Sr dating of glauconies. Chemical Geology, 247(1-2): 119-123. https://doi.org/10.1016/j.chemgeo.2007.10.004.

Haines, P.W., Hand, M., Sandiford, M., 2001. Palaeozoic synorogenic sedimentation in central and northern Australia: A review of distribution and timing with implications for the evolution of intracontinental orogens. Australian Journal of Earth Sciences, 48(6): 911-928. https://doi.org/10.1046/j.1440-0952.2001.00909.x.

Hand, M., Mawby, J., Kinny, P., Foden, J., 1999. U–Pb ages from the Harts Range, central Australia: evidence for early Ordovician extension and constraints on Carboniferous metamorphism. Journal of the Geological Society, 156(4): 715-730. https://doi.org/10.1144/gsjgs.156.4.0715.

Hogmalm, K.J., Zack, T., Karlsson, A.K.-O., Sjöqvist, A.S., Garbe-Schönberg, D., 2017. In situ Rb–Sr and K–Ca dating by LA-ICP-MS/MS: an evaluation of N 2 O and SF 6 as reaction gases. Journal of Analytical Atomic Spectrometry, 32(2): 305-313. https://doi.org/10.1039/C6JA00362A.

Hu, Z., Gao, S., Liu, Y., Hu, S., Chen, H., Yuan, H., 2008. Signal enhancement in laser ablation ICP-MS by addition of nitrogen in the central channel gas. Journal of Analytical Atomic Spectrometry, 23(8): 1093-1101. https://doi.org/10.1039/b804760j.

Ireland, B., Curtis, C., Whiteman, J., 1983. Compositional variation within some glauconites and illites and implications for their stability and origins. Sedimentology, 30(6): 769-786. https://doi.org/10.1111/j.1365-3091.1983.tb00710.x.

Kharkongor, M. B., Glorie, S., Mulder, J., Kirkland, C. L., Chew, D., Kohn, B., Simpson, A., 2023. Apatite laser ablation LuHf geochronology: a new tool to date mafic rocks. Chemical Geology, 636: 121630. https://doi.org/10.1016/j.chemgeo.2023.121630.

Khider, K., MacFarlane, S., Bradshaw, B.E., Carr, L., Henson, P., 2021. The Centralian Superbasin (Canning, Amadeus, Georgina and Officer basins) Stratigraphic Review and Well Correlations.

Kruse, P.D., 2008. Georgina Basin: Stratigraphic Drilling 2002-2006 and Petrography 2000-2007. Northern Territory Geological Survey.

Kruse, P., Dunster, J., Munson, T., 2013. Chapter 28: Georgina Basin, in Geology and Mineral Resources of the Northern Territory, Darwin: Northern Territory Geol. Surv. 28.1-28.56.

Lan, Z., Wu, S., Roberts, N. M., Zhang, S., Cao, R., Wang, H., Yang, Y., 2022. Geochronological and geochemical constraints on the origin of highly ^{13}Ccarb-depleted calcite in basal Ediacaran cap carbonate. Geological Magazine, 159(8): 1323-1334. https://doi.org/10.1017/S001675682200019X.

Lan, Z., Glorie, S., Löhr, S.C., Wang, R., Shen, B., 2025. Apatite Lu− Hf dating of late Archean banded iron formations. Geology, 53 (4): 338–342. https://doi.org/10.1130/G52919.1.

Laurie, J.R., 2022. Report on the biostratigraphy of the Georgina Basin succession in NDI Carrara 1. Geoscience Australia, Canberra. 1-7.

Li, Q., Parrish, R., Horstwood, M., McArthur, J., 2014. U–Pb dating of cements in Mesozoic ammonites. Chemical Geology, 376: 76-83.

https://doi.org/10.1016/j.chemgeo.2014.03.020.

Li, Z., Rankenburg, K., Normore, L. S., Evans, N. J., McInnes, B. I. A., Dent, L. M., Fielding, I. O. H., 2023. In situ calcite U–Pb geochronology of carbonate and clastic sedimentary rocks from the Canning Basin, Western Australia. Australian Journal of Earth Sciences, 70(3): 332-343. https://doi.org/10.1080/08120099.2023.2161635.

Löhr, S.C., Khazaie, E., Farkaš, J., Baldermann, A., Gilbert, S., Maas, R., Subarkah, D., Blades, M.L., Collins, A.S., 2024. Origin and Significance of Age Variability in the Glauconite Reference Material GL-O: Implications for In Situ Rb-Sr Geochronology. Geostandards and Geoanalytical Research. https://doi.org/10.1111/ggr.12588.

López-Quirós, A., Escutia, C., Sánchez-Navas, A., Nieto, F., Garcia-Casco, A., Martín-Algarra, A., Evangelinos, D., Salabarnada, A., 2019. Glaucony authigenesis, maturity and alteration in the Weddell Sea: An indicator of paleoenvironmental conditions before the onset of Antarctic glaciation. Scientific reports 9 (1), 13580. https://doi.org/10.1038/s41598-019-50107-1.

Loyola, C., Farkaš, J., Collins, A. S., Gilbert, S. E., Verdel, C., Löhr, S. C., Brock, G. A., Shields, G. A., Baldermann, A., Redaa, A., Blades, M., Subarkah, D., Bishop, C., Giles, S. M., Christie-Blick, N., Haines, P. W., 2025. In situ Rb–Sr dating and REE analysis of glauconites and detrital feldspars from the Ediacaran/Cambrian strata: Centralian and Adelaide Superbasins, Australia. Precambrian Res. 427, 107851. https://doi.org/10.1016/j. precamres.2025.107851.

Morton, J.P., Long, L.E., 1984. Rb-Sr ages of glauconite recrystallization; dating times of regional emergence above sea level. Journal of Sedimentary Research, 54(2): 495-506. https://doi.org/10.1306/212F8454-2B24-11D7-8648000102C1865D.

Munson, T., 2014. Petroleum geology and potential of the onshore Northern Territory, 2014. Northern Territory Geological Survey.

Neagu, N., Kylander-Clark, A., Fischer, W.W., Ryb, U., 2025. More than an age: U-Pb dating constrains alteration of Precambrian carbonates. Earth and Planetary Science Letters, 651: 119154. https://doi.org/10.1016/j.epsl.2024.119154.

Nixon, A. L., Glorie, S., Fernie, N., Hand, M., De Vries Van Leeuwen, A. T., Collins, A. S., Hasterok, D., Fraser, G., 2022. Intracontinental fault reactivation in high heat production areas of central Australia: insights from apatite fission track thermochronology. Geochemistry, Geophysics, Geosystems, 23(12): e2022GC010559. https://doi.org/10.1029/2022GC010559

Norris, A., Danyushevsky, L., 2018. Towards estimating the complete uncertainty budget of quantified results measured by LA-ICP-MS. Goldschmidt: Boston, MA, USA.

Odin, G.S., Matter, A., 1981. De glauconiarum origine. Sedimentology, 28(5): 611-641. https://doi.org/10.1111/j.1365-3091.1981.tb01925.x.

Odin, G., 1982. Interlaboratory standards for dating purposes. In: Odin, G. (Ed.), Numerical dating in stratigraphy. Wiley, New York, pp. 123-150.

Pagès, A., Schmid, S., Edwards, D., Barnes, S., He, N. and Grice, K., 2016. A molecular and isotopic study of palaeoenvironmental conditions through the middle Cambrian in the Georgina Basin, central Australia. Earth and Planetary Science Letters, 447: 21-32. https://doi.org/10.1016/j.epsl.2016.04.032.

Pan, L., Shen, A., Zhao, J. X., Hu, A., Hao, Y., Liang, F., Feng, Y., Wang, X., Jiang, L., 2020. LA-ICP-MS U-Pb geochronology and clumped isotope constraints on the formation and evolution of an ancient dolomite reservoir: The Middle Permian of northwest Sichuan Basin (SW China). Sedimentary Geology, 407: 105728. https://doi.org/10.1016/j.sedgeo.2020.105728.

Percival, I.G., Kruse, P.D., 2014. Middle Cambrian brachiopods from the southern Georgina Basin of central Australia. Memoirs of the Association of Australasian Palaeontologists(45): 349-402.

Piazolo, S., Daczko, N.R., Silva, D., Raimondo, T., 2020. Melt-present shear zones enable intracontinental orogenesis. Geology, 48(7): 643-648. https://doi.org/10.1130/G47126.1.

Rafiei, M., Löhr, S., Alard, O., Baldermann, A., Farkaš, J., Brock, G., 2023. Microscale petrographic, trace element, and isotopic constraints on glauconite diagenesis in altered sedimentary sequences: Implications for glauconite geochronology. Geochemistry, Geophysics, Geosystems 24, e2022GC010795. https://doi.org/10.1029/2022GC010795.

Redaa, A., Farkaš, J., Gilbert, S., Collins, A.S., Wade, B., Löhr, S., Zack, T., Garbe-Schönberg, D., 2021. Assessment of elemental fractionation and matrix effects during in situ Rb–Sr dating of phlogopite by LA-ICP-MS/MS: implications for the accuracy and precision of mineral ages. Journal of Analytical Atomic Spectrometry, 36(2): 322-344. https://doi.org/10.1039/D0JA00299B.

Redaa, A., Farkaš, J., Gilbert, S., Collins, A. S., Löhr, S., Vasegh, D., Forster, M., Blades. M., Zack., T., Giuliani, A., Maas, R., Baldermann, A., Dietzel, M., Garbe‐Schönberg, D., 2023. Testing Nano-Powder and Fused-Glass Mineral Reference Materials for In Situ Rb-Sr Dating of Glauconite, Phlogopite, Biotite and Feldspar via LA-ICP-MS/MS. Geostandards and Geoanalytical Research, 47(1): 23-48. https://doi.org/10.1111/ggr.12467.

Roberts, N.M., Walker, R.J., 2016. U-Pb geochronology of calcite-mineralized faults: Absolute timing of rift-related fault events on the northeast Atlantic margin. Geology, 44(7): 531-534. https://doi.org/10.1130/G37868.1.

Roberts, N. M., Rasbury, E. T., Parrish, R. R., Smith, C. J., Horstwood, M. S., Condon, D. J. , 2017. A calcite reference material for LA-ICP-MS U-Pb geochronology. Geochemistry, Geophysics, Geosystems, 18(7): 2807-2814. https://doi.org/10.1002/2016GC006784.

Roberts, N. M., Drost, K., Horstwood, M. S., Condon, D. J., Chew, D., Drake, H., Milodowski, A. E., McLean, N. M., Smye, A. J., Walker, R. J., Haslam, R., Hodson, K., Imber, J., Beaudoin, N., Lee, J. K., 2020. Laser ablation inductively coupled plasma mass spectrometry (LA-ICP-MS) U–Pb carbonate geochronology: strategies, progress, and limitations. Geochronology, 2(1): 33-61. https://doi.org/10.5194/gchron-2-33-2020.

Rubio, B., López-Pérez, A., 2024. Exploring the genesis of glaucony and verdine facies for paleoenvironmental interpretation: A review. Sedimentary Geology: 106579. https://doi.org/10.1016/j.sedgeo.2024.106579.

Scheiblhofer, E., Moser, U., Löhr, S., Wilmsen, M., Farkaš, J., Gallhofer, D., Bäckström, A. M., Zack, T., Baldermann, A., 2022. Revisiting Glauconite Geochronology: Lessons Learned from In Situ Radiometric Dating of a Glauconite-Rich Cretaceous Shelfal Sequence. Minerals, 12(7): 818. https://doi.org/10.3390/min12070818.

Selby, D., 2009. U-Pb zircon geochronology of the Aptian/Albian boundary implies that the GL-O international glauconite standard is anomalously young. Cretaceous Research, 30(5): 1263-1267. https://doi.org/10.1016/j.cretres.2009.07.001.

Simpson, A., Glorie, S., Morley, C. K., Roberts, N. M., Gillespie, J., Lee, J. K., 2021a. In-situ calcite U-Pb geochronology of hydrothermal veins in Thailand: New constraints on Indosinian and Cenozoic deformation. Journal of Asian Earth Sciences, 206: 104649. https://doi.org/10.1016/j.jseaes.2020.104649.

Simpson, A., Gilbert, S., Tamblyn, R., Hand, M., Spandler, C., Gillespie, J., Nixon, A., Glorie, S., 2021b. In-situ LuHf geochronology of garnet, apatite and xenotime by LA ICP MS/MS. Chemical Geology 577: 120299. https://doi.org/10.1016/j.chemgeo.2021.120299

Simpson, A., Glorie, S., Hand, M., Gilbert, S. E., Spandler, C., Dmitrijeva, M., Swain, G., Nixon, A., Mulder, J., Muenker, C., 2024. In situ apatite and carbonate Lu-Hf and molybdenite Re-Os geochronology for ore deposit research: Method validation and example application to Cu-Au mineralisation. Geoscience Frontiers, 15(5): 101867. https://doi.org/10.1016/j.gsf.2024.101867.

Smith, T., Kelman, A. P., Nicoll, R., Edwards, D., Hall, L., Laurie, J., Carr, L., 2013. An updated stratigraphic framework for the Georgina Basin, NT and Queensland. The APPEA Journal, 53(2): 487-487. https://doi.org/10.1071/AJ12098.

Smith, P.M., Brock, G.A., Paterson, J.R., 2015. Fauna and biostratigraphy of the Cambrian (Series 2, Stage 4; Ordian) Tempe Formation (Pertaoorrta Group), Amadeus Basin, Northern Territory. Alcheringa: An Australasian Journal of Palaeontology, 39(1): 40-70. https://doi.org/10.1080/03115518.2014.951917.

Solé, J., 2021. An automated System for measuring in situ K–Ar ages. Geostandards and Geoanalytical Research, 45(4): 659-678. https://doi.org/10.1111/ggr.12400.

Southgate, P., Shergold, J., 1991. Application of sequence stratigraphic concepts to Middle Cambrian phosphogenesis, Georgina Basin, Australia. BMR Journal of Australian

Geology and Geophysics, 12(2): 119-144.

Środoń, J., Williams, L., Szczerba, M., Zaitseva, T., Bojanowski, M. J., Marciniak-Maliszewska, B., Kuligiewicz, A., Starzec, K., Ciesielska, Z., Paszkowski, M., 2023. Mechanism of late diagenetic alteration of glauconite and implications for geochronology. Geochimica et Cosmochimica Acta, 352: 157-174. https://doi.org/10.1016/j.gca.2023.05.010.

Stacey, J.t., Kramers, J., 1975. Approximation of terrestrial lead isotope evolution by a two-stage model. Earth and planetary science letters, 26(2): 207-221. https://doi.org/10.1016/0012-821X(75)90088-6.

Starzec, K., Stadnik, R., Skiba, M., Bębenek, S., Waśkowska, A., 2023. Origin and paleoenvironmental significance of Al-rich glauconite in the Ediacaran/Cambrian deposits of the Lublin Basin, Poland (SW margin of Baltica). Precambrian Research, 397: 107165. https://doi.org/10.1016/j.precamres.2023.107165.

Subarkah, D., Blades, M. L., Collins, A. S., Farkaš, J., Gilbert, S., Löhr, S. C., Redaa, A., Cassidy, E., Zack, T., 2022a. Unraveling the histories of Proterozoic shales through in situ Rb-Sr dating and trace element laser ablation analysis. Geology, 50(1): 66-70. https://doi.org/10.1130/G49187.1.

Subarkah, D., Nixon, A. L., Jimenez, M., Collins, A. S., Blades, M. L., Farkaš, J., Gilbert, S. E., Holford, S., Jarrett, A., 2022b. Constraining the geothermal parameters of in situ Rb–Sr dating on Proterozoic shales and their subsequent applications. Geochronology, 4(2): 577-600. https://doi.org/10.5194/gchron-4-577-2022.

Subarkah, D., Nixon, A. L., Gilbert, S. E., Collins, A. S., Blades, M. L., Simpson, A., Lloyd, J., Virgo, G. M., Farkaš, J., 2024. Double dating sedimentary sequences using new applications of in-situ laser ablation analysis. Lithos, 480: 107649. https://doi.org/10.1016/j.lithos.2024.107649.

Thompson, J., Meffre, S., Maas, R., Kamenetsky, V., Kamenetsky, M., Goemann, K., Ehrig, K., Danyushevsky, L., 2016. Matrix effects in Pb/U measurements during LA-ICP-MS analysis of the mineral apatite. Journal of Analytical Atomic Spectrometry, 31(6): 1206-

1215. https://doi.org/10.1039/C6JA00048G.

Thomson, S.N., Gehrels, G.E., Ruiz, J., Buchwaldt, R., 2012. Routine low-damage apatite U-Pb dating using laser ablation–multicollector–ICPMS. Geochemistry, Geophysics, Geosystems, 13(2). https://doi.org/10.1029/2011GC003928.

Varga, J., Raimondo, T., Morrissey, L., Kelsey, D.E., Hand, M., 2021. Pressure–temperature–time constraints on gneiss dome formation in an intracontinental orogen. Journal of Metamorphic Geology, 40(3): 457-488. https://doi.org/10.1111/jmg.12635.

Vermeesch, P., 2018. IsoplotR: A free and open toolbox for geochronology. Geoscience Frontiers, 9(5): 1479-1493. https://doi.org/10.1016/j.gsf.2018.04.001

Walter, M., Veevers, J., Calver, C., Grey, K., 1995. Neoproterozoic stratigraphy of the Centralian superbasin, Australia. Precambrian Research, 73(1-4): 173-195. https://doi.org/10.1016/0301-9268(94)00077-5.

Woodhead, J., Petrus, J., 2019. Exploring the advantages and limitations of in situ U–Pb carbonate geochronology using speleothems. Geochronology, 1(1): 69-84. https://doi.org/10.5194/gchron-1-69-2019.

Wu, S., Yang, Y., Roberts, N. M., Yang, M., Wang, H., Lan, Z., Xie, B., Li, T., Xu, L., Huang, C., Xie, L., Yang, J., Wu, F., 2022. In situ calcite U– Pb geochronology by high-sensitivity single-collector LA-SF-ICP-MS. Science China Earth Sciences, 65(6): 1146-1160. http://dx.doi.org/10.1007/s11430-021-9907-1.

Wu, S., Wang, H., Yang, Y., Niu, J., Lan, Z., Zhang, L., Huang, C., Xie, L., Xu, L., Yang J., Wu, F., 2023a. In situ Lu–Hf geochronology with LA-ICP-MS/MS analysis. Journal of Analytical Atomic Spectrometry, 38(6): 1285-1300. https://doi.org/10.7185/gold2023.14178.

Wu, Y., Bai, X.-J., Shi, H.-S., He, L.-Y., Qiu, H.-N., 2023b. Dating of authigenic minerals in sedimentary rocks: A review. Earth-Science Reviews, 241: 104443. https://doi.org/10.1016/j.earscirev.2023.104443.

Xiong, S. F., Jiang, S. Y., Zhao, J. X., Niu, P. P., Ma, Y., Bai, X. Y., 2023. Dating Precambrian sedimentary carbonate strata by in situ U–Pb isotopes of dolomite. Precambrian Research, 393: 107088. https://doi.org/10.1016/j.precamres.2023.107088.

Zack, T., Hogmalm, K.J., 2016. Laser ablation Rb/Sr dating by online chemical separation of Rb and Sr in an oxygen-filled reaction cell. Chemical Geology, 437: 120-133. https://doi.org/10.1016/j.chemgeo.2016.05.027.

2.9 Supplementary Materials–Chapter 2

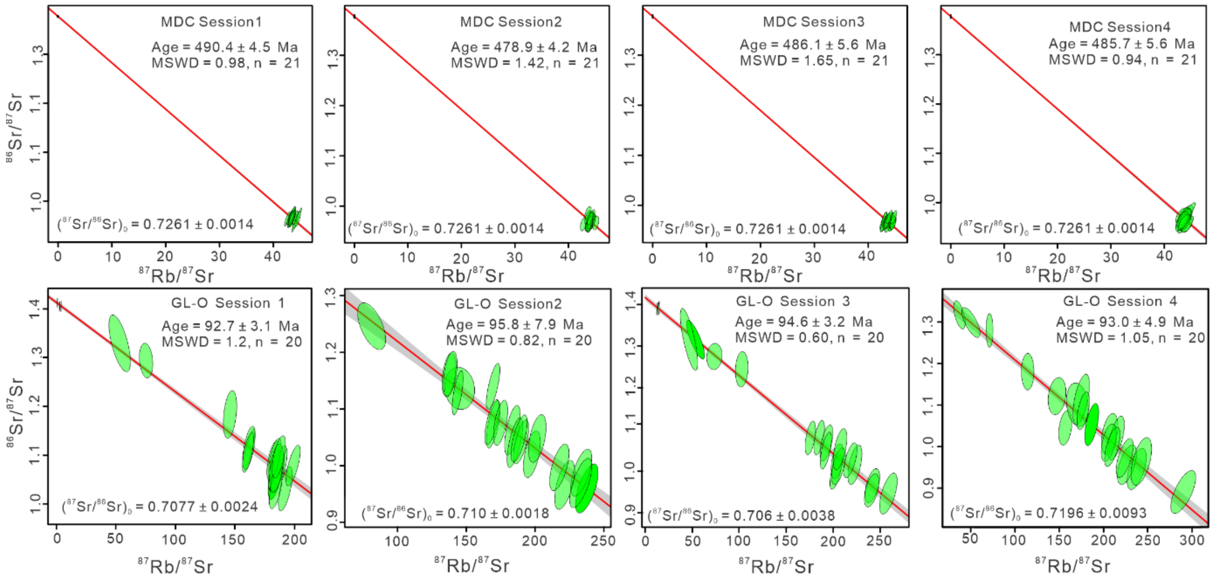

Supplementary Figure S1: Rb–Sr Weighted Mean Ages of MDC and Isochrons of GL-O in the in each analyzed sessions.

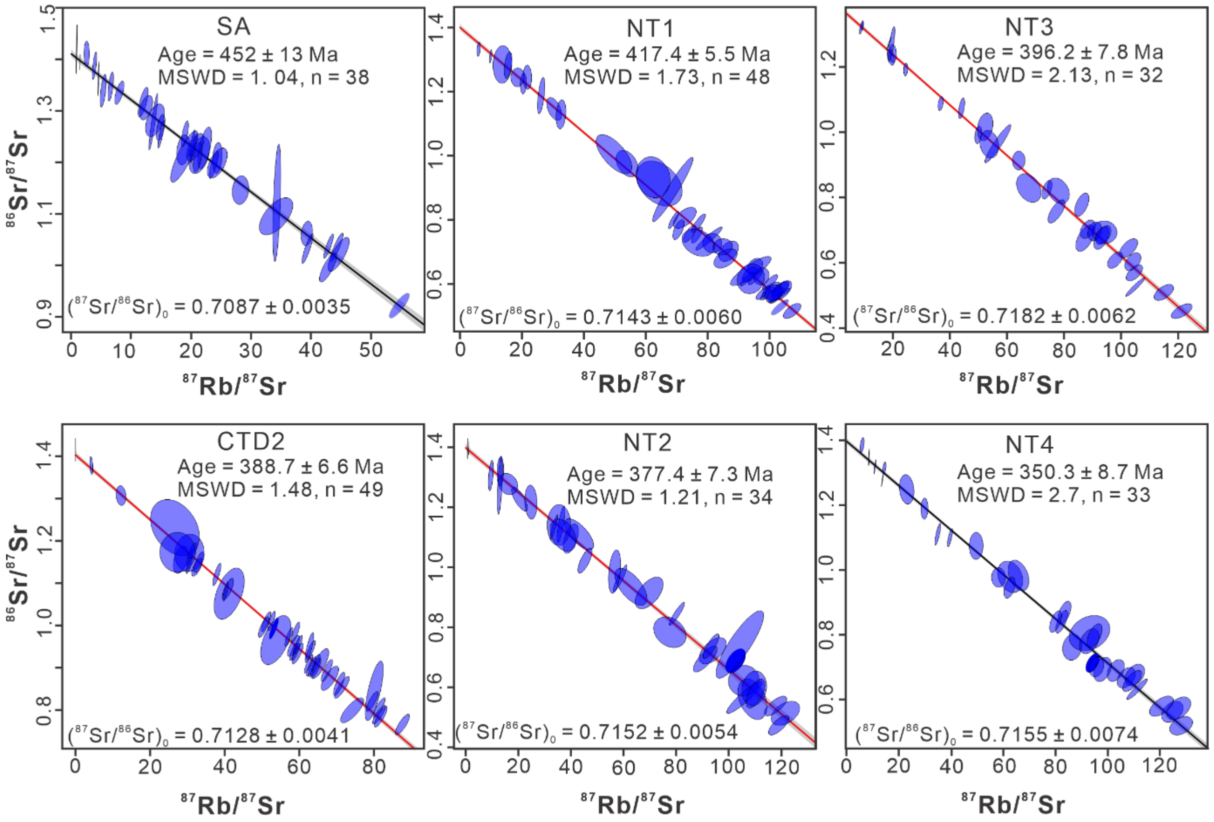

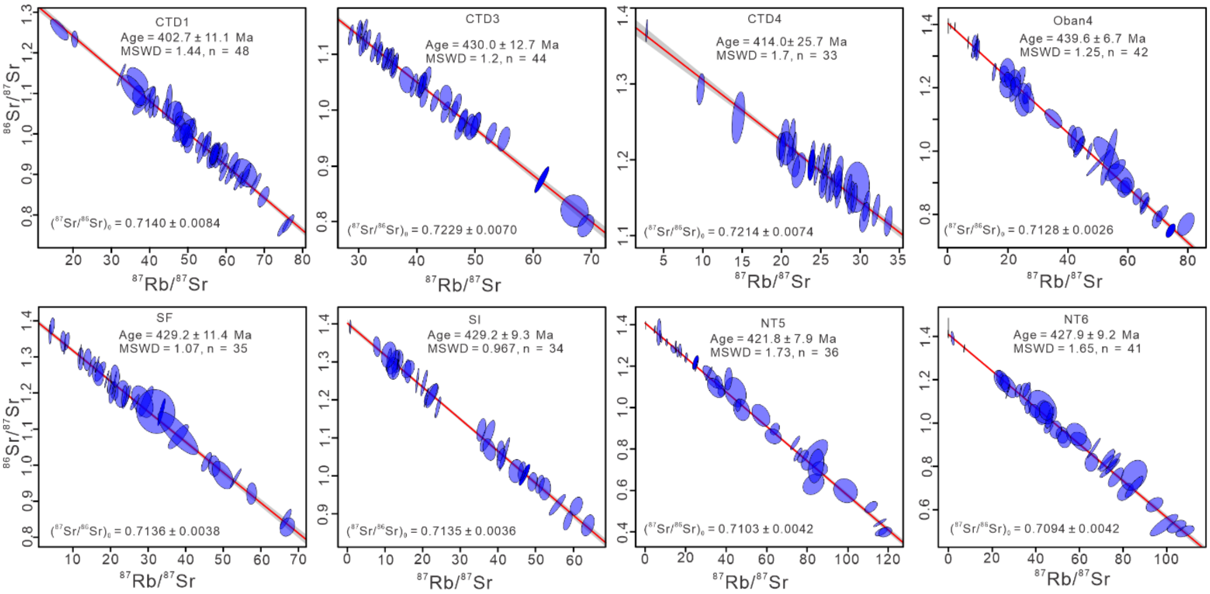

Supplementary Figure S2: *In situ* Rb–Sr isochrons of glauconite samples from the Georgina Basin.

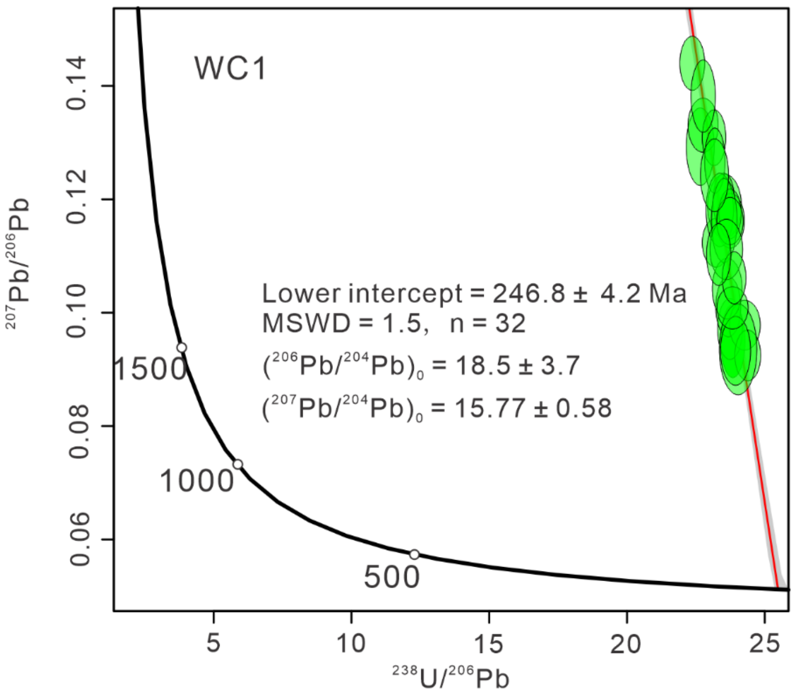

Supplementary Figure S3: 3D isochron in Tera-Wasserburg of WC1 based on $^{238}U/^{206}Pb$, $^{207}Pb/^{206}Pb$ and $^{204}Pb/^{206}Pb$.

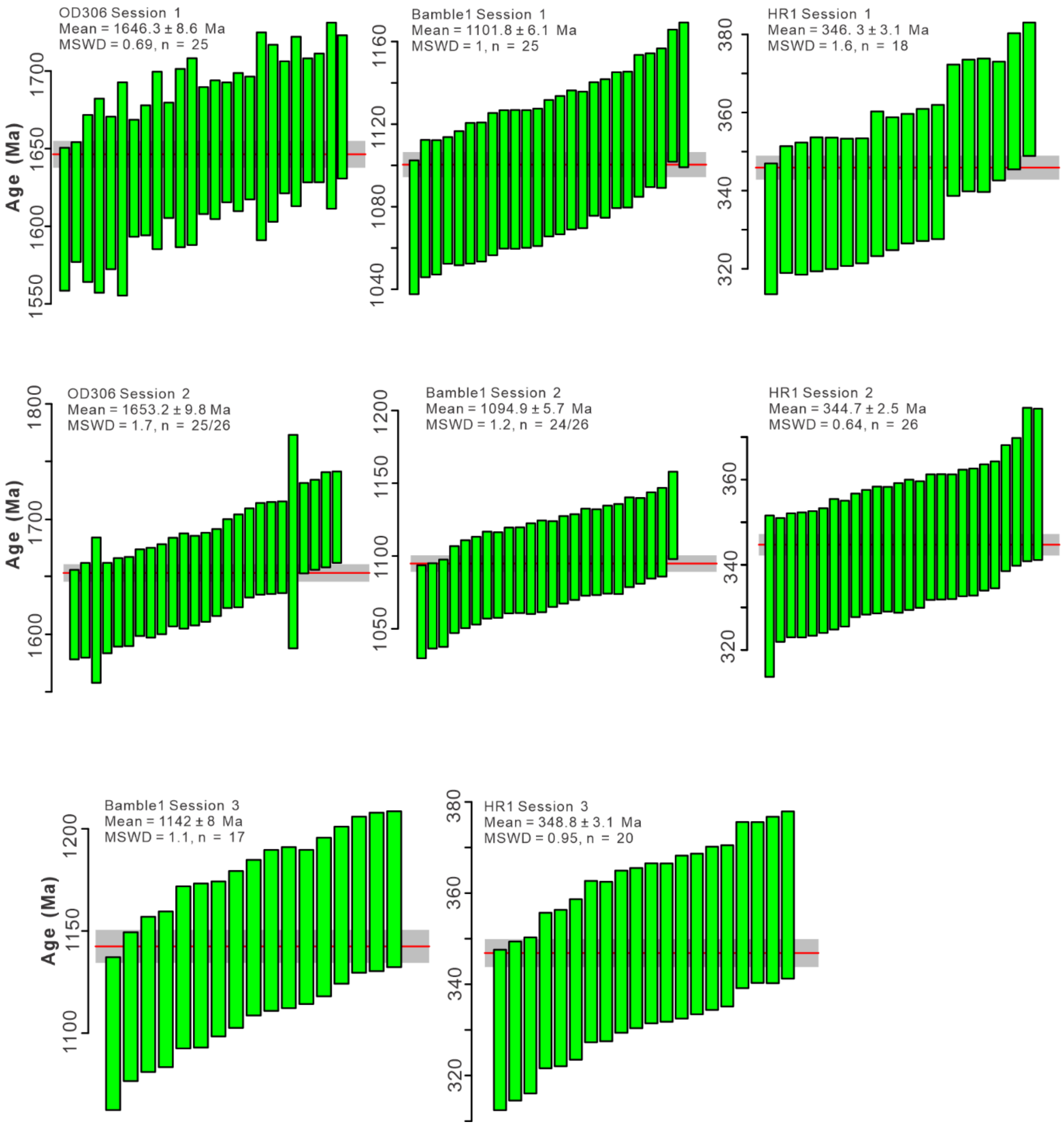

Supplementary Figure S4: Apatite Lu–Hf Dating: Weighted Mean Ages of Standards OD306, Bamble1, and HR1.

Chapter 2–Source Data

Note that all data, including the tables listed below, are available and accessible via the following link:

https://figshare.com/s/761bbbc87781cd22398d

Supplementary Table S1: Analytical parameters for 193 nm excimer laser ablation system (RESOlution-SE, Applied Spectra), and ICP-MS/MS (Agilent 8900x) used in this study.

Supplementary Table S2: Glauconie Rb–Sr dating data and elements.

Supplementary Table S3: Carbonate U–Pb dating data and elements.

Supplementary Table S4: Apaite U–Pb dating data and elements.

Supplementary Table S5: Apatite Lu–Hf dating data and elements.

Supplementary Table S6: Glauconite EPMA data.

Chapter 3: Coupling Potassium and Magnesium Isotope Proxies (δ^{41}K and δ^{26}Mg) in Cambrian Glauconites to Constrain Paleo-Seawater Composition and Diagenetic Alteration

Unpublished manuscript formatted for submission to *Earth and Planetary Science Letters*.

Zhufu Shao, Juraj Farkaš, Xin-Yuan Zheng, Alan S. Collins, Stefan C. Löhr, Sarah E. Gilbert, Andre Baldermann

Statement of Authorship

Title of Paper	Coupling Potassium and Magnesium Isotope Proxies (δ^{41}K and δ^{26}Mg) in Cambrian Glauconites to Constrain Paleo-Seawater Composition and Diagenetic Alteration
Publication Status	☐ Published ☐ Accepted for Publication ☐ Submitted for Publication ☒ Unpublished and Unsubmitted work written in manuscript style
Publication Details	This manuscript is to be submitted to the journal *Earth and Planetary Science Letters*.

Principal Author

Name of Principal Author (Candidate)	Zhufu Shao		
Contribution to the Paper	Work planning, sample preparation, laboratory analyses, data acquisition, processing, interpretation, and manuscript writing		
Overall percentage (%)	80%		
Certification:	This paper reports on original research I conducted during the period of my Higher Degree by Research candidature and is not subject to any obligations or contractual agreements with a third party that would constrain its inclusion in this thesis. I am the primary author of this paper.		
Signature		Date	06-May-25

Co-Author Contributions

By signing the Statement of Authorship, each author certifies that:

i. the candidate's stated contribution to the publication is accurate (as detailed above);

ii. permission is granted for the candidate in include the publication in the thesis; and

iii. the sum of all co-author contributions is equal to 100% less the candidate's stated contribution.

Name of Co-Author	Juraj Farkaš
Contribution to the Paper	Supervised work, helped with data interpretation and manuscript revision

Signature		Date	May 10, 2025
Name of Co-Author	Xin-Yuan Zheng		
Contribution to the Paper	Contributed to δ^{41}K and δ^{26}Mg isotope data acquisition, interpretation, and manuscript revision.		
Signature	Xinyuan Zheng	Date	07-May-25

Name of Co-Author	Alan S. Collins		
Contribution to the Paper	Supervised work, helped with data interpretation and manuscript revision.		
Signature		Date	21-05-25

Name of Co-Author	Stefan C. Löhr		
Contribution to the Paper	Helped with data interpretation and manuscript revision.		
Signature		Date	07/05/2025

Name of Co-Author	Sarah E. Gilbert		
Contribution to the Paper	Assisted with *in situ* Rb–Sr dating, data process and interpretation and manuscript revision.		
Signature		Date	06-May-25

Name of Co-Author	Andre Baldermann

Contribution to the Paper	Helped with data interpretation and manuscript revision.		
Signature		Date	10-May-25

Abstract

Marine authigenic clay formation via reverse weathering sequesters alkali/alkaline-earth metals (K^+, Mg^{2+}, Ca^{2+}, Li^+) from continental and seafloor weathering fluxes, playing a key role in regulating Earth's long-term carbon cycle and climate stability. We present $\delta^{41}K$ and $\delta^{26}Mg$ data from mid-Cambrian (~514–504 Ma) glauconites in the Georgina Basin (Australia) and North China Craton to: (i) characterize isotope fractionation during glauconitization and alteration, and (ii) reconstruct mid-Cambrian seawater $\delta^{41}K$ and $\delta^{26}Mg$ compositions. Integrated petrographic and geochemical analyses show extensive diagenetic alteration, evidenced by altered pellet morphologies, increased porosity, illitization, and secondary mineral inclusions (dolomite, calcite, apatite, pyrite, quartz), with systematically rejuvenated Rb–Sr ages (438–350 Ma). Systematic $\delta^{41}K$ (-0.41 to -0.11‰, NIST3141a) and $\delta^{26}Mg$ (-0.52 to 0.61‰, DSM3) variations in mid-Cambrian glauconites demonstrate that burial diagenetic illitization elevates both $\delta^{41}K$ and $\delta^{26}Mg$ values, while carbonate inclusions tend to decrease $\delta^{26}Mg$. Assuming constant isotopic fractionation factors between seawater and glauconite ($\Delta^{41}K_{\text{sw-glauconite}} \approx 0.90‰$, $\Delta^{26}Mg_{\text{sw-glauconite}} \approx 0.00‰$) through geological time, the least-altered glauconites yield estimated mid-Cambrian seawater values of +0.45 to +0.65‰ for $\delta^{41}K_{\text{sw}}$, and ~-0.20 to +0.1‰ for $\delta^{26}Mg_{\text{sw}}$, which are significantly heavier than modern seawater ($\delta^{41}K_{(\text{sw})}$ = +0.12‰; $\delta^{26}Mg_{(\text{sw})}$ = -0.83‰). The elevated $\delta^{41}K$ (~0.50‰ above modern) reflects enhanced reverse weathering in Cambrian oceans, which preferentially sequestered light ^{39}K and promoted CO_2 release, contributing to greenhouse conditions. Concurrently, the increased $\delta^{26}Mg$ (~0.60‰ above modern) indicates extensive Cambrian dolomitization compared to modern sea. These reconstructed seawater isotope compositions provide novel constraints on Cambrian marine geochemistry and its climate linkages.

Keywords: K and Mg isotopes, Rb–Sr dating, Cambrian, glauconite, paleo-seawater, diagenesis, illitization

3.1 Introduction

Marine reverse weathering acts as a critical sink for continental and seafloor weathering fluxes, incorporating alkali and alkaline earth metals (e.g., K^+, Mg^{2+}, Ca^{2+}, and Li^+) into the formation of marine authigenic clays (Dunlea et al., 2017; Farkaš et al., 2025; Li et al., 2022; Zheng et al., 2022a). Together with silicate weathering and carbonate reactions, it plays a key role in regulating global carbon cycling and maintaining long-term climate stability on Earth (Baldermann et al., 2025; Berg et al., 2019; Isson and Rauzi, 2024; Isson and Planavsky, 2018; Li et al., 2022; Mu et al., 2024; Xia et al., 2024). Chemical weathering of silicate rocks on continents sequesters atmospheric CO_2 and exports alkalinity and other soluble ions into the ocean. In contrast, reverse weathering in the ocean involves formation of new marine authigenic clays that consumes soluble cations and alkalinity, and releases CO_2 (Dunlea et al., 2017; Pogge von Strandmann et al., 2014; Santiago Ramos et al., 2018; Zheng et al., 2022a). A reduction in authigenic clay formation in the ocean would therefore decrease alkalinity consumption via reverse weathering, leading to an increase in the ocean's alkalinity inventory, a rise in seawater pH, and a subsequent decline in atmospheric CO_2. The resulting decrease in atmospheric CO_2 would promote global cooling and lower the rates of continental silicate and/or seafloor weathering until a new steady state is reached that balances the reduced alkalinity sink via authigenic marine clays production (Dunlea et al., 2017).

Potassium (K) and magnesium (Mg) are abundant in the continental crust, and are also major dissolved cations in modern seawater, where Mg^{2+} and K^+ are the second and fourth most abundant ions, respectively (Li et al., 2017; Ling et al., 2011; Morgan et al., 2018; Wang et al., 2021; Xia et al., 2024; Zheng et al., 2022a).

Dissolved K^+ cations present in seawater are primarily derived from continental silicate weathering and high-temperature basalt alteration, while its major sinks include the formation of authigenic K-Al-silicates/clays in marine sediments and low-temperature alteration of the oceanic crust (Li et al., 2022; Santiago Ramos et al., 2018; Wang et al., 2020; Zheng et al., 2022a). The marine Mg cycle is governed by a balance between continental weathering, high- and low-temperature hydrothermal alteration of the basaltic oceanic lithosphere, and the formation of sedimentary carbonates/dolomites and also Mg-Al-silicates/clays (Berg et al., 2019; Voigt et al., 2020). The primary source of Mg to the oceans is continental weathering of carbonate/dolomite and silicate rocks, delivered via rivers and groundwater, whereas the principal sinks include hydrothermal removal, dolomite formation, low-temperature clay formation during alteration of the oceanic crust, and the precipitation of evaporites (Pogge von Strandmann et al., 2014; Shalev et al., 2021; Voigt et al., 2020).

K has three naturally occurring isotopes, including two stable isotopes, ^{39}K (~93.26%) and ^{41}K (~6.73%), and one radioactive isotope, ^{40}K (~0.01%) (Li et al., 2021). Mg has three stable isotopes, including ^{24}Mg (~78.99%), ^{25}Mg (~10.00%), and ^{26}Mg (~11.01%) (Huang et al., 2020; Li et al., 2017; Ling et al., 2011). Stable K and Mg isotopes, expressed as δ^{41}K and δ^{26}Mg (in per mil, ‰), exhibit significant isotope fractionation during low-temperature biogeochemical processes, offering valuable insights into the pathways of silicate and reverse weathering, and the evolution of seawater geochemistry through geological time (Li et al., 2022; Ramos et al., 2018; Teng et al., 2010; Xia et al., 2024; Zheng et al., 2022a). The evolution of oceanic K and Mg cycles is thus closely linked to other major changes in the Earth system functioning (Gothmann et al., 2017), making them excellent targets (via the application of marine δ^{41}K and δ^{26}Mg proxies) to trace past oceanographic and biogeochemical conditions recorded in marine sedimentary rock archives and proxy data through geological time (Mavromatis et al., 2014).

Modern seawater exhibits homogeneous K and Mg isotope compositions, with δ^{41}K = 0.12 ± 0.07‰ (NIST3141a) and δ^{26}Mg = -0.83 ± 0.09‰ (DSM3) (Ling et al., 2011; Wang et al., 2021). These values show significant deviations from Bulk Silicate Earth (BSE) estimates (δ^{41}K = -0.43 ± 0.17‰; δ^{26}Mg = -0.25 ± 0.07‰ for upper mantle and -0.22‰ for upper continental crust) (Li et al., 2010; Ling et al., 2011; Teng et al., 2010). The observed isotopic offsets (~0.5‰ for δ^{41}K, and ~0.6‰ for δ^{26}Mg) primarily reflect isotopic fractionation during marine authigenesis (e.g., silicates and carbonates), combined with variable isotopic signatures from continental weathering, evaporite deposition, submarine hydrothermal systems, and marine porewater exchange (Hu et al., 2020; Hu et al., 2021; Huang et al., 2018, 2020; Li et al., 2019a; Li et al., 2022; Ramos et al., 2018; Ramos et al., 2020; Zheng et al., 2022a).

Reconstructing the composition of ancient seawater is crucial for understanding the long-term evolution and changes in Earth's surface palaeo-environments through time. The chemical and isotopic composition of seawater reflects the global balance among continental weathering, hydrothermal exchange, and sedimentary processes, and its variations record key geological processes such as tectonic activity, climate change, and carbon cycling (Dunlea et al., 2017; Li et al., 2022; Pogge von Strandmann et al., 2014; Zheng et al., 2022a). Thus far, most research on K and Mg isotopes has focused on igneous rocks, carbonates, and evaporites (Berg et al., 2019; Gothmann et al., 2017; Higgins et al., 2018; Shalev et al., 2021). For example, reconstructions of paleo-seawater δ^{26}Mg evolution over the past 2 billion years have largely relied on marine halite and dolomite archives (Xia et al., 2024). However, both types of archives are prone to alteration due to post-depositional processes, e.g., carbonates often undergo diagenetic recrystallization and isotopic exchange, which can reset primary signals, while evaporites form in restricted or hypersaline settings and are easily modified after deposition or during later dissolution/recrystallization. Thus far, a robust reconstruction of paleo-seawater δ^{41}K evolution is still lacking. Research on marine authigenic clays and other siliciclastic sedimentary archives remains in its infancy, with only a few published studies and limited δ^{41}K and δ^{26}Mg datasets available to date (Hu et al., 2020; Li et al., 2019a; Li et al., 2022; Mu et al., 2024). Moreover, combined K and Mg isotope studies have yet to be systematically conducted on isolated marine authigenic clays such as glauconite $(K,Na)(Fe^{3+},Al,Mg)_2(Si,Al)_4O_{10}(OH)_2$.

Glauconite is a common marine authigenic aluminosilicate clay mineral that typically forms near the sediment–water interface during the earliest stages of marine diagenesis (Odin and Matter, 1981), thereby preserving the chemical characteristics of seawater or local marine pore-fluids at the time of its formation. Its high K (and elevated Rb) contents have made glauconite a widely used geochronometer for K-Ar (and also Rb-Sr) dating of glauconite-bearing sedimentary sequences. In addition, it is increasingly recognized as a robust archive of paleo-seawater geochemistry, as well as past climate and sea-level fluctuations (Banerjee et al., 2016a; Banerjee et al., 2016b; Bayon et al., 2023; Wilmsen and Bansal, 2021; Scheiblhofer et al., 2022;

Środoń et al., 2023). As a widespread marine authigenic silicate phase, glauconite thus represents a promising archive for reconstructing the K and Mg isotopic composition of ancient seawater through geological time (Löhr et al., 2023; Shaikh et al., 2024). However, the effects of diagenesis and burial processes on glauconite-based $\delta^{41}K$ and $\delta^{26}Mg$ proxies, and the potential for isotopic resetting, remain poorly constrained, particularly for ancient glauconite pellets that have experienced prolonged diagenetic and post-depositional and deep burial histories. To address these questions and knowledge gaps, this chapter investigates stable K and Mg isotope variations (coupled with *in situ* Rb-Sr dating) in the Cambrian glauconites from Australia, complemented also by selected and coeval Cambrian glauconites from China.

The Cambrian was a critical period marked by the Cambrian Explosion of complex animal life forms, the assembly of the Gondwana supercontinent, widespread oceanic oxygenation, and elevated global temperatures (Peters and Gaines, 2012; Scotese et al., 2021; Sun et al., 2023). These events reflect complex, yet not fully understood, changes in seawater geochemistry. To explore this, we investigated glauconite-rich shallow marine carbonate archives deposited from the late Early Cambrian (Stage 4) to the Middle Cambrian (Drumian). Samples were collected from the Georgina Basin, Australia (10 samples), and the southeastern North China Craton (NCC, China, 2 samples). The primary aims of this study include (i) determination of the $\delta^{41}K$ and $\delta^{26}Mg$ variability, and *in situ* Rb–Sr ages, of the above mid-Cambrian glauconite samples/pellets from Australia and China, (ii) assessment of the impact of post-depositional processes on acquired 'ages' and $\delta^{41}K$ and $\delta^{26}Mg$ proxies, and (iii) reconstruction of the mid-Cambrian seawater $\delta^{41}K$ and $\delta^{26}Mg$ values based on the best preserved or least altered glauconite archives. Overall, our results show clear $\delta^{41}K$ and $\delta^{26}Mg$ changes in altered or illitized glauconite grains, highlighting K and Mg isotopic resetting (including Rb–Sr ages) during post-depositional diagenesis. The most altered grains exhibit the highest $\delta^{41}K$ and $\delta^{26}Mg$ values and the youngest (most rejuvenated) Rb–Sr ages. Critically, petrographic, elemental, and compositional screening of glauconite grains, combined with *in situ* Rb–Sr dating, enables identification of the best-preserved (least altered) samples. These pristine glauconites provide robust proxies for reconstructing paleo-seawater K and Mg isotope compositions.

3.2 Geological Background

During the Cambrian period, Australia (NT) and China (NCC) were near the equator and adjacent in northern East Gondwana (Fig. 1a), sharing similar climatic, paleo-oceanographic conditions, shallow marine platform settings, and faunal assemblages (Brock et al., 2000; McKenzie et al., 2011; Zhao et al., 2018).

The Georgina Basin in Australia is an intracratonic basin that records Neoproterozoic to mid-Paleozoic marine strata and forms a part of the Centralian Superbasin (Kruse et al., 2013; Walter et al., 1995). It comprises eight structural belts (Fig. 1b), and its stratigraphy includes Neoproterozoic rift-related fluvioglacial to marine siliciclastic rocks, Cambrian–Ordovician shallow marine carbonates, and Devonian foreland siliciclastics (Dunster et al., 2007; Khider et al., 2021; Walter et al., 1995). Sedimentation in the basin was interrupted by the Petermann (ca. 580–520 Ma) and Alice Springs (ca. 450–300 Ma) Orogenies (Haines et al., 2001; Kruse et al., 2013). Following a global transgression after the eruption of the Kalkarindji Large Igneous Province (LIP), middle Cambrian shallow-water carbonates of the Narpa Group were extensively deposited in the Georgina basin (Glass and Phillips, 2006). This group includes the fossiliferous and phosphorite-rich Thorntonia Limestone, Wonarah Formation, Inca Formation, and Camooweal Formation within the Central-Undilla Subbasin (Kruse et al., 2013). The Thorntonia Limestone consists of dolostone, limestone, and shale, with phosphorite and sandstone basal layers. The Wonarah Formation features dolostone interbedded with siltstone. The Inca Formation consists of carbonate deposits interbedded with sandstone and shale, while the Camooweal Dolostone is primarily dolostone in the eastern Central Subbasin, transitioning to limestone in the Undilla Subbasin. Glauconite mainly occurs in the Thorntonia Limestone, Wonarah Formation and Inca Formation that developed in a carbonate platform system (Fig. 1d).

The NCC in China is a multiphase tectonic block underlain by a Paleoproterozoic basement. After the Great Unconformity, which marks a period of non-deposition or erosion between the late Ediacaran and Early Cambrian (Sun et al., 2023; Zhang et al., 2022; Zheng et al., 2023), sedimentation resumed in a shallow-water platform dominated by mixed siliciclastic and carbonate deposits (He et al., 2022). The Cambrian sequences in the NCC are mainly distributed in the western (Ordos), southern, central, and eastern regions (Zheng et al., 2023), with well-exposed outcrops in the southeastern Xuzhou area (Fig. 1c). In this region, glauconite-bearing strata include the Houjiashan Formation and Mantou Group, with the latter further subdivided into the Mantou, Maozhuang, and Xuzhuang Formations (Fig. 1e).

The Houjiashan Formation consists of shale and siltstone in the lower section and thick-bedded mottled limestone in the upper section. The Mantou Formation features red shale in the lower section, thick-bedded limestone with oolitic limestone layers in the middle, and silty shale interbedded with thin-bedded siltstone and marlstone in the upper section. The Maozhuang Formation includes bioclastic micritic limestone in the lower section and silty shale in the upper section. The Xuzhuang Formation is composed of oolitic limestone in the lower section, siltstone and sandstone interbedded with limestone in the middle, and oolitic limestone in the upper section (Fig. 1e).

This study investigated 12 glauconite-rich Cambrian samples, including 10 from the middle Cambrian Central-Undilla Subbasin in the Georgina Basin (NT, Australia), collected from 4 cores: NTGS01/1, Oban 1, CTDD0001, and CTDD0002 (Fig. 1d). The other two samples, ‘Hou’ (from the Houjiashan Formation) and ‘Man’ (from the Mantou Formation), were collected from late Early to Middle Cambrian outcrops near Xuzhou City in the southeastern North China Craton (NCC; Fig. 1e). These glauconite-rich samples, deposited between approximately 514 and 504 Ma (He et al., 2022; Kruse et al., 2013; Laurie, 2022; Smith et al., 2013), likely record similar paleo-seawater K and Mg isotope compositions because of the long oceanic residence times of dissolved K^+ (~11 Ma) and Mg^{2+} (~13 Ma) (Wang et al., 2021; Ling et al., 2011). Thus, the differences observed in the glauconite-based δ^{41}K and δ^{26}Mg data from Australia and China likely reflect site-specific diagenetic or burial histories, rather than changes in the K and Mg isotope composition of mid-Cambrian seawater. Sample details are provided in the Supplementary Material (Table S1).

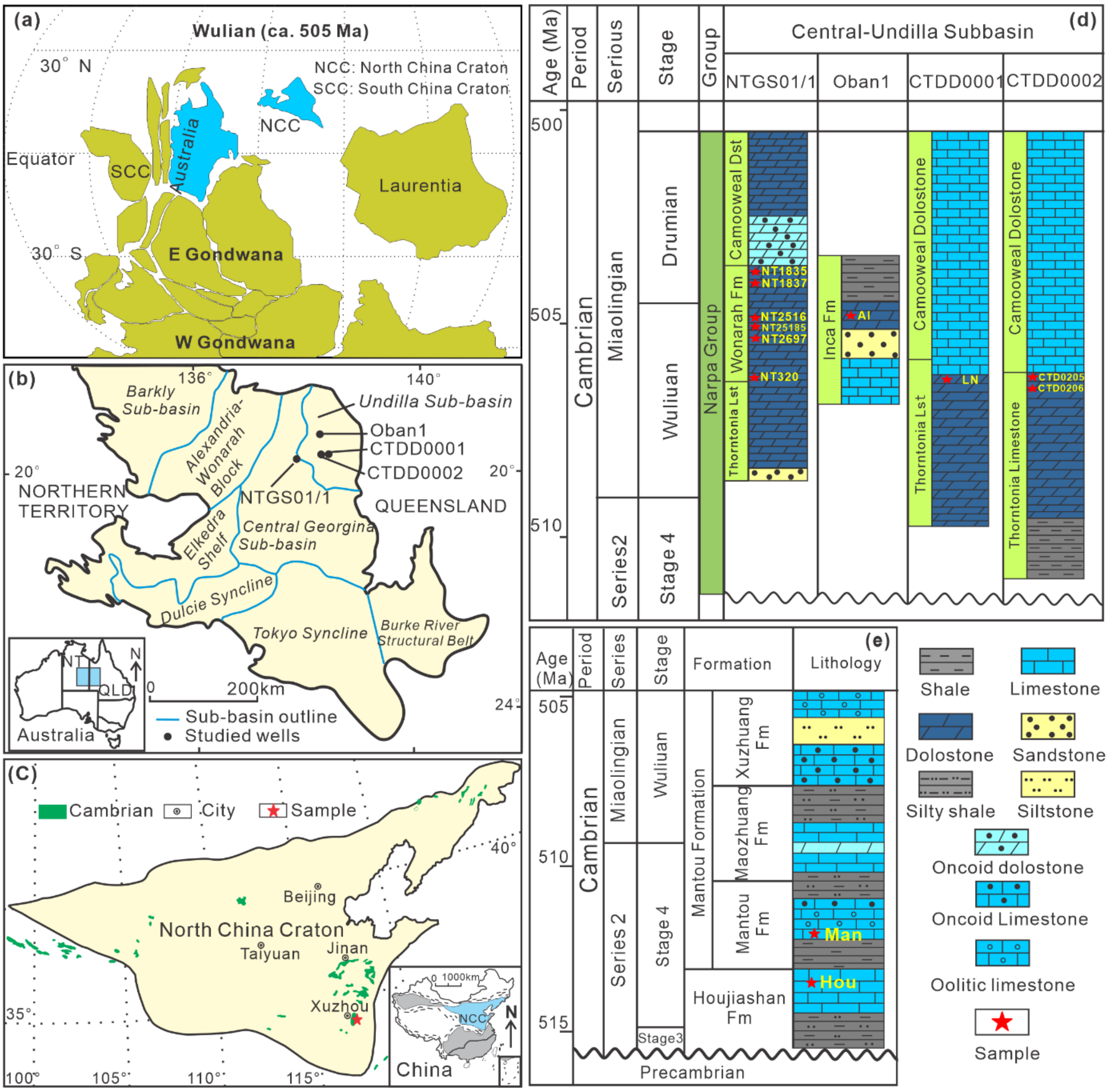

Figure 1. Locations of study areas and sample intervals for the studied Cambrian glauconite-rich strata in Australia and China: (**a**) Tectonic setting and paleogeographic reconstruction of Australia and the North China Craton (NCC) during the Cambrian (Wuliuan Stage) (adapted from Zhao et al., 2020); (**b**) Location of the Georgina Basin and the studied wells (adapted from Kruse et al., 2013); (**c**) Location of the NCC and studied Cambrian outcrop site (adapted from Zhang et al., 2022); (**d**) Middle Cambrian stratigraphy of the Narpa Group in the Georgina Basin (Australia, Northern Territory, NT), showing sampled intervals (adapted from Laurie, 2022; Smith et al., 2013); (**e**) Cambrian stratigraphy of the Xuzhou area (China) with sampled intervals (adapted from Zhang et al., 2022).

3.3 Sample Preparation and Analytical Methods

Glauconite-rich samples were prepared and analyzed through petrographic and mineralogical screening, electron probe microanalysis (EPMA), and *in situ* LA-ICP-MS/MS Rb–Sr dating at the Adelaide Microscopy (AM) Centre, the University of Adelaide. High-resolution scanning electron microscopy (SEM) coupled with energy-dispersive X-ray spectroscopy (EDS) was conducted at Macquarie University. Samples of glauconites from the Georgina Basin were also discussed and described in detail in Chapter 2, while samples from China represent newly collected glauconite samples.

To evaluate the impact of diagenesis on glauconite K and Mg isotopes, we intentionally avoided grinding the separated glauconite grains into powder and did not perform a second leaching of residual carbonates with 1 N HCl prior to total silicate digestion using an HF–HNO_3 acid mixture. This approach aimed to (1) minimize Mg and K loss from interlayer sites and preserve the structural integrity of glauconite, and (2) retain potential diagenetic signatures, particularly carbonate inclusions, to maximize recovery of primary geochemical and isotopic signals.

Chemical purification and K and Mg isotope analyses of glauconite were carried out at the University of Minnesota, USA. Elemental compositions of the separated glauconite pellets were determined by ICP-MS prior to purification. Chemical purification was performed in a class-100 clean laboratory, and isotope measurements were conducted using a Nu Instruments Sapphire MC-ICP-MS equipped with a collision/reaction cell. Two replicate samples (NT25185 from the Wonarah Formation in the Georgina Basin, Australia, and Man from the Mantou Formation in the North China Craton) were analyzed to evaluate analytical reproducibility.

3.3.1 Micro-Scale Petrography, Mineralogy and EMPA Analyses

In this study, we used and analyzed identical glauconite samples from the Georgina Basin, as discussed previously in Chapter 2, and these are complemented by three new glauconite samples from China that are analyzed and discussed in this chapter. Thin sections of the glauconite-rich samples were prepared for petrographic and mineralogical analysis using a

Leica DM2700 P microscope. Scanning electron microscopy (SEM), backscattered electron (BSE) imaging, and mineral liberation analysis (MLA) were performed on carbon-coated polished rock mounts at the University of Adelaide using Hitachi SU3800 and SU7000 SEM instruments, both equipped with energy-dispersive X-ray spectrometers (EDS).

The elemental composition of glauconite grains (wt% of major oxides) was determined using a Cameca SX-Five EPMA at the Adelaide Microscopy (AM) Center. Elemental concentrations of the studied glauconites, including Na, Mg, Al, Si, P, K, Ca, Fe, and Ti were measured via EPMA, with oxygen content calculated stoichiometrically. The analytical precision for all elements was better than 3% (1σ). Detailed EPMA results for glauconite are presented in Supplementary Material Table S2.

3.3.2 *In situ* Rb–Sr Dating of Glauconite via LA-ICP-MS/MS

In situ laser-based Rb–Sr dating of the studied Cambrian glauconites (and GL-O glauconite standard) was performed using the well-established LA-ICP-MS/MS approach at the University of Adelaide Analytical Mineralogy Centre (AM Centre) with an Agilent 8900x ICP-MS/MS, coupled with a RESOlution-LR ArF 193 nm excimer laser ablation system. The *in situ* Rb–Sr dating followed the established protocols of Redaa et al. (2021), Glorie et al. (2024), and Löhr et al. (2024). Briefly, laser ablation (LA) was performed using a carrier gas mixture of He (380 mL/min) and Ar (890 mL/min), with N_2 (3.5 mL/min) added before the ICP torch to improve signal sensitivity. A circular laser beam with a diameter of 67 µm, a fluence of 3.5 J/cm^2, and a repetition rate of 5 Hz was employed for the ablation. NIST 610 glass was used as a primary reference material for drift correction and normalization of elemental concentrations (Redaa et al., 2023). In addition, MDC phlogopite (519.4 ± 6.5 Ma, Hogmalm et al., 2017; Redaa et al., 2021) served as a secondary reference material for matrix-introduced fractionation correction of ^{87}Rb/^{86}Sr (Glorie et al., 2024); GL-O glauconite (K–Ar: 95 ± 1 Ma, Odin, 1982; Rb–Sr: 94 ± 3 Ma, Löhr et al., 2024) was used to verify data quality and age accuracy. Data processing was performed using LADR software (Norris and Danyushevsky, 2018), and ages were calculated and plotted as inverse isochrons using IsoplotR (Vermeesch, 2018). Glauconite samples were dated over five sessions. The Rb–Sr ages obtained for the GL-O ranged from

92.7 ± 3.1 Ma to 96.3 ± 3.5 Ma, which overlaps with previously reported values (Löhr et al., 2024; Odin, 1982). All isotopic ratios and corresponding isochron plots are provided in the Supplementary Materials (Table S3 and Figs. S2–S3). Detailed information on these samples and geochronological data can be found in Chapter 2 (see also Shao et al., 2025). The glauconite Rb–Sr ages from the Georgina Basin presented in this chapter are thus taken from the above sources.

3.3.3 Glauconite Separates and Solution-based Elemental Analysis

Glauconite-bearing carbonate rock samples were initially crushed to a fine powder and sieved through a 100 µm mesh to isolate the coarse fraction. The samples were then leached in 1N HCl to remove the carbonate matrix and associated micro-inclusions of calcite or apatite from glauconite grains. After the acid leaching, the samples were thoroughly washed with deionized (DI) water multiple times and then dried in an oven at 60°C. Magnetic separation was performed using a Frantz separator set to 0.6 and 0.4 A to isolate the glauconite grains. The separated grains were then manually picked under a microscope to remove any remaining impurities, with careful petrographic screening applied, particularly to exclude K-feldspar and illite grains.

Given that one aim of this study is to evaluate the impact of diagenesis on glauconite K and Mg isotopes, we chose not to grind the separated glauconite grains into powder and did not perform a second leaching of residual carbonate with 1 N HCl prior to total silicate digestion. This decision was guided by two key considerations: (1) to prevent excessive Mg leaching from interlayer sites and thus preserve the structural integrity of glauconite, and (2) to retain potential diagenetic signatures, especially carbonate inclusions, in order to maximize geochemical information extraction from the grains.

Approximately 5 mg of purified glauconite grains from each sample were weighed and dissolved in a mixture of HF-HNO_3 acids (prepared with 2.5 mL of HF and 0.5 mL of HNO_3, concentrated Optima -grade) for total silicate digestion. The capped Teflon beakers containing glauconite grains and HF-HNO_3 acid were heated at ~130°C on a hot plate for about one week to ensure complete dissolution of the glauconite grains, after which the solution was evaporated to dryness. The next steps involved sequentially adding concentrated HCl and HNO_3 acids to remove any remaining phases (e.g., CaF_2, organic material, *etc.*) and ensure the complete dissolution of the glauconite. Once fully dissolved and dried, the samples were re-dissolved in 5 mL of 6 N HCl. A small aliquot of the sample solution was taken for elemental concentration analysis using an iCAP TQ triple-quad ICP-MS at the University of Minnesota, with major elements including Mg, Al, P, K, Ca, and Fe analyzed, and the analytical precision for all elements being better than 5% (1σ), while the remaining sample solution was used for column chromatography to purify K and Mg fractions (see below) for subsequent isotope analyses.

3.3.4 K and Mg Isotope Analysis of Glauconite Separates

The chemical purification of K from the glauconite matrix and other components prior to K isotope analysis followed the protocols of Zheng et al. (2022b), while Mg purification was carried out according to the method outlined by Li et al. (2012). Briefly, an aliquot of glauconite sample solution containing 50–200 µg of K and 20–100 µg of Mg was transferred to an acid-cleaned Teflon beaker, evaporated to dryness, and re-dissolved in 0.4 ml of 0.4 N HCl, which served as the working acid for ion-exchange chromatography to separate K and Mg. The workflows for K and Mg purification via eluent chromatography are summarized in Tables 1 and 2.

After chemical purification (see above), the collected K and Mg fractions from the studied glauconites were analyzed for their isotope compositions, specifically $\delta^{41}K$ and $\delta^{26}Mg$ values, using a Nu Instruments Sapphire inductively coupled plasma mass spectrometer (MC-ICP-MS) equipped with a collision cell (CC).

Stable K isotope measurements ($\delta^{41}K$): The purified K fractions were diluted with 2% HNO_3 to match the concentration of the standard solution (~200 ppb) for each session. $\delta^{41}K$ measurements were conducted using a collision/reaction cell (CC) pathway of MC ICP MS, with Helium (He) and Hydrogen (H_2) as reaction gases to minimize isobaric interference from Ar (Zheng et al., 2022b). A sample–standard bracketing method was used to correct for instrumental drift and mass bias, with NIST 3141a as the bracketing standard. The accuracy and reproducibility of the K isotope measurements were further evaluated using additional in-house standards, including UMN-K (HPS elemental standard) (Zheng et al., 2022b), seawater, AGV-2a (andesite), and BHVO-2 (basalt). All δ^{41}K data are reported as mean values with 2 standard deviations (2SD). The total procedural K blank was less than 10 ng, which is negligible compared to the typical amount of K processed for a sample (Zheng et al., 2022b).

Stable Mg isotope measurements (δ^{26}Mg): The purified Mg fractions were similarly diluted with HNO_3 to a concentration of ~50 ppb for MC-ICP-MS analysis. δ^{26}Mg measurements were performed directly without the use of the collision cell, and the data were normalized relative to the DSM3 standard. Sample–standard bracketing was applied to correct for instrumental drift and mass bias, with DSM3 as the bracketing standard. Additional in-house standards, including UMN-K, seawater, AGV-2a, BHVO-2, and Cambridge-1, were used to assess measurement accuracy and reproducibility. All δ^{26}Mg data are reported as mean values with 2SD. The total procedural Mg blank was less than 10 ng, which is negligible compared to the typical amount of Mg processed for a sample of over 20 mg (Chen et al., 2020).

The δ^{41}K and δ^{26}Mg data for the standards above are summarized in Table S4. The average δ^{41}K values are 0.43 ± 0.03 ‰ (n = 15, where n refers to the number of replicates or brackets) for UMN-K, 0.13 ± 0.05 ‰ (n = 9) for seawater, -0.46 ± 0.05 ‰ (n = 6) for AGV-2a, and -0.42 ± 0.05‰ (n = 22) for BHVO-2. The average δ^{26}Mg values are -2.61 ± 0.06 (n = 26) for Cambridge-1, -0.79 ± 0.08 (n = 20) for seawater, -0.18 ± 0.04 (n = 8) for AGV-2a, and -0.19 ± 0.06 (n = 4) for BHVO-2. All values are consistent with those reported in previous studies within uncertainties (Gao et al., 2018; Harrison et al., 2021; Hu et al., 2018; Huang et al., 2018; Ling et al., 2011; Wang et al., 2020; Wang et al., 2021; Zheng et al., 2022b).

3.3.5 Mg Isotope Analysis of Carbonate Samples

To evaluate the potential effect of carbonate mineral inclusions on glauconite δ^{26}Mg values, four carbonate samples were also analyzed for their δ^{26}Mg compositions. Carbonate sample preparation followed the method described by Chen et al. (2020) and Ning et al. (2020). Similar to glauconite, carbonate Mg purification was carried out according to the procedures outlined by Li et al. (2012), involving a three-stage ion-exchange column process. In Stages 1 and 2, Bio-Rad AG MP-50 resin (100–200 mesh) was used with 2.2 M HCl and 0.5 M HCl, respectively. Stage 3 employed Bio-Rad AG 50W X8 resin (200–400 mesh) in an HNO_3 medium (Table 2). The carbonate reference material JDo-1 was also analyzed for data control, yielding an average value of -2.32 ± 0.06‰ (n = 4), which is consistent with reported values within uncertainties (Shalev et al., 2018).

Table 1. Procedures for K purification and Mg collection using ion-exchange chromatography in this study.

Column & resin	Bio-Rad AG 50W X8 (200–400 mesh) resin in Bio-Rad Poly-Prep columns (2 ml resin bed)
Resin cleaning /conditioning	8 ml 0.4 M HCl
Sample loading	0.4 ml 0.4 M HCl
Na removal	1 ml 0.4 M HCl; 3 ml 0.4 M HCl (2x); 8 ml 0.4 M HCl (2x)
K collection	4 ml 0.4 M HCl; 8 ml 0.4 M HCl (3x)
Mg collection	12 ml 6 N HCl

Table 2*. Procedure for Mg purification using ion-exchange chromatography in this study.

Stage 1	Column & resin	Bio-Rad (Hercules, CA, USA) AG MP-50 (100-200 mesh) with column of 6.25mm ID and 93mm resin height
	Resin cleaning/conditioning	10 ml 2.2 M HCl
	Sample loading	0.25 ml 2.2 M HCl
	Elution steps	0.2 ml 2.2 M HCl (5x); 0.5 ml 2.2 M HCl; 1 ml 2.2 M HCl
	Mg collection	8.75 ml 2.2 M HCl
Stage 2	Column & resin	Bio-Rad (Hercules, CA, USA) AG 50Wx8 (200-400 mesh) with column of 4.9mm ID and 18.5mm resin height
	Resin cleaning/conditioning	1 ml 4.5M HNO_3 (3x)/1 ml 0.2 M HNO_3 + 0.2 M HF
	Sample loading	0.2 ml 0.2 M HNO_3 + 0.2 M HF
	Elution steps	1 ml 0.2 M HNO_3 + 0.2 M HF(8x)
	Mg collection	1 ml 1 M HNO_3 (5x); 1 ml 1.5 M HNO_3 (3x)
Stage 3	Column & resin	Bio-Rad (Hercules, CA, USA) AG MP-50 (100-200 mesh) with column of 4.9mm ID and 18.5mm resin height

	Resin cleaning/conditioning	1ml 8 M HCl (3x); 1 ml DI water (2x); 1 ml 7% 0.5 M HCl + 93% acetone (v/v)
	Sample loading	0.5 ml 7% 0.5 M HCl + 93% acetone (v/v)
	Elution steps	0.5 ml 7% 0.5 M HCl + 93% acetone (v/v) (4x)
	Mg collection	1 ml 8 M HCl (3x)

* Note: Glauconite Mg purification follows the sequence of Stage 1, Stage 2, and Stage 3. In contrast, for carbonate Mg purification, the order of Stage 2 and Stage 3 is reversed, following Stage 1, Stage 3, and Stage 2.

3.4 Results

3.4.1 Petrography and Mineralogy of Mid-Cambrian Glauconites

Glauconite from both the Georgina Basin and the NCC is primarily hosted in carbonate rocks (Figs. 2–3). In the Georgina Basin, it mainly occurs within dolostone (Fig. 2), while in the NCC, the Hou and Man samples are hosted in limestone (Fig. 3).

Diagenetic alteration is a common feature in many ancient glauconite-bearing strata (Środoń et al., 2023), and similar processes are observed in the Cambrian glauconites from both the Georgina Basin and the NCC. Post-depositional dissolution and recrystallization are prevalent diagenetic processes affecting the studied mid-Cambrian glauconites, as evidenced by their porous and partly illitized microstructures observed under optical microscopy and in SEM-EDS mineral maps (Figs. 2–3). These observations are further supported by EPMA analyses, which reveal variations in major oxide concentrations compared to the homogeneous glauconite composition of the GL-O standard (Fig. 4; Supplementary Table S2).

Illitization is widespread in the glauconites from the Georgina Basin, as shown by high-resolution SEM-EDS mineral maps and variations in major oxide concentrations (Figs. 2d–e, 4). Illite is randomly distributed within the glauconite grains, with higher concentrations in more porous areas due to glauconite illitization. Carbonate minerals such as dolomite, calcite, and ankerite are commonly associated with glauconite grains (Figs. 2a–c, 2f). Apatite inclusions are frequently observed as well, possibly reflecting cogenetic authigenesis or diagenetic phosphatization (Fig. 2e).

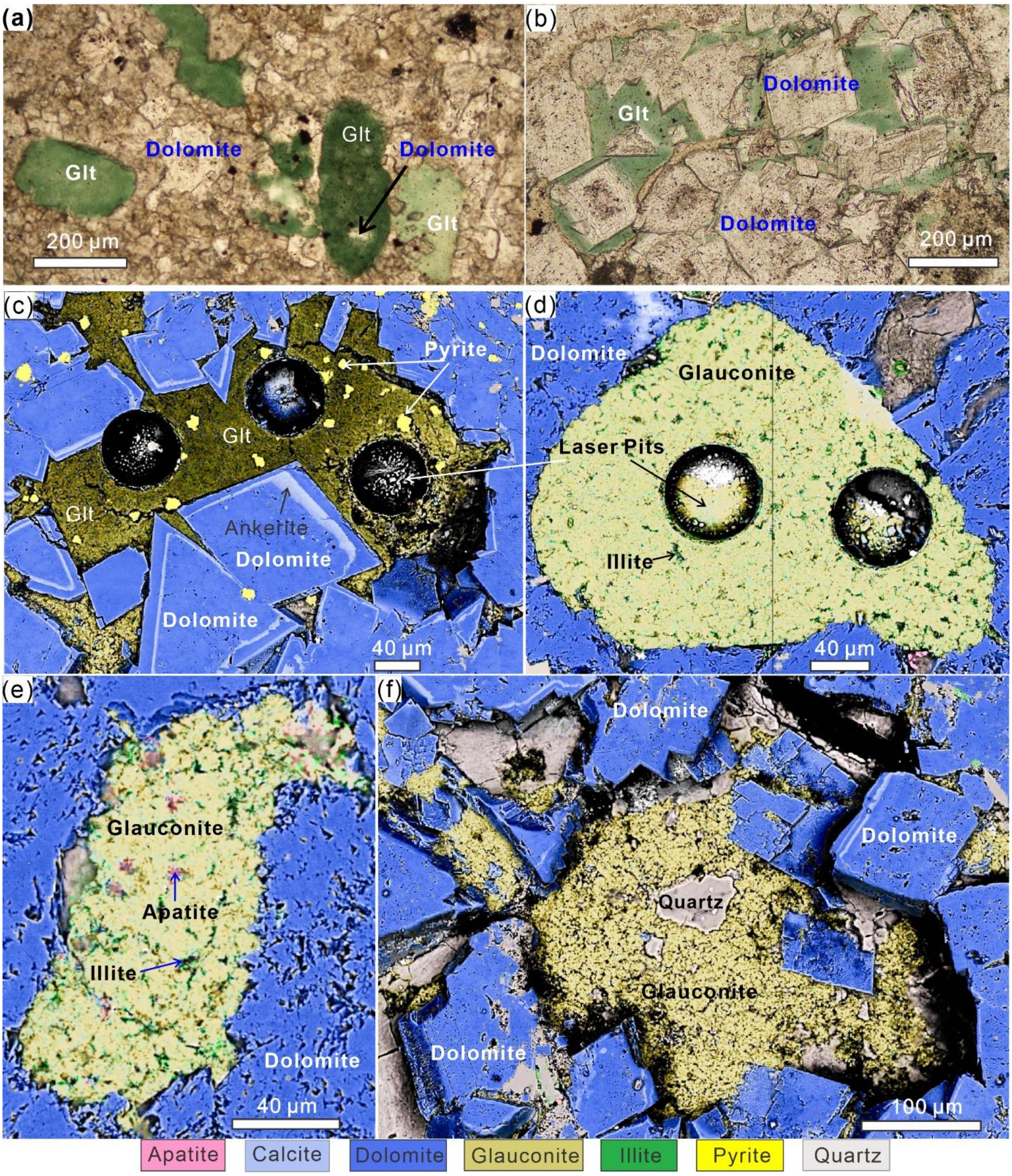

Figure 2. Petrography of glauconite-bearing dolostone samples from the Georgina Basin, Australia: (**a**)–(**b**) Transmitted light petrographic images; (**c**)–(**f**) Backscattered electron (BSE) images overlaid with mineral mapping from SEM-EDS analysis: (**a**) Glauconite pellets and/or infill hosted within fine- to medium-crystalline dolostone,showing dolomite micro-inclusions in glauconite (NT2516, Wonarah Formation); (**b**) Glauconite embedded in a coarse recrystallized dolomite matrix, displaying irregular shapes influenced by adjacent dolomite

crystals (NT1837, Wonarah Formation); (**c**) Glauconite infills a coarsely crystalline dolomitic matrix, containing abundant pyrite micro-inclusions and circular craters formed by laser ablation spots used for *in situ* Rb–Sr dating (NT1837, Wonarah Formation); (**d**) Partially illitized glauconite grain, with illite preferentially occupying more porous regions (LN, Thorntonia Limestone); (**e**) Illitized glauconite grain with apatite micro-inclusions (AI, Inca Formation); (**f**) Glauconite grain showing secondary alteration, deformation, partial dissolution and replacement by sparry dolomite and quartz (NT1835, Wonarah Formation).

Glauconite grains from the NCC are generally much larger than those from the Georgina Basin and exhibit clear signs of extensive diagenetic alteration. Micro-fractures cutting through glauconite grains, along with later-stage calcitic infills, are also commonly observed (Fig. 3a). These grains, typically > 1000 µm in diameter, often display a cauliflower-like micro-texture, due to the intergrowth of glauconite with carbonate minerals (Figs. 3a–d). A highly magnified SEM image of a glauconite grain and its rim from sample Man (Fig. 3f) shows calcite micro-inclusions with rhombohedral $CaCO_3$ crystals, enclosed in the mottled glauconite matrix. The mottled, cauliflower-like glauconites with calcite and dolomite micro-inclusions were less affected by illitization (Figs. 3–4).

The separated glauconite grains vary in size, color, and morphology among the samples analyzed in this study (Supplementary Fig. S1). In the Georgina Basin, glauconite grain sizes range from ~50 µm to ~400 µm. While some grains are well-formed and rounded, most are irregular, serrated, or angular. Petrographic analysis shows that these irregular shapes are due to morphological constraints imposed by recrystallized diagenetic phases, such as adjacent sparry dolomite crystals (Fig. 2). In contrast, glauconite grains from the NCC sites are systematically larger, ranging from ~200 µm to > 1000 µm, with well-developed spherical or ellipsoidal shapes, or pellets. In many of the studied samples, Fe-oxides and/or Fe-sulfides are commonly associated or attached to glauconite grains (Supplementary Fig. S1). In terms of coloration, most glauconite grains appear dark green under binocular microscopy in regular daylight conditions. However, samples CTD0205, CTD0206, and LN display a lighter green color.

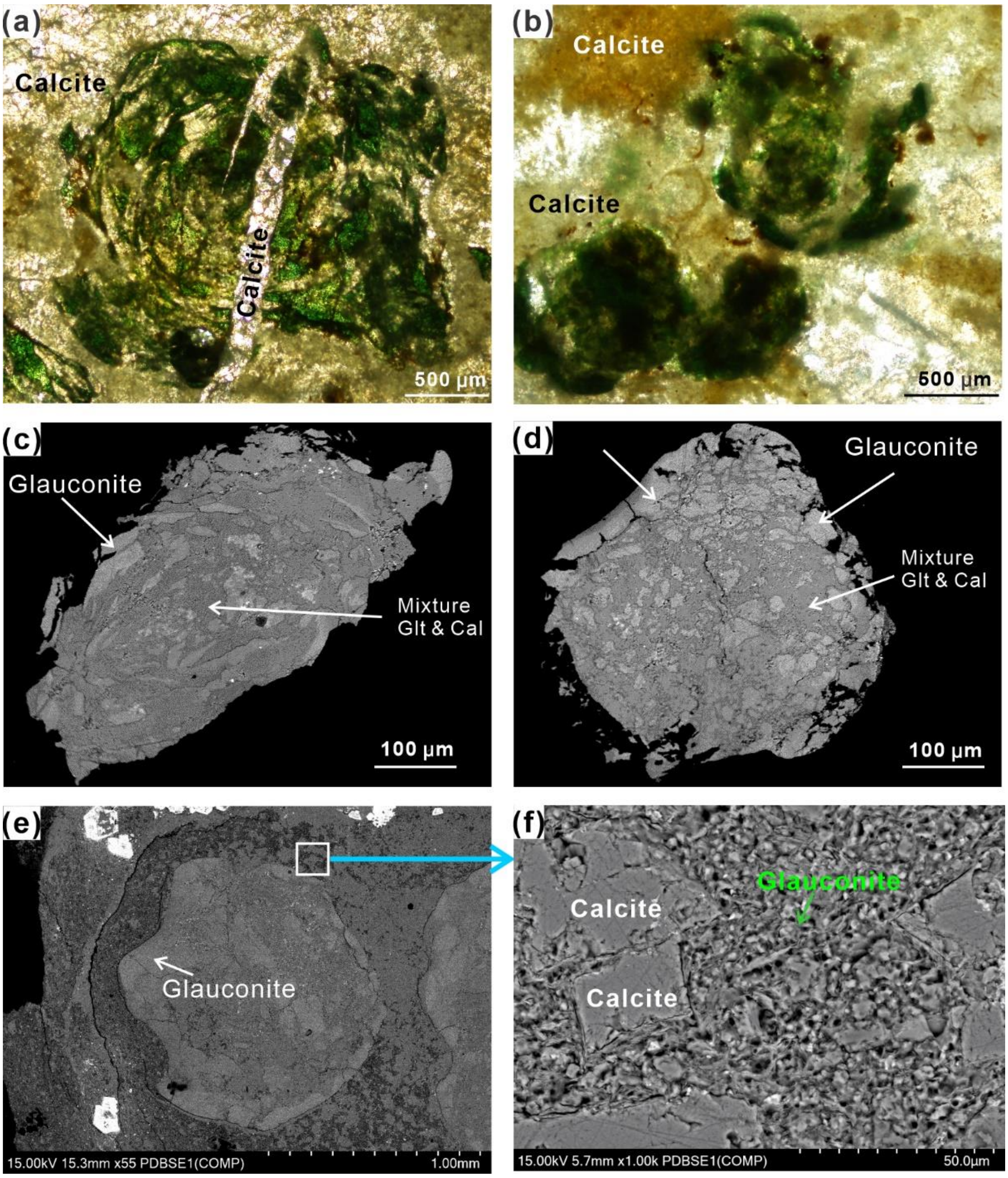

Figure 3. Petrography and diagenetic features of glauconites from China (NCC): (**a**) Large, cauliflower-like glauconite with abundant microfractures and post-depositional calcite veins (sample Hou, Houjiashan Formation), transmitted light; (**b**) Cauliflower-shaped glauconite intergrown with dolomite (sample Man, Mantou Formation), transmitted light; (**c**–**f**) BSE images showing glauconite grains containing carbonate mineral inclusions (**c**: sample Hou, Houjiashan Formation; **d**–**f:** sample Man, Mantou Formation); (**f**) Magnified BSE image of the rectangular area in (**e**), highlighting calcite micro-inclusions and/or infills within the glauconite.

3.4.2 Major Element Composition of Mid-Cambrian Glauconites

The heterogeneity of the studied glauconite grains is evident not only in visual and microscopic observations, but also in their chemical composition (Fig. 4). For consistency and quality control, we also analyzed the major oxide contents of the GL-O standard (i.e., Glauconite-Odin reference material) using EPMA. This standard, derived from the Albian-Cenomanian boundary at the Cauville Cliff section in Normandy, France (Odin, 1982; Löhr et al., 2024), is presented alongside the studied mid-Cambrian glauconites in Fig. 4 and listed in the Supplementary Table S2.

The mid-Cambrian glauconites from both the Georgina Basin and the NCC have a lower Fe_2O_3 content than GL-O, along with decreasing K_2O, increasing Al_2O_3, and a trend toward the illite (or Fe-illite) stability field (Fig. 4a). This trend is further supported by the cross plot of K_2O and MgO (Fig. 4b), which shows that the progressive illitization of glauconite leads to systematically lower K and Mg contents, with an increase in Al in illitized grains. This trend also aligns with micro-scale (SEM-EDS) elemental/mineralogical imaging results (Figs. 2b–c). Additionally, in the samples with elevated CaO and P_2O_5 contents (Figs. 4e–f), the glauconites contain calcite and/or apatite micro-inclusions, as well as glauconite dissolution, particularly notable in the samples from the Georgina Basin (Figs. 2c–f).

The MgO content in the mid-Cambrian glauconite samples also shows significant variation (Fig. 4e). Specifically, glauconite grains from the Georgina Basin have, on average, higher MgO contents (~6.4 wt%) compared to those from the NCC (average of ~4.7 wt%). Some EPMA spots in the studied samples show decreased MgO and increased CaO, with a negative correlation between the two (Fig. 4e), which may result from the precipitation of calcite/apatite micro-inclusions, in spaces created by progressive illitization and/or dissolution of glauconite grains.

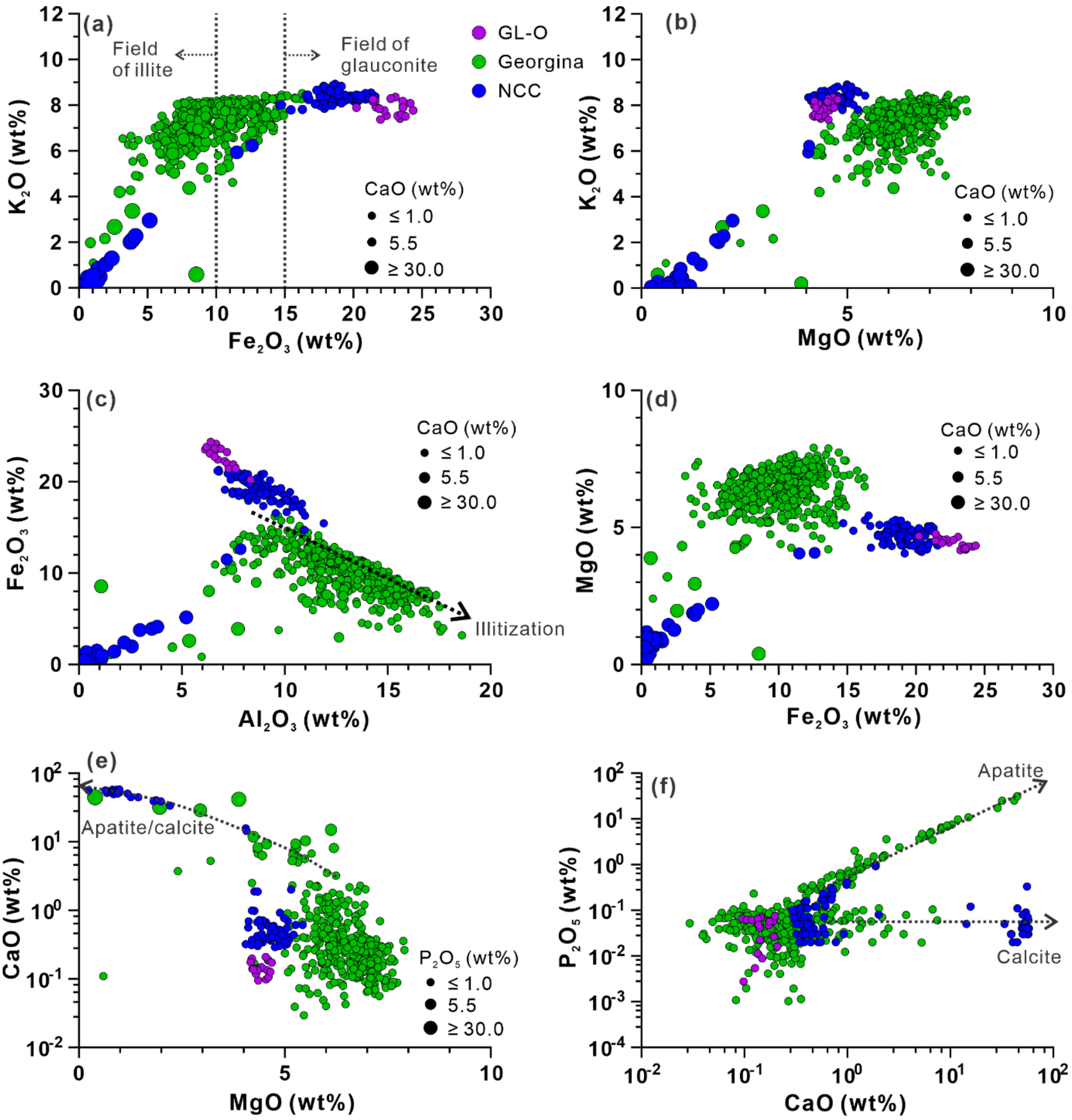

Figure 4. Elemental cross-plots with major oxides concentrations (wt%) in the studied mid-Cambrian glauconite and GL-O standard analyzed via EPMA: (**a**) K_2O vs. Fe_2O_3 with CaO content shown by variable circle sizes; (**b**) K_2O vs. MgO; (**c**) Fe_2O_3 vs. Al_2O_3 with CaO shown by variable circle sizes; (**d**) Fe_2O_3 vs. MgO with CaO shown by variable circle sizes; (**e**) MgO vs. CaO; (**f**) P_2O_5 vs. CaO contents. Note: The EPMA data for samples from the Georgina Basin were presented in Chapter 2 (see also Shao et al., 2025), whereas the EPMA data for the samples from China are newly collected.

Based on previous studies, ‘evolved’ or mature glauconite is characterized by high K_2O (> 6 wt%) and Fe_2O_3 (15 wt%) contents, whereas ‘nascent’ and/or ‘slightly evolved’ glauconite has a K_2O content below 4 wt% (Odin and Matter, 1981; Rubio and López-Pérez, 2024). In the Georgina Basin, most glauconite grains exhibit K_2O contents above 5 wt%, with an average of ~7.4 wt%. Glauconites from the NCC display more variable K_2O contents, but non-illitized grains with limited inclusions yielded an average of ~8.2 wt% (Figs. 4a–b), suggesting ‘evolved’ or mature glauconite, partially overlapping with GL-O data, which represent glauconite in its evolved to highly evolved stages.

Overall, the variations in major oxide levels in glauconites from the Georgina Basin and NCC indicate significant diagenetic alteration, such as glauconite recrystallization, illitization, and the formation of secondary carbonates and phosphates (Fig. 4).

3.4.3 *In situ* Rb–Sr ages of Mid-Cambrian Glauconites

In situ Rb–Sr ages of glauconite from the Georgina Basin yield ages between 350.3 ± 8.7 and 438.4 ± 5.2 Ma (Shao et al., 2025; Fig 5a), while those from the NCC range from 401.7 ± 5.6 to 437.2 ± 6.6 Ma. Initial $^{87}Sr/^{86}Sr$ ratios vary from 0.7094 ± 0.0042 to 0.7229 ± 0.0070 in the Georgina Basin and from 0.7083 ± 0.0023 to 0.7090 ± 0.0013 in the NCC (Supplementary Fig. S3).

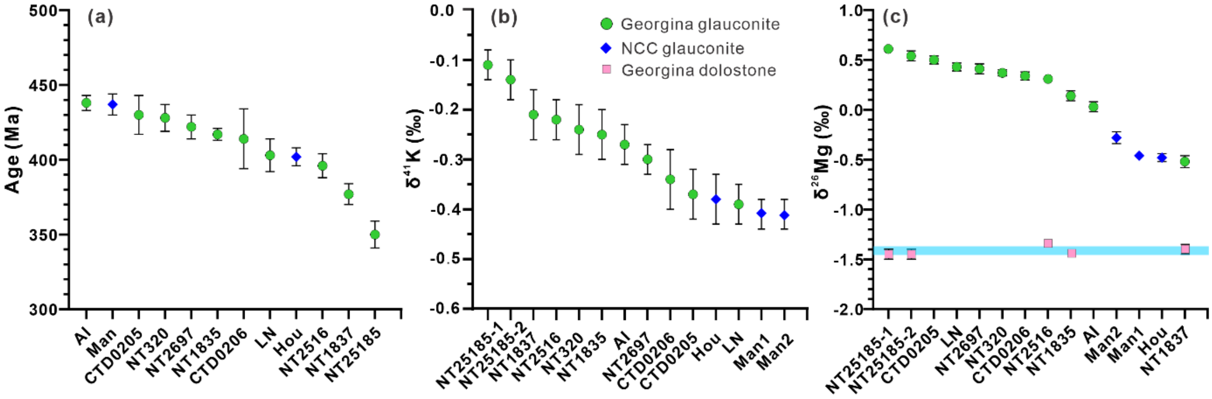

Figure 5. *In situ* Rb–Sr ages and K–Mg isotope compositions ($\delta^{41}K$ and $\delta^{26}Mg$) of mid-Cambrian glauconites from Australia (Georgina Basin) and China (NCC). Samples are

arranged from left to right in order of decreasing Rb–Sr age and from heavier to lighter isotope values. (**a**) Rb–Sr isochron ages of glauconite; (**b**) δ^{41}K values of glauconite; (**c**) δ^{26}Mg values of glauconite, along with δ^{26}Mg values of associated carbonate samples from the Georgina Basin. Note: The Rb–Sr ages for samples from the Georgina Basin were presented in Chapter 2 (see also Shao et al., 2025), whereas the Rb–Sr ages for the samples from China are newly collected.

3.4.4 Variability of δ^{41}K and δ^{26}Mg in Mid-Cambrian Glauconites and δ^{26}Mg in Coeval Carbonates

The mid-Cambrian glauconites from the Georgina Basin and NCC yield δ^{41}K values ranging from -0.41 ± 0.03‰ to -0.11 ± 0.03‰ (Supplementary Table S1), showing an overall variability of about 0.3‰ (Fig. 5b). The δ^{26}Mg values of the studied glauconites also vary widely, ranging from -0.52 ± 0.06‰ to +0.61 ± 0.03‰, covering a significant overall δ^{26}Mg range of about 1.1‰ (Fig. 5c). In general, the glauconite samples from the NCC exhibit lower δ^{41}K and δ^{26}Mg values compared to those from the Georgina Basin. The extremes of isotopic variation are represented by samples NT25185, NT1837 and Man. NT25185 exhibits the highest δ^{41}K and δ^{26}Mg values, while Man and NT1837 show the lowest δ^{41}K δ^{26}Mg values, respectively (Figs. 5b–5c). Notably, sample NT1837 from the Georgina Basin is one of the most severely altered, exhibiting significant recrystallization and illitization (Figs. 2b–c).

Four dolostone samples from the Georgina Basin yield δ^{26}Mg ranging from -1.45 ± 0.05‰ to -1.34 ± 0.03‰, with an average of -1.41 ± 0.04‰ (Fig. 5c; Supplementary Table S1). These values show an offset of ~0.8 to 1.3‰ relative to the δ^{26}Mg values of glauconite.

3.5 Discussion

3.5.1 Diagenetic Impact on δ^{41}K Proxy in Glauconite Archives

Stable K isotope fractionation between minerals and fluids occurs through natural processes such as leaching/dissolution, absorption, cation exchange, and clay mineral formation. Light ^{39}K is preferentially incorporated into authigenic clay minerals, leaving the remaining fluid or seawater enriched in ^{41}K (Li et al., 2019b; Li et al., 2021; Ramos et al., 2018; Wang et al., 2021).

Glauconitization involves the incorporation of dissolved K^+ ions from seawater, marine pore fluids, and detrital K-rich silicate minerals. These variable K sources can result in 'mixed' or non-marine $\delta^{41}K$ values in newly formed clays, particularly in nascent or incompletely matured glauconite that has not fully equilibrated with marine fluids. In contrast, fully matured or evolved glauconite grains, which have had enough time to chemically and isotopically equilibrate with ambient seawater, should record pristine marine $\delta^{41}K$ values, albeit with a specific isotope fractionation (between seawater and glauconite, $\Delta^{41}K_{\text{seawater-glauconite}}$) of about 0.90‰ (Löhr et al., 2025, under review). Importantly, since the residence time of dissolved K^+ in seawater (~11 Ma, Wang et al., 2021) is much longer than both the glauconite formation time (~0.1 to 1 Ma) and the ocean mixing time (~1000 years), the global ocean is well-mixed in K isotope composition, with a modern $\delta^{41}K$ value of $+0.12 \pm 0.07$‰ (Wang et al., 2021). Therefore, well-preserved (unaltered) and evolved glauconite grains (with $K_2O > 6$ wt%) should record the global paleo-seawater $\delta^{41}K$ signature at the time of glauconite formation.

In this study, most of the non-illitized mid-Cambrian glauconite pellets exhibit high K_2O contents exceeding 6 wt% (Figs. 4a–b), indicating evolved compositions and potentially recording paleo-seawater $\delta^{41}K$ values. The depositional ages of the studied mid-Cambrian glauconites from Australia and China range from ~514 Ma to ~504 Ma (He et al., 2022; Kruse et al., 2013; Laurie, 2022; Smith et al., 2013), suggesting that these evolved glauconites likely formed from coeval (within ~10 Ma) mid-Cambrian seawater, with presumably identical or similar initial $\delta^{41}K$ values at the time of glauconite formation.

However, petrographic and compositional evidence reveals varying degrees of post-depositional alteration in the studied mid-Cambrian glauconites (e.g., in illitized or partially illitized grains), which may have affected and partially reset their original marine $\delta^{41}K$ signature (Figs. 2–6; Supplementary Table S2). These diagenetic features are evident in some samples through more porous micro-textures and 'non-pelletal' morphologies, characterized by irregular, angular and serrated shapes, as well as signs of significant post-depositional recrystallization, deformation and glauconite dissolution and alteration, or precipitation as cements (Figs. 2c–2f; Supplementary Fig. S1). Altered glauconites commonly show microfracture and pore space infillings by secondary phases such as calcite, dolomite, and apatite (Figs. 2–3), with illitization particularly prevalent in more porous areas (Figs. 2d–e). These diagenetic features, including glauconite dissolution, illitization, and micro-inclusions, are also reflected in their elemental compositions, as observed in EPMA data (Fig. 4).

In situ Rb–Sr dating of the mid-Cambrian glauconites from Australia and China revealed reset ages ranging from 438 ± 5 Ma to 350 ± 9 Ma (Fig. 5a; Supplementary Table S3 and Fig. S3), significantly younger than their expected depositional ages of 514–504 Ma. Importantly, these reset or 'rejuvenated' Rb–Sr ages show a moderate but statistically significant correlation ($R = -0.74$, $p < 0.005$) with $\delta^{41}K$ values (Fig. 6a), where younger, more strongly reset or rejuvenated glauconite samples exhibit isotopically heavier $\delta^{41}K$ values (Fig. 6a) and vice versa. The $\delta^{41}K$ values are also negatively correlated with glauconite K_2O content ($R = -0.82$, $p < 0.001$), where higher $\delta^{41}K$ values correspond to lower K_2O levels (Fig. 6b). This relationship is likely due to post-depositional recrystallization and illitization associated with increased burial diagenesis and/or fluid-rock interaction, leading to K loss and potential isotope resetting (Hu et al., 2021). Additionally, glauconite diagenesis and illitization also causes Al^{3+} to substitute for Fe^{3+}/Fe^{2+} (and possibly also Mg^{2+}) in the octahedral sites, leading to an increase in Al_2O_3 content in the altered glauconites (Baldermann et al., 2017; Starzec et al., 2023; Środoń et al., 2023), accompanied by a decrease in Fe_2O_3 content and lower K/Al ratios (Fig. 6c). Furthermore, the illitization process decreases the Rb content in glauconites, leading to a progressive decrease in Rb/K ratios in the more altered samples. These diagenetic effects are also reflected in a negative correlation between Rb/K ratios and $\delta^{41}K$, as well as *in situ* Rb–Sr ages (Fig. 6a, d).

We propose that the observed correlation between the $\delta^{41}K$ proxy and the geochemical parameters (i.e., elemental indices of alteration, Figs. 6a–c) suggests that higher $\delta^{41}K$ values in more altered glauconites result from the preferential loss of K and lighter ^{39}K due to illitization. Alternatively, this may reflect isotope resetting or equilibration of altered glauconite with diagenetic fluids or basinal brines carrying heavier $\delta^{41}K$ signatures (Fig. 6). The impact of illitization appears more pronounced in more porous glauconite, where dissolution and recrystallization likely enhance diagenetic fluid flows and mineral-water interactions (Figs. 2–3), promoting cation exchange and driving the observed elemental and isotope variations (Figs. 4–5).

Overall, these observations suggest that the δ^{41}K proxy in glauconite archives can be reset during burial diagenesis and post-depositional processes (e.g., illitization), despite K being a major element in glauconite (~50,000–75,000 ppm or ~6–8 wt% K_2O). In contrast, trace elements like Rb (typically present at only a few hundred to a few thousand ppm) are more susceptible to diagenetic alteration. This is evident from the substantial loss of Rb relative to K in altered glauconite grains, resulting in lower Rb/K ratios and 'rejuvenated' Rb–Sr ages.

Notably, the reset Rb–Sr ages of glauconite from both the Georgina Basin and the NCC coincide with major tectonic orogenic events. In the Georgina Basin, the rejuvenated Rb–Sr ages align with the Alice Springs Orogeny (ca. 450–300 Ma; Haines et al., 2001; Kruse et al., 2013), during which the Thorntonia Limestone experienced burial temperatures exceeding 130 °C (Dunster et al., 2007). In the NCC, the reset ages are associated with the Caledonian-aged Qinling Orogeny (ca. 480–420 Ma), part of the Central Asian Orogenic Belt (Dong et al., 2016; Zhao et al., 2018). These tectonic events likely facilitated the resetting of Rb–Sr ages and altered both the chemical and isotopic compositions of glauconite through elevated basin temperatures and intensified fluid–rock interactions.

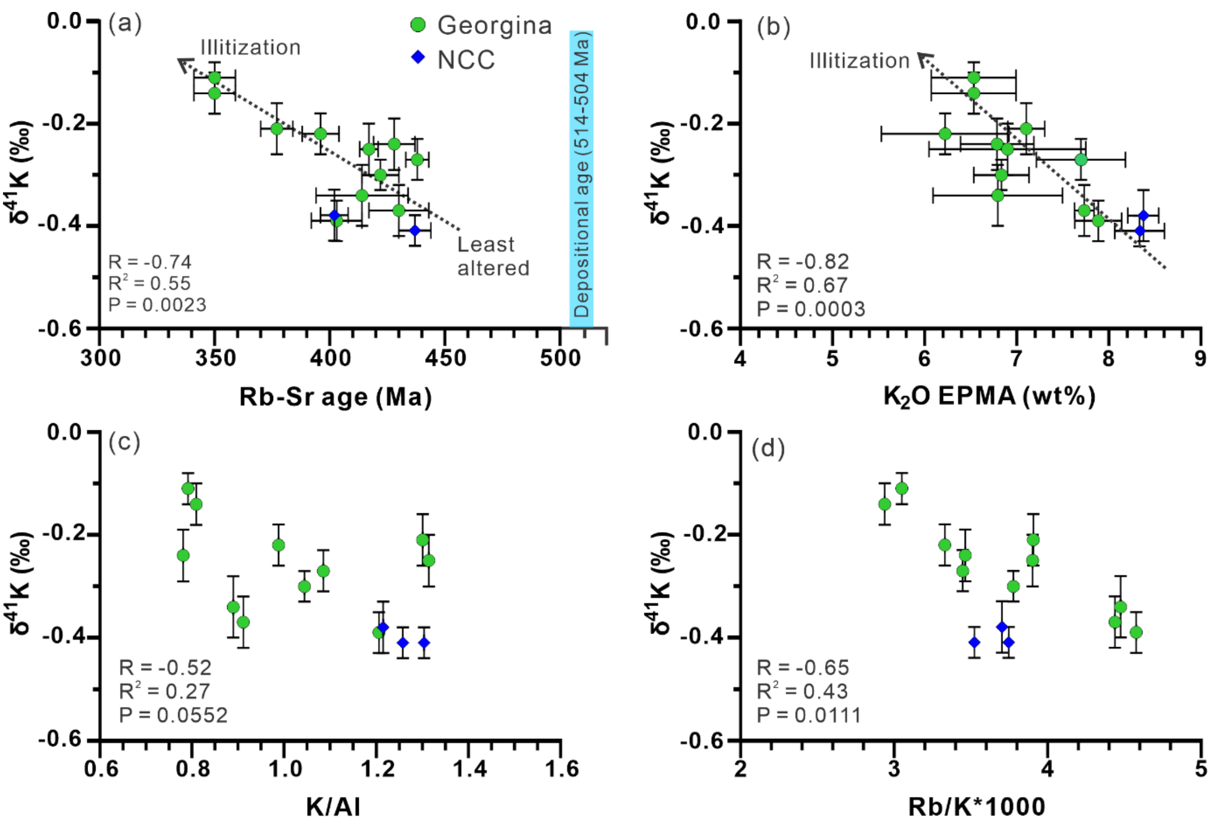

Figure 6. Cross-plots of mid-Cambrian glauconite $\delta^{41}K$ values as a function of (**a**) *in situ* Rb–Sr ages of glauconite; (**b**) K_2O (wt%) concentration (EPMA data); (**c**) K/Al (ppm), and (**d**) Rb/K (ppm) ratios (ICP-MS data).

3.5.2 Diagenetic Impact on δ^{26}Mg Proxy in Glauconite Archives

Given the long residence time of Mg in the ocean (~13 Ma; Ling et al., 2011), which leads to globally homogeneous paleo-seawater δ^{26}Mg signatures, the mid-Cambrian glauconites studied from Australia and China should have had identical or similar original δ^{26}Mg signatures at the time of their formation. Accordingly, the observed variations in δ^{26}Mg values are thus most likely due to (i) site-specific paleo-depositional conditions (e.g., different precursor phases, local isotope effects, *etc.*), or alternatively (ii) distinct diagenetic processes and burial histories at these Georgina Basin and NCC sites.

Our results show that diagenetic overprinting and post-depositional alteration of the δ^{26}Mg proxy in glauconite is more complex than for K isotopes (Fig. 7). The main controls on Mg isotope alteration are (i) progressive illitization and (ii) the formation of secondary diagenetic carbonate phases and micro-inclusions due to recrystallization (i.e., dolomitization and calcification). These processes shift δ^{26}Mg values to heavier compositions, likely due to isotopic exchange or equilibrium with isotopically heavier diagenetic fluids or basinal brines, and/or recrystallization and dissolution processes that enrich glauconite in ^{26}Mg while releasing lighter ^{24}Mg into local porewater. This interpretation is supported by experimental studies on the dissolution of K-rich silicate (e.g., biotite) and clay synthesis, which show lighter δ^{26}Mg isotopes are preferentially retained in reactive fluids (Dunlea et al., 2017; Hindshaw et al., 2020; Ryu et al., 2016).

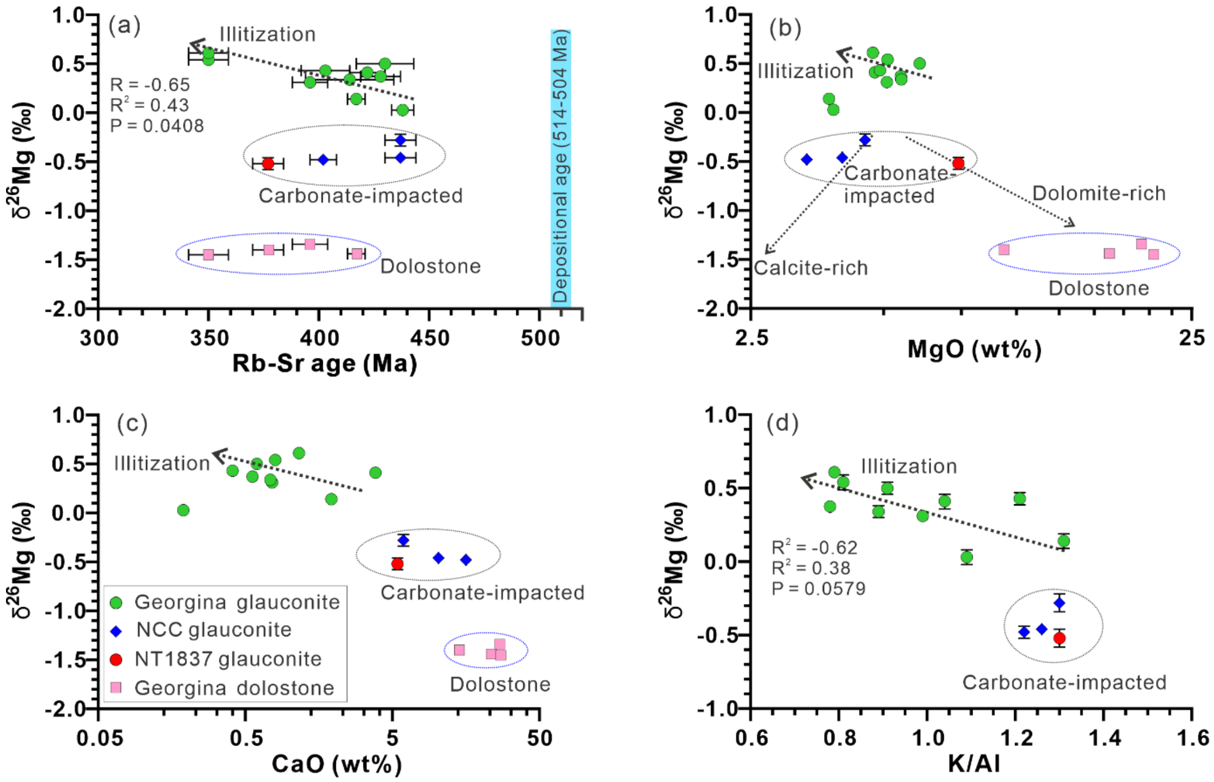

Figure 7. Cross-plots showing δ^{26}Mg values of mid-Cambrian glauconites as a function of (**a**) *in situ* Rb–Sr ages, (**b**) MgO (wt%) content, (**c**) CaO (wt%) content, and (**d**) K/Al (ppm) ratios, based on ICP-MS data.

The impact of illitization on the δ^{26}Mg of altered glauconites is further supported by changes in elemental compositions and observed correlations between the Mg isotope proxy (δ^{26}Mg) and K/Al ratios (Fig. 7d). Finally, the degree of isotope resetting or 'rejuvenation' of glauconite

Rb–Sr ages is closely related to the extent of illitization and the shift to higher δ^{26}Mg values, as illustrated by the green circles in Fig. 7.

Theoretically, illitization could cause MgO depletion in altered glauconites through dissolution and Mg^{2+} leaching, typically leading to a negative correlation between MgO content and δ^{26}Mg values. However, this trend is not observed in our mid-Cambrian glauconite data (Fig. 7b). This may be attributed to two factors: (1) not all glauconite grains from the Georgina Basin underwent illitization, and (2) the data may be affected by matrix effects or the influence of carbonate micro-inclusions.

The Georgina Basin glauconites exhibit consistently higher MgO concentrations (Figs. 4e, 7b), likely due to the presence of Mg-rich carbonate precursors during glauconite formation. In particular, the exceptionally high MgO content of sample NT1837 is attributed to abundant dolomite micro-inclusions (Figs. 2b–c), which also drive its δ^{26}Mg to the lowest value observed (red circle in Fig. 7b). In contrast, NCC glauconites display higher CaO concentrations with lower δ^{26}Mg values than those from the Georgina Basin (Fig. 7c), reflecting a greater abundance of calcite micro-inclusions formed during diagenetic alteration (Figs. 3, 4e–f). This is further supported by the replicate samples Man 1 and Man 2, which were taken from the same bulk sample (Man) but exhibit different δ^{26}Mg values (Fig. 5c), suggesting varying contributions from carbonate phases within the sample (Fig. 5c).

The interaction or incorporation of carbonate minerals such as calcite and dolomite with glauconite shifts δ^{26}Mg towards lighter values (Fig. 7), as these carbonate phases preferentially incorporate light ^{24}Mg during their formation (Galy et al., 2002; Hu et al., 2017; Huang et al., 2012; Huang et al., 2015; Farkaš et al., 2025). This isotope fractionation pattern observed in the mid-Cambrian glauconite is consistent with the general behavior of carbonate and silicate minerals, whereby carbonate-rich phases typically yield lower δ^{26}Mg values, while clay-rich minerals tend to exhibit higher δ^{26}Mg (Higgins and Schrag, 2010; Hu et al., 2017; Huang et al., 2015; Shalev et al., 2020; Xia et al., 2024).

In particular, the influence of carbonate phases and micro-inclusions in mid-Cambrian glauconites, especially those from China (NCC), is reflected in their elevated CaO/MgO ratios, lower Rb/Sr ratios, and lighter δ^{26}Mg values (Fig. 8). Glauconite typically has high Rb and low Sr and Ca, whereas carbonate minerals (calcite, dolomite) are enriched in Sr and Ca but depleted in Rb. Consequently, glauconite samples with high CaO content and low Rb/Sr ratios are more likely to have been impacted by carbonate phases (Fig. 8a). Thus, we propose that carbonate-impacted glauconites (e.g., from NCC) exhibit lower δ^{26}Mg values, distinguishing them from illitized glauconites (from the Georgina Basin), which tend to yield higher or isotopically heavier δ^{26}Mg signatures (Fig. 8b).

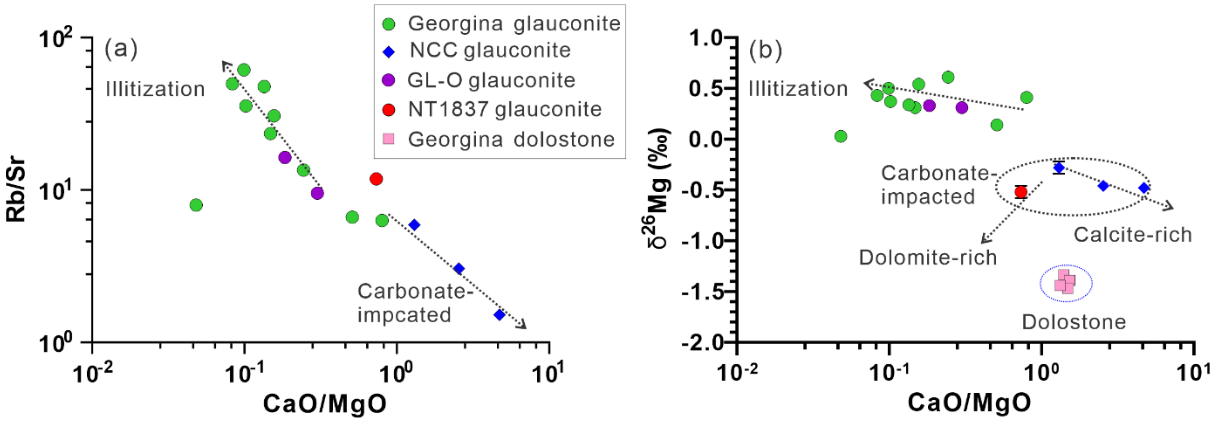

Figure 8. Cross-plots of mid-Cambrian glauconite: (**a**) Rb/Sr vs. CaO/MgO ratios; (**b**) δ^{26}Mg values vs. CaO/MgO ratios. All elemental data and ratios are from a solution-based ICP-MS analysis.

3.5.3 Constraints on δ^{41}K and δ^{26}Mg of the Mid-Cambrian Seawater

(1) Reconstruction of the Mid-Cambrian Seawater δ^{41}K and δ^{26}Mg

As discussed above, most studied glauconites show post-depositional alteration or illitization, leading to reset Rb–Sr ages and shifts in δ^{41}K and δ^{26}Mg values. However, a subset of least-altered or best-preserved glauconites can still be identified and used for paleo-seawater reconstruction. Glauconites with the oldest Rb–Sr ages, minimal illitization (indicated by high K_2O and Fe_2O_3, and low Al_2O_3), and low carbonate contamination represent the most reliable archives for constraining the K and Mg isotope composition of mid-Cambrian seawater. Based on the above criteria, the best-preserved glauconites from Australia (Georgina Basin) and China

(NCC) yield δ^{41}K values between ~-0.45 and -0.25‰, and δ^{26}Mg values between ~-0.20 and +0.10‰ (Fig. 9). In contrast, more altered glauconite, impacted by illitization, show higher δ^{41}K and δ^{26}Mg values, while those with carbonate micro-inclusions (calcite, dolomite) tend to have lower (isotopically lighter) δ^{26}Mg signatures.

To translate the best preserved glauconite data to plausible K and Mg isotope signatures of mid-Cambrian seawater, isotope fractionation or offsets (Δ) between glauconite and seawater must be considered. Based on recent studies, the isotopic offsets between modern seawater (sw) and recent glauconite are estimated at $\Delta^{41}K_{\text{(sw-glauconite)}} \approx 0.90$‰ (Löhr et al., 2023; Löhr et al., 2025) and $\Delta^{26}Mg_{\text{(sw-glauconite)}} \approx 0.00$‰ (Shaikh et al., 2024). Assuming these isotope fractionation factors remained constant through geological time, the inferred mid-Cambrian seawater compositions based on glauconite range from ~+0.45 to +0.65‰ for δ^{41}K and from ~-0.20 to +0.10‰ for δ^{26}Mg (Fig. 9c). Importantly, the latter estimate for the mid-Cambrian seawater ($\delta^{26}Mg_{\text{(sw)}}$ = ~-0.20 to +0.10‰) overlaps with a recently reported δ^{26}Mg of the Cambrian oceans of -0.08‰ (Li et al., 2023) and -0.20‰ (Xia et al., 2024), based on marine dolomite and halite archives, respectively.

Li et al. (2022) reported a δ^{41}K value of -0.18 ± 0.03‰ for modern marine glauconite from bulk sediments, implying a ~0.3‰ fractionation relative to seawater. Applying this would suggest mid-Cambrian $\delta^{41}K_{\text{sw}}$ values of -0.15 to -0.05‰. However, their value was derived from indirect linear fitting of bulk sediments potentially contaminated by illite and K-feldspar, and the maturity of the glauconite remains uncertain, despite the absence of detectable smectite, which may result from analytical limitations (Li et al., 2022).

Glauconite-derived estimates suggest that, compared to modern seawater ($\delta^{41}K_{\text{(sw)}} = +0.12 \pm 0.07$‰; $\delta^{26}Mg_{\text{(sw)}} = -0.83 \pm 0.09$‰), the Cambrian ocean was isotopically heavier in both K and Mg (Hu et al., 2020; Li et al., 2022; Ling et al., 2011; Wang et al., 2021).

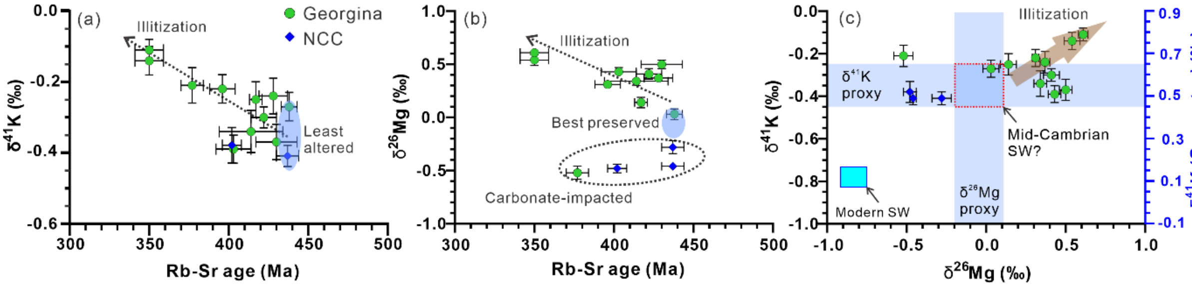

Figure 9. Cross plots of the mid-Cambrian glauconite data, including: (**a**) δ^{41}K vs. Rb–Sr ages; (**b**) δ^{26}Mg vs. Rb–Sr ages; and (**c**) δ^{41}K vs. δ^{26}Mg glauconite values, including the 'best-preserved' or least altered samples (i.e., blue ellipses) and the inferred δ^{41}K and δ^{26}Mg compositions of the mid-Cambrian ocean water (i.e., pink dashed rectangle).

(2) Quantifying Carbonate Contribution to Glauconite δ^{26}Mg Isotopic Signature

As discussed earlier, the observed lighter δ^{26}Mg values from the NCC and the Georgina Basin sample NT1837 are attributed to the presence of carbonate matrix and micro-inclusions (Figs. 7–8). To quantify a possible contribution of such carbonate minerals (i.e., dolomite and calcite micro-inclusions) to the measured δ^{26}Mg values in glauconites, a simple isotope mass-balance model was applied using the following equations:

$$\delta_{MIX} = (F_{glt}\, \delta_{glt}\, C_{glt} + F_X\, \delta_X\, C_X)/(F_{glt}\, C_{glt} + F_X\, C_X)$$

where:

δ_{MIX} represents the 'mixed' δ^{26}Mg values; C_{MIX} represents the 'mixed' Mg concentration (see also equation below); F_{glt} and F_X are the mass fractions (from 0 to 1) of glauconite and carbonate (X = dolomite or calcite), respectively; δ_{glt} and δ_X are their respective δ^{26}Mg values; and C_{glt} and C_X are their respective Mg concentrations.

The abovementioned 'mixed' Mg concentration (C_{MIX}) can be calculated based on the following equation:

$$C_{MIX} = F_{glt}\, C_{glt} + F_X\, C_X$$

In this study, the δ^{26}Mg values of glauconite (δ_{glt}) range from -0.5 to +0.6‰, with an average of 0.05‰, while the δ^{26}Mg values for dolomite and calcite are -1.4‰ and -2.1‰, respectively (see Fig. 8b, and also Hu et al., 2017). The average Mg concentration in the studied glauconites (C_{glt}) is ~3.2 wt%, based on the best-preserved glauconite samples (Fig. 7). The Mg concentration for dolomite ($C_{dolomite}$) is derived from a theoretical stoichiometric value of 13.18%, while that for calcite ($C_{calcite}$) is estimated at 1.2 wt%.

The two-component 'glauconite-carbonate' modelling results are presented in Fig. 10. In this study, the carbonate-affected glauconite grains exhibit δ^{26}Mg values ranging from -0.52 to -0.3‰ (see blue bar in Fig. 10a). Based on our isotope mass-balance modeling, only about 5 to 15% of Mg derived from dolomite is needed to explain the measured δ^{26}Mg values in the affected glauconites, while for calcite one would need up to 30 to 45% contribution (Fig. 10a).

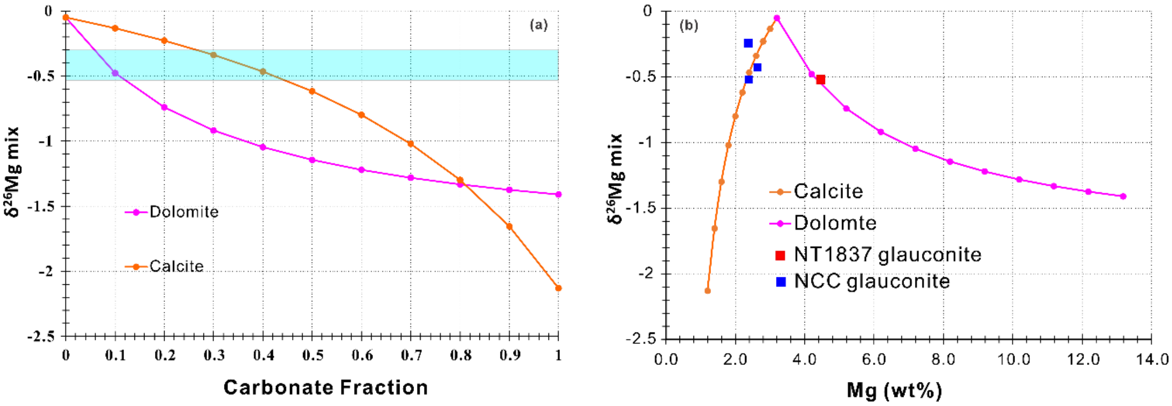

Figure 10. Calculated mixing δ^{26}Mg trends for (a) carbonate fractions contributing to glauconites, and (b) calculated mixing trends for δ^{26}Mg vs Mg concentrations. The blue bar represents the range of measured δ^{26}Mg values in the studied Cambrian glauconites.

3.6 Conclusions

This study applies and investigates K and Mg isotope variations, *in situ* Rb–Sr dating, and elemental/mineral mapping of Middle Cambrian glauconites from the Georgina Basin (Australia) and the North China Craton (NCC, China). The key findings are as follows:

(1) Glauconite pellets from the Georgina Basin and the NCC (deposited between ~514 and 504

Ma) are highly heterogeneous and complex marine archives, as indicated by variations in their color, size, and morphology, micro-porosity, the degree of alteration (illitization), and the presence of abundant micro-inclusions (dolomite, calcite, apatite, pyrite, quartz). These features reflect the complex diagenetic histories of the glauconites.

(2) Significant and systematic variations in δ^{41}K and δ^{26}Mg values were observed in the mid-Cambrian glauconites, with δ^{41}K ranging from -0.41 to -0.11‰, and δ^{26}Mg ranging from -0.52‰ to 0.61‰. These variations are attributed to (i) progressive alteration or illitization, which increases both δ^{41}K and δ^{26}Mg, and (ii) the impact of carbonate (dolomite, calcite) micro-inclusions, which tend to shift δ^{26}Mg to lower values in glauconite. Simple isotope mass-balance modeling indicates that calcite inclusions might contribute between ~30 to 45% of the Mg to the altered glauconite δ^{26}Mg signals in the NCC, while dolomite phases account for only 5 to 15% of the Mg in the most altered samples in the Georgina Basin.

(3) Based on the best-preserved or least altered mid-Cambrian glauconite samples, and assuming that the isotopic fractionation between modern seawater (sw) and glauconite (Δ^{41}K $_{\text{sw-glauconite}} \approx 0.9$‰, Δ^{26}Mg $_{\text{sw-glauconite}} \approx 0$‰) has remained constant through geological time, the inferred δ^{41}K and δ^{26}Mg values for mid-Cambrian seawater are estimated to range from +0.45 to +0.65‰ for δ^{41}K $_{\text{sw}}$, and from ~-0.20 to +0.1‰ for δ^{26}Mg $_{\text{sw}}$. These heavier δ^{41}K and δ^{26}Mg values, relative to modern seawater, suggest more intense reverse weathering (marine clay authigenesis) and widespread dolomitization in the Cambrian oceans.

3.7 Acknowledgments

This research was supported by the ARC Discovery Project (DP210100462), titled "Glauconite: Archive recording the timing and triggers of Cambrian radiation", and ARC Linkage project (LP210100462), titled “Novel isotope techniques to explore the Centralian Superbasin, Australia”. Further support via the MinEx Cooperative Research Centre (MinEx CRC), specifically the MinEx PhD research bursary to Z.S., is also greatly acknowledged. X.Z. is supported by a CAREER Award (#2238685) by the US National Science Foundation. This manuscript represents the MinEx CRC Contribution Number: #286/81130467. We extend our gratitude also to Dr. Ming Li for his guidance and assistance during the field sampling in China, and to Dr. Benjamin Wade for his invaluable support with the EPMA analysis at the University of Adelaide (Adelaide Microscopy Centre). Special thanks go to Dr. Juzer Shaikh and Yisheng Yin at the University of Minnesota for their assistance with the K and Mg column chemistry and MC-ICP-MS analysis. The authors acknowledge the instruments and expertise of Microscopy Australia (ROR: 042mm0k03) at Adelaide Microscopy, University of Adelaide, enabled by NCRIS, university, and state government support.

3.8 References

Baldermann, A., Banerjee, S., Löhr, S.C., Rudmin, M., Warr, L.N., Chakraborty, A., 2025. Exploring reverse silicate weathering across geological time: a review. Clay Minerals, 1-93.

Baldermann, A., Dietzel, M., Mavromatis, V., Mittermayr, F., Warr, L. N., Wemmer, K. 2017. The role of Fe on the formation and diagenesis of interstratified glauconite-smectite and illite-smectite: A case study of Upper Cretaceous shallow-water carbonates. Chemical Geology, 453, 21-34.

Banerjee, S., Bansal, U., Pande, K., Meena, S., 2016b. Compositional variability of glauconites within the Upper Cretaceous Karai Shale Formation, Cauvery Basin, India: implications for evaluation of stratigraphic condensation. Sedimentary Geology 331, 12-29.

Banerjee, S., Bansal, U., Thorat, A.V., 2016a. A review on palaeogeographic implications and temporal variation in glaucony composition. Journal of Palaeogeography 5, 43-71.

Bayon, G., Giresse, P., Chen, H., Rouget, M.-L., Gueguen, B., Moizinho, G.R., Barrat, J.-A., Beaufort, D., 2023. The Behavior of Rare Earth Elements during Green Clay Authigenesis on the Congo Continental Shelf. Minerals 13, 1081.

Brenot, A., Cloquet, C., Vigier, N., Carignan, J., France-Lanord, C., 2008. Magnesium isotope systematics of the lithologically varied Moselle river basin, France. Geochimica et Cosmochimica Acta 72, 5070-5089.

Brock, G., Engelbretsen, M., Jago, J., Kruse, P., Laurie, J., Shergold, J., Shi, G., Sorauf, J.,

2000. Palaeobiogeographic affinities of Australian Cambrian faunas. Memoirs of the Association of Australasian Palaeontologists, 1-61.

Burst, J.F., 1958. Mineral heterogeneity in "glauconite" pellets. American Mineralogist: Journal of Earth and Planetary Materials 43, 481-497.

Chen, X., Zhou, Y., Shields, G.A., 2022. Progress towards an improved Precambrian seawater 87Sr/86Sr curve. Earth-Science Reviews 224, 103869.

Dong, Y., Santosh, M., 2016. Tectonic architecture and multiple orogeny of the Qinling Orogenic Belt, Central China. Gondwana Research 29, 1-40.

Dunster, J., Kruse, P., Duffett, M., Ambrose, G., 2007. Geology and resource potential of the southern Georgina Basin. Digital information package DIP007. Darwin: Northern Territory Geological Survey. 1-243.

Farkaš, J., Wallmann, K., Mosley, L., Staudigel, P., Zheng, X.-Y., Leyden, E., Shao, Y., Fryda, J., Holmden, C., Eisenhauer, A., 2025. Alkalinity and elemental cycles in present and past ocean: Insight from geochemical modeling and alkali and alkaline earth metal isotopes. Treatise on Geochemistry (Third Edition), pp. 33-87.

Galy, A., Bar-Matthews, M., Halicz, L., O'Nions, R.K., 2002. Mg isotopic composition of carbonate: insight from speleothem formation. Earth and Planetary Science Letters 201, 105-115.

Gao, T., Ke, S., Li, R., Meng, X.n., He, Y., Liu, C., Wang, Y., Li, Z., Zhu, J.M., 2018. High-precision magnesium isotope analysis of geological and environmental reference materials by multiple-collector inductively coupled plasma mass spectrometry. Rapid Communications in Mass Spectrometry 33, 767-777.

Glass, L.M., Phillips, D., 2006. The Kalkarindji continental flood basalt province: A new Cambrian large igneous province in Australia with possible links to faunal extinctions. Geology 34, 461-464.

Glorie, S., Gilbert, S.E., Hand, M., Lloyd, J.C., 2024. Calibration methods for laser ablation Rb–Sr geochronology: comparisons and recommendation based on NIST glass and natural reference materials. Geochronology 6, 21-36.

Haines, P.W., Hand, M., Sandiford, M., 2001. Palaeozoic synorogenic sedimentation in central and northern Australia: a review of distribution and timing with implications for the evolution of intracontinental orogens. Australian Journal of Earth Sciences 48, 911-928.

Han, S., Löhr, S.C., Abbott, A.N., Baldermann, A., Farkaš, J., McMahon, W., Milliken, K.L., Rafiei, M., Wheeler, C., Owen, M., 2022. Earth system science applications of next-generation SEM-EDS automated mineral mapping. Frontiers in Earth Science 10, 956912.

Harrison, A.L., Bénézeth, P., Schott, J., Oelkers, E.H., Mavromatis, V., 2021. Magnesium and carbon isotope fractionation during hydrated Mg-carbonate mineral phase transformations. Geochimica et Cosmochimica Acta 293, 507-524.

He, W.-Y., Qi, Y.-A., Dai, M.-Y., Liu, B.-C., Li, J.-B., Xu, G.-X., Wang, M., Li, D., 2022. Facies Changes, Evolution of Biogenic Structures, and Carbon Isotope Stratigraphy of the Cambrian Series 2 to Miaolingian Transition on the Southern North China Craton. Minerals 12, 1526.

Higgins, J.A., Schrag, D., 2010. Constraining magnesium cycling in marine sediments using magnesium isotopes. Geochimica et Cosmochimica Acta 74, 5039-5053.

Higgins, J.A., Schrag, D.P., 2015. The Mg isotopic composition of Cenozoic seawater–evidence for a link between Mg-clays, seawater Mg/Ca, and climate. Earth and Planetary Science Letters 416, 73-81.

Hu, Y., Chen, X.-Y., Xu, Y.-K., Teng, F.-Z., 2018. High-precision analysis of potassium isotopes by HR-MC-ICPMS. Chemical Geology 493, 100-108.

Hu, Y., Teng, F.-Z., Chauvel, C., 2021. Potassium isotopic evidence for sedimentary input to the mantle source of Lesser Antilles lavas. Geochimica et Cosmochimica Acta 295, 98-111.

Hu, Y., Teng, F.-Z., Plank, T., Chauvel, C., 2020. Potassium isotopic heterogeneity in subducting oceanic plates. Science Advances 6, eabb2472.

Hu, Z., Hu, W., Wang, X., Lu, Y., Wang, L., Liao, Z., Li, W., 2017. Resetting of Mg isotopes between calcite and dolomite during burial metamorphism: Outlook of Mg isotopes as geothermometer and seawater proxy. Geochimica et Cosmochimica Acta 208, 24-40.

Hu, Z., Yang, S., Yang, C., Guo, Y., Xu, J., Zhang, C., 2023. Mg isotopes of siliciclastic sediments on continental marginal sea: Insights for the potential to trace silicate weathering. Global and Planetary Change 231, 104307.

Huang, K.-J., Shen, B., Lang, X.-G., Tang, W.-B., Peng, Y., Ke, S., Kaufman, A.J., Ma, H.-R., Li, F.-B., 2015. Magnesium isotopic compositions of the Mesoproterozoic dolostones: Implications for Mg isotopic systematics of marine carbonates. Geochimica et Cosmochimica Acta 164, 333-351.

Huang, K.-J., Teng, F.-Z., Elsenouy, A., Li, W.-Y., Bao, Z.-Y., 2013. Magnesium isotopic variations in loess: Origins and implications. Earth and Planetary Science Letters 374, 60-70.

Huang, K.-J., Teng, F.-Z., Plank, T., Staudigel, H., Hu, Y., Bao, Z.-Y., 2018. Magnesium isotopic composition of altered oceanic crust and the global Mg cycle. Geochimica et Cosmochimica Acta 238, 357-373.

Huang, K.-J., Teng, F.-Z., Wei, G.-J., Ma, J.-L., Bao, Z.-Y., 2012. Adsorption-and desorption-controlled magnesium isotope fractionation during extreme weathering of basalt in Hainan Island, China. Earth and Planetary Science Letters 359, 73-83.

Huang, T.-Y., Teng, F.-Z., Rudnick, R.L., Chen, X.-Y., Hu, Y., Liu, Y.-S., Wu, F.-Y., 2020. Heterogeneous potassium isotopic composition of the upper continental crust. Geochimica et Cosmochimica Acta 278, 122-136.

Isson, T., Rauzi, S., 2024. Oxygen isotope ensemble reveals Earth's seawater, temperature, and carbon cycle history. Science 383, 666-670.

Isson, T.T., Planavsky, N.J., 2018. Reverse weathering as a long-term stabilizer of marine pH and planetary climate. Nature 560, 471-475.

Khider, K., MacFarlane, S., Bradshaw, B.E., Carr, L., Henson, P., 2021. The Centralian Superbasin (Canning, Amadeus, Georgina and Officer basins) Stratigraphic Review and Well Correlations.

Kruse, P., Dunster, J., Munson, T., 2013. Chapter 28: Georgina Basin, in Geology and Mineral Resources of the Northern Territory, Darwin: Northern Territory Geol. Surv. 28.1-28.56.

Laurie, J.R., 2022. Report on the biostratigraphy of the Georgina Basin succession in NDI Carrara 1. Geoscience Australia, Canberra. 1-7.

Li, S., Li, W., Beard, B.L., Raymo, M.E., Wang, X., Chen, Y., Chen, J., 2019a. K isotopes as a tracer for continental weathering and geological K cycling. Proceedings of the national academy of sciences 116, 8740-8745.

Li, W.-Y., Teng, F.-Z., Ke, S., Rudnick, R.L., Gao, S., Wu, F.-Y., Chappell, B., 2010. Heterogeneous magnesium isotopic composition of the upper continental crust. Geochimica et Cosmochimica Acta 74, 6867-6884.

Li, W., Beard, B.L., Li, C., Xu, H., Johnson, C.M., 2015. Experimental calibration of Mg isotope fractionation between dolomite and aqueous solution and its geological implications. Geochimica et Cosmochimica Acta 157, 164-181.

Li, W., Chakraborty, S., Beard, B.L., Romanek, C.S., Johnson, C.M., 2012. Magnesium isotope fractionation during precipitation of inorganic calcite under laboratory conditions. Earth and Planetary Science Letters 333, 304-316.

Li, W., Kwon, K.D., Li, S., Beard, B.L., 2017. Potassium isotope fractionation between K-salts and saturated aqueous solutions at room temperature: Laboratory experiments and theoretical calculations. Geochimica et Cosmochimica Acta 214, 1-13.

Li, W., Li, S., Beard, B.L., 2019b. Geological cycling of potassium and the K isotopic response: Insights from loess and shales. Acta Geochimica 38, 508-516.

Li, W., Liu, X.-M., Hu, Y., Teng, F.-Z., Hu, Y., 2021. Potassium isotopic fractionation during clay adsorption. Geochimica et Cosmochimica Acta 304, 160-177.

Li, W., Liu, X.-M., Wang, K., McManus, J., Haley, B.A., Takahashi, Y., Shakouri, M., Hu, Y., 2022. Potassium isotope signatures in modern marine sediments: Insights into early diagenesis. Earth and Planetary Science Letters 599, 117849.

Li, X., Zhu, G., Li, T., Zhou, L., Wu, Y., Shen, B., Ning, M., 2023. Conservative behavior of Mg isotopes in dolomite during diagenesis and hydrothermal alteration: A case study in the Lower Cambrian Qiulitage Formation, Gucheng area, Tarim Basin. Applied Geochemistry 148, 105540.

Ling, M.X., Sedaghatpour, F., Teng, F.Z., Hays, P.D., Strauss, J., Sun, W., 2011. Homogeneous magnesium isotopic composition of seawater: an excellent geostandard for Mg isotope analysis. Rapid Communications in Mass Spectrometry 25, 2828-2836.

Liu, C., Wang, Z., Raub, T.D., Macdonald, F.A., Evans, D.A., 2014. Neoproterozoic cap-dolostone deposition in stratified glacial meltwater plume. Earth and Planetary Science Letters 404, 22-32.

Löhr, C.S., Zheng, X.-Y., Farkaš, J., Abbott, N.A., Baldermann, A., Weissgerber, J., 2025. Marine clay authigenesis controls seawater potassium isotope composition. Under review.

Löhr, S., Zheng, X., Lv, Y., Weissgerber, J., Baldermann, A., Farkas, J., Abbott, A.N., 2023. Mineralogical, chemical and isotopic evolution of recent glauconite in two contrasting marine settings, Goldschmidt 2023 Conference. GOLDSCHMIDT.

Löhr, S.C., Khazaie, E., Farkaš, J., Baldermann, A., Gilbert, S., Maas, R., Subarkah, D., Blades, M.L., Collins, A.S., 2024. Origin and Significance of Age Variability in the Glauconite Reference Material GL-O: Implications for In Situ Rb-Sr Geochronology. Geostandards and Geoanalytical Research. 49.1: 197-216.

McKenzie, N.R., Hughes, N.C., Myrow, P.M., Choi, D.K., Park, T.-y., 2011. Trilobites and zircons link north China with the eastern Himalaya during the Cambrian. Geology 39, 591-594.

Mu, J., Chen, T., Yu, Q., An, S., Chen, J., Shi, X., Li, W., 2024. Potassium isotopic signatures of modern offshore detrital sediments from different climatic regimes and the implications. Science China Earth Sciences 67, 405-419.

Odin G.S. 1982. Interlaboratory standards for dating purposes. In: Odin G.S. (ed.), Numerical dating in stratigraphy. Wiley (New York), 123–150.

Odin, G.S., Matter, A., 1981. De glauconiarum origine. Sedimentology 28, 611-641.

Ramos, D.P.S., Coogan, L.A., Murphy, J.G., Higgins, J.A., 2020. Low-temperature oceanic crust alteration and the isotopic budgets of potassium and magnesium in seawater. Earth and Planetary Science Letters 541, 116290.

Peters, S.E., Gaines, R.R., 2012. Formation of the ‘Great Unconformity’as a trigger for the

Cambrian explosion. Nature 484, 363-366.

Ramos, D.P.S., Morgan, L.E., Lloyd, N.S., Higgins, J.A., 2018. Reverse weathering in marine sediments and the geochemical cycle of potassium in seawater: Insights from the K isotopic composition (^{41}K/^{39}K) of deep-sea pore-fluids. Geochimica et Cosmochimica Acta 236, 99-120.

Redaa, A., Farkaš, J., Gilbert, S., Collins, A.S., Wade, B., Löhr, S., Zack, T., Garbe-Schönberg, D., 2021. Assessment of elemental fractionation and matrix effects during in situ Rb–Sr dating of phlogopite by LA-ICP-MS/MS: implications for the accuracy and precision of mineral ages. Journal of Analytical Atomic Spectrometry 36, 322-344.

Rubio, B., López-Pérez, A., 2024. Exploring the genesis of glaucony and verdine facies for paleoenvironmental interpretation: A review. Sedimentary Geology, 106579.

Ryu, J.-S., Vigier, N., Decarreau, A., Lee, S.-W., Lee, K.-S., Song, H., Petit, S., 2016. Experimental investigation of Mg isotope fractionation during mineral dissolution and clay formation. Chemical Geology 445, 135-145.

Scheiblhofer, E., Moser, U., Löhr, S., Wilmsen, M., Farkaš, J., Gallhofer, D., Bäckström, A.M., Zack, T., Baldermann, A., 2022. Revisiting Glauconite Geochronology: Lessons Learned from In-situ Radiometric Dating of a Glauconite-Rich Cretaceous Shelfal Sequence. Minerals 12, 818.

Scotese, C.R., Song, H., Mills, B.J., van der Meer, D.G., 2021. Phanerozoic paleotemperatures: The earth’s changing climate during the last 540 million years. Earth-Science Reviews 215, 103503.

Shaikh, J.I., Löhr, S., Baldermann, A., Farkaš, J., Abbott, A.N., Zheng, X.-Y., 2024. Marine glauconites: A potential new archive of paleo seawater magnesium isotopes, Goldschmidt Conference 2024: Goldschmidt 2024.

Shalev, N., Bontognali, T.R., Vance, D., 2020. Sabkha dolomite as an archive for the magnesium isotope composition of seawater. Geology 49, 253-257.

Shao, Z., Farkaš, J., Glorie, S., Collins, S.A., Gilbert, E.S., Subarkah, D., 2025. Dating of marine authigenic minerals via in situ Rb–Sr, U–Pb, and Lu–Hf: A case study from the

Georgina Basin, Australia. Chemical Geology: 123042.

Shen, B., Jacobsen, B., Lee, C.-T.A., Yin, Q.-Z., Morton, D.M., 2009. The Mg isotopic systematics of granitoids in continental arcs and implications for the role of chemical weathering in crust formation. Proceedings of the National Academy of Sciences 106, 20652-20657.

Smith, T., Kelman, A.P., Nicoll, R., Edwards, D., Hall, L., Laurie, J., Carr, L., 2013. An updated stratigraphic framework for the Georgina Basin, NT and Queensland. The APPEA Journal 53, 487-487.

Środoń, J., Williams, L., Szczerba, M., Zaitseva, T., Bojanowski, M.J., Marciniak-Maliszewska, B., Kuligiewicz, A., Starzec, K., Ciesielska, Z., Paszkowski, M., 2023. Mechanism of late diagenetic alteration of glauconite and implications for geochronology. Geochimica et Cosmochimica Acta 352, 157-174.

Starzec, K., Stadnik, R., Skiba, M., Bębenek, S., Waśkowska, A., 2023. Origin and paleoenvironmental significance of Al-rich glauconite in the Ediacaran/Cambrian deposits of the Lublin Basin, Poland (SW margin of Baltica). Precambrian Research 397, 107165.

Stille, P., Clauer, N., 1994. The process of glauconitization: chemical and isotopic evidence. Contributions to Mineralogy and Petrology 117, 253-262.

Sun, Y., Ouyang, Q., Lang, X., Pang, K., Wu, C., Chen, Z., Zhou, C., 2023. Global sea-level fall triggered Ediacaran–Cambrian unconformity in North China craton. Earth and Planetary Science Letters 622, 118411.

Teng, F.-Z., Li, W.-Y., Rudnick, R.L., Gardner, L.R., 2010. Contrasting lithium and magnesium isotope fractionation during continental weathering. Earth and Planetary Science Letters 300, 63-71.

Tipper, E., Galy, A., Gaillardet, J., Bickle, M., Elderfield, H., Carder, E., 2006. The magnesium isotope budget of the modern ocean: constraints from riverine magnesium isotope ratios. Earth and Planetary Science Letters 250, 241-253.

Walter, M., Veevers, J., Calver, C., Grey, K., 1995. Neoproterozoic stratigraphy of the

Centralian superbasin, Australia. Precambrian Research 73, 173-195.

Wang, K., Close, H.G., Tuller-Ross, B., Chen, H., 2020. Global average potassium isotope composition of modern seawater. ACS Earth and Space Chemistry 4, 1010-1017.

Wang, K., Peucker-Ehrenbrink, B., Chen, H., Lee, H., Hasenmueller, E.A., 2021. Dissolved potassium isotopic composition of major world rivers. Geochimica et Cosmochimica Acta 294, 145-159.

Wilmsen, M., Bansal, U., 2021. Depositional setting and limiting factors of early Late Cretaceous glaucony formation: implications from Cenomanian glauconitic strata (Elbtal Group, Germany). Facies 67, 24.

Xia, Z., Li, S., Hu, Z., Bialik, O., Chen, T., Weldeghebriel, M.F., Fan, Q., Fan, J., Wang, X., An, S., 2024. The evolution of Earth's surficial Mg cycle over the past 2 billion years. Science Advances 10, eadj5474.

Zhang, B., Zheng, D., Liu, Y., Shi, M., 2022. Palaeogeography and provenance transition of Precambrian–Cambrian unconformity at the southern margin of the North China Craton. Geological Journal 57, 3721-3735.

Zhao, G., Wang, Y., Huang, B., Dong, Y., Li, S., Zhang, G., Yu, S., 2018. Geological reconstructions of the East Asian blocks: From the breakup of Rodinia to the assembly of Pangea. Earth-Science Reviews 186, 262-286.

Zhao, H., Zhang, S., Zhu, M., Ding, J., Li, H., Yang, T., Wu, H., 2020. Paleomagnetic insights into the Cambrian biogeographic conundrum: Did the North China craton link Laurentia and East Gondwana? Geology 49, 372-376.

Zheng, W., Wang, X., Wan, B., Pang, K., Tang, Q., 2023. Early Cambrian evaporite deposits in the North China Craton and their event stratigraphic, paleogeographic, and paleoenvironmental implications. Journal of Asian Earth Sciences 242, 105489.

Zheng, X.-Y., Beard, B.L., Neuman, M., Fahnestock, M.F., Bryce, J.G., Johnson, C.M., 2022a. Stable potassium (K) isotope characteristics at mid-ocean ridge hydrothermal vents and its implications for the global K cycle. Earth and Planetary Science Letters 593, 117653.

Zheng, X.-Y., Chen, X.-Y., Ding, W., Zhang, Y., Charin, S., Gérard, Y., 2022b. High precision analysis of stable potassium (K) isotopes by the collision cell MC-ICP-MS “Sapphire” and a correction method for concentration mismatch. Journal of Analytical Atomic Spectrometry 37, 1273-1287.

3.9 Supplementary Materials–Chapter 3

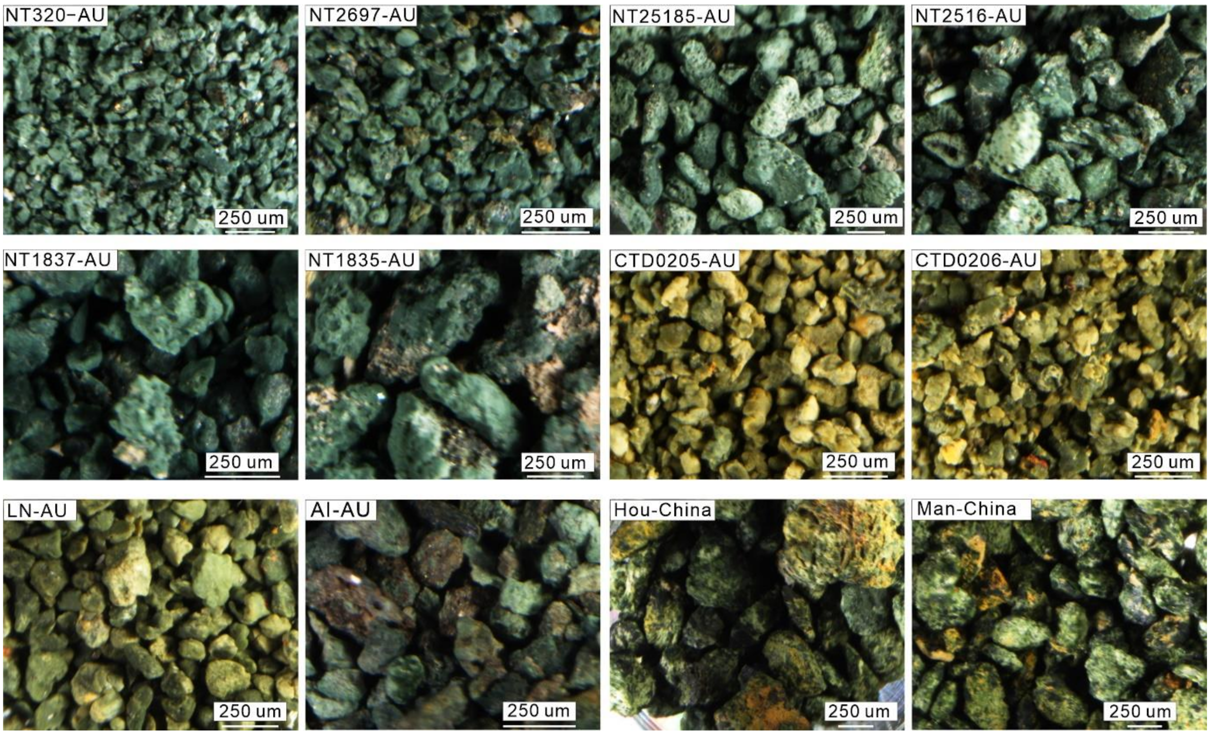

Figure. S1: Separated glauconite grains from rock samples, with sample IDs and their collection localities.

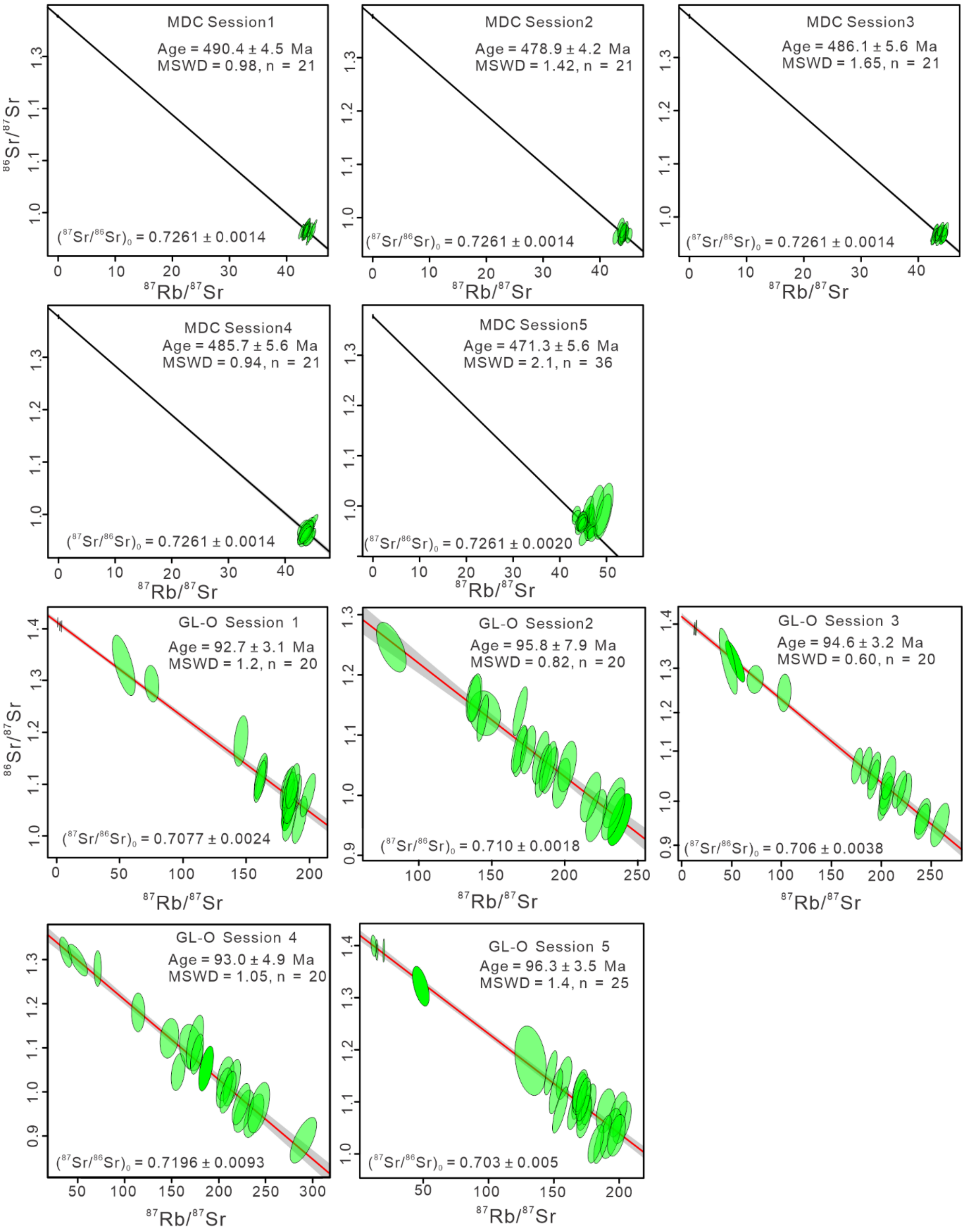

Figure S2: *In situ* Rb–Sr Isochrons of MDC and GL-O from each analyzed session.

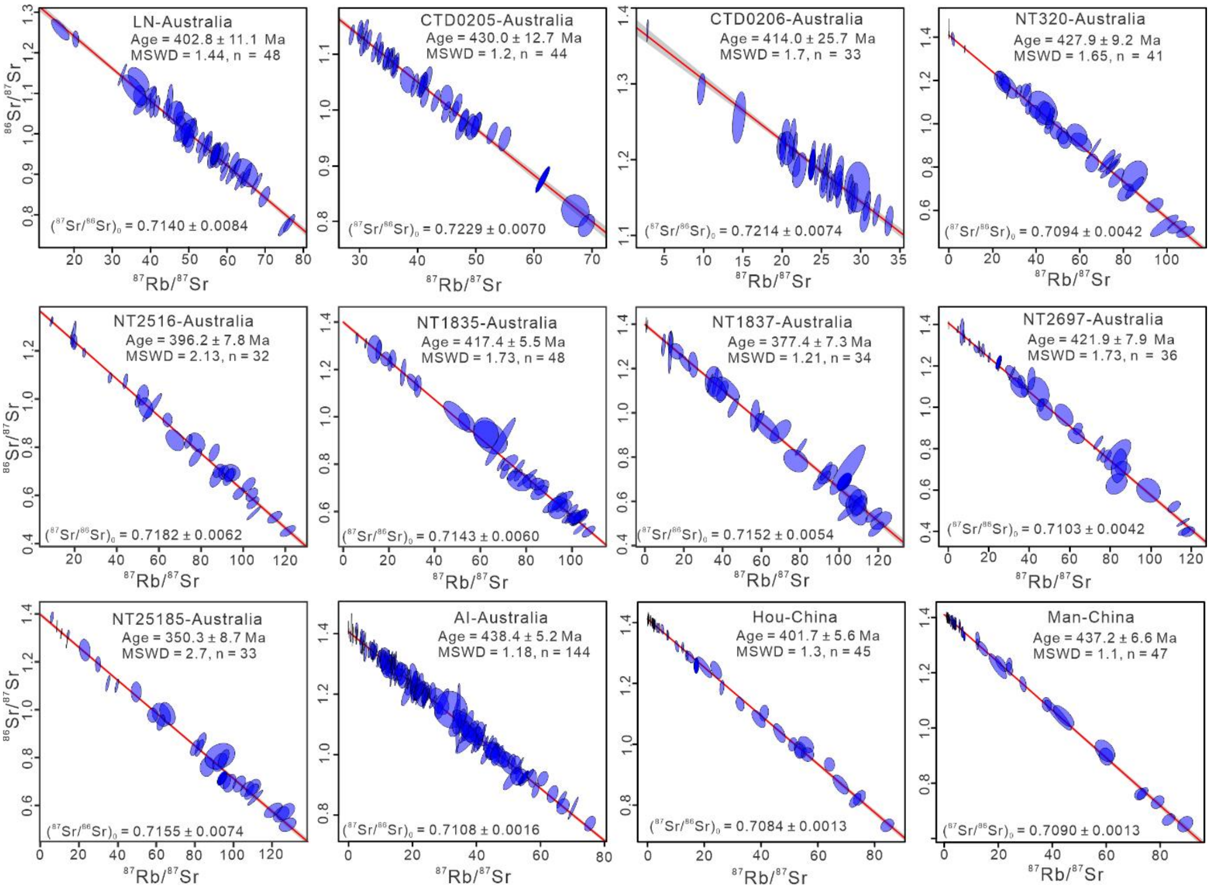

Figure S3: *In situ* Rb–Sr isochrons of glauconite samples from the Georgina Basin (Australia) and the North China Craton.

Chapter 3–Source Data

Note that all data, including the tables listed below, are available and accessible via the following link:

https://figshare.com/s/daba1676ffca8e64863e

Supplementary Table S1: Detailed information about the studied samples.

Supplementary Table S2: Glauconie EPMA data.

Supplementary Table S3: Isotopic ratios and uncertainties of standards and analyzed samples.

Supplementary Table S4: δ^{41}K and δ^{26}Mg Isotopic Compositions for standards.

Chapter 4: Magnesium isotope constraints on the mid-Cambrian seawater, marine Mg cycling and dolomitization during the Drumian Carbon Isotope Excursion (DICE) event

Unpublished manuscript formatted for submission to *Geochimica et Cosmochimica Acta*.

Zhufu Shao, Juraj Farkaš, Xin-Yuan Zheng, Glenn A. Brock, Alan S. Collins

Statement of Authorship

Title of Paper	Magnesium isotope constraints on the mid-Cambrian seawater, marine Mg cycling and dolomitization during the Drumian Carbon Isotope Excursion (DICE) event
Publication Status	☐ Published ☐ Accepted for Publication ☐ Submitted for Publication ☒ Unpublished and Unsubmitted work written in manuscript style
Publication Details	This manuscript is to be submitted to the journal *Geochimica et Cosmochimica Acta*.

Principal Author

Name of Principal Author (Candidate)	Zhufu Shao		
Contribution to the Paper	Work planning, sample preparation, laboratory analyses, data acquisition, processing, interpretation, and manuscript writing		
Overall percentage (%)	80%		
Certification:	This paper reports on original research I conducted during the period of my Higher Degree by Research candidature and is not subject to any obligations or contractual agreements with a third party that would constrain its inclusion in this thesis. I am the primary author of this paper.		
Signature		Date	06-May-25

Co-Author Contributions

By signing the Statement of Authorship, each author certifies that:

i. the candidate's stated contribution to the publication is accurate (as detailed above);

ii. permission is granted for the candidate in include the publication in the thesis; and

iii. the sum of all co-author contributions is equal to 100% less the candidate's stated contribution.

Name of Co-Author	Juraj Farkaš
Contribution to the Paper	Supervised work, helped with data interpretation and manuscript revision

Signature	Fang	Date	May 10, 2025
Name of Co-Author	Xin-Yuan Zheng		
Contribution to the Paper	Contributed to δ^{26}Mg isotope data acquisition, interpretation, and manuscript revision.		
Signature	Xinyuan Zheng	Date	07-May-25

Name of Co-Author	Glenn A. Brock		
Contribution to the Paper	Contributed to phosphatic fossil separation, data interpretation, and manuscript revision.		
Signature	G. Brock	Date	12-05-2025

Name of Co-Author	Alan S. Collins		
Contribution to the Paper	Supervised work, helped with data interpretation and manuscript revision.		
Signature		Date	21-05-25

Abstract

The Drumian Carbon Isotope Excursion (DICE; ~505 Ma) represents a global negative $\delta^{13}C$ anomaly linked to perturbations in the oceanic carbon cycle, redox shifts, sea-level rise, and biological turnover. This study employs multi-proxy isotope chemostratigraphy ($\delta^{26}Mg$, $\delta^{13}C$, $\delta^{18}O$, and $^{87}Sr/^{86}Sr$) derived from bulk rock carbonate and well preserved phosphatic fossils from the Georgina Basin, Australia, to: (1) reconstruct mid-Cambrian seawater Mg cycling, (2) trace marine dolomitization processes, and (3) identify diagenetic overprints.

Three stratigraphic sections record a complete transgressive–regressive cycle in the Narpa Group, subdivided into Sequence 1 and Sequence 2 successions. Well-preserved carbonates from the transgressive Sequence 2 capture a $\delta^{13}C$ peak of -3.9‰ interpreted as the DICE isotopic event. This negative anomaly is interpreted to reflect marine redox changes and potential upwelling of ^{12}C-rich anoxic waters.

Pristine low-Mg limestone with minimal alteration reveal $^{87}Sr/^{86}Sr$ values close to the mid-Cambrian seawater Sr isotope composition (~0.70880–0.70900). In contrast, elevated $^{87}Sr/^{86}Sr$ ratios, along with higher Mn/Sr, Mg/Ca, Al, and Rb values, suggest diagenetic alteration, detrital input, and dolomitization. Phosphatic microfossils show variable $^{87}Sr/^{86}Sr$ values deviating from the expected seawater signatures, with smaller fragments exhibiting more radiogenic values due to enhanced diagenetic alteration.

Carbonate $\delta^{26}Mg$ (DSM3) values range from -3.05‰ to -1.00‰, reflecting a mix of pure calcite and dolomite. Fully dolomitized samples yield $\delta^{26}Mg$ values from -1.92‰ to -1.00‰. Using a $\Delta^{26}Mg_{\text{sw-dolomite}}$ fractionation of ~1.73–2.00‰, the mid-Cambrian seawater $\delta^{26}Mg$ is estimated to be ~-0.19 to +0.08‰, heavier than modern oceans (-0.83‰), but consistent with other reconstructions.

Dolomite-based $\delta^{26}Mg$ chemostratigraphy is a valuable tool for tracing the timing, fluid source, and migration pathways of dolomitizing fluids across depositional sequences. Penecontemporaneous dolomitization is characterized by an upward-increasing $\delta^{26}Mg$ trend, which is associated with early diagenesis in restricted peritidal settings. In contrast, the seepage-reflux dolomitization process exhibits a downward-increasing $\delta^{26}Mg$ trend, driven by

brine reflux during sea-level fall.

Keywords: Mg-C-Sr isotopes, Cambrian seawater, DICE, dolomitization, Georgina Basin, Australia

4.1 Introduction

The early to middle Cambrian Period records the rapid diversification of clades (phyla) and the synchronous emergence of biomineralized skeletons (the Cambrian radiation event), reflecting a significant biogeochemical and ecological transition in the oceans (Peters and Gaines, 2012; Wang et al., 2024a; Zhang et al., 2020). Several carbon isotope ($\delta^{13}C$) excursions in marine carbonates have been identified throughout the Cambrian, suggesting links between the global C cycle, sea-level fluctuations, biotic events and environmental change (Gill et al., 2011; Wang et al., 2024a; Zhang et al., 2020; Zhu et al., 2006), indicating complex cyclic patterns of extinctions and radiations during this period (Holmes et al., 2025). The boundary between the Wuliuan and the Drumian stages of the mid-Cambrian Miaolingian Series (ca. 504.5 Ma) is defined by the Global Boundary Stratotype Section and Point (GSSP), marked by the first appearance datum (FAD) of the diagnostic trilobite Ptychagnostus atavus, which also coincides with a global negative Drumian Carbon Isotope Excursion (DICE) recorded just above this boundary (Babcock et al., 2004; Babcock et al., 2007; Chen et al., 2022; Howley and Jiang, 2010; Pagès and Schmid, 2016; Yang et al., 2021; Zhu et al., 2006). The seawater $^{87}Sr/^{86}Sr$ record reveals a progressive increase from the Neoproterozoic into the Cambrian, reaching a Phanerozoic maximum of ~0.70920 (Chen et al., 2022; McArthur et al., 2020; Peng et al., 2020).

The Earth's surface and oceanic calcium (Ca) and magnesium (Mg) cycles also play a crucial role in regulating the global C cycle and the Earth’s climate through geological time. Dissolved magnesium (Mg^{2+}) represents the fourth most abundant cation in the ocean, with a seawater residence time of ~13 million years (Ma) (Ling et al., 2011; Tipper et al., 2006). Mg has three naturally occurring stable isotopes with the following abundances: ^{24}Mg (~79%), ^{25}Mg (~10%), and ^{26}Mg (~11%) (Ling et al., 2011; Wang et al., 2014).

The oceanic Mg cycle is mainly governed by the balance between continental weathering (of carbonates/dolomites and silicates) as the dominant source, balanced by several marine sinks, including dolomitization, authigenic Mg-clay formation, and both high- and low-temperature alteration of oceanic crust. Each of these processes exerts a distinct influence on the Mg isotopic composition of seawater (Tipper et al., 2006; Xia et al., 2024; Farkas et al., 2024). Experimental and natural data indicate that Mg isotope fractionation between seawater and dolomite (Δ^{26}Mg $_{\text{sw-dolomite}}$) is typically ~1.73–2.00‰ , whereas the offset between dolomite and calcite (Δ^{26}Mg $_{\text{dolomite-calcite}}$) is around ~0.7‰ (Hu et al., 2017; Xia et al., 2024).

Reconstruction of paleo-seawater δ^{26}Mg values from marine dolostones and evaporites reveals a long-term secular decrease of approximately 1.4‰ from the Paleoproterozoic to the present. Based on the latest studies the Cambrian seawater δ^{26}Mg values are estimated at about -0.2‰ (Xia et al., 2024), approximately 0.6‰ heavier than modern ocean water (δ^{26}Mg $_{\text{sw}}$ = -0.83‰; Ling et al., 2011). Magnesium isotope fractionation between carbonate minerals and aqueous fluid is temperature-dependent (Hu et al., 2017; Hu et al., 2021; Li et al., 2015), but these effects are relatively small. Calcite generally exhibits lower (isotopically lighter) δ^{26}Mg values than dolomite. However, both calcite and dolomite are systematically depleted in heavy Mg isotopes compared to the source fluid or seawater (Hu et al., 2017; Huang et al., 2015; Li et al., 2015; Xia et al., 2024).

Marine carbonates serve as key archives for reconstructing past seawater chemistry and Earth system evolution (Chen et al., 2022; Li et al., 2020; Swart, 2015; Ahm et al., 2018; Banner and Hanson, 1990). Compared to marine limestones ($CaCO_3$, with limited Mg in their lattice), dolostones ($MgCa(CO_3)_2$) are less susceptible to post-depositional diagenetic overprinting. Consequently, dolomite is regarded as a more robust archive for tracing paleo-seawater δ^{26}Mg evolution through geological times (Bialik et al., 2018; Chanda and Fantle, 2017; Hu et al., 2017; 2019; Xia et al., 2024).

To validate these reconstructions, this study investigated mid-Cambrian marine carbonate and phosphate archives from the Georgina Basin in Australia. The Georgina Basin (in Northern

Territory and Queensland, Australia) contains widely distributed suite of Cambrian shallow marine carbonates including facies that can be attributed to restricted lagoons through epeiric shelf to ramp depositional systems (Ambrose et al., 2001; Smith et al., 2013). However, δ^{26}Mg in these Cambrian carbonate archives remains unstudied, despite their critical importance for paleo-seawater chemistry, including marine C and Mg cycling, as well as potential links to major Cambrian biotic diversification and extinction events. Although high-resolution ^{87}Sr/^{86}Sr analyses of Miaolingian carbonates have been conducted at multiple locations, these studies predominantly focus on carbonate phases (e.g., micrites and cements) while phosphatic microfossils such as small shelly fossils (SSFs), and linguliform brachiopods remain understudied (Chen et al., 2022; Peng et al., 2020). To address these gaps, this study couples ^{87}Sr/^{86}Sr data derived from the phosphatic linguliform brachiopods and SSFs with δ^{26}Mg, δ^{13}C and δ^{18}O records from the mid-Cambrian Wuliuan to Drumian (Australian late Ordian to Undillan stages) carbonates in the Georgina Basin. This study focuses on three drillholes from the central-northern Georgina Basin: Carrara 1 NDI (Australian National Drilling Initiative), NTGS01/1, and BNO4DD01. Integrated multi-proxy data, including δ^{26}Mg and ^{87}Sr/^{86}Sr isotopes, elemental geochemistry, and petrography, are used to constrain diagenetic processes and reconstruct mid-Cambrian seawater chemistry during the DICE event, while also assessing the influence of depositional environments, dolomitization mechanisms, and post-depositional alteration.

4.2 Geological Background

The Georgina Basin is located in the northeastern parts of the Centralian Superbasin, Australia, spanning across western Queensland (QLD) and into the central Northern Territory (NT), covering an area of approximately 3.3×10^5 km^2 (Fig. 1a; Dunster et al., 2007; Kruse et al., 2013; Walter et al., 1995). The Centralian Superbasin, a large polyphase intracratonic basin, evolved from the Neoproterozoic (ca. 850 Ma) to the mid-Paleozoic (ca. 450 Ma) (Pagès and Schmid, 2016; Walter et al., 1995). The basin's evolution was interrupted by the Petermann Orogeny (ca. 570–530 Ma), which created a sedimentary hiatus that divided it into two phases:

Centralian Superbasin A (pre-Petermann) and Centralian Superbasin B (post-Petermann) (Walter et al., 1995). The latter phase (Superbasin B) was ultimately terminated during the Alice Springs Orogeny (ca. 450 to 350 Ma) (Haines et al., 2001; Hand et al., 1999; Khider et al., 2021; Kruse et al., 2013; Nixon et al., 2022; Piazolo et al., 2020; Varga et al., 2022). In addition, the Georgina Basin is further divided into eight different structural belts. To the north, the Alexandria-Wonarah Block separates the Undilla Subbasin from the Central Subbasin. To the south, the Dulcie Syncline and Toko Syncline connect the Elkedra Shelf in the west to the Burke River Structure Belt in the east (Fig. 1a; Khider et al., 2021; Pagès et al., 2016; Smith et al., 2013). In the late Early Cambrian (Stage 4), following the eruption and emplacement of the Kalkarindji Large Igneous Province (LIP) at ca. 511 Ma (Glass and Phillips, 2006; Khider et al., 2021; Nixon et al., 2022), rift-related sedimentation resumed in the Georgina Basin, leading to subsequent deposition of platform carbonates of the mid-Cambrian Narpa Group (Fig. 1b; Kruse et al., 2013; Pagès and Schmid, 2016).

The Narpa Group comprises two depositional sequences (Fig. 1b; Southgate and Shergold, 1991). Sequence 1 (Ordian) consists of shallow-water peritidal marine carbonates, phosphorites, and siliciclastic rocks, represented by the Thortonia Limestone in the southern Georgina Basin (Holmes et al., 2025), which correlates with the lower Thorntonia Limestone and Border Waterhole Formation in the Undilla Subbasin, and Gum Ridge Formation in the Barkly Subbasin (Fig. 1b). Sequence 2 (latest Ordian–Mindyallan), the primary focus of this study, represents a transgressive phase characterized by deeper marine carbonaceous black shales and marine carbonates of the Arthur Creek Formation in southern depocenters, with a greater proportion of siliciclastic rocks. This sequence is correlated with the upper Thorntonia Limestone, Wonarah Formation, Inca Formation, Ranken Formation, Currant Bush Limestone, and Camooweal Formation in the Undilla Subbasin, as well as the Anthony Lagoon Formation in the Barkly Subbasin (Kruse et al., 2013).

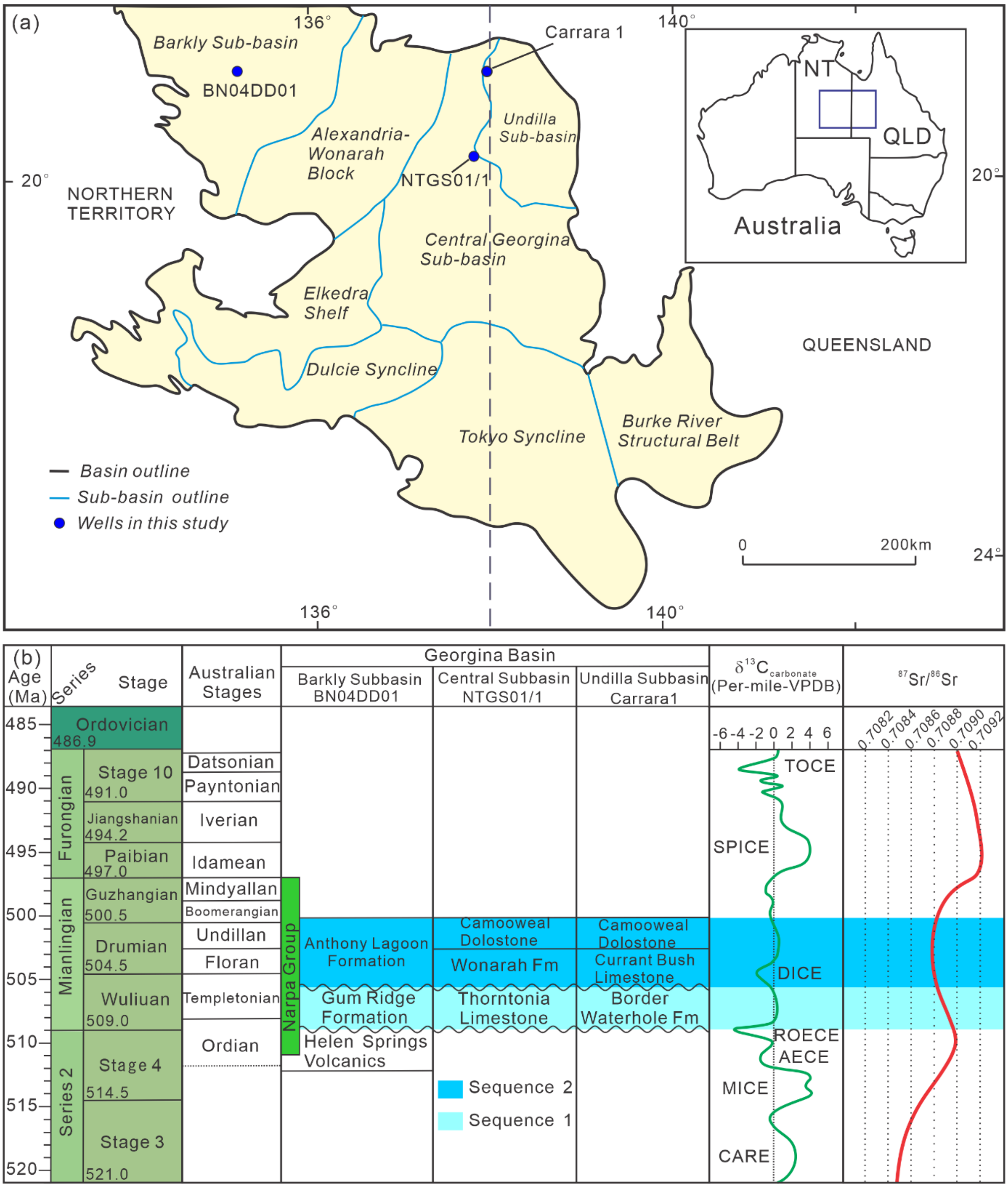

Figure 1. (**a**) Location of the Georgina Basin in Australia (NT and QLD), with solid blue circles marking the locations of the studied wells (adapted from Kruse et al., 2013; Walter et al., 1995); (**b**) Stratigraphy of the Middle Cambrian Narpa Group in the studied wells, with sampled intervals shaded in blue (adapted from Laurie, 2022; Pagès and Schmid, 2016; Smith et al., 2013). The $\delta^{13}C$ isotope curve (green) with major C isotope anomalies (including DICE) is adapted from Peng et al. (2020), and the marine $^{87}Sr/^{86}Sr$ curve (red) is from Chen et al. (2022).

A euxinic marine depositional environment is recognized at the base of Sequence 2, coinciding with the DICE event and the onset of the Drumian Stage (Pagès and Schmid, 2016; Pagès et al., 2016). The fossil record includes a diverse assemblage of small shelly fossils (SSFs) within the Cambrian sequences of the Georgina Basin, comprising trilobites, brachiopods, molluscs, echinoderms, archaeocopids, sponge spicules, hyoliths, and algae (Laurie, 2012; Pagès et al., 2016). Extensive biostratigraphic studies of Cambrian Series 2 and 3 of the Georgina Basin and other Australian basins have been published (Betts et al., 2016, 2017, 2018; Birksmith et al., 2025; Castle-Jones et al., 2025; Laurie, 2004; 2005, 2006, 2012, 2022; Öpik, 1968; Öpik, 1975; Öpik, 1979; Southgate and Shergold, 1991). Recent updates to the biostratigraphic subdivision at the Ordian–Templetonian boundary within the Series 2–Miaolingian interval, based on SSFs and $\delta^{13}C/\delta^{18}O$ chemostratigraphy, have been proposed by Holmes et al. (2025) and Laurie et al. (2024). In the Carrara 1 NDI drillhole, the upper Border Waterhole Formation is assigned to the Templetonian Stage, while the Currant Bush Limestone spans from the late Templetonian Zone to the late Floran Zones (Fig. 1b; Laurie, 2022). A specimen of *Xystridura lauta* (Öpik, 1975) was discovered at the base of the Wonarah Formation in the NTGS01/1, confirming its Templetonian age (Fig. 1b; Laurie, 2004). Additionally, *Redlichia forresti* was reported from the base of the Gum Ridge Formation in the BN04DD01 drillhole, indicating a latest Ordian age (Fig. 1b; Holmes et al., 2025; Kruse et al., 2004; Laurie, 2024).

4.3 Materials and Methods

4.3.1 Sampled Materials

This study analyzed a total of 230 samples from the Georgina Basin, including 212 carbonate samples collected for stable C and O isotope analysis, 51 carbonates for stable Mg isotope analysis (including 3 duplicates), and 18 phosphatic fossil samples analyzed for the radiogenic Sr isotope analysis. Specifically, from the Carrara 1 NDI well, 10 fossil-rich samples were collected for $^{87}Sr/^{86}Sr$ analysis, and 14 samples for $\delta^{26}Mg$ analysis (Fig. 4). In NTGS01/1 well, 106 samples were analyzed for $\delta^{13}C$ and $\delta^{18}O$ values, 7 fossil-rich samples for $^{87}Sr/^{86}Sr$, and 23 samples for $\delta^{26}Mg$ analysis (Fig. 5). In BN04DD01 well, 106 samples were analyzed for $\delta^{13}C$

and $\delta^{18}O$, 1 fossil-rich sample for $^{87}Sr/^{86}Sr$, and 14 samples for $\delta^{26}Mg$ values (Fig. 6). Additionally, a dataset of 107 previously reported and analyzed samples from Carrara 1 well was compiled from the literature, including C, O and Sr isotope data (Carson et al., 2023), quantitative X-ray diffraction (XRD) data (Carson et al., 2022), carbonate elemental composition data (Carson et al., 2021), and total organic carbon (TOC) data (Butcher et al., 2021). All datasets are provided in Supplementary Table S1.

4.3.2 Carbon ($\delta^{13}C$) and Oxygen ($\delta^{18}O$) Isotope Analysis of Carbonates via IRMS

A total of 212 carbonate samples from NTGS01/1 and BN04DD01 were micro-drilled into powder and weighed into vials. Each vial was purged using He gas and then reacted with 105% phosphoric acid (H_3PO_4) at 70 °C for approximately two hours. The evolved CO_2 was analyzed for carbon and oxygen isotopes ($\delta^{13}C$ and $\delta^{18}O$) using a Nu Instruments Horizon - Isotope Ratio Mass Spectrometer (IRMS) in continuous flow mode, with in-line GasPrep carbonate preparation system at the University of Adelaide. Isotopic measurements were calibrated against the Vienna Pee Dee Belemnite (VPDB) standard and are reported in delta (δ) notation, as per mil (‰) variations, relative to VPDB:

$$\delta^{13}C = [(^{13}C/^{12}C)_{sample}/(^{13}C/^{12}C)_{standard} - 1] \times 1000\text{; and}$$

$$\delta^{18}O = [(^{18}O/^{16}O)_{sample}/(^{18}O/^{16}O)_{standard} - 1] \times 1000$$

Internal standards ANU-P3 ($\delta^{13}C = +2.24‰$, $\delta^{18}O = -0.32‰$) and UAC ($\delta^{13}C = -15.00‰$, $\delta^{18}O = -18.40‰$) were used to monitor the accuracy and reproducibility, complemented also by additional in-house reference materials CO-8 and NBS 19 to assess data quality. Based on these assessments, the analytical precision via IRMS is better than ± 0.05‰ (1SD) for both $\delta^{13}C$ and $\delta^{18}O$. All isotopic data are presented in Supplementary Table S2.

4.3.3 Strontium Isotope ($^{87}Sr/^{86}Sr$) Analysis of Phosphates via TIMS/ATONA

A total of 18 phosphatic fossil samples, mainly comprising phosphatic linguliform brachiopods and some SSFs, were analyzed for $^{87}Sr/^{86}Sr$ ratios, with 10 samples from Carrara 1, 7 from NTGS01/1, and 1 from BN04DD01. Detailed isotope data and SEM images from these fossil samples are provided in Supplementary Table S2 and Fig. S1.

Sample preparation was carried out in the Acid Leaching Facility (ALF) associated with the sedimentological/paleontological laboratories at Macquarie University. Briefly, the fossiliferous samples were first leached in 10% acetic acid for one week to completely dissolve the carbonate matrix and associated inclusions, then rinsed with deionised (DI) water, dried, and sieved using a 64 µm mesh. Larger fossils or phosphatic fragments were subsequently manually picked under a microscope for SEM and energy dispersive X-ray spectroscopy (EDS) analysis and imaging following the approaches used by Liu et al. (2022). Selected fossil shells or fragments were cleaned three times in an ultrasonic bath using ethanol and then leached with 0.5% acetic acid to remove clays and/or other minerals attached to the fossil surfaces. EDS was performed before and after this cleaning stage to check the effectiveness, with the resulting images and elemental spectra of the cleaned fossils shown in Supplementary Figs. S1–2. For digestion, approximately 2 mg of cleaned material was reacted with ultrapure 6 N HCl in Teflon vials on a hotplate at a 130°C until complete dissolution, followed by centrifugation to remove insoluble residues. Sr was purified from the phosphatic matrix using a conventional column chromatography system with Sr-Spec resin in HNO_3, and Milli-Q water (Krabbenhoft et al., 2009).

The $^{87}Sr/^{86}Sr$ measurements of the phosphate and carbonate samples were conducted using an IsotopX Phoenix Thermal Ionization Mass Spectrometer (TIMS), equipped with an ATONA signal amplification system, at the University of Adelaide, with reproducibility better than 0.000005 (2σ). Standard materials SRM987 and JCP-1 (carbonate) were included in each TIMS analytical session. SRM987 gave an $^{87}Sr/^{86}Sr$ ratio of 0.710260 ± 0.000001 (SD, n = 2), while JCP-1 yielded 0.70917 ± 0.000005, both of which agree with the published $^{87}Sr/^{86}Sr$ values for these standard materials (Krabbenhoft et al., 2009).

4.3.4 Magnesium Isotope ($\delta^{26}Mg$) and Elemental Analysis of Carbonates via ICP-MS

A total of 54 bulk rock carbonate samples (14 from Carrara 1, 23 from NTGS01/1, and 14 from BN04DD01), plus 3 duplicate samples for quality control, were used for elemental and Mg isotope analyses via ICP-MS instruments. Sample preparation followed established protocols

(Chen et al., 2020; Li et al., 2012; Ning et al., 2020), where ca. 30–50 mg of powdered carbonate samples were dissolved in 10 mL of suprapure 0.5 N acetic acid and shaken for ca. 12 hours. After centrifugation, 8 mL of supernatant was aliquoted for separate elemental and isotopic analyses. Major and trace element concentrations were determined using a Thermo Scientific iCAP TQ triple-quadrupole ICP-MS, with samples diluted in 2% HNO_3 and quantified against reference materials. Analytical precision for all elements was better than 5% (1σ).

For Mg isotope analysis via MC-ICP-MS, the Mg fraction was purified from the carbonate matrix following the procedures outlined by Li et al. (2012). Briefly, aliquots containing approximately 30 μg of Mg were purified through ion-exchange columns in three stages. Stage 1 used Bio-Rad AG MP-50 resin (100–200 mesh) with a column of 6.25 mm inner diameter and 93 mm resin height; Stage 2 used Bio-Rad AG MP-50 resin (100–200 mesh) with a column of 4.9 mm inner diameter and 18.5 mm resin height; and Stage 3 used Bio-Rad AG 50W×8 resin (200–400 mesh) with a column of 4.9 mm inner diameter and 18.5 mm resin height. Detailed procedures are provided in Table 2 of Chapter 3.

The Mg isotope composition (δ^{26}Mg values) of the purified Mg fractions was measured using a Nu Sapphire multi-collector inductively coupled plasma mass spectrometer (MC-ICP-MS). Instrumental mass bias during Mg isotope measurements was corrected using a standard-sample-standard bracketing approach, with the DSM3 standard employed for δ-normalization. Mg isotope data are presented as the δ-notation: $\delta^{x}\mathrm{Mg} = [(^{X}\mathrm{Mg}/^{24}\mathrm{Mg})_{\mathrm{sample}}/(^{X}\mathrm{Mg}/^{24}\mathrm{Mg})_{\mathrm{DSM3}} - 1] \times 1000$, where x = 25 or 26. All Mg isotope data (δ^{26}Mg) presented in this study are reported with 2 standard deviations (2SD) uncertainty. External standards (seawater, Cambridge-1, AGV-2a, BHVO-2, and JDo-1) were analyzed to verify data quality and analytical precision. The average δ^{26}Mg values for these standards are: -2.61 ± 0.06‰ (n = 26) for Cambridge-1, -0.79 ± 0.08‰ (n = 20) for seawater, -0.18 ± 0.04‰ (n = 8) for AGV-2a, -0.19 ± 0.06‰ (n = 4) for BHVO-2, and -2.32 ± 0.06‰ (n = 4) for JDo-1. These δ^{26}Mg values are all consistent within uncertainties with those reported for these standards in previous studies (Gao et al., 2018; Harrison et al., 2021; Huang et al., 2018; Ling et al., 2011; Shalev et al., 2018). All analyzed

δ^{26}Mg data for the standards and samples are provided in Supplementary Tables S3–S4.

4.4 Results

4.4.1 Petrography and Mineralogy

In the Carrara 1 NDI drillhole (Undilla Subbasin), the Border Waterhole Formation was deposited during the development of Sequence 1 strata (Southgate and Shergold, 1991) and is primarily composed of dolostone, chertified limestone, marl, and siltstone (Fig. 2a). The conformably overlying Currant Bush Limestone corresponds to transgressive early Sequence 2 packages (Southgate and Shergold, 1991), consisting mainly of bioclastic limestone, shaly limestone, ooid grainstone and marl, interbedded with dolomitic limestone and siltstone. This succession contains abundant SSFs and exhibits an increased proportion of siliciclastic components (Figs. 2b–c; Kruse et al., 2013; Pagès and Schmid, 2016). The Camooweal Dolostone, corresponding to late Sequence 2, is dominated by a high proportion of dolomite minerals and dolomitized components, as illustrated in Fig. 4.

In the NTGS01/1 drillhole from the Central Subbasin, the Thorntonia Limestone (Sequence 1) is primarily composed of chertified limestone, dolomitic limestone, dolostone, pyritic-carbonaceous dolostone, mudstone, siltstone, marl, phosphorite, and stromatolites (Fig. 2d). The Wonarah Formation (early Sequence 2) comprises dolostone, calcareous to dolomitic mudstone, phosphorite, and siltstone (Fig. 2e). The overlying Camooweal Dolostone (late Sequence 2) includes dolostone, ooid and oncoid dolostone, dolomitic limestone, and shaly mudstone (Fig. 2f).

Core recovered from the BN04DD01 well in the Barkly Subbasin includes the Gum Ridge Formation (Sequence 1), which mainly consists of dolomitic limestone, dolostone, and silty mudstone (Figs. 2g–h). The overlying Anthony Lagoon Formation (Sequence 2) is primarily composed of reddish shale, dolomitic siltstone interbedded with dolostone, and nodular and bedded evaporites (Fig. 2i).

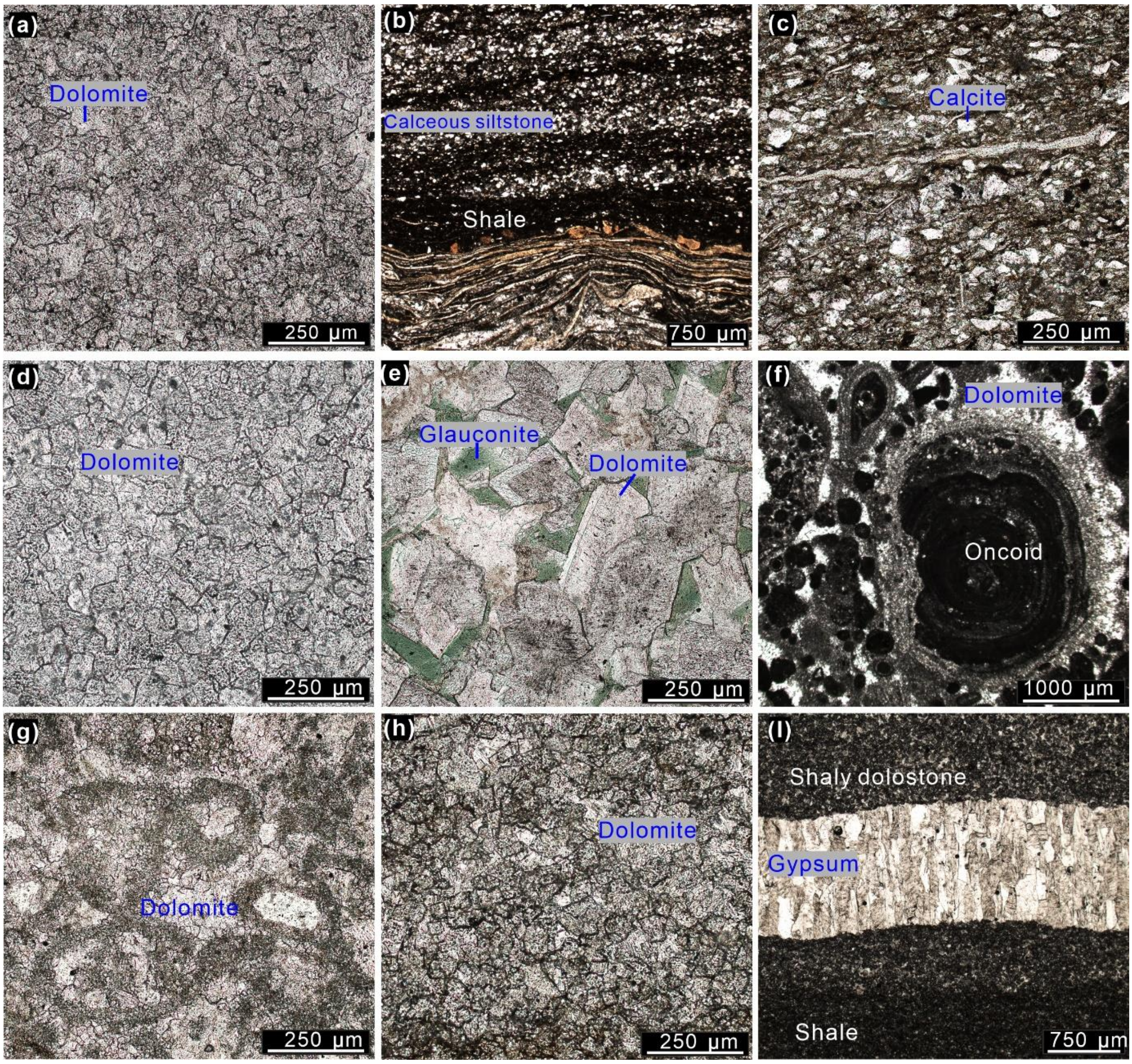

Figure 2. Photomicrographs of thin-sections (in transmitted light) showing representative petrographic and mineralogical features of the studied mid-Cambrian samples from the Georgina Basin. (**a**) Fine- to medium-grained dolostone from Carrara 1 (585.62 m, Border Waterhole Formation); (**b**) Thinly interbedded shale, siltstone, and calcareous siltstone with abundant fossil fragments, predominantly trilobites (Carrara 1, 405.95 m, Current Bush Limestone); (**c**) Argillaceous fine-grained limestone with fossil fragments (Carrara1, 350.2 m, Currant Bush Limestone); (**d**) Medium crystalline dolostone (NTGS01/1, 365.3 m, Thorntonia Limestone); (**e**) Coarse recrystallized dolomite with cloudy cores and bright rims, and abundant glauconite (NTGS01/1, 183.7 m, Wonarah Formation); (**f**) Sparry oncoid dolostone, featuring microbial concentric laminations in oncoids, grain-supported (NTGS01/1, 124.8 m, Camooweal Dolostone); (**g**) Sparry peloid dolostone with recrystallized dolomite cores in

peloids (BN04DD01, 380.7 m, Gum Ridge Formation); (**h**) Fine- to medium-grained dolostone (BN04DD01, 310.0 m, Gum Ridge Formation); (**i**) Shale interbedded with shaly dolostone and gypsum (BN04DD01, 202.42 m, Anthony Lagoon Formation).

In general, the dolomite phases in the studied mid-Cambrian samples from the Georgina Basin can be categorized into three groups or types based on dolomite crystal size: finely crystalline (< 100 µm), medium crystalline (100–200 µm), and coarsely crystalline dolomite (> 200 µm). Finely crystalline dolomite is mainly found in the Currant Bush Limestone, Anthony Lagoon Formation, and Gum Ridge Formation, while medium to coarsely crystalline dolomite is primarily present in the Camooweal Dolostone, Wonarah Formation, and Thorntonia Limestone. Glauconite (Fe- and K-rich authigenic clay) occurs commonly throughout the studied intervals, with the Wonarah Formation showing the highest abundance (Fig. 2e). Pyrite is also prevalent, particularly in organic-rich layers, occurring as very fine-grained crystals at the micrometer scale.

4.4.2 $\delta^{13}C$ and $\delta^{18}O$ Variations in Mid-Cambrian Carbonates from the Georgina Basin

Across the three wells studied, the analyzed carbonate $\delta^{13}C$ values range from -3.89‰ to +3.85‰, while the $\delta^{18}O$ values range from -13.8‰ to -3.52‰ (Fig. 3a; Supplementary Material, File S2). Specifically, in Carrara 1, the $\delta^{13}C$ values range from -2.41‰ to +3.27‰, with $\delta^{18}O$ values between -9.36‰ and -3.99‰ (Fig. 4). In NTGS01/1, $\delta^{13}C$ values range from -3.89‰ to +1.77‰, and $\delta^{18}O$ from -9.89‰ to -4.55‰ (Fig. 5). In BN04DD01, $\delta^{13}C$ values range from -3.06‰ to +3.85‰, and $\delta^{18}O$ values range from -9.89‰ to -3.52‰ (Fig. 6).

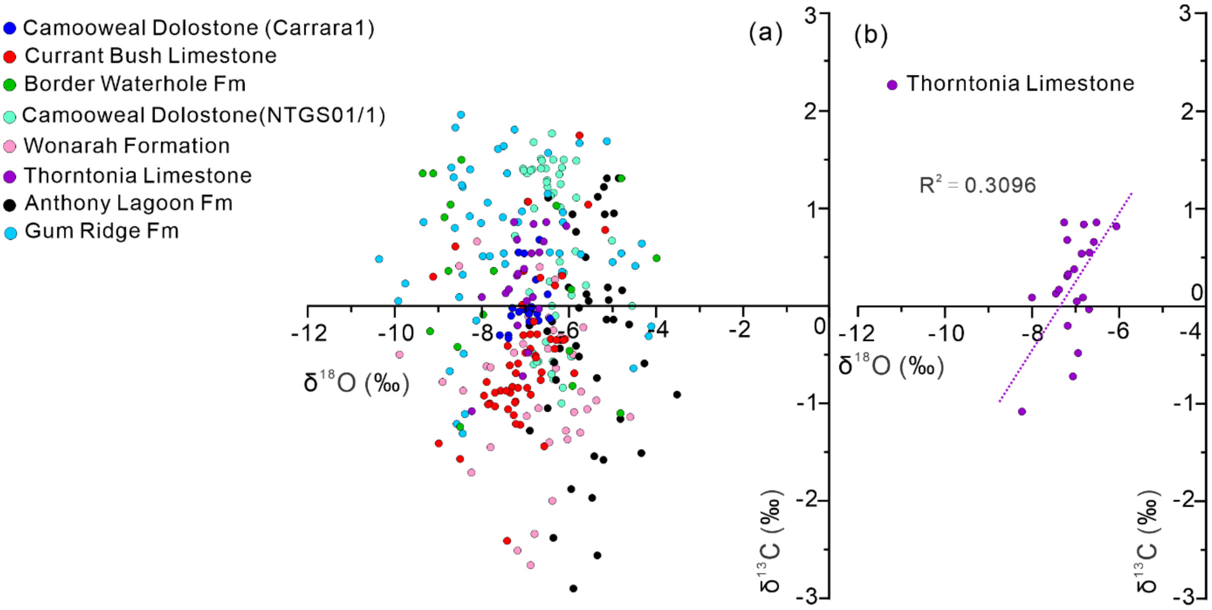

Figure 3. Cross plots of $\delta^{13}C$ and $\delta^{18}O$ values from the mid-Cambrian carbonates of the Georgina Basin (**a**) Compilation of $\delta^{13}C$ and $\delta^{18}O$ from three drillholes (Carrara 1, NTGS01/1, and BN04DD01), with data points color-coded by formation; (**b**) Cross plot of carbonate $\delta^{13}C$ vs. $\delta^{18}O$ data from the Thorntonia Limestone in NTGS01/1. Note that data from Carrara 1 are sourced from Carson et al. (2023).

No statistically significant correlation exists between $\delta^{13}C$ and $\delta^{18}O$ values across most of the analyzed samples or formations, except in data from the Thorntonia Limestone (from NTGS01/1), which shows a weak positive correlation (Fig. 3b). In contrast, the Border Waterhole Formation displays a highly variable and noisy relationship between $\delta^{13}C$ and $\delta^{18}O$ data, with large fluctuations and generally more negative $\delta^{18}O$ values (below -7‰) (Fig. 4). A similar pattern occurs in the lower part of the Gum Ridge Formation, where both $\delta^{13}C$ and $\delta^{18}O$ values fluctuate significantly, and $\delta^{18}O$ values consistently fall below -8‰ (Fig. 6).

Importantly, a distinct and pronounced negative $\delta^{13}C$ excursion (interpreted as the DICE event) with a magnitude of approximately -3‰ has been identified in all three drillholes (Figs. 4–6). In Carrara 1, the DICE is recorded within the 247–363 m interval of the Currant Bush Limestone; in NTGS01/1, it spans from 177 m to 297 m in the Wonarah Formation; and in BN04DD01, it is observed between 108 m and 190 m in the Anthony Lagoon Formation (Figs. 4–6). Additionally, a positive $\delta^{13}C$ excursion of approximately +2.5‰ is identified in the

Currant Bush Limestone of Carrara 1 between 385–425 m, coinciding with elevated TOC content in this interval (Fig. 4). Similar positive $\delta^{13}C$ excursions, preceding the DICE, are also observed in NTGS01/1 and BN04DD01, spanning 300–320 m in the Wonarah Formation and 238–300 m across the Gum Ridge and Anthony Lagoon Formations, respectively (Figs. 5–6).

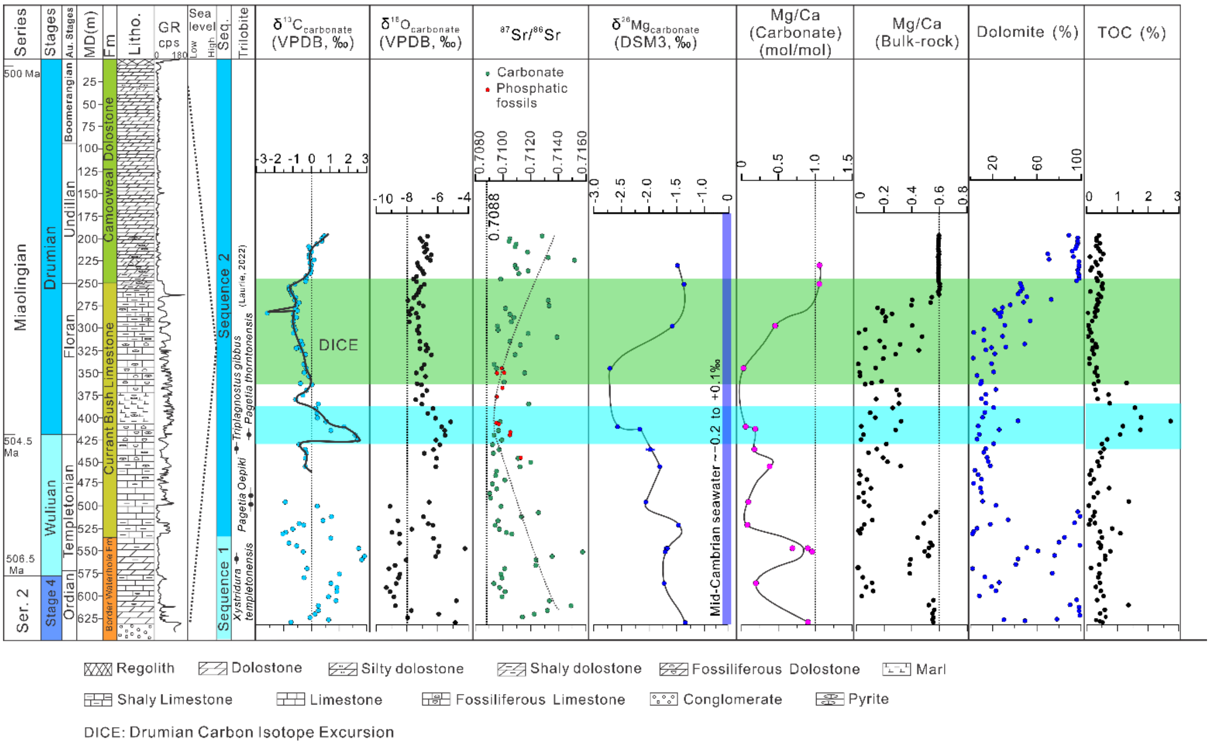

Figure 4. Compiled lithology and isotope/elemental chemostratigraphy data from the Carrara 1 drillhole. The lithostratigraphic column modified from Bailey et al. (2022). $\delta^{26}Mg$ data are from this study, and $\delta^{13}C$, $\delta^{18}O$, and $^{87}Sr/^{86}Sr$ data are from Carson et al. (2023); bulk-rock elemental data (Mg/Ca) are from Carson et al. (2021); dolomite fractions (%, in carbonate rocks) are from Carson et al. (2022); and TOC data are from Butcher et al. (2021).

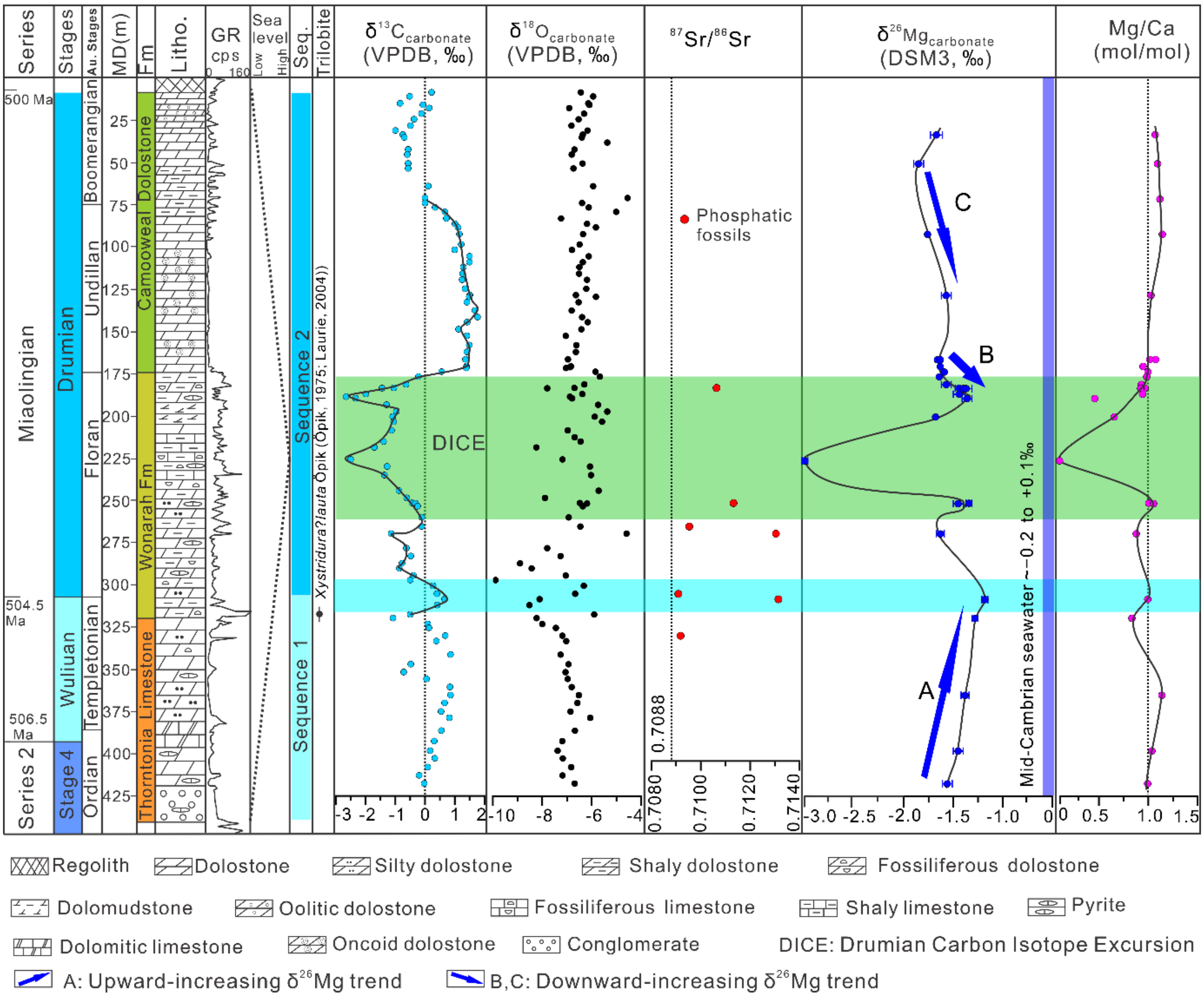

Figure 5. Lithology and chemostratigraphy data from the NTGS01/1 drillhole, including $\delta^{13}C$, $\delta^{18}O$, $^{87}Sr/^{86}Sr$, and $\delta^{26}Mg$ isotope data, along with elemental Mg/Ca ratios (all produced in this study). The lithology column is modified from Kruse (2008).

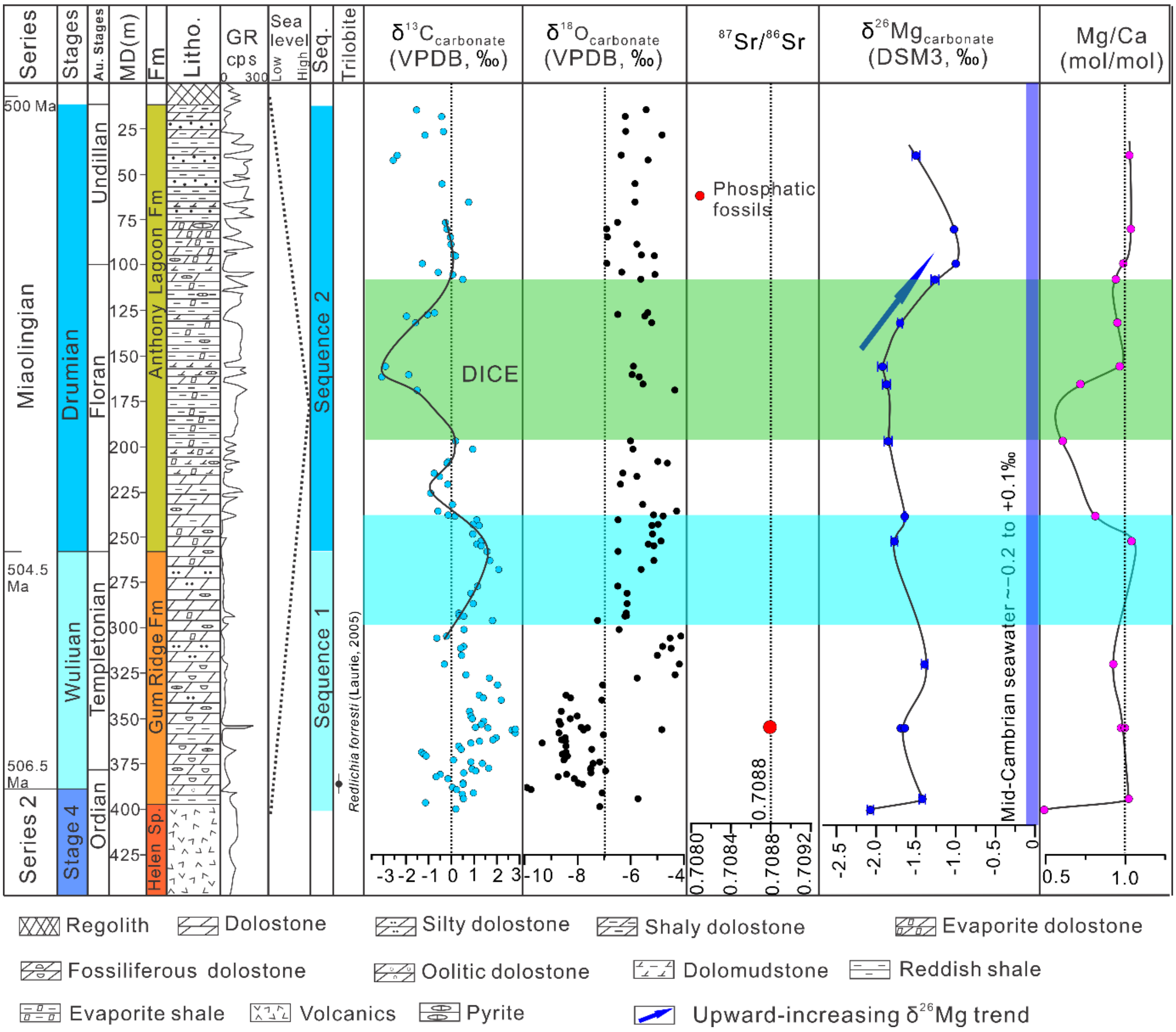

Figure 6. Lithology and chemostratigraphy data from the BN04DD01 drillcore, including $\delta^{13}C$, $\delta^{18}O$, $^{87}Sr/^{86}Sr$, and $\delta^{26}Mg$ isotope data, along with Mg/Ca elemental ratios (all produced in this study). The lithology column is modified from Kruse (2008).

4.4.3 Strontium Isotope ($^{87}Sr/^{86}Sr$) Variations in the Mid-Cambrian Carbonates and Fossil Phosphates (SSFs)

Carbonate $^{87}Sr/^{86}Sr$ data were exclusively collected from Carrara 1, showing significant variations ranging from 0.70903 to 0.73615 (Fig. 4; Supplementary Table S1). These values differ from the expected mid-Cambrian seawater range of ~0.70880 to ~0.70900 (Chen et al., 2022; Peng et al., 2020). The acquired $^{87}Sr/^{86}Sr$ data correlate with the lithology across different formations. Specifically, the Currant Bush Limestone (early Sequence 2), primarily composed of relatively pure limestone (calcite), exhibits lower or less radiogenic $^{87}Sr/^{86}Sr$ values, with some measurements actually closely matching the mid-Cambrian paleo-seawater values, particularly at depths of 420–430 m and 480–490 m. In contrast, the Border Waterhole Formation (Sequence 1) and the Camooweal Dolostone (late Sequence 2), dominated by dolomite mineralogy, show elevated and more radiogenic $^{87}Sr/^{86}Sr$ ratios. This observed lithological control and correlation with Sr isotopes, is further supported by the relationship between $^{87}Sr/^{86}Sr$ and Mg/Ca ratios, where higher Mg/Ca (more dolomitized samples) tend to yield higher $^{87}Sr/^{86}Sr$ values (Fig. 4).

The $^{87}Sr/^{86}Sr$ data from phosphatic linguliform brachiopods and SSFs also display considerable variations, ranging from ~0.70879 to ~0.71314 (Figs. 4–6). Although most samples exhibit higher or more radiogenic $^{87}Sr/^{86}Sr$ signatures (above the expected value for the mid-Cambrian seawater), a sample from BN04DD01 (depth of 355.1 m) in the Gum Ridge Formation yields a value of 0.70879, which aligns closely with the mid-Cambrian seawater range. Similarly, a sample from NTGS01/1 at a depth of 305.3 m in the Wonarah Formation produced a marine or close-to-marine $^{87}Sr/^{86}Sr$ value of 0.70909 (Chen et al., 2022; Peng et al., 2020).

4.4.4 Magnesium Isotope ($\delta^{26}Mg$) Variations in Mid-Cambrian Carbonates from the Georgina Basin

The studied carbonate samples yielded $\delta^{26}Mg$ data that range from -3.05‰ to -1.00‰, showing an overall isotope offset of approximately 2.05‰ between calcite/limestone and dolomite/dolostone (Supplementary Table S4). In Carrara 1, $\delta^{26}Mg$ values range from -2.71‰ to -1.37‰ (Fig. 4), which are, on average, lower (isotopically lighter) than the Mg isotope data from NTGS01/1 and BN04DD01. Carbonates from NTGS01/1 exhibit $\delta^{26}Mg$ values ranging from -3.05‰ to -1.18‰ (Fig. 5), while samples from BN04DD01 show $\delta^{26}Mg$ values between -2.20‰ and -1.00‰ (Fig. 6).

Notably, $\delta^{26}Mg$ values in Carrara 1 carbonates show a statistically significant positive correlation with the Mg/Ca (mol/mol) ratios, where more dolomitized samples (higher Mg/Ca) display heavier (higher) $\delta^{26}Mg$ values (Fig. 4). A similar trend is observed in NTGS01/1 carbonates within the Wonarah Formation, where the most negative $\delta^{26}Mg$ value of -3.05‰ (at

225.8 m depth) corresponds to the lowest Mg/Ca (mol/mol) ratio of ~0.024 (Figs. 5, 11). However, this correlation is less pronounced in carbonates from BN04DD01 and NTGS01/1 drill cores (e.g., Camooweal Dolostone), where dolostone samples with molar Mg/Ca ratios of ~1 exhibit highly variable δ^{26}Mg values ranging from -2.20‰ to -1.00‰ (Figs. 5–6). Additionally, two monotonic decreases in δ^{26}Mg values are observed in NTGS01/1 carbonates at depths of 50–130 m and 166–189 m, while a gradual increase is seen between 308 m and 417 m (Fig. 5). A similar monotonic increase in δ^{26}Mg is observed in dolomite from BN04DD01 between 100 m and 156 m (Fig. 6).

4.5 Discussion

4.5.1 Sedimentary Environment Reconstruction

Following the Kalkarindji volcanic event (~511 Ma, Glass and Phillips, 2006; Khider et al., 2021; Nixon et al., 2022), a phase of rapid thermal subsidence driven by post-volcanic lithospheric cooling triggered a major marine transgression across northern Australia (Bradshaw et al., 2021; Munson et al., 2013). In the Georgina Basin, this mid-Cambrian transgression established a southeast–northwest trending seaway, resulting in the deposition of Sequence 1, preserved in the mid-Cambrian Narpa Group (Pagès and Schmid, 2016; Southgate and Shergold, 1991). Sequence 1 comprises platform to shallow marine carbonates, represented by the Border Waterhole Formation in the Undilla Subbasin and the Thorntonia Limestone in the Central Subbasin (Figs. 4–5, 7a), as well as restricted lagoonal to shallow marine deposits of the Gum Ridge Formation in BN04DD01 within the Barkly Subbasin (Figs. 6, 9a; Kruse, 2013). In the southern Georgina Basin, Sequence 1 is characterized by slope to basinal limestone, shale, and turbidites within the Dulcie and Toko Synclines (Munson, 2014).

Transgressional early Sequence 2 (Currant Bush Limestone, Wonarah Formation, and lower Anthony Lagoon Formation) overlies Sequence 1 either conformably or unconformably and is characterized by mixed marine carbonate–siliciclastic deposition (Kruse et al., 2013; Southgate and Shergold, 1991). In Carrara 1, the Currant Bush Limestone comprises limestone, fine-grained shale, and siltstone, indicating deposition in a deeper marine slope environment (Figs.

4, 9b). In NTGS01/1, the Wonarah Formation consists of subtidal to shallow marine muddy limestone, dolostone, and phosphorite (Figs. 5, 9b; Kruse, 2013). In BN04DD01, the lower part of the Anthony Lagoon Formation is dominated by tidal flat shaly dolostone interbedded with siltstone (Figs. 6, 9b).

Following a sea-level fall, carbonate platforms re-emerged in the Undilla and Central Subbasins (Pagès and Schmid, 2016). In these areas, peritidal to restricted marine dolostone, oolites, and oncoids were deposited within the Camooweal Formation, as recorded in Carrara 1 and NTGS01/1 (Figs. 4–5, 7c). In the Barkly Subbasin, the upper Anthony Lagoon Formation is characterized by lagoonal to supratidal, thinly bedded silty shale and evaporite deposits (Figs. 6, 9c).

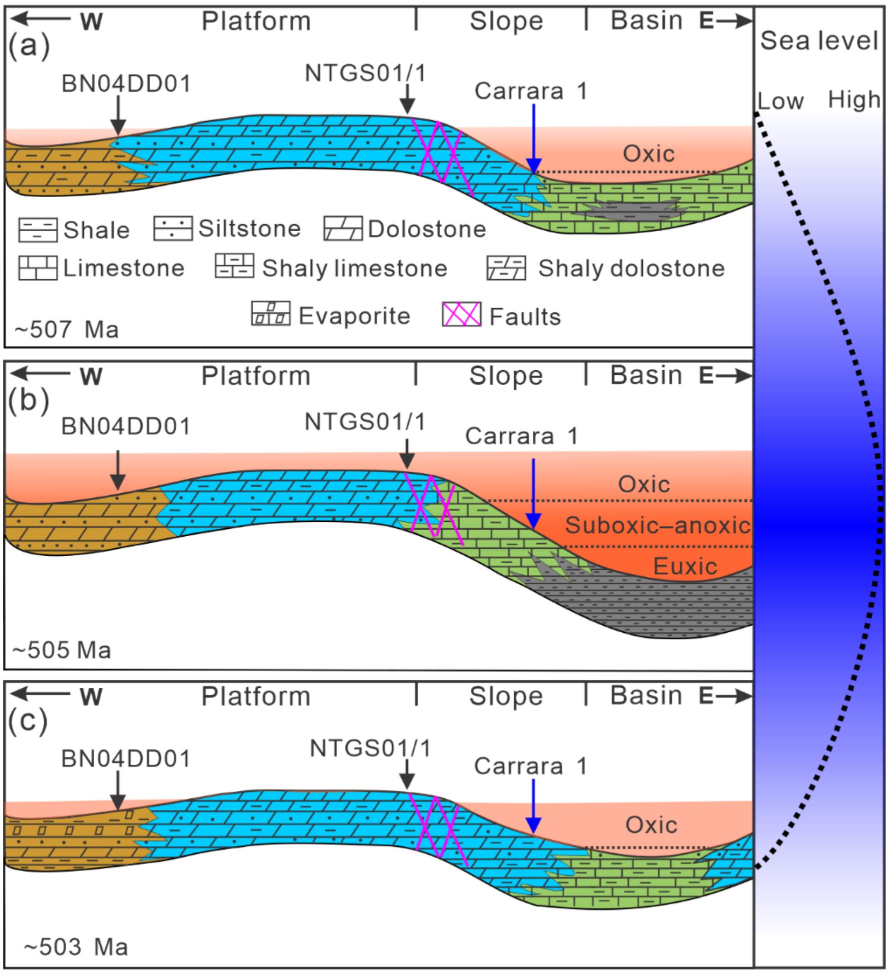

Figure 7. Schematic representation of the paleoenvironmental evolution during the Miaolingian deposition of the Narpa Group in the Georgina Basin, from BN04DD01 in the

Barkly Subbasin, through NTGS01/1 in the Central Subbasin, to Carrara 1 in the Undilla Subbasin. (**a**) Sequence 1 (~507 Ma): peritidal to semi-restricted, shallow marine deposition during a sea-level lowstand; (**b**) early Sequence 2 (~505 Ma): transgressive platform carbonates to deep marine deposition during a sea-level highstand; (**c**) late Sequence 2 (~503 Ma): peritidal to restricted marine settings during a sea-level fall.

4.5.2 Impact of Diagenesis on Carbonate $\delta^{13}C$, $\delta^{18}O$, $\delta^{26}Mg$ and $^{87}Sr/^{86}Sr$ Isotope Proxies

The covariation between carbon and oxygen isotopes in marine carbonates has conventionally served as a diagnostic indicator of diagenetic alteration (Banner and Hanson, 1990). In this study, a positive correlation between $\delta^{13}C$ and $\delta^{18}O$ data is observed only in the Thorntonia Limestone from drillhole NTGS01/1 ($R^2 = 0.3096$; Fig. 3b). This pattern potentially reflects either meteoric diagenesis during subaerial exposure or burial–hydrothermal alteration processes (Allan and Matthews, 1982; Chen et al., 2024; Derry, 2010; Kaufman and Knoll, 1995; Li et al., 2020; Swart and Eberli, 2005). In addition, significant and high-frequency variations in both $\delta^{13}C$ and $\delta^{18}O$ data observed within the Border Waterhole Formation (Carrara 1) further support possible diagenetic overprinting (Fig. 4). Similarly, the generally low (less than -8‰) and more scattered $\delta^{18}O$ values in the Gum Ridge Formation also indicate diagenetic modification and resetting (Fig. 6). All three formations—Thorntonia Limestone, Border Waterhole Formation, and Gum Ridge Formation—belong to Sequence 1 and display consistent evidence of deeper burial, likely resulting in more intense diagenetic alteration or possible meteoric modification during early exposure phases. Among the carbon and oxygen isotope systems, $\delta^{18}O$ in marine carbonates appears to be more sensitive to diagenetic resetting than the $\delta^{13}C$ proxy, consistent with theories and water-rock interaction models (Derry, 2010; Kaufman and Knoll, 1995; Li et al., 2020; Swart and Eberli, 2005; Zhang et al., 2022; Zhang et al., 2023). Hence, the $\delta^{13}C$ record of the mid-Cambrian carbonates from the Georgina Basin—particularly in the less altered Sequence 2 formations—appears to be predominantly well preserved, likely retaining their primary marine or depositional $\delta^{13}C$ signatures with minimal overprinting. To further validate these interpretations, other geochemical indices for diagenetic alteration of marine carbonates, such as elemental ratios or additional isotope proxies, are discussed in the sections below.

The Mn/Sr ratio is another useful tool for assessing the preservation of primary marine carbonate isotopic signals, as diagenetic alteration by non-marine or burial fluids typically enriches Mn and depletes Sr in progressively altered carbonates (Banner and Hanson, 1990; Brand and Veizer, 1980; Chang et al., 2017; Chen et al., 2022; Zhang et al., 2022; Zhang et al., 2023). In this study, Mn/Sr ratios in the mid-Cambrian carbonates range from 0.09 to 50.16, with an average of 6.03 (Figs. 8a–c). Although $\delta^{13}C$ data do not show a systematic correlation with Mn/Sr ratios, even within presumably more altered Sequence 1 units, these units generally exhibit higher Mn/Sr values (> 2) compared to Sequence 2. These findings collectively demonstrate that Sequence 2 carbonates retain more pristine $\delta^{13}C$ signatures, providing a more reliable record of Cambrian seawater isotopic composition.

Low-Mg calcitic (LMC) carbonates, or marine LMC limestones, are generally considered less susceptible to post-depositional diagenetic alteration compared to high-Mg calcite (HMC) or aragonite counterparts, which are more prone to recrystallization and thus diagenetic modification (Brand and Veizer, 1982; Ahm et al., 2018). Consequently, both marine LMC deposits and potentially primary marine dolomites are more likely to preserve the original $\delta^{26}Mg$ signatures of paleo-seawater or dolomitizing fluids (Bialik et al., 2018; Hu et al., 2019; Hu et al., 2017; Huang et al., 2015; Ning et al., 2019; Ning et al., 2020; Xia et al., 2024). In the studied mid-Cambrian carbonates, $\delta^{26}Mg$ values show no systematic correlation with Mn/Sr ratios (Fig. 8b) or $\delta^{13}C$ data (Fig. 8d), suggesting that the $\delta^{26}Mg$ signatures are relatively well preserved and not significantly affected by burial diagenesis. A more detailed discussion of the $\delta^{26}Mg$ dataset is provided in Section 4.5.4.

As a trace element in marine carbonates, Sr and its radiogenic isotope system ($^{87}Sr/^{86}Sr$) are particularly susceptible to diagenetic alteration. This is supported by results from this study: although a few carbonate and phosphate samples yielded $^{87}Sr/^{86}Sr$ close to those of contemporaneous mid-Cambrian seawater (~0.70880 to 0.70900; Figs. 4–6; Chen et al., 2022; Peng et al., 2020), the majority exhibit more radiogenic or non-marine signatures, along with a positive correlation with Mn/Sr ratios (Fig. 8c), indicating a diagenetic overprint of the Sr isotope system. In contrast, no clear correlations are observed between $^{87}Sr/^{86}Sr$ data and either $\delta^{13}C$ or $\delta^{26}Mg$ (Figs. 8e, f). This decoupling reinforces that the Sr isotopic system is more vulnerable to post-depositional alteration than carbon or magnesium isotope systems in these mid-Cambrian carbonates.

Elevated or more radiogenic $^{87}Sr/^{86}Sr$ values may result from the impact of K- and Rb-rich detrital or authigenic clays during recrystallization, as the decay of ^{87}Rb produces radiogenic ^{87}Sr (Fairchild et al., 2018). Alternatively, such values may reflect enhanced continental input in restricted or semi-restricted marine environments (Chen et al., 2022), or the impact of non-marine, meteoric (continent-derived) fluids, including basinal brines or distinct dolomitization fluids (Derry et al., 1994; Peng et al., 2020). In Carrara 1, strong positive correlations between $^{87}Sr/^{86}Sr$ data and Al, Rb concentrations, as well as Mg/Ca ratios (Figs. 4, 9a–c), suggest that these radiogenic signatures likely reflect a combined influence from non-marine diagenetic or dolomitizing fluids and associated silicate phases. The latter is supported by the presence of siliciclastic detritus and authigenic glauconite (Fig. 2). Overall, the best-preserved mid-Cambrian carbonate samples for reconstructing paleo-seawater Sr isotope composition appear to be low-Mg, fine-grained limestones (LMC) with minimal influence from detrital and authigenic clays (Fig. 4; Derry et al., 1994; Peng et al., 2020).

Finally, some studied phosphatic microfossils yielded non-marine $^{87}Sr/^{86}Sr$ values that deviate from the expected mid-Cambrian seawater composition, indicating diagenetic alteration and isotopic resetting. Notably, a clear negative correlation was observed between fossil size (in micrometers, μm) and their measured $^{87}Sr/^{86}Sr$ ratios (Fig. 9d), further supporting the interpretation of diagenetic overprint. Specifically, smaller phosphatic fossils (e.g., < 1000 μm) appear more susceptible to alteration by diagenetic or non-marine fluids, whereas larger fossils (~1500 mm) tend to retain primary $^{87}Sr/^{86}Sr$ signatures reflective of mid-Cambrian seawater (Fig. 9d). Consequently, Sr isotope data from ancient phosphatic microfossils require careful evaluation when used for paleo-seawater reconstruction and strontium isotope stratigraphy (SIS). We recommend focusing on larger specimens (> 1000 μm), as they are more resistant to diagenetic overprinting and more likely to preserve primary $^{87}Sr/^{86}Sr$ signatures.

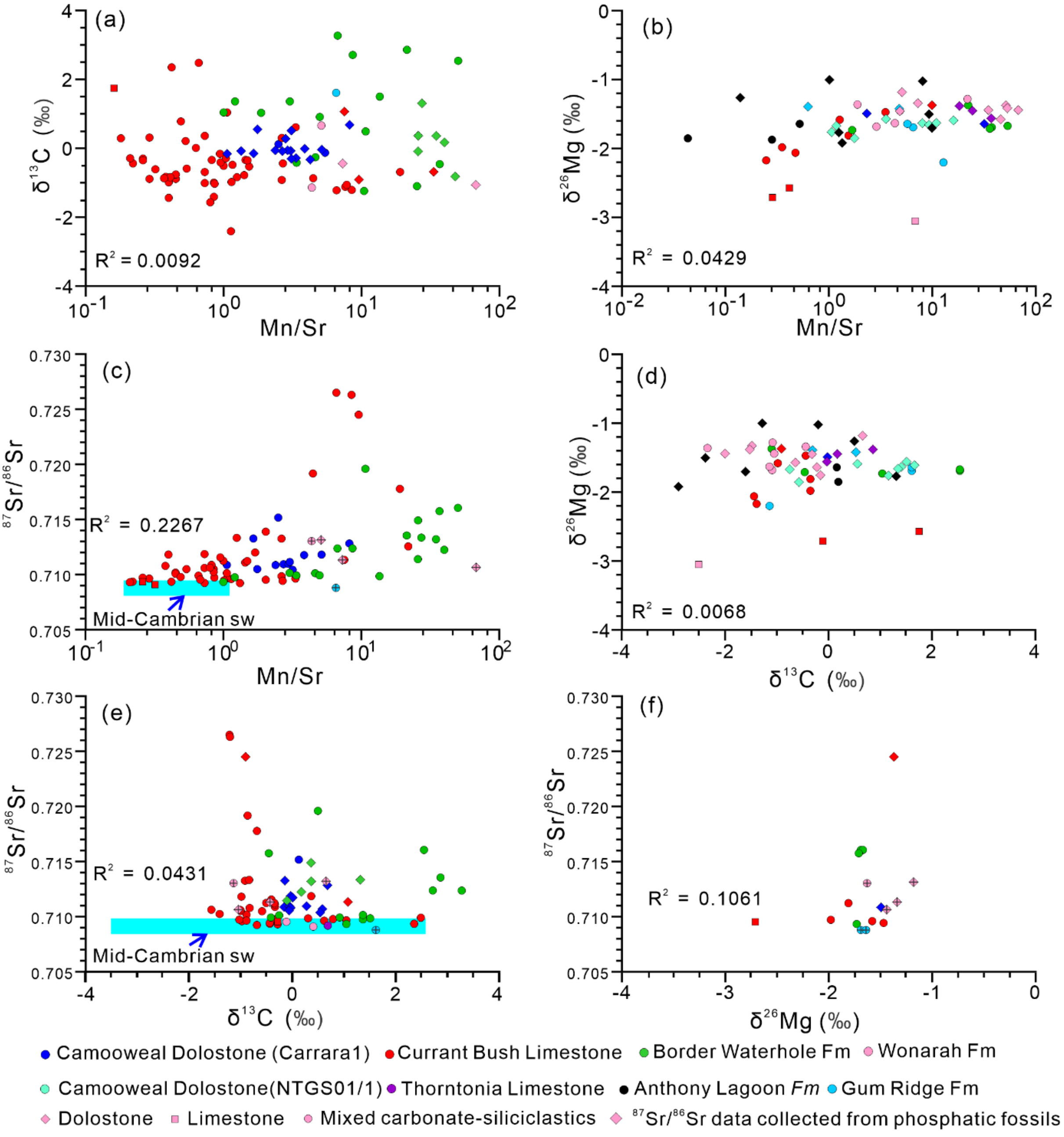

Figure 8. Cross plots illustrating the relationships between Sr, C, and Mg isotopic proxies and elemental ratios in mid-Cambrian marine archives from the Georgina Basin. Data points are color-coded by formation: (**a**) $\delta^{13}C$ vs. Mn/Sr; (**b**) $\delta^{26}Mg$ vs. Mn/Sr; (**c**) $^{87}Sr/^{86}Sr$ vs. Mn/Sr; (**d**) $\delta^{26}Mg$ vs. $\delta^{13}C$; (**e**) $^{87}Sr/^{86}Sr$ vs. $\delta^{13}C$; and (**f**) $^{87}Sr/^{86}Sr$ vs. $\delta^{26}Mg$. Note that $\delta^{13}C$, $^{87}Sr/^{86}Sr$, and Mn/Sr data for Carrara 1 samples are sourced from Carson et al. (2023), while all other datasets were generated in this study.

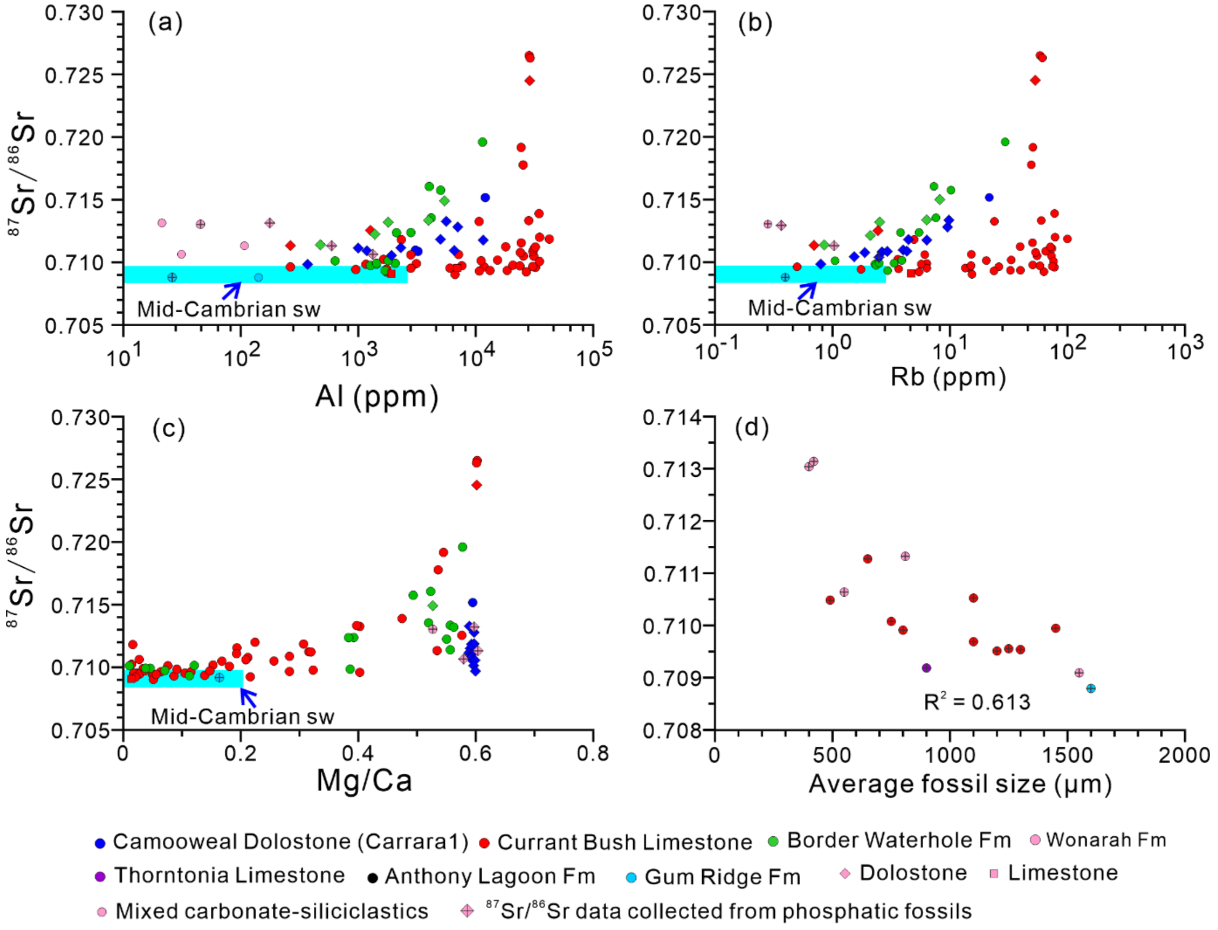

Figure 9. Cross plots showing correlations between the ^{87}Sr/^{86}Sr ratios and selected parameters of the studied samples, including elemental composition and average fossil size: (**a**) ^{87}Sr/^{86}Sr vs. Al concentration; (**b**) ^{87}Sr/^{86}Sr vs. Rb concentration; (**c**) ^{87}Sr/^{86}Sr vs. Mg/Ca; (**d**) ^{87}Sr/^{86}Sr vs. average fossil size. Note that elemental data for Carrara 1 samples are sourced from Carson et al. (2021), while all other data were generated in this study.

4.5.3 The Mid-Cambrian Carbon Isotope Excursion (DICE) in Georgina Basin and Global Correlations

In the Georgina Basin, the eodiscid trilobite *Pagetia thorntonensis* was identified in the Currant Bush Limestone of Carrara 1 at a depth of 419.5 m, indicating the *Acidusus atavus* Zone of the Australian Floran Age. Another trilobite, *Triplagnostus gibbus*, was recovered at a depth of 425 m, marking the late Templetonian Stage (Fig. 4; Laurie, 2022). These two diagnostic fossils suggest that the boundary between the Wuliuan Stage and overlying Drumian Stage lies between 419.5 m and 425 m in Carrara 1 (Fig. 4). *Xystridura lauta* (Öpik, 1975) was discovered at the base of the Wonarah Formation in NTGS01/1 (316.51–317.27 m), indicating a Templetonian age (Fig. 5; Laurie, 2004). *Redlichia forresti* was reported from the base of the Gum Ridge Formation in BN04DD01 at a depth of 385.5 m, indicating a latest Ordian age (Fig. 6; Kruse et al., 2004; Laurie, 2024).

Interestingly, the positive carbon isotope excursion recorded at the Wuliuan-Drumian boundary is documented in all three studied drillholes. This anomaly aligns closely with global $\delta^{13}C$ chemostratigraphic records (Figs. 4–6, 10; Babcock et al., 2004; Montañez et al., 2000). Specifically, this positive C isotope excursion corresponds to the onset of a globally recognized sea-level rise (Babcock et al., 2004), likely driven by enhanced primary productivity and/or increased organic matter burial (Berner, 1998; Kump and Arthur, 1999; Wang et al., 2024b; Zondervan et al., 2023), as evidenced also by the elevated TOC content in Carrara 1 (Fig. 4).

The major negative carbon isotope excursion (DICE) above the Wuliuan–Drumian boundary is identified in all three studied wells. The $\delta^{13}C$ shifts are -2.41‰ in Carrara 1 (~60 m above the boundary), -3.89‰ in NTGS01/1 (~40 m above), and -3.06‰ in BN04DD01 (~65 m above) (Figs. 4–6). These trends correlate closely with the DICE recorded in the Drum Mountains (Fig. 10; Howley and Jiang, 2010; Pagès and Schmid, 2016). While the negative DICE has been widely documented across Laurentia, Baltica, South China, North China, and Siberia, inconsistencies in its stratigraphic position have raised questions about its global correlation (Howley and Jiang, 2010; Pagès and Schmid, 2016; Peng et al., 2020). In the Drum Mountains, the DICE occurs above the FAD of *P. atavus* (Fig. 10; Howley and Jiang, 2010), whereas in the Canadian Rocky Mountains, the negative carbon shift occurs below the *Bolaspidella* (equivalent to *P. atavus*) Zone (Fig. 10; Montañez et al., 2000). In the Wangcun section of the South China Craton, two negative C isotope excursions are reported, one above the FAD of *P. atavus* and one below the boundary (Fig. 10; Zhu et al., 2004). However, only one negative C excursion near the FAD of *P. atavus* was reported from the same section by Li et al. (2020). In the central Undilla Subbasin of the Georgina Basin, Australia, two negative C isotope excursions are reported, one above the Drumian Stage and one below the boundary (Pagès and Schmid, 2016). However, the basal negative C excursion was not found in our studied cores (Figs. 4–6, 10).

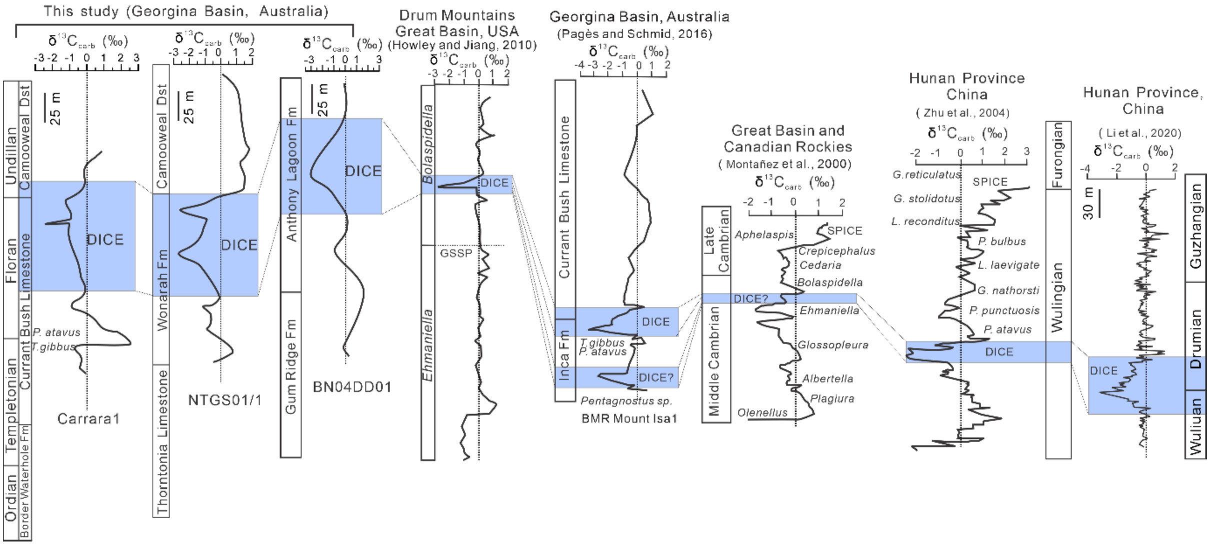

Figure 10. The DICE negative carbon isotope anomaly (blue rectangles) and the underlying positive carbon isotope excursions identified in this study, as well as those in the central Undilla Subbasin of the Georgina Basin (Pagès and Schmid, 2016). Global correlations are also illustrated with coeval Cambrian sections from the Drum Mountains, USA (Howley and Jiang, 2010), the Great Basin and Canadian Rockies (Montañez et al., 2000), and the South China Craton (Li et al., 2020; Zhu et al., 2004).

Previous studies suggest that inconsistencies in the stratigraphic position and global correlation of the DICE may result from low sampling resolution at specific sites and/or the influence of local events (Li et al., 2020; Pagès and Schmid, 2016). We hypothesize that these discrepancies may also reflect the complex interplay between sea-level fluctuations and depositional environments (e.g., basin subsidence, local tectonic regimes, *etc*.), which can vary significantly across different depositional systems and between deep and shallow platform settings, even within a single basin.

For instance, the basal negative C isotope excursion (possibly the DICE) identified in the lower

Inca Formation of the central Undilla Subbasin (Fig. 10) has been interpreted as a signal of platform drowning (Pagès and Schmid, 2016). In contrast, the contemporaneous deposition of Sequence 1 in our study area occurred primarily in peritidal and restricted shallow marine environments (Fig. 7a), likely reflecting more localized marine carbon cycling under restricted conditions, which resulted in a distinct carbon isotope signature (Fig. 7). These contrasting depositional settings, modulated by local sea-level changes and basin tectonics, may account for regional variations in both the magnitude and timing of mid-Cambrian carbon isotope excursions such as the DICE (Fig. 10). This could also explain the observed differences in the shape and intensity of the negative $\delta^{13}C$ shift across the three studied drillholes—for example, two distinct negative $\delta^{13}C$ peaks are identified in NTGS01/1 (Figs. 5, 10).

In summary, the DICE event represents a globally recognized C isotope event linked to a sea-level rise and a major perturbation of the oceanic carbon cycle. This event coincides with a period marked by extinction, including the collapse of reef systems, and a proliferation of microbialites (Li et al., 2020; Pagès and Schmid, 2016; Yang et al., 2021). In association with this biotic crisis, widespread anoxic–euxinic conditions during the DICE have been documented in mid-Cambrian oceans (Howley and Jiang, 2010; Li et al., 2020; Pagès and Schmid, 2016). This is further supported by evidence from paleo-redox proxies (U and Mo concentrations) in the central Undilla Subbasin (Pagès and Schmid, 2016), and paleoenvironmental reconstructions from this study (Fig. 7b). Several mechanisms have been proposed to explain the mid-Cambrian DICE event, including the eruption of large igneous provinces (LIPs), which released ^{12}C-enriched (or isotopically light) carbon into the ocean-atmosphere system (Hough et al., 2006; Jourdan et al., 2014). Other proposed causes include elevated freshwater input (Howley and Jiang, 2010; Wang et al., 2024b), which could have enhanced respiration and mineralization of marine organic matter associated with a major transgressive episode (Howley and Jiang, 2010; Pagès and Schmid, 2016). A recent study by Li et al. (2020) also suggests that the parallel negative excursions in $\delta^{12}C_{carb}$ (carbonate) and $\delta^{13}C_{org}$ (organic shales) observed during the DICE were likely caused by the oxidation of dissolved organic carbon (DOC) in mid-Cambrian oceans. Such oxidation was triggered by the shoaling and upward incursion of anoxic, ^{12}C-rich deep waters into shallower marine settings during the widespread transgression (Fig. 7b). The resulting increase in ^{12}C-rich dissolved inorganic carbon (DIC) in the shallow water column was subsequently recorded in coeval mid-Cambrian marine carbonate archives, manifesting as the globally recognized DICE event (Wang et al., 2024b; Yang et al., 2021; Zondervan et al., 2023).

4.5.4 Constraints on Mg Isotope Composition (δ^{26}Mg) of Mid-Cambrian Seawater

Significant Mg isotope fractionation occurs during the formation and precipitation of carbonate minerals from aqueous fluids or seawater. During dolomitization, the lighter ^{24}Mg isotopes are preferentially incorporated into the crystal lattice of early-formed dolomite (or calcite, whether LMC or HMC), thereby enriching the residual fluid in heavier ^{26}Mg isotopes. Consequently, later-formed dolomite (dolostones) tends to show progressively higher ^{26}Mg values than early-formed dolomite, assuming closed-system conditions (Bialik et al., 2018; Blättler et al., 2015; Fantle and Higgins, 2014; Geske et al., 2015; Higgins and Schrag, 2010; Huang et al., 2015). In this context, the most negative (i.e.,lowest) ^{26}Mg value provides key insight into the initial composition of the dolomitizing fluid, and likely reflects a seawater signature if the fluid was sourced from seawater (Bialik et al., 2018; Bryant et al., 2022; Shalev et al., 2020).

Results from this study confirm the presence of isotopically lighter δ^{26}Mg values in the mid-Cambrian carbonates, ranging from -3.05‰ to -1.00‰ (Fig. 11). The most negative ^{26}Mg values are observed in calcite-rich limestones, while dolomite/dolostone samples exhibit relatively heavier compositions. This pattern results in an overall positive correlation between δ^{26}Mg values Mg/Ca ratios, consistent with a two-component mixing trend among the studied carbonates (Figs. 4–6, 11). Specifically, the calcite-rich limestone (molar Mg/Ca < 0.05) from the Wonarah Formation (NTGS01/1 core) exhibits the lowest δ^{26}Mg value of -3.05‰ (Fig. 5). In contrast, stoichiometric dolostone samples (molar Mg/Ca ≈ 1) yielded higher δ^{26}Mg values ranging from -1.92‰ to -1.00‰ (Fig. 11). In the Carrara 1 core, most carbonate samples were collected from the calcite-dominated Currant Bush Limestone, and thus exhibit correspondingly lighter δ^{26}Mg values (highlighted by red rectangles in Fig. 11). In contrast, the

Thorntonia Limestone and Camooweal Dolostone from the NTGS01/1 core, as well as the Gum Ridge Formation from the BNO4DDO1 core, are composed of fully dolomitized carbonates and yield higher δ^{26}Mg values and Mg/Ca ratios close to unity (Fig. 11). The remaining samples represent mixtures between calcite and dolomite end-members.

Recent studies have identified an isotope fractionation of approximately 1.73–2.00‰ (Δ^{26}Mg $_{\text{sw-dolomite}}$) between the δ^{26}Mg values of seawater (fluid) and dolomite (mineral) (Fantle and Higgins, 2014; Higgins et al., 2010; Higgins et al., 2018; Hu et al., 2017; Hu et al., 2019; Li et al., 2015; Shalev et al., 2020; Xia et al., 2024). A fractionation offset of approximately 0.72–1.60‰ is also reported between dolomite and calcite minerals (Δ^{26}Mg $_{\text{dolomite-calcite}}$), with calcite being the isotopically lighter and dolomite heavier carbonate phase (Bryant et al., 2022; Hu et al., 2017; Hu et al., 2021; Li et al., 2015; Peng et al., 2016).

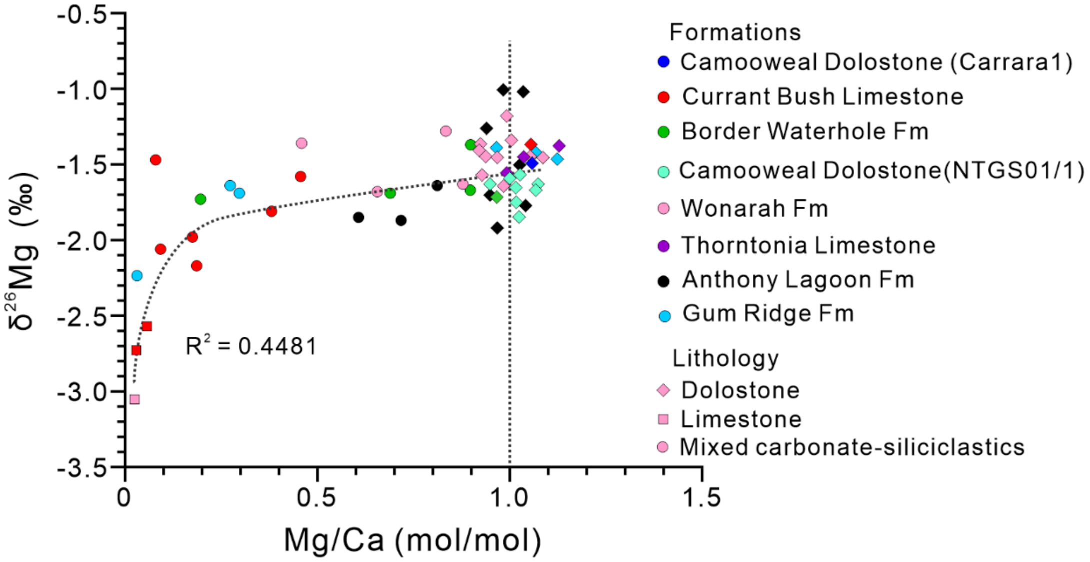

Figure 11. A cross-plot of δ^{26}Mg values vs Mg/Ca (molar) ratios from the studied mid-Cambrian carbonates (from the Georgina Basin, Australia), with data color-coded based on their formations.

In our dataset, the lowest δ^{26}Mg value for mid-Cambrian dolomite is approximately -1.92‰, while the lightest calcite δ^{26}Mg value is -3.05‰, yielding a maximum dolomite–calcite offset (Δ^{26}Mg $_{\text{dolomite-calcite}}$) of ~1.13‰, consistent with previously reported values. Based on these observations, and using the Mg isotope fractionation factors between seawater and dolomite

(Δ^{26}Mg $_{\text{sw-dolomite}}$), the δ^{26}Mg value of the inferred mid-Cambrian seawater can be estimated to range from approximately -0.19 to +0.08‰, based on the following calculation: -1.92 ‰ (lowest dolomite value) + 1.73 to 2.00‰ (Δ^{26}Mg offset) = -0.19 to +0.08‰ (paleo-seawater). These estimates for the δ^{26}Mg signatures of the mid-Cambrian seawater are consistent with recent paleo-seawater reconstructions based on halite and dolomite archives, as well as geochemical modeling constraints (Li et al., 2015; Li et al., 2023; Xia et al., 2024).

As discussed in Section 4.2, marine low-Mg calcitic (LMC) limestones, which typically precipitate directly from seawater and are less susceptible to post-depositional diagenetic alteration, serve as reliable archives of original seawater chemistry, making them ideal proxies for reconstructing paleo-seawater ^{87}Sr/^{86}Sr ratios (Chen et al., 2022; Li et al., 2020; Swart, 2015; Ahm et al., 2018; Banner and Hanson, 1990). In the Currant Bush Limestone from the Carrara 1 drillhole, the calcite-dominated limestones exhibit lower ^{87}Sr/^{86}Sr values that closely align with the expected mid-Cambrian seawater composition (~0.70880 to 0.70900; Fig. 4; Chen et al., 2022; Peng et al., 2020), suggesting these limestones likely precipitated directly from seawater and have preserved their primary marine Sr and Mg isotopic signatures (light blue rectangles in Figs. 7–8). Based on these observations, the Mg isotope fractionation (Δ^{26}Mg $_{\text{sw-calcite}}$) between LMC limestone and mid-Cambrian seawater in the Georgina Basin is approximately 2.86–3.13‰, which aligns with the value of 2.75 ± 0.37‰ reported by Bryant et al. (2022).

4.5.5 Marine Dolomitization in the Georgina Basin: Insights from δ^{26}Mg Proxy

Apart from the high- and low-temperature alteration of the oceanic crust at MORs, the process of marine dolomitization represents the largest sink of dissolved Mg^{2+} in the ocean, with associated Mg isotope fractionation during dolomite formation from seawater (see the section above; Higgins et al., 2010; Huang 2015; Li et al., 2015; Peng et al., 2016; Farkas et al., 2024). Based on recent studies, δ^{26}Mg values in marine dolomite typically overlap within a range of lithologies and sedimentary microfacies, indicating that δ^{26}Mg signatures are not significantly affected by dolomite crystal morphology or depositional setting (Huang et al., 2015; Ning et al., 2019; Ning et al., 2020). However, the δ^{26}Mg of dolomite seems to be primarily influenced by the Mg isotope composition of dolomitizing fluids as well as specific mechanisms of dolomitization (Geske et al., 2015; Peng et al., 2016; Zhu et al., 2023). As mentioned previously, during progressive dolomitization in a closed system (i.e., Rayleigh-type isotope fractionation) the Mg isotope signature of a residual fluid/seawater becomes increasingly enriched in heavy ^{26}Mg, causing the progressive or later-stage dolomite to be isotopically heavier or with more positive δ^{26}Mg values (Bialik et al., 2018). Therefore, δ^{26}Mg signatures of ancient marine dolomites can serve as useful tracer of past dolomitization fluid and its isotope evolution and migration pathways (Ning et al., 2020; Zhu et al., 2023).

However, the δ^{26}Mg values of partially dolomitized samples (i.e., calcite-dolomite mixtures) typically provide more complex Mg isotope signals impacted by the composition of seawater/fluids but also the carbonate mineralogy, the latter reflected in the molar Mg/Ca ratios (Fig. 11). Such mixed δ^{26}Mg signals thus reduce their reliability and robustness for reconstructing the dolomitization processes. In contrast, complete dolomitization, characterized by a molar Mg/Ca ratio of ~1, provides a more reliable basis for tracing the sources of the seawater/marine fluids and associated dolomitization processes (Ning et al., 2020). Based on these assumptions, the Mg isotope variations or the δ^{26}Mg chemostratigraphy of fully dolomitized samples or stoichiometric dolostones (Figs. 11, 5–6), might be used to identify distinct dolomitization processes in the Georgina Basin, as discussed in the sections or possible scenarios below.

(1) Penecontemporaneous Dolomitization

Penecontemporaneous or syndepositional dolomitization typically develops in restricted to semi-restricted marine environments, such as lagoons and sabkhas, where intense evaporation and intermittent influx of Mg^{2+} are common, thus causing elevated Mg/Ca in local seawater/brines and dolomite precipitation or the conversion of limestones to dolostones (Huang et al., 2015; Ning et al., 2020; Peng et al., 2016; Zhu et al., 2023). In such settings, characterized by evaporative pumping and dolomitization driven by capillary forces, dolomite typically precipitates directly from seawater or brine, coexisting with Ca-carbonate during the early stages of sedimentation and dolomitization. Stratigraphically, this process often produces an upward progression of increased dolomitization, whereby earlier-formed dolomite appears in lower intervals and later-formed dolomite in the overlying strata. This results in a positive δ^{26}Mg trend in vertical sedimentary profiles, as illustrated in Fig. 12a. Such progressive and penecontemporaneous dolomitization can be also simulated using a diffusion–advection–reaction modeling (Huang et al., 2015; Ning et al., 2020).

Considering the above processes and possible scenarios, the penecontemporaneous dolomitization in the Georgina Basin might be identified within Sequence 1, and the upper portion of Sequence 2, in association with relative sea-level fluctuations and corresponding shifts in depositional environments (Figs. 4–6). Accordingly, the δ^{26}Mg values or profile from an interval A (in NTGS01/1 core) exhibits a distinct and upward-increasing trend, with δ^{26}Mg values increasing from -1.56‰ to -1.18‰ up the stratigraphic column. This increasing Mg isotope trend may thus reflect progressive penecontemporaneous dolomitization of the Thorntonia Limestone facies, which was deposited under partially restricted peritidal conditions (Figs. 5, 7a). A comparable and upward increasing δ^{26}Mg trend, ranging from -1.92‰ to -1.00‰, is also observed in data from the upper Anthony Lagoon Formation, where restricted lagoon to supratidal conditions might have developed following a sea-level fall during Sequence 2 (Figs. 6, 7c).

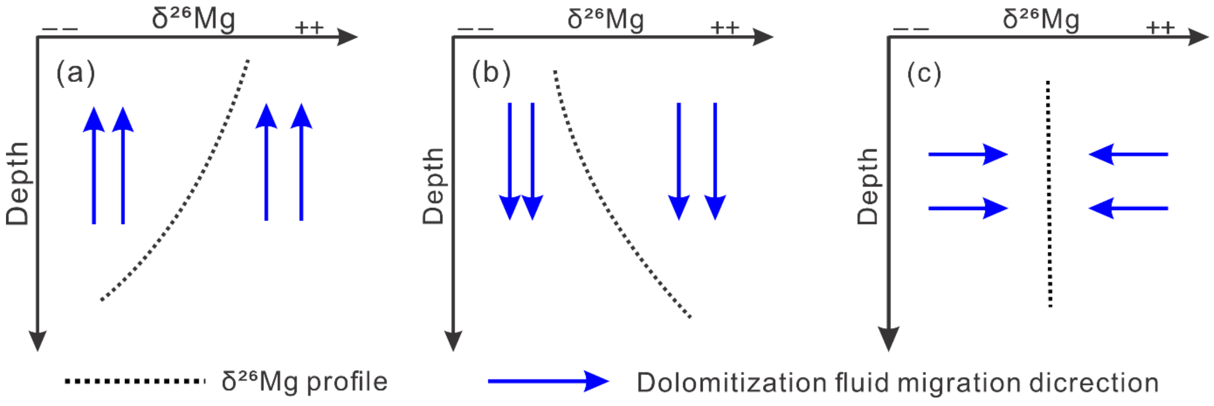

Figure 12. Conceptual vertical δ^{26}Mg profiles (dashed lines) in hypothetical sedimentary columns, associated with different dolomitization processes in the Georgina Basin. (**a**) upward-

increasing δ^{26}Mg trend indicative of penecontemporaneous dolomitization; (**b**) downward-increasing δ^{26}Mg trend reflecting seepage-reflux dolomitization; (**c**) vertically constant δ^{26}Mg values, suggesting possible lateral migration of dolomitizing fluids.

(2) Seepage-Reflux Dolomitization

An alternative process, involving a seepage-reflux dolomitization, also occurs in restricted to semi-restricted intertidal marine environments, particularly during sea-level fall events (Ning et al., 2020; Peng et al., 2016; Zhu et al., 2023). In this process or dolomitization model, dense and Mg-rich brines produced by seawater evaporation migrate downward, replacing earlier-formed Ca-carbonate (i.e., limestones being converted to dolostones). As a result, shallower dolomite/dolostones, higher up in the stratigraphic column, would thus be formed earlier, while deeper dolomites precipitate later and from more evolved and isotopically heavier fluids (with high δ^{26}Mg), thus producing a progressively heavier δ^{26}Mg trend with increasing depth in the stratigraphic column (Fig. 12b). A closely related advective-flow dolomitization model may also be involved in this process and contribute to the observed Mg isotope fractionation trends (Ning et al., 2020; Peng et al., 2016).

In this study, possible evidence for the seepage-reflux dolomitization is primarily reflected in the Mg isotope data from the NTGS01/1 core, particularly within intervals B and C (Fig. 5), which exhibit δ^{26}Mg values ranging from -1.66‰ to -1.36‰; and from -1.85‰ to -1.57‰, respectively. The cyclic nature of the reflux dolomitization process in these intervals may be linked to fluctuations in relative sea-level. Additionally, the location of NTGS01/1 is near the platform margin, along the boundary between the Central and Undilla Subbasins. Hence, the basin-bounding graben faults and syn-depositional structures in this area could have provided fluid pathways, facilitating such downward and lateral migration of dolomitizing fluids (Fig. 7; Dunster et al., 2007; Kruse et al., 2013).

Finally, in both penecontemporaneous and reflux dolomitization models, Mg-rich fluids or evolved marine brines may have migrated laterally across the mid-Cambrian carbonate platform. Such lateral fluid flows within the Georgina Basin carbonate platform could also lead to widespread dolomitization but presumably reflected as relatively uniform δ^{26}Mg values or trends in the vertical profile, as illustrated and hypothesized in Fig. 12c.

4.6 Conclusions

This study integrates δ^{26}Mg, δ^{13}C, δ^{18}O, and ^{87}Sr/^{86}Sr proxies for isotope chemostratigraphy of mid-Cambrian marine carbonates and phosphates from the Georgina Basin, Australia, to investigate seawater composition, dolomitization, and diagenetic effects. The main conclusions are as follows:

(1) The mid-Cambrian Narpa Group, sampled from cores extracted from Carrara 1, NTGS01/1, and BN04DD01 drillholes, record a complete transgressive–regressive cycle, divided into three phases: (i) an initial phase of shallow-water peritidal to restricted marine carbonate deposition during a sea-level lowstand (Sequence 1); (ii) a transgressive phase marked by deepening waters, suboxic to anoxic conditions, increased siliciclastic input, and Ca-carbonate accumulation (early Sequence 2); and (iii) a final regressive phase with a return to shallow, restricted marine to supratidal environments and dolostone-dominated sedimentation during sea-level fall (late Sequence 2).

(2) The δ^{26}Mg data from the mid-Cambrian carbonates (limestones, dolostones and mixtures) are relatively resistant to post-depositional diagenetic resetting, potentially preserving the primary marine Mg isotope signature of paleo-seawater and/or local dolomitizing fluids. However, δ^{13}C and δ^{18}O values, especially from Sequence 1, show signs of diagenetic overprinting, likely due to deep burial and/or meteoric alteration, with δ^{18}O being more negative and susceptible to fluid-mediated modification. In contrast, carbonates from Sequence 2 show better preservation, with δ^{13}C values aligning closely with the expected mid-Cambrian marine C isotope trends, including positive δ^{13}C and negative DICE isotope anomalies.

(3) The ^{87}Sr/^{86}Sr data from well-preserved, low-Mg calcite (LMC) or limestones fall within the expected mid-Cambrian seawater Sr isotope range (~0.70880–0.70900), indicating minimal post-depositional alteration. In contrast, carbonates from stratigraphic intervals with elevated, non-marine ^{87}Sr/^{86}Sr ratios display strong correlations with Mn/Sr ratios, and Al and Rb

concentrations, suggesting the influence of siliciclastic detrital or authigenic mineral phases, and/or radiogenic non-marine diagenetic fluids. Phosphatic microfossils (linguliform brachiopods, SSFs) yielded variable $^{87}Sr/^{86}Sr$ values, with a notable correlation between the fossil sizes and Sr isotopes, indicating that smaller fossils (< 1000 mm) are more susceptible to diagenetic alteration, while larger phosphatic shells have $^{87}Sr/^{86}Sr$ values closer to the mid-Cambrian seawater.

(4) The major negative carbon isotope anomaly (DICE event) is identified within the transgressive Sequence 2 units of the Georgina Basin, stratigraphically above the Wuliuan–Drumian boundary. It is marked by a pronounced negative $\delta^{13}C$ excursion of up to –3.9‰ and correlates well with global DICE records. The excursion is interpreted as reflecting marine redox changes and potential upwelling of ^{12}C-rich anoxic waters. Additionally, a positive $\delta^{13}C$ excursion of up to +2.5‰ is observed at the Wuliuan-Drumian boundary, closely matching global C isotope records in coeval marine carbonates.

(5) The $\delta^{26}Mg$ values of the mid-Cambrian carbonates from the Georgina Basin range from -3.05‰ to -1.00‰, showing a mixing trend between calcite/limestone and dolomite/dolostone end-members, as indicated by the strong correlation with Mg/Ca ratios. The lowest $\delta^{26}Mg$ value in dolomite is -1.92‰, and in calcite, it is -3.05‰. Based on the Mg isotope fractionation between seawater and dolomite ($\Delta^{26}Mg_{\text{sw-dolomite}}$ of ~1.73–2.00‰), the inferred $\delta^{26}Mg$ value of the mid-Cambrian seawater is approximately 0.19 to +0.08‰. This aligns with previous studies but significantly heavier than present-day seawater ($\delta^{26}Mg_{\text{sw}}$ = -0.83‰).

(6) The chemostratigraphic profiles of dolomite-hosted $\delta^{26}Mg$ values can help identify the sources and modes of dolomitization in the Georgina Basin, serving as records of Mg isotope evolution in paleo-seawater or local dolomitizing fluids. A penecontemporaneous dolomitization process is proposed for dolomites in Sequence 1 and the upper Sequence 2, formed in restricted to semi-restricted marine environments. This process is characterized by an upward progression of dolomitization, indicated by a positive shift in $\delta^{26}Mg$ values in stratigraphic profiles. In contrast, a seepage-reflux dolomitization mode is suggested for the upper Sequence 2, linked to restricted to semi-restricted intertidal settings during sea-level fall.

In this case, dolomitization occurs downward due to the migration of dense brines or seawater derived fluids, resulting in an increase in δ^{26}Mg values downward in the stratigraphic column. Lateral fluid migration across the mid-Cambrian carbonate platform in the Georgina Basin may also have contributed to dolomitization, potentially leading to more uniform δ^{26}Mg values in the vertical profiles.

4.7 Acknowledgments

This study was supported by the ARC Discovery Project (DP210100462) “Glauconite: Archive Recording Timing and Triggers of Cambrian Radiation”, and the ARC Linkage Project (LP210200822) “Novel Isotope Techniques to Explore the Centralian Superbasin, Australia”. Additional financial support was provided by MinEx CRC through a PhD research bursary awarded to ZS. XZ is supported by a CAREER Award (#2238685) by the US National Science Foundation. We are also grateful for the laboratory and technical assistance offered by Dr. Robert Klaebe (δ^{13}C, δ^{18}O, and ^{87}Sr/^{86}Sr analyses), Dr. Juzer Shaikh and Dr. Yisheng Yin (δ^{26}Mg analysis), and Jack Castle-Jones (phosphatic fossil separation). The authors acknowledge the instrumentation and expertise provided by Microscopy Australia (ROR: 042mm0k03) at Adelaide Microscopy, University of Adelaide, supported by NCRIS, the university, and state government initiatives. This research represents a contribution to the MinEx CRC (Contribution #286/81130467).

4.8 References

Ahm, A.-S.C., Bjerrum, C.J., Blättler, C.L., Swart, P.K. and Higgins, J.A., 2018. Quantifying early marine diagenesis in shallow-water carbonate sediments. Geochimica et Cosmochimica Acta, 236: 140-159.

Algeo, T.J. and Tribovillard, N., 2009. Environmental analysis of paleoceanographic systems based on molybdenum–uranium covariation. Chemical Geology, 268(3-4): 211-225.

Allan, J. and Matthews, R.K., 1982. Isotope signatures associated with early meteoric diagenesis. Carbonate diagenesis: 197-217.

Ambrose, G.J., Kruse, P.D. and Putnam, P.E., 2001. Geology and hydrocarbon potential of the southern Georgina Basin, Australia. The APPEA Journal: 41(1), 139-163.

Babcock, L.E., Rees, M.N., Robison, R.A., Langenburg, E.S. and Peng, S., 2004. Potential Global Standard Stratotype-section and Point (GSSP) for a Cambrian stage boundary defined by the first appearance of the trilobite Ptychagnostus atavus, Drum Mountains, Utah, USA. Geobios, 37(2): 149-158.

Babcock, L.E., Robison, R.A., Rees, M.N., Peng, S. and Saltzman, M.R., 2007. The global boundary stratotype section and point (GSSP) of the Drumian Stage (Cambrian) in the Drum Mountains, Utah, USA. Episodes Journal of International Geoscience, 30(2): 85-95.

Bailey, A., Wang, L., Grosjean, E., Carson, C., Butcher, G., Jarrett, A. and Henson, P., 2022. New geomechanical and petrophysical data from NDI Carrara 1; implications for Carrara Sub-basin unconventional prospectivity, 2: 99-116.

Banner, J.L. and Hanson, G.N., 1990. Calculation of simultaneous isotopic and trace element variations during water-rock interaction with applications to carbonate diagenesis. Geochimica et Cosmochimica Acta, 54(11): 313-3137.

Berg, R.D., Solomon, E.A., Teng, F.-Z., 2019. The role of marine sediment diagenesis in the modern oceanic magnesium cycle. Nature communications 10, 4371.

Berner, R.A., 1998. The carbon cycle and carbon dioxide over Phanerozoic time: the role of land plants. Philosophical Transactions of the Royal Society of London. Series B: Biological Sciences, 353(1365): 75-82.

Betts, M.J., Paterson, J.R., Jago, J.B., Jacquet, S.M., Skovsted, C.B., Topper, T.P., Brock, G.A., 2016. A new lower Cambrian shelly fossil biostratigraphy for South Australia. Gondwana Research 36: 176–208.

Betts, M.J., Paterson, J.R., Jago, J.B., Jacquet, S.M., Skovsted, C.B., Topper, T.P., Brock, G.A., 2017. Global correlation of the early Cambrian of South Australia: Shelly fauna of the *Dailyatia odyssei* Zone. Gondwana Research 46: 240–279

Betts, M.J., Paterson, J.R., Jacquet, S.M., Andrew, A.S., Hall, P.A., Jago, J.B., Jagodzinski, E.A., Preiss, W.V., Crowley, J.L. and Birch, S.A., 2018. Early Cambrian chronostratigraphy and geochronology of South Australia. Earth-Science Reviews, 185: 498-543.

Bialik, O.M., Wang, X., Zhao, S., Waldmann, N.D., Frank, R. and Li, W., 2018. Mg isotope response to dolomitization in hinterland-attached carbonate platforms: outlook of δ26Mg as a tracer of basin restriction and seawater Mg/Ca ratio. Geochimica et Cosmochimica Acta, 235: 189-207.

Birksmith, C., Betts, M.J., Holmes, J.D., Castle-Jones, J., Hall, P.A., Klaebe, R.M., Zhang, Z.-L., Brock, G.A., 2025. Identification of the Cambrian Series 2 – Miaolingian boundary, western Stansbury Basin, South Australia using multiproxy chronostratigraphy. Australasian Palaeontological Memoirs 57: 21-47.

Blättler, C.L., Miller, N.R. and Higgins, J.A., 2015. Mg and Ca isotope signatures of authigenic dolomite in siliceous deep-sea sediments. Earth and Planetary Science Letters, 419: 32-42.

Bradshaw, B.E., Khider K., MacFarlane S., Carr L. and P., H., 2021. Tectonostratigraphic Evolution of the Centralian Superbasin (Australia) Revealed Through Three-Dimensional Well Correlations, Geoscience Australia.

Brand, U. and Veizer, J., 1980. Chemical diagenesis of a multicomponent carbonate system; 1, Trace elements. Journal of Sedimentary Research, 50(4): 1219-1236.

Bryant, R.N., Present, T.M., Ahm, A.-S.C., McClelland, H.-L.O., Razionale, D. and Blättler, C.L., 2022. Early diagenetic constraints on Permian seawater chemistry from the Capitan Reef. Geochimica et Cosmochimica Acta, 328: 1-18.

Butcher, G., Grosjean, E., Jarrett, A.J., Boreham, C.J., Jinadasa, N., Webster, T., Hong, Z., Carson, C.J. 2021. Exploring for the Future - Rock-Eval pyrolysis data from NDI Carrara 1, South Nicholson region, Australia: Destructive Analysis Report. Record 2021/26. Geoscience Australia, Canberra.

Carson, C. J., Grosjean, E., Butcher, G., Webber, S., Gilmore, S., Henson, P. A. 2022. Exploring for the Future – Quantitative X-ray diffraction data release of NDI Carrara 1, South

Nicholson region, Northern Territory. Record 2022/05. Geoscience Australia, Canberra.

Carson, C. J., Main, P., Champion, D. C., Grosjean, E., Butcher, G., Gilmore, S. and Henson, P. A. 2021. Exploring for the Future – Whole rock inorganic geochemistry data release of NDI Carrara 1, South Nicholson region, Northern Territory. Record 2021/32. Geoscience Australia, Canberra.

Carson, C.J., Anderson, J.R., Klaebe, R., Hall, T., Farkas, J., Gilbert, S., Grosjean, E. and Butcher, G. 2023. Exploring for the Future – Strontium, Oxygen and Carbon Isotopes from NDI Carrara 1, South Nicholson Region, Australia. Geoscience Australia, Canberra.

Castle-Jones, J., Betts, M.J., Jacquet, S.M., Chen, F., Zhang, Z., Hall, P.A., Klaebe, R.M., Brock, G.A., 2025. A new integrated lower Cambrian chronostratigraphy for the Normanville Group, eastern Stansbury Basin, with definition of the oldest small shelly fossil zones in South Australia. Australasian Palaeontological Memoirs 57: 465–489.

Chanda, P. and Fantle, M.S., 2017. Quantifying the effect of diagenetic recrystallization on the Mg isotopic composition of marine carbonates. Geochimica et Cosmochimica Acta, 204: 219-239.

Chang, C., Hu, W., Wang, X., Yu, H., Yang, A., Cao, J. and Yao, S., 2017. Carbon isotope stratigraphy of the lower to middle Cambrian on the eastern Yangtze Platform, South China. Palaeogeography, Palaeoclimatology, Palaeoecology, 479: 90-101.

Chen, X.-Y., Teng, F.-Z., Huang, K.-J. and Algeo, T.J., 2020. Intensified chemical weathering during Early Triassic revealed by magnesium isotopes. Geochimica et Cosmochimica Acta, 287: 263-276.

Chen, X., Yang, A., Du, S., Jahangir, H., Chen, J., Liu, F., Hu, C. and Yan, G., 2024. Upper Cambrian and lower Ordovician conodont and carbon isotope bio-chemostratigraphy of the eastern North China Platform: Implications for global correlation and palaeoenvironments. Journal of Asian Earth Sciences, 264: 106077.

Chen, X., Zhou, Y. and Shields, G.A., 2022. Progress towards an improved Precambrian seawater Sr/Sr curve. Earth-Science Reviews, 224: 103869.

Derry, L., Brasier, M., Corfield, R.e.a., Rozanov, A.Y. and Zhuravlev, A.Y., 1994. Sr and C isotopes in Lower Cambrian carbonates from the Siberian craton: a paleoenvironmental record during the 'Cambrian explosion'. Earth and Planetary Science Letters, 128(3-4): 671-681.

Derry, L.A., 2010. A burial diagenesis origin for the Ediacaran Shuram–Wonoka carbon isotope anomaly. Earth and Planetary Science Letters, 294(1-2): 152-162.

Dunlea, A.G., Murray, R.W., Santiago Ramos, D.P., Higgins, J.A., 2017. Cenozoic global cooling and increased seawater Mg/Ca via reduced reverse weathering. Nature communications 8, 844.

Dunster, J., Kruse, P., Duffett, M. and Ambrose, G., 2007. Geology and resource potential of the southern Georgina Basin. Digital information package DIP007. Darwin: Northern Territory Geological Survey.

Fairchild, I.J., Spencer, A.M., Ali, D.O., Anderson, R.P., Anderton, R., Boomer, I., Dove, D., Evans, J.D., Hambrey, M.J. and Howe, J., 2018. Tonian-Cryogenian boundary sections of Argyll, Scotland. Precambrian Research, 319: 37-64.

Fantle, M.S. and Higgins, J., 2014. The effects of diagenesis and dolomitization on Ca and Mg isotopes in marine platform carbonates: implications for the geochemical cycles of Ca and Mg. Geochimica et Cosmochimica Acta, 142: 458-481.

Farkaš, J., Wallmann, K., Mosley, L., Staudigel, P., Zheng, X.-Y., Leyden, E., Shao, Y., Fryda, J., Holmden, C., Eisenhauer, A., 2024. Alkalinity and elemental cycles in present and past ocean: Insight from geochemical modeling and alkali and alkaline earth metal isotopes. Treatise on Geochemistry (Third Edition), pp. 33-87.

Gao, T., Ke, S., Li, R., Meng, X.n., He, Y., Liu, C., Wang, Y., Li, Z. and Zhu, J.M., 2018. High-precision magnesium isotope analysis of geological and environmental reference materials by multiple-collector inductively coupled plasma mass spectrometry. Rapid Communications in Mass Spectrometry, 33(8): 767-777.

Geske, A., Goldstein, R.H., Mavromatis, V., Richter, D.K., Buhl, D., Kluge, T., John, C.M. and Immenhauser, A., 2015. The magnesium isotope (δ26Mg) signature of dolomites. Geochimica et Cosmochimica Acta, 149: 131-151.

Gill, B.C., Lyons, T.W., Young, S.A., Kump, L.R., Knoll, A.H. and Saltzman, M.R., 2011. Geochemical evidence for widespread euxinia in the Later Cambrian ocean. Nature, 469(7328): 80-83.

Glass, L.M. and Phillips, D., 2006. The Kalkarindji continental flood basalt province: A new Cambrian large igneous province in Australia with possible links to faunal extinctions. Geology, 34(6): 461-464.

Gothmann, A.M., Stolarski, J., Adkins, J.F., Higgins, J.A., 2017. A Cenozoic record of seawater Mg isotopes in well-preserved fossil corals. Geology 45, 1039-1042.

Haines, P.W., Hand, M. and Sandiford, M., 2001. Palaeozoic synorogenic sedimentation in central and northern Australia: a review of distribution and timing with implications for the evolution of intracontinental orogens. Australian Journal of Earth Sciences, 48(6): 911-928.

Hand, M., Mawby, J., Kinny, P. and Foden, J., 1999. U–Pb ages from the Harts Range, central Australia: evidence for early Ordovician extension and constraints on Carboniferous metamorphism. Journal of the Geological Society, 156(4): 715-730.

Harrison, A.L., Bénézeth, P., Schott, J., Oelkers, E.H. and Mavromatis, V., 2021. Magnesium and carbon isotope fractionation during hydrated Mg-carbonate mineral phase transformations. Geochimica et Cosmochimica Acta, 293: 507-524.

Higgins, J.A. and Schrag, D., 2010. Constraining magnesium cycling in marine sediments using magnesium isotopes. Geochimica et Cosmochimica Acta, 74(17): 5039-5053.

Holmes, J.D., Smith, P.M., Paterson, J.R., Brock, G.A. and Betts, M.J., 2025. The Cambrian Series 2–Miaolingian boundary interval in Australia: Biostratigraphic subdivision and implications for global multi-proxy correlation. Earth-Science Reviews: 105106.

Hough, M., Shields, G., Evins, L., Strauss, H., Henderson, R. and Mackenzie, S., 2006. A major sulphur isotope event at c. 510 Ma: a possible anoxia–extinction–volcanism connection during the Early–Middle Cambrian transition? Terra Nova, 18(4): 257-263.

Howley, R.A., Jiang, G., 2010. The Cambrian Drumian carbon isotope excursion (DICE) in the Great Basin, western United States. Palaeogeography, Palaeoclimatology, Palaeoecology, 296(1-2): 138-150.

Hu, Z., Hu, W., Liu, C., Sun, F., Liu, Y. and Li, W., 2019. Conservative behavior of Mg isotopes in massive dolostones: From diagenesis to hydrothermal reworking. Sedimentary Geology, 381: 65-75.

Hu, Z., Hu, W., Wang, X., Lu, Y., Wang, L., Liao, Z. and Li, W., 2017. Resetting of Mg isotopes between calcite and dolomite during burial metamorphism: Outlook of Mg isotopes as geothermometer and seawater proxy. Geochimica et Cosmochimica Acta, 208: 24-40.

Hu, Z., Li, W., Zhang, H., Krainer, K., Zheng, Q.-f., Xia, Z., Hu, W. and Shen, S.-z., 2021. Mg isotope evidence for restriction events within the Paleotethys ocean around the Permian-Triassic transition. Earth and Planetary Science Letters, 556: 116704.

Huang, K.-J., Shen, B., Lang, X.-G., Tang, W.-B., Peng, Y., Ke, S., Kaufman, A.J., Ma, H.-R. and Li, F.-B., 2015. Magnesium isotopic compositions of the Mesoproterozoic dolostones: Implications for Mg isotopic systematics of marine carbonates. Geochimica et Cosmochimica Acta, 164: 333-351.

Huang, K.-J., Teng, F.-Z., Plank, T., Staudigel, H., Hu, Y. and Bao, Z.-Y., 2018. Magnesium isotopic composition of altered oceanic crust and the global Mg cycle. Geochimica et Cosmochimica Acta, 238: 357-373.

Jourdan, F., Hodges, K., Sell, B., Schaltegger, U., Wingate, M., Evins, L., Söderlund, U., Haines, P., Phillips, D. and Blenkinsop, T., 2014. High-precision dating of the Kalkarindji large igneous province, Australia, and synchrony with the Early–Middle Cambrian (Stage 4–5) extinction. Geology, 42(6): 543-546.

Kaufman, A.J. and Knoll, A.H., 1995. Neoproterozoic variations in the C-isotopic composition of seawater: stratigraphic and biogeochemical implications. Precambrian research, 73(1-4): 27-49.

Khider, K., MacFarlane, S., Bradshaw, B.E., Carr, L. and Henson, P., 2021. The Centralian Superbasin (Canning, Amadeus, Georgina and Officer basins) Stratigraphic Review and Well Correlations.

Krabbenhöft, A., Fietzke, J., Eisenhauer, A., Liebetrau, V., Böhm, F. and Vollstaedt, H., 2009.

Determination of radiogenic and stable strontium isotope ratios (87 Sr/86 Sr; δ 88/86 Sr) by thermal ionization mass spectrometry applying an 87 Sr/84 Sr double spike. Journal of Analytical Atomic Spectrometry, 24(9): 1267-1271.

Kruse, P., Dunster, J., Munson, T., 2013. Chapter 28: Georgina Basin, in: Ahmad, M., Munson, T. (Eds.), Geology and mineral resources of the Northern Territory. Northern Territory, Northern Territory, pp. 28:21-28:56.

Kruse, P., Laurie, J. and Webby, B., 2004. Cambrian geology and palaeontology of the Ord Basin. Memoirs of the Association of Australasian Palaeontologists, 30: 1-58.

Kruse, P.D., 2008. Georgina Basin: Stratigraphic Drilling 2002-2006 and Petrography 2000-2007. Northern Territory Geological Survey.

Kump, L.R. and Arthur, M.A., 1999. Interpreting carbon-isotope excursions: carbonates and organic matter. Chemical Geology, 161(1-3): 181-198.

Laurie, J.R., 2004. Macrofossils from surface outcrop on Avon Downs and Ranken 1:250,000 map sheet areas and core from NTGS 01/1 and BMR GRG 16 drillholes, Geosceence Australia.

Laurie, J.R., 2005. Macrofossils from BMR Alroy 2, BMR Ranken 2 and BN04-DD01 drillholes, Georgina Basin, Northern Territory, Geosceence Australia.

Laurie, J.R., 2006. Early Middle Cambrian trilobites from Pacific Oil & Gas Baldwin 1 well, southern Georgina Basin, Northern Territory. MEMOIR-ASSOCIATION OF Australasian Palaeontologists, 32: 127.

Laurie, J.R., 2012. Biostratigraphy of the Arthur Creek Formation and Thorntonia Limestone, Georgina Basin.

Laurie, J.R., 2022. Report on the biostratigraphy of the Georgina Basin succession in NDI Carrara 1. 1-7.

Laurie, J.R., Kruse, P.D., Brock, G.A., Holmes, J.D., Jago, J.B., Betts, M.J., Paterson, J.R. and Smith, P.M., 2024. The quest for an Australian Cambrian stage scale. Alcheringa: An Australasian Journal of Palaeontology: 1-20.

Li, D., Zhang, X., Zhang, X., Zhu, H., Peng, S., Sun, L. and Shen, Y., 2020. A paired carbonate–

organic δ13C approach to understanding the Cambrian Drumian carbon isotope excursion (DICE). Precambrian Research, 349: 105503.

Li, W., Beard, B.L., Li, C. and Johnson, C.M., 2014. Magnesium isotope fractionation between brucite [Mg $(OH)_2$] and Mg aqueous species: Implications for silicate weathering and biogeochemical processes. Earth and Planetary Science Letters, 394: 82-93.

Li, W., Beard, B.L., Li, C., Xu, H. and Johnson, C.M., 2015. Experimental calibration of Mg isotope fractionation between dolomite and aqueous solution and its geological implications. Geochimica et Cosmochimica Acta, 157: 164-181.

Li, X., Zhu, G., Li, T., Zhou, L., Wu, Y., Shen, B. and Ning, M., 2023. Conservative behavior of Mg isotopes in dolomite during diagenesis and hydrothermal alteration: A case study in the Lower Cambrian Qiulitage Formation, Gucheng area, Tarim Basin. Applied Geochemistry, 148: 105540.

Ling, M.X., Sedaghatpour, F., Teng, F.Z., Hays, P.D., Strauss, J. and Sun, W., 2011. Homogeneous magnesium isotopic composition of seawater: an excellent geostandard for Mg isotope analysis. Rapid Communications in Mass Spectrometry, 25(19): 2828-2836.

Liu, K., Jiang, M., Huang, T., Zhang, L., Wang, Y. and Chen, D., 2022. A reassessment on the timing and potential drivers of the major seawater 87Sr/86Sr drop in the Ordovician Period: New evidence from conodonts in China. Chemical Geology: 120906.

Mavromatis, V., Meister, P., Oelkers, E.H., 2014. Using stable Mg isotopes to distinguish dolomite formation mechanisms: A case study from the Peru Margin. Chemical Geology 385, 84-91.

McArthur, J., Howarth, R., Shields, G. and Zhou, Y., 2020. Strontium isotope stratigraphy, Geologic Time Scale 2020. Elsevier, pp. 211-238.

Montañez, I.P., Osleger, D.A., Banner, J.L., Mack, L.E. and Musgrove, M., 2000. Evolution of the Sr and C isotope composition of Cambrian oceans. GSA today, 10(5): 1-7.

Munson, T., 2014. Petroleum geology and potential of the onshore Northern Territory, 2014. Northern Territory Geological Survey.

Munson TJ, Kruse PD and Ahmad M, 2013. Chapter 22: Centralian Superbasin: in Ahmad M and Munson TJ (compilers). ‘Geology and mineral resources of the Northern Territory’. Northern Territory Geological Survey, Special Publication 5.

Ning, M., Huang, K., Lang, X., Ma, H., Yuan, H., Peng, Y. and Shen, B., 2019. Can crystal morphology indicate different generations of dolomites? Evidence from magnesium isotopes. Chemical Geology, 516: 1-17.

Ning, M., Lang, X., Huang, K., Li, C., Huang, T., Yuan, H., Xing, C., Yang, R. and Shen, B., 2020. Towards understanding the origin of massive dolostones. Earth and Planetary Science Letters, 545: 116403.

Nixon, A., Glorie, S., Fernie, N., Hand, M., De Vries Van Leeuwen, A., Collins, A., Hasterok, D. and Fraser, G., 2022. Intracontinental fault reactivation in high heat production areas of central Australia: insights from apatite fission track thermochronology. Geochemistry, Geophysics, Geosystems, 23(12): e2022GC010559.

Öpik, A., 1968. The Ordian stage of the Cambrian and its Australian Metadoxididae. Bulletin, Bureau of Mineral Resources, Geology and Geophysics, Australia, 92: 135-70.

Öpik, A., 1975. Templetonian and Ordian xystridurid trilobites of Australia. Bureau of Mineral Resources, Geology and Geophysics, Bulletin 121, 1–84.

Öpik, A., 1979. Middle Cambrian agnostids: systematics and biostratigraphy. Bureau of Mineral Resources, Geology and Geophysics, Bulletin 172, 1–188.

Pagès, A. and Schmid, S., 2016. Euxinia linked to the Cambrian Drumian carbon isotope excursion (DICE) in Australia: Geochemical and chemostratigraphic evidence. Palaeogeography, Palaeoclimatology, Palaeoecology, 461: 65-76.

Pagès, A., Schmid, S., Edwards, D., Barnes, S., He, N. and Grice, K., 2016. A molecular and isotopic study of palaeoenvironmental conditions through the middle Cambrian in the Georgina Basin, central Australia. Earth and Planetary Science Letters, 447: 21-32.

Peng, S.C., Babcock, L.E. and Ahlberg, P., 2020. The cambrian period, Geologic time scale 2020. Elsevier, pp. 565-629.

Peng, Y., Shen, B., Lang, X.G., Huang, K.J., Chen, J.T., Yan, Z., Tang, W.b., Ke, S., Ma, H.R. and Li, F.B., 2016. Constraining dolomitization by Mg isotopes: A case study from partially dolomitized limestones of the middle C ambrian X uzhuang F ormation, N orth C hina. Geochemistry, Geophysics, Geosystems, 17(3): 1109-1129.

Peters, S.E. and Gaines, R.R., 2012. Formation of the ‘Great Unconformity’as a trigger for the Cambrian explosion. Nature, 484(7394): 363-366.

Piazolo, S., Daczko, N.R., Silva, D. and Raimondo, T., 2020. Melt-present shear zones enable intracontinental orogenesis. Geology, 48(7): 643-648.

Pogge von Strandmann, P.A., Forshaw, J., Schmidt, D.N., 2014. Modern and Cenozoic records of seawater magnesium from foraminiferal Mg isotopes. Biogeosciences 11, 5155-5168.

Shalev, N., Farkaš, J., Fietzke, J., Novák, M., Schuessler, J.A., Pogge von Strandmann, P.A. and Törber, P.B., 2018. Mg isotope interlaboratory comparison of reference materials from Earth-surface low-temperature environments. Geostandards and Geoanalytical Research, 42(2): 205-221.

Shalev, N., Lazar, B., Halicz, L., Gavrieli, I., 2021. The Mg isotope signature of marine Mg-evaporites. Geochimica et Cosmochimica Acta 301, 30-47.

Smith, T., Kelman, A.P., Nicoll, R., Edwards, D., Hall, L., Laurie, J. and Carr, L., 2013. An updated stratigraphic framework for the Georgina Basin, NT and Queensland. The APPEA Journal, 53(2): 487-487.

Southgate, P. and Shergold, J., 1991. Application of sequence stratigraphic concepts to Middle Cambrian phosphogenesis, Georgina Basin, Australia. BMR Journal of Australian Geology and Geophysics, 12(2): 119-144.

Swart, P.K. and Eberli, G., 2005. The nature of the $\delta^{13}C$ of periplatform sediments: Implications for stratigraphy and the global carbon cycle. Sedimentary Geology, 175(1-4): 115-129.

Taylor, S.R. and McLennan, S.M., 1985. The continental crust: its composition and evolution.

Tipper, E., Galy, A., Gaillardet, J., Bickle, M., Elderfield, H. and Carder, E., 2006. The magnesium isotope budget of the modern ocean: constraints from riverine magnesium isotope ratios. Earth and Planetary Science Letters, 250(1-2): 241-253.

Tribovillard, N., Algeo, T., Baudin, F. and Riboulleau, A., 2012. Analysis of marine environmental conditions based onmolybdenum–uranium covariation—Applications to

Mesozoic paleoceanography. Chemical Geology, 324: 46-58.

Varga, J., Raimondo, T., Morrissey, L., Kelsey, D.E. and Hand, M., 2022. Pressure-temperature-time constraints on gneiss dome formation in an intracontinental orogen. Journal of Metamorphic Geology, 40(3): 457-488.

Voigt, M., Pearce, C.R., Fries, D.M., Baldermann, A., Oelkers, E.H., 2020. Magnesium isotope fractionation during hydrothermal seawater-basalt interaction. Geochimica et Cosmochimica Acta 272, 21-35.

Walter, M., Veevers, J., Calver, C. and Grey, K., 1995. Neoproterozoic stratigraphy of the Centralian superbasin, Australia. Precambrian Research, 73(1-4): 173-195.

Wang, H., Zhang, H., Zhang, Y., Cheng, B., Deng, Q., Wang, D., Zhao, G. and Liao, Z., 2024a. Sedimentary facies controlled biogeochemical process of biotic extinction and turnover across the Cambrian SPICE event. Communications Earth & Environment, 5(1): 683.

Wang, H., Zhang, S., Wang, X., Su, J., Ye, Y. and Liu, Y., 2024b. A novel model of the carbon cycle in the Cambrian ocean. Science China Earth Sciences, 67(6): 1759-1778.

Wang, S.-J., Teng, F.-Z., Li, S.-G. and Hong, J.-A., 2014. Magnesium isotopic systematics of mafic rocks during continental subduction. Geochimica et Cosmochimica Acta, 143: 34-48.

Xia, Z., Li, S., Hu, Z., Bialik, O., Chen, T., Weldeghebriel, M.F., Fan, Q., Fan, J., Wang, X. and An, S., 2024. The evolution of Earth's surficial Mg cycle over the past 2 billion years. Science Advances, 10(9): eadj5474.

Yang, X., Li, Z., Gao, B. and Zhou, Y., 2021. The Cambrian Drumian carbon isotope excursion (DICE) in the Keping area of the northwestern Tarim Basin, NW China. Palaeogeography, Palaeoclimatology, Palaeoecology, 571: 110385.

Zhang, P., Wang, Y., Zhang, X., Wei, Z., Wang, G., Zhang, T., Ma, H., Wei, J., He, W. and Ma, X., 2022. Carbon, oxygen and strontium isotopic and elemental characteristics of the Cambrian Longwangmiao Formation in South China: Paleoenvironmental significance and implications for carbon isotope excursions. Gondwana Research, 106: 174-190.

Zhang, Y., Yang, T., Hohl, S.V., Zhu, B., He, T., Pan, W., Chen, Y., Yao, X. and Jiang, S., 2020.

Seawater carbon and strontium isotope variations through the late Ediacaran to late Cambrian in the Tarim Basin. Precambrian Research, 345: 105769.

Zhang, Y., Yang, T., Newton, R.J., Pan, W., Chen, Y. and Yu, H., 2023. Seawater carbon and strontium isotope variations in the eastern Tarim Basin during the Cambrian: Implications for connection with the open ocean. Journal of Asian Earth Sciences, 253: 105702.

Zhu, G., Li, X., Li, T., Zhou, L., Wu, Y., Shen, B. and Ning, M., 2023. Genesis mechanism and Mg isotope difference between the Sinian and Cambrian dolomites in Tarim Basin. Science China Earth Sciences, 66(2): 334-357.

Zhu, M.-Y., Babcock, L.E. and Peng, S.-C., 2006. Advances in Cambrian stratigraphy and paleontology: integrating correlation techniques, paleobiology, taphonomy and paleoenvironmental reconstruction. Palaeoworld, 15(3-4): 217-222.

Zondervan, J.R., Hilton, R.G., Dellinger, M., Clubb, F.J., Roylands, T. and Ogrič, M., 2023. Rock organic carbon oxidation CO2 release offsets silicate weathering sink. Nature, 623(7986): 329-333.

4.9 Supplementary Materials–Chapter 4

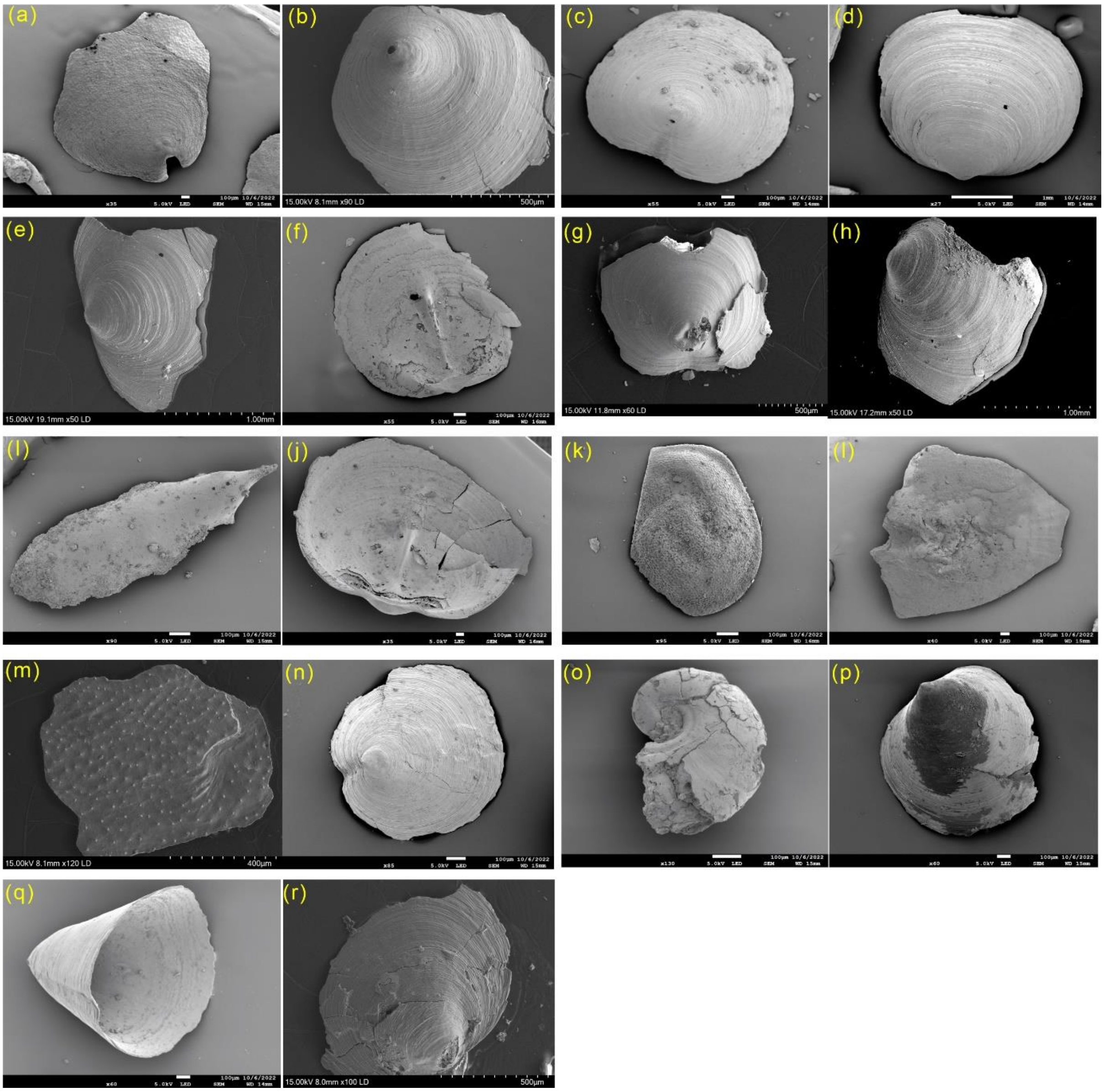

Supplementary Figure S1: Scanning electron microscope (SEM) images of selected phosphatic fossils. (a) BN04DD01,355.1 m, Gum Ridge Formation; (b) Carrara 1, 344.82 m, Currant Bush Limestone; (c) Carrara 1, 349.6 m, Currant Bush Limestone; (d) Carrara 1, 350.3 m, Currant Bush Limestone; (e) Carrara 1, 366.75 m, Currant Bush Limestone; (f) Carrara 1, 75.65 m, Currant Bush Limestone; (g) Carrara 1, 405.95 m, Currant Bush Limestone; (h) Carrara 1, 407.2 m, Currant Bush Limestone; (i) Carrara 1, 416.3 m, Currant Bush Limestone; (j) Carrara 1, 419.61 m, Currant Bush Limestone; (k) Carrara 1, 445.16 m, Currant Bush

Limestone; (l) NTGS01/1, 183.5 m, Woarah Formation; (m) NTGS01/1, 251.6 m, Woarah Formation; (n) NTGS01/1, 265.5 m, Woarah Formation; (o) NTGS01/1, 269.7 m, Woarah Formation; (p) NTGS01/1, 305.3 m, Woarah Formation; (q) NTGS01/1, 308.5 m, Woarah Formation; (r) NTGS01/1, 330.1 m, Woarah Formation.

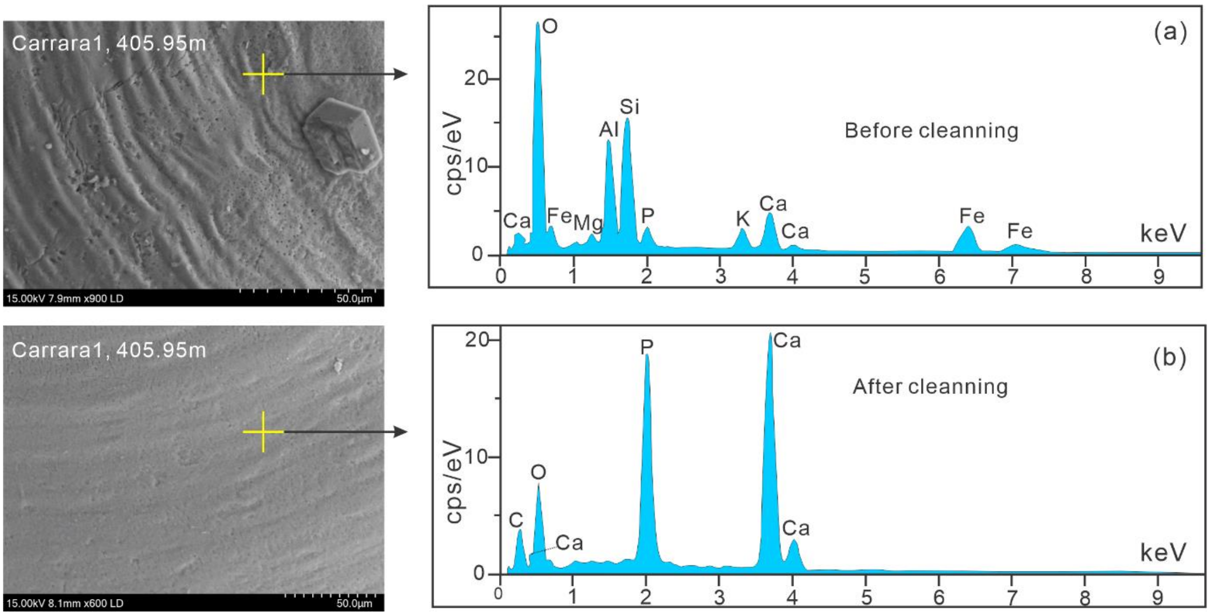

Supplementary Figure S2: Energy Dispersive X-ray Spectroscopy (EDS) spectra of selected phosphatic fossils. (a) Spectrum acquired before cleaning, showing clay minerals adhering to the phosphatic shell, indicated by elevated levels of Al, Si, Fe, and Mg; (b) Spectrum of the cleaned fossil shell, composed primarily of apatite.

Chapter 4–Source Data

Note that all data, including the tables listed below, are available and accessible via the following link:

https://figshare.com/s/859882b23cd4ae4582c7

Supplementary Table S1: Geochemical data from Carrara1.

Supplementary Table S2: Analyzed $\delta^{13}C$, $\delta^{18}O$, and $^{87}Sr/^{86}Sr$ data in this study.

Supplementary Table S3: $\delta^{26}Mg$ data of standards.

Supplementary Table S4: Carbonate $\delta^{26}Mg$ adnd element concentrations.

Chapter 5: Summary and Conclusions

This chapter reviews and summarizes key findings of this thesis (Chapters 2 to 4) and highlights the potential of novel *in situ* geochronology and metal isotopic proxies for basin exploration, and possible future research directions to further expand and develop these new techniques.

5.1 Summary

Chapters 2 focuses on *in situ* geochronology of authigenic minerals, including Rb–Sr dating of glauconite, U–Pb dating of carbonates, and both U–Pb and Lu–Hf dating of bioapatite (published in Shao et al., 2025). These geochronometers have potential to provide original or close-to-depositional (early authigenic) ages, but also the timing of post-depositional/diagenetic events impacting the basin, likely due to local/regional tectonic processes or orogenies. The acquired *in situ* Rb–Sr ages of the mid-Cambrian glauconites from the Georgina Basin are systematically and consistently younger than the expected depositional age, and these rejuvenated ages closely correspond to two phases of the Alice Springs Orogeny, which impacted the Georgina Basin during the Ordovician to Devonian (450–300 Ma). Chapters 2 also more generally discusses the strategies and limitations of using *in situ* LA-ICP-MS/MS techniques for dating authigenic silicate and carbonate minerals in ancient sedimentary basins.

Chapter 3 uses a multi-proxy isotope chemostratigraphy and tries to constrain the mid-Cambrian seawater chemistry in the Georgina Basin by using glauconite as an archive of marine K and Mg isotope composition. Importantly, this study combines *in situ* Rb–Sr glauconite dating, with δ^{41}K and δ^{26}Mg proxies, to assess the impact of diagenetic alteration on these metal isotope proxies with implications for paleo-seawater reconstructions.

Chapter 4 explores the sedimentary/depositional and paleo-environment conditions for mid-Cambrian carbonates from the Georgina Basin. It also tries to reconstruct paleo-seawater composition (based on dolostones and limestones) and global correlations by integrating carbonate-based δ^{26}Mg, δ^{13}C, and δ^{18}O datasets, along with ^{87}Sr/^{86}Sr ratios from both carbonates and phosphatic microfossils, while evaluating diagenetic impacts on these isotopic systems.

5.1.1 *In situ* Geochronology of Authigenic Minerals

This study highlights the utility and limitations of a triple dating method (via LA-ICP-MS/MS) that integrates Rb–Sr, U–Pb, and Lu–Hf isotopic systems for marine authigenic minerals. This laser-based approach enables rapid, direct determination of depositional and/or diagenetic ages in carbonates, phosphates, and authigenic clays, offering high spatial resolution with minimal sample preparation. Results confirmed that *in situ* Rb–Sr ages of the studied mid-Cambrian glauconites are consistently younger (ranging from 452 ± 13 Ma to 351 ± 8 Ma) than the expected depositional age of 505 ± 3 Ma. These rejuvenated glauoconite ages can be broadly grouped into two populations that correspond to two episodes of the Alice Springs Orogeny (450–300 Ma; Haines et al., 2001; Hand et al., 1999; Khider et al., 2021; Kruse et al., 2013; Nixon et al., 2022; Piazolo et al., 2020; Varga et al., 2022). The Rb–Sr system in glauconite is thus susceptible to post-depositional resetting due to burial-related diagenetic processes, likely triggered by tectonic and orogenic events.

Carbonate-based *in situ* U–Pb dating also provided mostly reset ages and rather complex results. However, the samples of well-preserved micrite and fine crystalline dolomite yielded U–Pb ages of 500 ± 17 Ma and 513 ± 19 Ma, respectively, aligning with the mid-Cambrian depositional age. In contrast, a coarse crystalline dolomite gave an age of 478 ± 23 Ma, with a significantly lower initial Pb value, indicating a disturbed U–Pb system due to U loss. An open U–Pb system was also observed in bioapatite, as shown by its highly scattered and unreliable U–Pb ages.

Three bioapatite samples from dolostone yielded *in situ* Lu–Hf ages of 497 ± 69 Ma, 495 ± 79 Ma, and 493 ± 74 Ma that overlap with the mid-Cambrian depositional age. However, the large age uncertainties (~15%), due to low Lu concentrations, limit the ability to draw more definitive conclusions from these ages. Additionally, bioapatite from the phosphorite sample yielded an *in situ* Lu–Hf age of 425 ± 49 Ma, corresponding to the Rodingan event.

Overall, these results suggest that the Lu–Hf system is likely more reliable or robust (with respect to diagenetic resetting) than the U–Pb system for dating authigenic bioapatite. In addition to being affected by low U concentrations and high common Pb content, the U–Pb system is more susceptible to disturbance due to the mobility of both U and Pb (Lan et al., 2025; Robert et al., 2020; Simpson et al., 2024). However, obtaining high-precision Lu–Hf ages requires sufficiently high Lu concentrations (Simpson et al., 2021), which are however rarely present in marine authigenic minerals. In contrast, the Rb–Sr system in glauconite is known to be sensitive to diagenetic alteration (Ireland et al., 1983; Scheiblhofer et al., 2022; Selby, 2009), which was also confirmed by results and *in situ* Rb–Sr ages from this study. Systematic petrographic screening and high-resolution SEM/EDS imaging are essential for identifying suitable authigenic minerals for *in situ* dating, ensuring reliable data and interpretations.

5.1.2 Glauconite K and Mg Isotopes and Past Seawater Chemistry and Diagenesis

Studied mid-Cambrian glauconite pellets from the Cambrian Georgina Basin (Australia) and the North China Craton (NCC, China) exhibit notable heterogeneity, including variations in color, size, morphology, porosity, and the presence of inclusions such as dolomite, calcite, apatite, and pyrite. These characteristics indicate complex diagenetic histories of the studied glauconites. Significant variations in δ^{41}K and δ^{26}Mg values were observed in glauconite from both the Georgina Basin and the NCC, with δ^{41}K values ranging from -0.41‰ to -0.11‰ and δ^{26}Mg values spanning from -0.52‰ to 0.61‰. These variations reflect K and Mg isotopic fractionation caused by diagenetic processes such as illitization and the presence of carbonate inclusions. Specifically, progressive illitization tends to lead to heavier or higher δ^{41}K and δ^{26}Mg values, whereas carbonate inclusions result in lighter or lower δ^{26}Mg.

Assuming similar isotopic fractionation between modern seawater (sw) and glauconite ($\Delta^{41}K_{\text{sw-glauconite}}$ = ~+0.90‰, $\Delta^{26}Mg_{\text{sw-glauconite}}$ = 0.00‰) (Löhr et al., 2023; Löhr et al., 2025, under review; Shaikh et al., 2024), the inferred δ^{41}K and δ^{26}Mg values for mid-Cambrian seawater are estimated to range from +0.45 to +0.65‰, and -0.20 to +0.10‰, respectively. These values are both higher or isotopically heavier than the modern seawater values (i.e., +0.12‰ for δ^{41}K and -0.83‰ for δ^{26}Mg; Ling et al., 2011; Wang et al., 2021). Such higher δ^{41}K of the Cambrian seawater points to more intense reverse weathering, which releases CO_2 into the atmosphere, contributing to the higher temperatures during the Cambrian period (Scotese et al., 2021). The inferred higher or heavier δ^{26}Mg values of the mid-Cambrian seawater are likely due to large-scale dolomite formation, a process largely absent in modern oceans.

5.1.3 Multi-Proxy Isotope Chemostratigraphy of Mid-Cambrian Carbonates Across the DICE Event

Mid-Cambrian sedimentary records from the Georgina Basin from three correlative wells reveal a complete transgressive–regressive cycle, which can be stratigraphically divided into three stages: (a) an initial phase of shallow-water peritidal to restricted marine carbonate deposition during a relative sea-level lowstand (Sequence 1); (b) a transgressive phase characterized by deepening water and stratified, suboxic to anoxic conditions, with increased siliciclastic input and Ca-carbonate accumulation (early Sequence 2); and (c) a final regressive phase characterized by a return to shallow, restricted marine to supratidal environments, with dolostone-dominated sedimentation during sea-level fall (late Sequence 2).

Carbonate-based δ^{26}Mg record of dolostones seems relatively resistant to later stage diagenesis (due to the high Mg content in dolomite) and can thus potentially retain primary marine δ^{26}Mg signals as a reflection of mid-Cambrian seawater Mg isotope composition or dolomitization processes. In contrast, δ^{13}C proxy record, and especially δ^{18}O values, from Sequence 1 show signs of possible alteration, likely due to deep burial or meteoric fluids. Sequence 2 carbonates are better preserved, with δ^{13}C values aligning well with the expected mid-Cambrian seawater. The negative DICE event is recorded within transgressive Sequence 2 and is characterized by a δ^{13}C shift of up to –3.89‰, correlating well with equivalent global carbon isotope excursions (Babcock et al., 2004; Babcock et al., 2007; Howley and Jiang, 2010; Pagès and Schmid, 2016; Yang et al., 2021; Zhu et al., 2006).

Similarly, ^{87}Sr/^{86}Sr values from well-preserved, low-Mg limestones fall within the mid-Cambrian seawater range (~0.70880–0.70900; Chen et al., 2020; Peng et al., 2020), suggesting minimal diagenetic alteration. Intervals with elevated ^{87}Sr/^{86}Sr values correlate with higher Mn/Sr, Al, Rb, and Mg/Ca ratios, reflecting the influence of detrital silicate input and dolomitization. Phosphatic microfossils show variable ^{87}Sr/^{86}Sr values, with a strong negative correlation between fossil size and their ^{87}Sr/^{86}Sr values, indicating that smaller fossils are more susceptible to diagenetic alteration and resetting of primary marine Sr isotope signatures.

Finally, the mid-Cambrian carbonate $\delta^{26}Mg$ record or values from the Georgina Basin range from -3.05‰ to -1.00‰, showing a mixed trend between calcite and dolomite, with a negative correlation between $\delta^{26}Mg$ and Mg/Ca ratios. The lowest $\delta^{26}Mg$ value in dolomite is -1.92‰, and the lightest calcite value is -3.05‰. Based on the Mg isotope fractionation factor between seawater and dolomite ($\Delta^{26}Mg_{\text{sw–dolomite}}$ = ~1.73–2.00‰), the inferred mid-Cambrian paleo-seawater $\delta^{26}Mg$ value (based on our carbonate data) is approximately -0.19 to +0.08‰, which is generally consistent with previous studies (Hu et al., 2017; Xia et al., 2024).

5.2 Future Plans

5.2.1 Carbonate *in situ* Lu–Hf dating

This study highlights both the potential and limitations of novel *in situ* LA-ICP-MS/MS geochronology for dating various authigenic minerals, including carbonates, phosphates, and clays from the Narpa Group in the Georgina Basin. For phosphates, the Lu–Hf system has proven to be more robust than the U–Pb system (Glorie et al., 2024; Simpson et al., 2024). *In situ* Lu–Hf dating of carbonates is also an emerging technique with broad implications (Simpson et al., 2022; Simpson et al., 2024). Although U–Pb dating has been applied to carbonates in the Georgina Basin, *in situ* Lu–Hf dating of carbonates, especially well-preserved calcite cements, and recrystallized dolomite, deserves further investigation to constrain both depositional age and the timing of diagenesis, even though most samples examined in this study contain limited (typically < 2 ppm) Lu concentrations.

5.2.2 Glauconite Fe isotopes Tracing Redox Conditions and Diagenesis in Basins

In this thesis, suboxic to anoxic seawater column conditions are proposed for Sequence 2 (DICE) in the central and northern platform of the Georgina Basin. There is a potential to use redox-sensitive metal isotope proxies such as iron isotopes in glauconites to further constrain paleo-redox conditions in the basin, or during later stage diagenetic processes.

Glauconite is a K, Mg, and Fe-rich authigenic clay mineral that typically forms as a result of reverse weathering at the seawater-sediment interface (Löhr et al., 2024; López-Quirós et al., 2019; Rubio and López-Pérez, 2024; Środoń et al., 2023). It is also considered as a potentially robust archive of paleo-seawater geochemistry, climate, and sea-level changes (Banerjee et al., 2016; Bayon et al., 2023; Scheiblhofer et al., 2022; Środoń et al., 2023). Iron (Fe) is highly sensitive to changes in marine redox conditions, and Fe isotopes (δ^{56}Fe) exhibit notable fractionation driven by redox processes and variations in Fe sources (Johnson et al., 2003; Meng et al., 2024; Ordoñez Rendón et al., 2024; Sperling et al., 2021).

In this thesis, glauconite-based K and Mg isotope variations have been used to infer the mid-Cambrian paleo-seawater K and Mg isotope compositions, and to assess the potential impact of post-depositional diagenetic alteration. Future studies could investigate Fe isotope variations (d^{56}Fe) in ancient glauconites, in combination with other redox-sensitive elements (including REEs and e.g., Ce anomalies), to trace changes in the redox conditions of paleo-seawater or marine pore fluids during glauconite formation, particularly during the DICE event. Such investigations may provide insights into the mechanisms underlying proposed redox shifts associated with the upwelling of euxinic mid-Cambrian seawater during episodes of global transgression. Additionally, further work is needed to evaluate the extent of diagenetic overprinting on the δ^{56}Fe proxy recorded in ancient glauconite archives.

5.3 References

Babcock, L.E., Rees, M.N., Robison, R.A., Langenburg, E.S. and Peng, S., 2004. Potential Global Standard Stratotype-section and Point (GSSP) for a Cambrian stage boundary defined by the first appearance of the trilobite Ptychagnostus atavus, Drum Mountains, Utah, USA. Geobios, 37(2): 149-158.

Babcock, L.E., Robison, R.A., Rees, M.N., Peng, S. and Saltzman, M.R., 2007. The global boundary stratotype section and point (GSSP) of the Drumian Stage (Cambrian) in the Drum Mountains, Utah, USA. Episodes Journal of International Geoscience, 30(2): 85-95.

Banerjee, S., Bansal, U., Pande, K., Meena, S., 2016b. Compositional variability of glauconites within the Upper Cretaceous Karai Shale Formation, Cauvery Basin, India: implications for evaluation of stratigraphic condensation. Sedimentary Geology 331, 12-29.

Bayon, G., Giresse, P., Chen, H., Rouget, M.-L., Gueguen, B., Moizinho, G.R., Barrat, J.-A., Beaufort, D., 2023. The Behavior of Rare Earth Elements during Green Clay Authigenesis on the Congo Continental Shelf. Minerals 13, 1081.

Bradshaw, B.E., Khider K., MacFarlane S., Carr L. and P., H., 2021. Tectonostratigraphic Evolution of the Centralian Superbasin (Australia) Revealed Through Three-Dimensional Well Correlations, Geoscience Australia.

Chen, X., Zhou, Y. and Shields, G.A., 2022. Progress towards an improved Precambrian seawater Sr/Sr curve. Earth-Science Reviews, 224: 103869.

Glorie, S., Hand, M., Mulder, J., Simpson, A., Emo, R. B., Kamber, B., Fernie, N., Nixon, A., Gilbert, S., 2024b. Robust laser ablation Lu–Hf dating of apatite: an empirical evaluation. Geological Society, London, Special Publications, 537(1): 165-184.

Haines, P.W., Hand, M. and Sandiford, M., 2001. Palaeozoic synorogenic sedimentation in central and northern Australia: a review of distribution and timing with implications for the evolution of intracontinental orogens. Australian Journal of Earth Sciences, 48(6): 911-928.

Hand, M., Mawby, J., Kinny, P. and Foden, J., 1999. U–Pb ages from the Harts Range, central Australia: evidence for early Ordovician extension and constraints on Carboniferous metamorphism. Journal of the Geological Society, 156(4): 715-730.

Howley, R.A. and Jiang, G., 2010. The Cambrian Drumian carbon isotope excursion (DICE) in the Great Basin, western United States. Palaeogeography, Palaeoclimatology, Palaeoecology, 296(1-2): 138-150.

Hu, Z., Hu, W., Wang, X., Lu, Y., Wang, L., Liao, Z. and Li, W., 2017. Resetting of Mg isotopes between calcite and dolomite during burial metamorphism: Outlook of Mg isotopes as geothermometer and seawater proxy. Geochimica et Cosmochimica Acta, 208: 24-40.

Ireland, B., Curtis, C., Whiteman, J., 1983. Compositional variation within some glauconites and illites and implications for their stability and origins. Sedimentology, 30(6): 769-786.

Johnson, C.M., Beard, B.L., Beukes, N.J., Klein, C., O'Leary, J.M., 2003. Ancient geochemical cycling in the Earth as inferred from Fe isotope studies of banded iron formations from the Transvaal Craton. Contributions to Mineralogy and Petrology 144, 523-547.

Khider, K., MacFarlane, S., Bradshaw, B.E., Carr, L. and Henson, P., 2021. The Centralian Superbasin (Canning, Amadeus, Georgina and Officer basins) Stratigraphic Review and Well Correlations.

Kruse, P., Dunster, J., Munson, T., 2013. Chapter 28: Georgina Basin, in Geology and Mineral Resources of the Northern Territory, Darwin: Northern Territory Geol. Surv. 28.1-28.56.

Lan, Z., Glorie, S., Löhr, S.C., Wang, R., Shen, B., 2025. Apatite Lu− Hf dating of late Archean banded iron formations. Geology, 53 (4): 338–342.

Ling, M.X., Sedaghatpour, F., Teng, F.Z., Hays, P.D., Strauss, J., Sun, W., 2011. Homogeneous magnesium isotopic composition of seawater: an excellent geostandard for Mg isotope analysis. Rapid Communications in Mass Spectrometry 25, 2828-2836.

Löhr, S., Zheng, X., Lv, Y., Weissgerber, J., Baldermann, A., Farkas, J., Abbott, A.N., 2023. Mineralogical, chemical and isotopic evolution of recent glauconite in two contrasting marine settings, Goldschmidt 2023 Conference. Goldschmidt.

Löhr, S. C., Khazaie, E., Farkas, J., Baldermann, A., Gilbert, S., Maas, R., Subarkah, D., Collins, A. S., 2024. Origin and Significance of Age Variability in the Glauconite Reference Material GL-O: Implications for In Situ Rb-Sr Geochronology. Geostandards and Geoanalytical Research, 49(1): 197-216.

López-Quirós, A., Escutia, C., Sánchez-Navas, A., Nieto, F., Garcia-Casco, A., Martín-Algarra, A., Evangelinos, D., Salabarnada, A., 2019. Glaucony authigenesis, maturity and alteration in the Weddell Sea: An indicator of paleoenvironmental conditions before the onset of Antarctic glaciation. Scientific Reports 9, 13580.

Meng, Z., Wang, Z., Ju, P., Zhou, X., Li, C., Zhang, Z., Zhang, X., Huang, K.-J., 2024. Marine redox fluctuations during the Marinoan glaciation. Global and Planetary Change 235, 104396.

Munson, T., 2014. Petroleum geology and potential of the onshore Northern Territory, 2014. Northern Territory Geological Survey.

Nixon, A., Glorie, S., Fernie, N., Hand, M., De Vries Van Leeuwen, A., Collins, A., Hasterok, D. and Fraser, G., 2022. Intracontinental fault reactivation in high heat production areas of central Australia: insights from apatite fission track thermochronology. Geochemistry, Geophysics, Geosystems, 23(12): e2022GC010559.

Ordoñez Rendón, L.G., Neugebauer, I., Thomas, C., Chiaradia, M., Waldmann, N., Ariztegui, D., 2024. Sediment-redox dynamics in an oligotrophic deep-water lake in Tierra del Fuego: insights from Fe isotopes. Journal of paleolimnology 72, 129-143.

Pagès, A. and Schmid, S., 2016. Euxinia linked to the Cambrian Drumian carbon isotope excursion (DICE) in Australia: Geochemical and chemostratigraphic evidence. Palaeogeography, Palaeoclimatology, Palaeoecology, 461: 65-76.

Peng, S.C., Babcock, L.E. and Ahlberg, P., 2020. The cambrian period, Geologic time scale 2020. Elsevier, pp. 565-629.

Piazolo, S., Daczko, N.R., Silva, D. and Raimondo, T., 2020. Melt-present shear zones enable intracontinental orogenesis. Geology, 48(7): 643-648.

Roberts, N. M., Drost, K., Horstwood, M. S., Condon, D. J., Chew, D., Drake, H., Milodowski, A. E., McLean, N. M., Smye, A. J., Walker, R. J., Haslam, R., Hodson, K., Imber, J., Beaudoin, N., Lee, J. K., 2020. Laser ablation inductively coupled plasma mass spectrometry (LA-ICP-MS) U–Pb carbonate geochronology: strategies, progress, and limitations. Geochronology, 2(1): 33-61.

Rubio, B., López-Pérez, A., 2024. Exploring the genesis of glaucony and verdine facies for paleoenvironmental interpretation: A review. Sedimentary Geology, 106579.

Scheiblhofer, E., Moser, U., Löhr, S., Wilmsen, M., Farkaš, J., Gallhofer, D., Bäckström, A.M., Zack, T., Baldermann, A., 2022. Revisiting Glauconite Geochronology: Lessons Learned from In-situ Radiometric Dating of a Glauconite-Rich Cretaceous Shelfal Sequence. Minerals 12, 818.

Scotese, C.R., Song, H., Mills, B.J., van der Meer, D.G., 2021. Phanerozoic paleotemperatures: The earth's changing climate during the last 540 million years. Earth-Science Reviews 215, 103503.

Selby, D., 2009. U-Pb zircon geochronology of the Aptian/Albian boundary implies that the GL-O international glauconite standard is anomalously young. Cretaceous Research, 30(5): 1263-1267.

Shaikh, J.I., Löhr, S., Baldermann, A., Farkaš, J., Abbott, A.N., Zheng, X.-Y., 2024. Marine glauconites: A potential new archive of paleo seawater magnesium isotopes, Goldschmidt Conference 2024. Goldschmidt.

Shao, Z., Farkaš, J., Glorie, S., Collins, S.A., Gilbert, E.S., Subarkah, D., 2025. Dating of marine authigenic minerals via in situ Rb–Sr, U–Pb, and Lu–Hf: A case study from the Georgina Basin, Australia. Chemical Geology: 123042.

Simpson, A., Glorie, S., Hand, M., Gilbert, S. E., Spandler, C., Dmitrijeva, M., Swain, G., Nixon, A., Mulder, J., Muenker, C., 2024. In situ apatite and carbonate Lu-Hf and molybdenite Re-Os geochronology for ore deposit research: Method validation and example application to Cu-Au mineralisation. Geoscience Frontiers, 15(5): 101867.

Simpson, A., Gilbert, S., Tamblyn, R., Hand, M., Spandler, C., Gillespie, J., Nixon, A., Glorie, S., 2021. In-situ LuHf geochronology of garnet, apatite and xenotime by LA-ICP-MS/MS/MS. Chemical Geology 577, 120299.

Simpson, A., Glorie, S., Hand, M., Spandler, C., Gilbert, S., Cave, B., 2022. In-situ Lu–Hf geochronology of calcite. Geochronology Discussions 2022, 1-18.

Smith, T., Kelman, A.P., Nicoll, R., Edwards, D., Hall, L., Laurie, J., Carr, L., 2013. An updated stratigraphic framework for the Georgina Basin, NT and Queensland. The APPEA Journal 53, 487-487.

Southgate, P. and Shergold, J., 1991. Application of sequence stratigraphic concepts to Middle Cambrian phosphogenesis, Georgina Basin, Australia. BMR Journal of Australian Geology and Geophysics, 12(2): 119-144.

Sperling, E.A., Melchin, M.J., Fraser, T., Stockey, R.G., Farrell, U.C., Bhajan, L., Brunoir, T.N., Cole, D.B., Gill, B.C., Lenz, A., 2021. A long-term record of early to mid-Paleozoic marine redox change. Science Advances 7, eabf4382.

Środoń, J., Williams, L., Szczerba, M., Zaitseva, T., Bojanowski, M.J., Marciniak-Maliszewska, B., Kuligiewicz, A., Starzec, K., Ciesielska, Z., Paszkowski, M., 2023. Mechanism of late diagenetic alteration of glauconite and implications for geochronology. Geochimica et

Cosmochimica Acta 352, 157-174.

Tenthorey, E., and B. Ayling. 2021. Geomechanical evaluation of a middle Cambrian unconventional oil and gas play in the southern Georgina Basin, northern Australia. Australian Journal of Earth Sciences 68.5: 697-716.

Varga, J., Raimondo, T., Morrissey, L., Kelsey, D.E. and Hand, M., 2022. Pressure-temperature-time constraints on gneiss dome formation in an intracontinental orogen. Journal of Metamorphic Geology, 40(3): 457-488.

Wang, K., Peucker-Ehrenbrink, B., Chen, H., Lee, H., Hasenmueller, E.A., 2021. Dissolved potassium isotopic composition of major world rivers. Geochimica et Cosmochimica Acta 294, 145-159.

Xia, Z., Li, S., Hu, Z., Bialik, O., Chen, T., Weldeghebriel, M.F., Fan, Q., Fan, J., Wang, X. and An, S., 2024. The evolution of Earth’s surficial Mg cycle over the past 2 billion years. Science Advances, 10(9): eadj5474.

Yang, X., Li, Z., Gao, B. and Zhou, Y., 2021. The Cambrian Drumian carbon isotope excursion (DICE) in the Keping area of the northwestern Tarim Basin, NW China. Palaeogeography, Palaeoclimatology, Palaeoecology, 571: 110385.

Zhu, M.-Y., Babcock, L.E. and Peng, S.-C., 2006. Advances in Cambrian stratigraphy and paleontology: integrating correlation techniques, paleobiology, taphonomy and paleoenvironmental reconstruction. Palaeoworld, 15(3-4): 217-222.

Appendix

Conference Abstracts

1. Goldschmidt 2025 Conference Abstract 1

Abstract #27917

Abstract Information

Abstract ID:
27917

Primary Session:
12c-O2 The Evolution of Seawater Chemistry Through Time: Insights into Interactions Among Earth's Spheres

Secondary Session:
07a - Application and development of non-traditional geochemical (isotope) proxies for paleoclimate & environment

Abstract Title:
Potassium Isotope Variations (δ^{41}K) in Cambrian Glauconites from Australia and China: Insights into Paleo-Seawater and Diagenetic Alteration

Authors (presenting author in bold):
Zhufu Shao[1], Juraj Farkaš[1], Xin-Yuan Zheng[2], Alan S. Collins[3] and Dr. Stefan Löhr[1], (1)Metal Isotope Group (MIG), Earth Sciences, University of Adelaide, (2)University of Minnesota - Twin Cities, (3)University of Adelaide

Abstract Text:

Reverse weathering in the oceans acts as a critical sink for alkali/alkaline earth metals (e.g., K^+, Rb^+, Li^+, Mg^{2+}) derived from silicate weathering through the formation of authigenic clay minerals. K isotopes undergo significant fractionation during low-temperature continental weathering and reversing weathering processes [1]. Glauconite, a common marine authigenic clay mineral, is a plausible archive of paleo-seawater and marine pore fluid K isotope compositions. However, K isotope fractionation during glauconite formation and post-depositional diagenesis remains poorly understood. Additionally, the evolution of K isotopic composition of paleo-seawater over geological time remains unconstrained.

This study presents δ^{41}K data and *in situ* Rb-Sr dating of glauconite samples from the mid-Cambrian Georgina Basin (Australia), and the southeastern North China Craton, with depositional ages ranging from ~514 Ma to ~504 Ma. Petrographic and elemental analyses reveal that most glauconite samples exhibit high porosity, extensive illitization and secondary mineral reprecipitation, consistent with post-depositional alteration. *In situ* glauconite Rb-Sr dating yielded 'reset' ages ranging from 451±13 Ma to 349±9 Ma. Glauconite K isotopic measurements (δ^{41}K against NIST SRM3141a) show considerable variability, ranging from -0.57‰ to -0.11‰. Illitization of glauconite caused K and Rb loss, with Al substituting for Fe and Mg, and is associated with systematically higher δ^{41}K values. δ^{41}K also correlates with Rb-Sr ages, with more extensively reset samples showing higher values.

Despite diagenesis, the least altered glauconite appears to preserve the mid-Cambrian seawater K isotopic signatures. Assuming the isotopic fractionation between present-day seawater and recent glauconite ($\Delta^{41}K_{SW\text{-}glauconite} \approx 0.92‰$; [2]) applies to mid-Cambrian glauconites, the estimated mid-Cambrian seawater δ^{41}K is 0.52 ± 0.2‰, about 0.4‰ heavier than present-day seawater δ^{41}K value (-0.8 ± 0.1‰, [2]). This indicates intensified reverse weathering in the mid-Cambrian ocean, likely linked to elevated CO_2 in the atmosphere, high surface temperatures, and enhanced continental weathering, consistent with increased mid-Cambrian seawater $^{87}Sr/^{86}Sr$ ratios observed.

References

[1] Wang, et al., 2021. Dissolved potassium isotopic composition of major world rivers. Geochimica et Cosmochimica Acta 294, 145-159.

[2] Löhr, et al., 2025. Marine clay authigenesis controls seawater potassium isotope composition. Under review.

Keywords:
Cambran seawater, Glauconte and K isotopes

Submitter's E-mail Address:
zhufu.shao@adelaide.edu.au

Submitter Full Name:
Zhufu Shao

2. Goldschmidt 2023 Conference Abstract 1

Goldschmidt 2023 Abstract
https://doi.org/10.7185/gold2023.16352

In-situ triple dating (Rb-Sr, Lu-Hf, U-Pb) of carbonate-hosted glauconite and bioapatite from the Middle Cambrian Georgina Basin, Australia

ZHUFU SHAO[1,2], JURAJ FARKAS[2], ALAN S. COLLINS[1,3], STIJN GLORIE[2], DARWINAJI SUBARKAH[2], SARAH GILBERT[4], DR. STEFAN LÖHR, PHD[2], CHARLES VERDEL[5], DR. DIANA ZIVAK, PHD[2] AND CARL SPANDLER[2]

[1]Metal Isotope Group (MIG), Earth Sciences, University of Adelaide
[2]University of Adelaide
[3]University of Adelaide, Earth Sciences
[4]Adelaide Microscopy
[5]Northern Territory Geological Survey (NTGS), Alice Springs, Australia
Presenting Author: zhufu.shao@adelaide.edu.au

In-situ laser ablation inductively coupled plasma mass spectrometry (LA-ICP-MS and MS/MS) techniques are useful for directly dating authigenic minerals and fossils, providing valuable insights into depositional ages and stratigraphic correlation, as well as diagenetic and isotopic overprinting within sedimentary basins. The feasibility of in-situ Rb-Sr, Lu-Hf and U-Pb dating techniques are tested here using carbonate-hosted glauconite and bioapatite from the Thorntonia and overlying Currant Bush Formations of the Mid-Cambrian Georgina Basin (expected depositional age of 505 ± 2 Ma).

A U-Pb age of 501 ± 22 Ma was obtained for fine-crystalline dolomite from the Thorntonia Formation, interpreted to record 'primary' carbonate precipitation or an early marine dolomitization event. In contrast, a medium to coarsely crystallized dolomite yielded a younger age of 459 ± 22 Ma, suggesting a diagenetic origin. In addition, U-Pb dating of dolo-micrite from the Currant Bush Formation produced an age of 506 ± 25 Ma, within uncertainties of the U-Pb fine-crystalline dolomite and the Lu-Hf bioapatite ages. For the latter, in-situ Lu-Hf dating of bioapatite produced dates ranging from 499 ± 98 Ma to 473 ± 157 Ma, which overlap with the depositional age, but with significant uncertainties. The large uncertainties are due to low Lu concentrations (0.5-2 ppm with 120μm spot size) within the studied fossils.

Finally, in-situ Rb-Sr dating of glauconite yielded younger dates ranging from 439 ± 16 Ma to 402 ± 13 Ma, which are interpreted to record the later post-depositional events. The glauconite Rb-Sr system is readily reset, but the dates appear geologically meaningful and likely reflect isotopic disturbances during the Rodingan orogenic event (~450 to 430 Ma). Secondary coarsely crystallized dolomite U-Pb ages also appear to record the same event.

Overall, our triple dating approaches (in-situ Rb-Sr, Lu-Hf and U-Pb) demonstrate different behaviours of these geochronometers during the post-depositional histories, linked to complex factors such as mineralogy, porosity/recrystallisation, and ambient diagenetic conditions.

Encouragingly, the Lu-Hf dates for fossil bioapatite, U-Pb dates of dolo-micrite, and early finely crystalline dolomite overlap with the expected depositional age, suggesting these methods can potentially yield stratigraphic age constraints provided sufficient parent isotope concentrations.

3. Goldschmidt 2023 Conference Abstract 2

Goldschmidt 2023 Abstract
https://doi.org/10.7185/gold2023.16372

New ways to date old rocks: novel applications of in situ geochronology to constrain the sedimentary archive

DARWINAJI SUBARKAH[1], ANGUS NIXON[2], ALAN S. COLLINS[3], SARAH GILBERT[4], MORGAN L. BLADES[3], GEORGINA M. VIRGO[1], ALEXANDER SIMPSON[1], ZHUFU SHAO[1] AND JURAJ FARKAS[3]

[1]University of Adelaide
[2]The University of Adelaide
[3]University of Adelaide, Earth Sciences
[4]Adelaide Microscopy
Presenting Author: darwinaji.subarkah@adelaide.edu.au

Ancient marine sedimentary rocks provide important insight into how the planet's surface environments have evolved through deep time. However, they can be difficult to date. This is particularly true for Precambrian sediments, where the lack of a diverse fossil record makes biostratigraphy inapplicable. Here, we display emerging in situ laser-based methods that have the potential to quickly and accurately define the depositional window of a sedimentary package.

The first method aims to date authigenic clay minerals in shales using Rb–Sr geochronology [2]. A gas in a reaction-cell laser ablation–inductively coupled plasma–tandem mass spectrometer is used to remove the isobaric interference between ^{87}Rb and ^{87}Sr. The sample's petrographic information is preserved with this approach, and zones can be targeted for analysis to give a more accurate age. The second method aims to date carbonate sedimentation using U–Pb geochronology via an image mapping approach [1]. Laser rasters are compiled into isotopic maps, and this spatial information is used to target subdomains within the sample. Detrital or altered regions can be avoided by monitoring chemical signatures such as low Si and Mn/Sr ratios, respectively. Pixels corresponding to the most authigenic domains are then subdivided into analyses that give the best spread of data on an isochron. This can yield a more precise result for samples that may exhibit poor isotopic spread under traditional procedures.

These techniques were tested in several case studies in basin systems across Australia. Samples were sourced from the Mesoproterozoic greater McArthur Basin, the Neoproterozoic Adelaide Superbasin, and the Cambrian Georgina Basin. Results from each sample were accurate to the expected age of their respective formations based on tuff dating or biostratigraphic correlations. As such, we show that these new in situ dating approaches are powerful tools to constrain the sedimentary archive.

[1] Drost, Kerstin, et al. "An image mapping approach to U–Pb LA–ICP–MS carbonate dating and applications to direct dating of carbonate sedimentation." *Geochemistry, Geophysics, Geosystems* 19.12 (2018): 4631-4648.

[2] Subarkah, Darwinaji, et al. "Unraveling the histories of Proterozoic shales through in situ Rb-Sr dating and trace element laser ablation analysis." *Geology* 50.1 (2022): 66-70.

4. IAGS 2024 Conference Abstract

Diagenetic Constraints on Glauconite Rb–Sr Ages: In-Situ LA-ICP-MS/MS, Geochronology, Micropetrography, and Elements—A Case Study from the Mid-Cambrian Georgina Basin, Australia

Zhufu Shao[1,2], Juraj Farkas[1,2], Alan S. Collins[1,2], Sarah Gilbert[3], Darwinaji Subarkah[1],

[1] School of Physics, Chemistry and Earth Sciences, The University of Adelaide, Adelaide, SA 5005, Australia. [2] Mineral Exploration Cooperative Research Centre, The University of Adelaide, SA5005, Australia. [3] Adelaide Microscopy, The University of Adelaide, Adelaide, SA 5005, Australia

While glauconite has traditionally played a crucial role in dating depositional ages within sedimentary strata using methods such as K–Ar, Rb–Sr, K–Ca, and ^{40}Ar–^{39}Ar dating, conventional approaches involving chemical elemental separation are time-consuming and limit the amount of data realistically obtainable. Frequently, reported glauconite ages are observed to be younger than depositional ages. These are commonly assumed to result from burial diagenetic alteration. In this study, we introduce an innovative approach using laser ablation inductively coupled tandem quadrupole mass spectrometry (LA-ICP-MS/MS) for Rb–Sr dating of glauconite, complemented by petrographic analyses, high-resolution imaging, as well as quantitative major and trace element characterisation. The goal is to investigate the potential diagenetic overprinting of Rb–Sr ages in shallow marine ramp carbonate-hosted glauconite within mid-Cambrian sequences (ca. 505 Ma) from the Georgina Basin in Australia. Our observed younger ages can be categorised into approximately 450–410 Ma (Age Group 1, AG1) and around 400–350 Ma (Age Group 2, AG2). These closely correspond to two episodes of the Alice Springs Orogeny, specifically the Rodingan and Pertnjara-Brewer events. Early dissolution and illitization were the primary factors driving the first-stage alteration of glauconite (AG1), while de-illitization and dolomitization played key roles in the second-stage alteration (AG2). Apatite, dolomite, and calcite were prevalent inclusions within glauconite, impacting the overprinted ages, with AG1 glauconite being richer in impurities. Additionally, quartz and pyrite inclusions were observed in the glauconite, although they didn't significantly influence the rejuvenated ages. We conclude that orogenesis was crucial in promoting burial fluid-rock interaction, leading to the dissolution of glauconite with subsequent illitization. This was followed by de illitization, accompanied by phosphatization, calcification, and dolomitization. These cumulative processes collectively re-equilibrated the Rb–Sr system within glauconite, ultimately resulting in the observed younger ages. Our study's refined age calibration method (NIST 610 + MDC) for LA-ICP- MS/MS data processing yielded ages 2–3% younger than those obtained through the traditional approach, showing enhanced precision with lower uncertainties.